QST-M-47

QST Takasaki Annual Report 2022

Takasaki Institute for Advanced Quantum Science

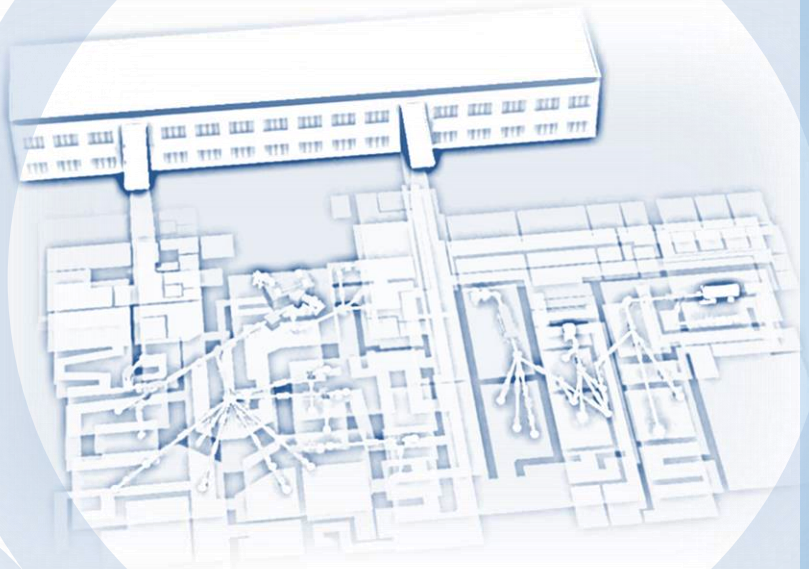

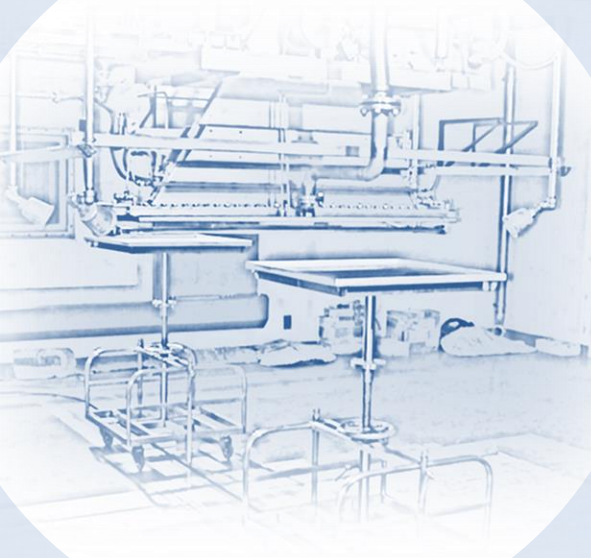

National Institutes for Quantum Science and Technology

Preface

MAEKAWA Yasunari

Director General
Takasaki Institute for Advanced Quantum Science
Foundational Quantum Technology Research Directorate
National Institutes for Quantum Science and Technology

The National Institutes for Quantum Science and Technology (QST) was established in April 2016 by combining two research directorates, Quantum Beam Science and Nuclear Fusion Research in the Japan Atomic Energy Agency (JAEA), with the National Institute of Radiological Sciences (NIRS). Currently, the QST has three research and development (R&D) directorates: Foundational Quantum Technology Research, Quantum Life and Medical Science, and Fusion Energy. The Foundational Quantum Technology Research Directorate comprises the Takasaki Institute for Advanced Quantum Science, the Kansai Institute for Photon Science, and the Institute for Advanced Synchrotron Light Source. Using advanced beam facilities, we conducted intensive fundamental and applied research in fields such as quantum materials and applications, materials science, life science, and quantum beam technology. The Takasaki Institute manages three main radiation facilities: Takasaki Ion Accelerators for Advanced Radiation Application (TIARA), a 2 MeV electron accelerator, and ^{60}Co gamma-ray irradiation facilities.

At the Takasaki Institute in the fiscal year 2022 (FY2022), we had 19 research projects and groups conducting quantum technology and quantum beam science R&Ds with the aforementioned three main radiation facilities, which contributed to the development of science and technology as well as the promotion of industry. The Quantum Materials and Applications Research Center (QUARC) was established in 2022 as “Quantum Functionalization,” one of the Quantum Technology Innovation Hubs (QIH) in Japan, to conduct fundamental and applied research for developing quantum devices, such as quantum sensors, quantum bits, and spin transistors, based on wide-bandgap semiconductors, including diamonds and 2D materials. Furthermore, we conduct R&D on advanced ion beam technology at the Beam Engineering Section of the Department of Advanced Quantum Beam Technology. Our beam facilities are available to industry, academia, and governmental research institutes, and beam time is allocated to users based on the evaluation of their R&D programs.

This annual report covers research activities at the Takasaki Institute for FY2022. This report is composed of two parts. Part I describes the recent activities of all research projects and groups. Part II presents recent R&D results obtained using the quantum beam facilities of QST Takasaki. This part contains 67 research papers in the fields of quantum materials and applications, materials science, life science, and advanced quantum beam technology, as well as eight status reports on the operation and maintenance of the quantum beam facilities.

The following three topics are the research highlights for FY2022. Electron spin waves in semiconductors have been successfully observed electrically in the field of quantum materials. These waves are expected to be new information carriers that enable parallel computation via wave superposition. However, electron spin waves have only been detected optically and can be observed in a limited number of materials that absorb light. Therefore, electron spin waves must be detected in various semiconductors. In this study, a new principle was established to electrically observe waves in various semiconductors. These results greatly expand the range of material selection and advance the development of semiconductor materials for electron spin-wave information processing. In the field of materials science, a new analytical method incorporating partial scattering functions into small-angle neutron scattering measurements has been applied to a "graft-type PEM" fabricated by radiation-induced graft polymerization, which is used in many products such as button cells and salt production membranes. For the first time, this technique revealed that the grafted polymer and water in the hydrophilic phase are independently linked in a phase-separated structure, which has not been clarified for many years. These results provide structural design guidelines for PEMs with excellent ionic conductivity and stability. This is expected to significantly improve the power-generation performance and durability of fuel cells. In the field of life sciences, ^{11}C-photosynthates in rice plants have been imaged. They selectively deliver carbon to their roots, which extend deep into the ground in search of water. In this study, a new imaging technique was developed to explore the function of underground roots by combining X-ray CT with positron imaging to visualize the movement of nutrients in the plant body. Using this technique, the movements of carbon in a soil environment in which rice roots were subjected to drought and in a soil environment with sufficient moisture were observed and compared. The results showed that under drought, the roots distributed nutrients to roots growing downward in search of water deep underground, whereas when the soil moisture increased, they distributed nutrients to roots developing laterally near the ground surface. Rice plants have been shown to adapt differentially to the dynamics of photosynthate translocation, depending on soil and water conditions.

An azimuthally varying field (AVF) cyclotron and three electrostatic ion beam accelerators at TIARA, as well as a MeV electron accelerator and ^{60}Co gamma-ray irradiation facilities, have been operated continuously and safely. The key components of the accelerator system at TIARA are updated annually to maintain global technological superiority. In this fiscal year (FY2022), we developed a new elemental imaging system that analyzes sputtered secondary ions from the surface of a sample using a MeV energy C60 ion microbeam from a 3 MV tandem accelerator. This system is expected to be a powerful tool for visualizing the distribution of polysaccharides in plants with micrometer-level resolution. We plan to replace the electron accelerator with a new accelerator, which will be primarily dedicated to developing quantum materials and is scheduled for completion in FY2026.

Finally, we would like to extend our gratitude to our domestic and foreign colleagues for their cooperation and support in our quantum technology and quantum beam science R&D and the technological advances in the facilities of QST Takasaki.

Quantum Beam Facilities in QST Takasaki

Takasaki Ion Accelerators for Advanced Radiation Application (TIARA) consisting of four ion accelerators, an electron accelerator, and gamma-ray irradiation facilities are available to researchers in QST and other organizations for R&D activities on new functional and environmentally friendly materials, biotechnology, radiation effects of materials, and quantum beam analysis. We are developing various shape area irradiation technique at the cyclotron. In addition, technical developments of elemental map imaging by C_{60} fullerene microbeam at the electrostatic accelerators are in progress.

Takasaki Ion Accelerators for Advanced Radiation Application: TIARA

TIARA facility

Cyclotron

Tandem accelerator

Single-ended accelerator

Ion implanter

Typical available ions

Accelerator	Ion	Energy (MeV)
AVF Cyclotron (K=110MeV)	H	10～ 80
	He	20～107
	C	75～320
	Ne	75～350
	Ar	150～520
	Fe	200～400
	Kr	210～520
	Xe	324～560
	Os	490
Tandem Accelerator (3 MV)	H	0.8～ 6.0
	C	0.8～18.0
	Ni	0.8～18.0
	Au	0.8～18.0
	C_{60}	0.8～9.0
Single-ended Accelerator (3 MV)	H	0.4～ 3.0
	D	0.4～ 3.0
	He	0.4～ 3.0
	e^-	0.4～ 3.0
Ion Implanter (400 kV)	H	0.02～0.38
	Ar	0.02～0.38
	Bi	0.02～0.37
	C_{60}	0.02～0.36

Energy-element range covered by the four accelerators

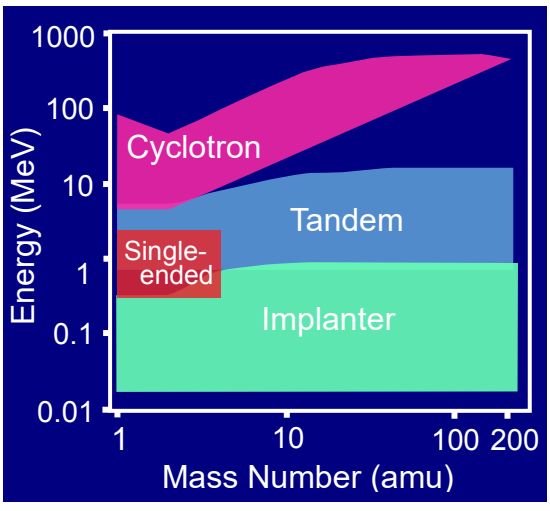

Cobalt-60 gamma-ray and electron beam irradiation facilities

Gamma-ray irradiation facility building

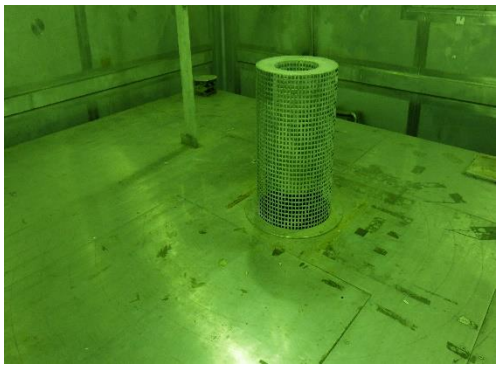

Gamma-rays irradiation room

Electron accelerator
(0.5～2.0 MeV, 0.1～30 mA)

Electron irradiation room with conveyor system

Specification

Apr. 2023

Name of facility	Cobalt-60 activity (PBq)	Number of rooms	Principal utilization
Co No.1 bld.	4.5	3	Radiation-resistance test, radiation effects on materials as polymers, semiconductors, and biological substances as bacteria, cell, plant
Co No.2 bld.	6.5	3	R & D on functional organic materials, inorganic materials and dosimetry

Dose-rate range

Unit：kGy/h

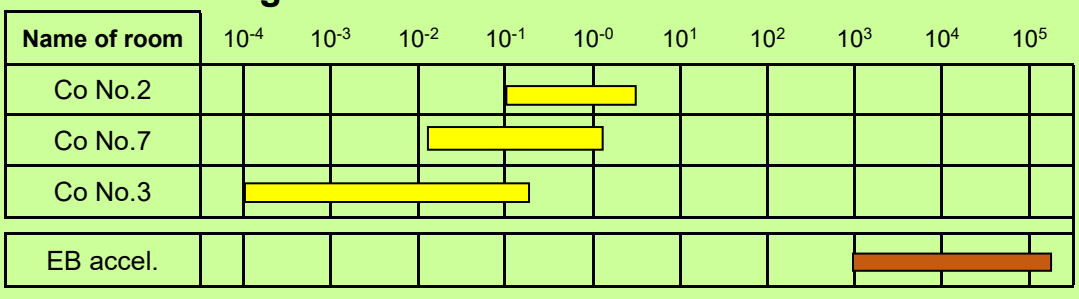

Contents

Appendix

Part Ⅰ

Part Ⅰ

1. Quantum Materials and Applications

P1-1 Quantum Sensing Project

Leader : OHSHIMA Takeshi

To realize Super Smart Society, it is necessary to develop quantum technologies such as quantum sensing, quantum information and quantum computing. Therefore, R&D for quantum technologies are intensively carried out all over the world now. Quantum Sensing Project studies quantum technologies based on spin defects/single photon emitters formed in wide bandgap semiconductors. For example, we create nitrogen-vacancy (NV) center in diamond and silicon vacancy in silicon carbide (SiC) using energetic particle irradiation (both ion and electron beams) and investigate their optical/spin properties in order to obtain high quality quantum sensors/spin qubits. We also study the radiation effects on semiconductor materials and devices to develop radiation resistant technologies for space and nuclear applications, of which technologies can be applied to quantum devices used in such harsh environments in the future.

Electrical detection of nuclear spins using V_{Si} in SiC

Negatively charged silicon vacancy (V_{Si}) at a qubic lattice site in SiC is known as a quantum defect of which spin can be manipulated even at room temperature or higher [1]. Optical magnetic resonance (ODMR) is used as the most popular methodology to manipulate spins in spin defects. However, an electrical readout technique is also important for miniaturizing and integrating quantum and classical devices. In a previous study, Niethammer *et al.* reported photocurrent-detected magnetic resonance (PDMR) for V_{Si}. In this study [2], we electrically observe the spin coherence of the V_{Si} and clearly resolve the hyperfine splitting of the electron spin signal for the V_{Si} coupled with next-nearest-neighbor ^{29}Si atoms. Furthermore, we apply PDMR to electron–nuclear double resonance (PD-ENDOR) to detect nuclear magnetic resonance of ^{29}Si at room temperature and find that this method can resolve nuclear spins coupled with neighboring electron spins in V_{Si}s. The realization of PD-ENDOR is expected to be a critical step toward the development of electrically driven integrated quantum devices.

In this study, 4H-SiC with 50 μm tick n-type epitaxial layer grown on n-type 4H-SiC substrate was used. V_{Si}s were created in SiC samples by 2 MeV electron irradiation at 1×10^{17} /cm^2 at room temperature. After irradiation, samples were annealed at 600 °C for 30 min in Ar atmosphere to reduce residual defects. Ti electrodes covered with Pt/Au were formed on the samples. PDMR measurements were carried out under the external magnetic field of ~4.56 mT at room temperature. Laser with 905 nm wavelength was applied for the excitation of V_{Si}.

Figure 1 shows pulsed PDMR signal observed with microwave pulse length of 200 ns. Two peaks with a separation of 140.0 MHz are obtained as shown in Fig. 1.

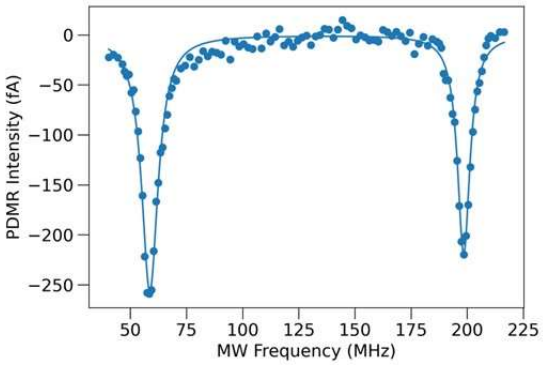

Fig. 1 PDMR spectrum. Dot symbol represents experimental results. The solid line is a Lorentzian fitting result. [2]

The difference between those two peaks correspond to 4D (where D=35 MHz [3]), and peaks at 58.4 and 198.4 MHz indicate the transition of spin sublevel -1/2 ↔ -3/2 and +1/2 ↔ +3/2, respectively.

Furthermore, we obtained a pulsed PDMR spectrum clearly resolving the selective electron spin transitions. Thus, a central peak at 197.7MHz and two weak side peaks separated by 4.4±1 MHz from the central peak were observed. These side peaks indicate the nuclear-spin-selective transitions, which is caused by the hyperfine interaction with the NNN ^{29}Si. Finally, PD-ENDOR signal was also obtained [2]. Thus, three peaks at RF frequencies of 11.68±0.02, 12.37±0.03, and 12.81±0.02 MHz were observed. And, the peak intensity was 0.29±0.10 : 0.40±0.14 : 0.82±0.16, or approximately 1:1:2. The hyperfine constants obtained by our PD-ENDOR experiment agree well with those from the W-band study, except for A = 8.41 MHz. Although the detailed peak assignment still remains as further investigations, the obtained result indicates that PDMR is promising methodology toward selective coherent control of nuclear spins, facilitating the development of electrical-driven integrated quantum applications.

References

[1] S. Motoki *et al.*, J. Appl. Phys. **133**, 154402 (2023). DOI: 10.1063/5.0139801

[2] T. Nishikawa *et al.*, Appl. Phys. Lett. **121**. 184005 (2022). DOI: 10.1063/5.0115928

[3] E. Janzen *et al.*, Physica B **404**, 4354 (2009). DOI: 10.1016/j.physb.2009.09.023

P1-2 Spin-photonics in 2D Materials Project

Leader : SAKAI Seiji

Our project aims to develop novel spin-photonic devices for future information technology applications by taking advantages of the low dimensionality and quantum electronic properties of two-dimensional (2D) materials and related low-dimensional nanostructures. Advanced quantum beam techniques available at QST enable us to control and design the local atomic structures and spin-/photon-related properties in low-dimensional systems.

During this fiscal year, we developed a novel ferrimagnetic Heusler compound with a half-metallic-like band structure which also exhibits an extremely large perpendicular magnetic anisotropy (PMA) under a tetragonal lattice strain [1]. The ferrimagnetism, large PMA and possibility of high spin polarization in this material make it an ideal candidate for magnetic recording materials such as optical-to-electrical (O-E) conversion non-volatile memory devices used in future all-optical networks. Thanks to advanced experimental techniques, in particular QST's synchrotron Mössbauer spectroscopy, this novel material was successfully realized.

Development of half-metallic Heusler compound Mn_2FeGa with large perpendicular magnetic anisotropy

We demonstrated the development of novel ferrimagnetic cubic Heusler compound Mn_2Fe_xGa (MFG) thin films with large PMA and a half-metallic band structure. By growing MFG(x = 1.0~1.3) on a Cr buffer layer and optimizing the growth conditions, a ferrimagnetic inverse cubic full-Heusler (Xa) phase with a small saturation magnetization was obtained. A combined experimental and theoretical study revealed that the tetragonal strain in MFG induced by the buffer layer leads to large PMA which exceeds 0.75 MJm^{-3}, reaching a practical level (~1 MJm^{-3}) for ultra-high-density magnetic memory applications, without destroying the half-metallic nature of MFG. Ferrimagnetic cubic MFG with its small magnetization, large PMA, and possibility of being highly spin polarized make this material an ideal candidate for the development of O-E conversion non-volatile magnetic memory and other spin-photonic devices.

Figures 1(a) shows a transmission electron microscope (TEM) image for a stochiometric 30 nm-thick Mn_2FeGa thin film grown on a 20 nm-thick Cr buffer layer on a MgO(001) substrate. The sample showed a smooth film surface and clear interfaces between each of the layers. X-ray diffraction analysis revealed the epitaxial growth of a novel cubic phase in the range of $x \geq 1.0$ by using Cr as a buffer layer, whereas the growth of a tetragonal phase below x < 1.0. A tetragonal strain of ~5% was found to be induced in the cubic MFG thin films due to the lattice matching between cubic MFG and Cr.

Figure 1(b) shows the in-plane (IP) and out-of-plane (OP) magnetization curves for the stoichiometric MFG/Cr sample. It was found that all the MFG/Cr samples show an out-of-plane easy axis of magnetization. In the case of the stoichiometric sample composed of cubic MFG, the OP curve showed a square shape and large coercive field, meanwhile the IP curve showed no saturation by 7 T. The magnetocrystalline anisotropy energy evaluated from the IP and OP curves was greater than 0.75 MJm^{-3} in stoichiometric Mn_2FeGa. First-principles calculations demonstrated that the origin of the large PMA in cubic MFG is due to the specific electronic features of Fe *d* orbitals located around the Fermi level, which give rise to a large magnetocrystalline anisotropy under the tetragonal strain; and, furthermore, that the high spin polarization of cubic MFG due to its half-metallic nature can be preserved even under the tetragonal strain.

Finally, the local atomic structure and chemical ordering in the MFG thin films were explored using synchrotron Mössbauer spectroscopy. Figure 1(c) shows a synchrotron Mössbauer spectrum for the stoichiometric MFG/Cr sample. The sample exhibited a single magnetic component with a small internal magnetic hyperfine field of ~3 T and zero quadrupole shift. The magnetic moment of Fe atoms estimated from the hyperfine field was 0.25 μ_B. The zero quadrupole shift indicates a cubic symmetry in the local environment of Fe atoms. These results are well in agreement with theoretical expectations for the Fe atoms on the ideal atomic site in the Xa structure. This provides a direct proof of the formation of the half-metallic Xa phase with a high degree of chemical ordering in the cubic Mn_2FeGa thin film.

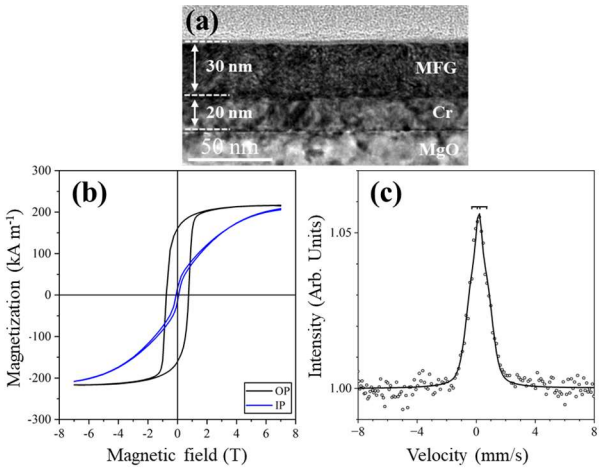

Fig. 1 (a) Cross-sectional TEM image, (b) magnetization curves and (c) synchrotron Mössbauer spectrum of Mn_2FeGa/Cr sample.

Reference

[1] P. D. Bentley *et al*., Phys. Rev. Mater. **7**, 064404 (2023). DOI: 10.1103/PhysRevMaterials.7.064404

P1-3 Laser-cooled Ion Research Project

Leader : NARUMI Kazumasa

Our project has two objectives: One is to develop an ultrahigh-precision single-ion-implantation system to create a nitrogen-vacancy (NV) center in diamond. The other is to establish fundamental technologies to realize a quantum computer based on ion traps. The key techniques for both the objectives are trapping ions and laser cooling.

Formation of a Coulomb crystal

When ions trapped in a linear Paul trap (LPT) are cooled enough with the Doppler laser-cooling technique, the balance between a confinement electric field and Coulomb repulsion among the ions makes the ions almost rest. This state is called a Coulomb crystal. The Coulomb crystal is regarded as a kind of important milestone in achievement of trapping and laser-cooling ions. We had been trying the formation of Coulomb crystals of calcium (Ca) ions and have succeeded in it. Figure 1 shows examples of Coulomb crystals, laser-induced-fluorescence (LIF) images observed with a CCD camera. In the figure, each spot represents a single $^{40}Ca^{+}$. The ions construct “string" and “shell” crystals in Fig. 1(a) and (b), respectively. The structure of a Coulomb crystal is determined by the number of ions and the transverse and longitudinal focusing forces.

Simulation study of ultrahigh-precision single-ion extraction from a linear Paul trap [1]

NV centers in diamond is regarded as a platform for some important quantum technologies because they can be applied to quantum bits (qubits) and quantum sensors. For such purposes, it is necessary to array NV centers in a nanometer scale. We are facing such a challenge with the single-ion implantation of nitrogen into diamond. Trapping and laser-cooling ions make it possible to provide extremely high-quality ion beams, whose emittance is close to zero. If an extremely low emittance is available, the beam size can be a nanometer scale with an appropriate focusing lens. Moreover, these techniques enable us to irradiate a target with single ions one by one.

In order to realize such ultrahigh-precision single-ion implantation, a detailed simulation study has been performed to explore the possibility of transporting a single ion precisely along a particular design beam line. We considered nitrogen (N) ions cooled sympathetically with ultracold Ca ions produced in an LPT by the Doppler laser-cooling technique. A single N ion almost completely frozen in the laboratory frame was extracted from the LPT by manipulating the axial potential barriers. We have conducted systematic 3D simulations taking account of a standard LPT structure and figured out the necessary conditions to achieve the ultrahigh-precision irradiation of any target with a single N ion. In addition to the “string” Coulomb crystal, we have shown that even the “shell” crystalline structure can be used for our purpose.

In the case of string-crystal ejection, it was found that the spatial arrangement of the two ion species was essential in minimizing the collisional heating effect. Specifically, the N ion has to be sitting at the position closest to the exit end of the trap; otherwise, it inevitably collides with the preceding Ca ion as the velocity of the extracted N ion is faster. Moreover, we can separate the leading nitrogen from all the others simply by switching a potential barrier on and off or by introducing a short mass-filtering section. The attainable root-mean-squared emittance of the N ions separated from properly arranged two-component crystals reaches the order of 10^{-16} m·rad in transverse dimensions perpendicular to the design beam line.

The use of a shell crystal may be more advantageous from a practical point of view because we do not have to make the extra effort to put a N ion at the head of the crystal; the ion species sitting on both ends of the two-component shell crystal is always N. We can launch only the leading N ion from the LPT by slowly increasing the Gate voltage. The quality of the ejected N ions is not seriously degraded, depending on the order of extraction.

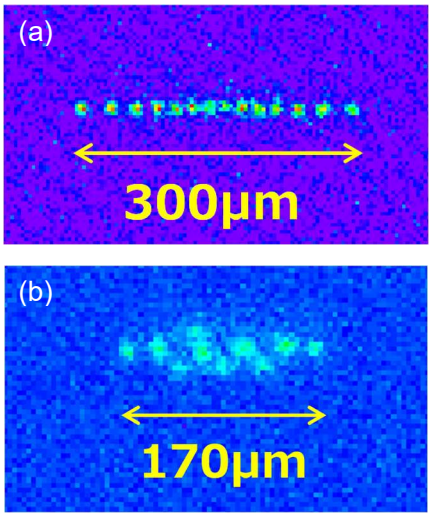

Fig. 1 LIF images of $^{40}Ca^{+}$ observed with a CCD camera: (a) a string crystal and (b) a shell crystal.

Reference

[1] K. Muroo *et al.*, Prog. Theor. Exp. Phys. **2023**, 063G01 (2023). DOI: 10.1093/ptep/ptad071

P1-4 Quantum Optical and Spin State Control Project

Leader : KOHDA Makoto

By precisely controlling defects in semiconductor quantum structures and in two-dimensional materials such as graphene, we aim to establish the quantum technology necessary for the future quantum information society. In particular, by utilizing a relativistic effect, we investigate a persistent spin helix where the electron spins rotate statesimultaneously by an effective magnetic field and generate an electron spin wave. We also focus on the precise control of the quantum state of a single electron spin by using a defect in widegap semiconductors such as diamond and SiC. We cover a broad spectrum of research ranging from the creation of two-dimensional materials to the optical and electrical control of spin defects, as well as quantum device applications utilizing spin degree of freedom in semiconductors.

Electrical detection of electron spin waves by quantum interference effects

In semiconductors, two types of electron spin waves can exist stably as eigenstates of the spin diffusion equation shown in Fig. 1(a) and (b) ((a) helical spin wave and (b) homogenous spin wave). However, due to the limitation of the optical selection rule, conventional optical detection methods can only detect the helical spin wave (Fig. 1(a)), and no method has been established to simultaneously detect all electron spin waves (Fig. 1(a) and (a)) that can be used as information carriers. We therefore focus on the quantum interference effect when an external magnetic field is applied. Based on the induced conductivity modulation, we propose and demonstrate the principle of electrically detecting two types of electron spin waves [1]. By focusing on the relaxation time of the electron spin waves in magneto-conductance, we derive a new theoretical expression for the quantum interference effect, and find the principle that the lifetimes of the two types of spin waves can be measured by electrical means. We then proceed to measure magneto-conductance at a temperature of T = 0.3 K using GaAs/AlGaAs semiconductor quantum wells. As a result, we succeeded in extracting the relaxation rates of helical and homogenous spin waves, as shown in Fig. 1(c). We are able to establish a basis for the simultaneous detection of multiplexed electron spin waves.

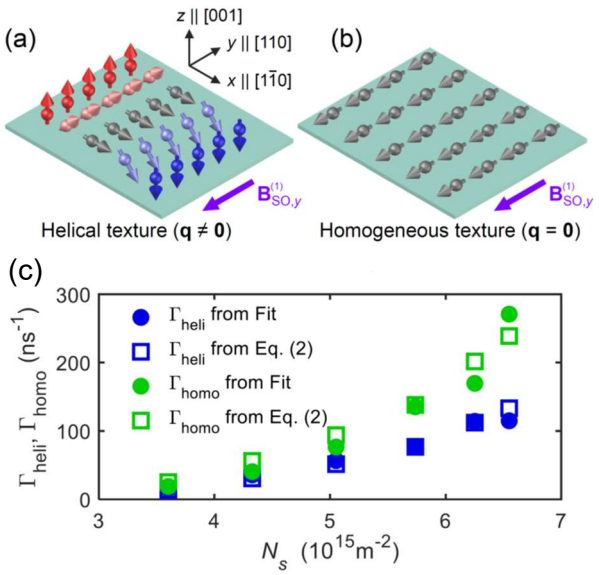

Fig. 1 Schematic diagrams of (a) helical spin wave (b) and uniform spin wave, which can exist stably in semiconductors. (c) Dependence of the relaxation rates of helical and uniform spin waves on the carrier concentration, obtained from quantum interference effects in magnetoconductivity measurements.

New principle of highly efficient magnetization reversal using spin currents

While the current magnetization reversal by spin current is established by introducing the spin current generated in the particular direction, we demonstrate the efficient magnetization reversal by simultaneous utilization of spin current generated in all directions [2]. By using full potential of spin current, low current density and magnetic field-free magnetization switching is achieved in epitaxial Cobalt / non-magnetic layer / perpendicularly magnetized ferromagnetic layer (Fig. 2). Because relative magnetization directions between bottom and top ferromagnetic layers are perpendicular to each other, x, y ad z directions of induced spin currents are contributed to magnetization reversal. This improvement in field-free magnetization switching efficiency is also achieved in a polycrystalline CoFeB/Ti/CoFeB structure fabricated by sputtering, which is currently the mass production method for nonvolatile magnetic memory.

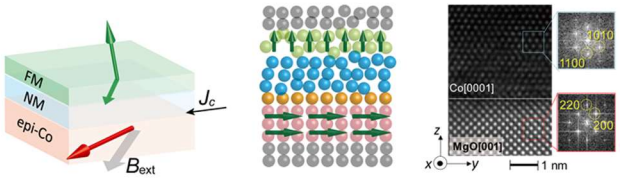

Fig. 2 New structure for magnetization switching with epitaxial Cobalt / non-magnetic layer / perpendicularly magnetized ferromagnetic layer. Bottom Cobalt layer is epitaxially grown on the substrate with strong magnetic anisotropy, enabling us to independently control the top and bottom magnetic layers.

References

[1] T. Saito *et al*., Physical Review Research **4**, 043217 (2022). DOI: 10.1103/PhysRevResearch.4.043217

[2] J. Ryu *et al*., Nature Electronics **5**, 217–223 (2022). DOI: https://doi.org/10.1038/s41928-022-00790-2

P1-5 Quantum Materials Theory Project

Chief : MATSUSHITA Yu-ichiro

To further accelerate the adoption of quantum devices, the challenge is to understand and improve device properties in detail and to reduce noise under real-world conditions. The Quantum Materials Theory Project will analyze the fundamental properties of quantum devices, search for new materials for quantum devices, and develop protocols for noise reduction under real-world conditions from an approach based on theoretical simulations in collaboration with the experimental groups at the Quantum Materials and Applications Research Center (QUARC).

Preparation of first-principles computational tools for the analysis of quantum sensing devices

This year, we started to develop a system for analyzing electronic states in quantum sensor devices. In particular, we aimed to semi-automate the analysis system for future efficient operation of the project. The stage on which the quantum sensor is manifested is a point defect in the bulk, which is a spin localized in the vicinity of the point defect. The principle of sensing is that the localized spins couple with the environment to be sensed and change their spin state. As an analysis program, we have constructed a system that automatically extracts the spin state localized at the defect from the bulk state (Fig. 1). Furthermore, we have implemented a function that automatically determines the symmetry of the wavefunction of the extracted localized spins and semi-automatically determines the transition selection rule between the ground and excited states. This is a first step towards more efficient wavefunction analysis in the future search for new semiconductor spin defects.

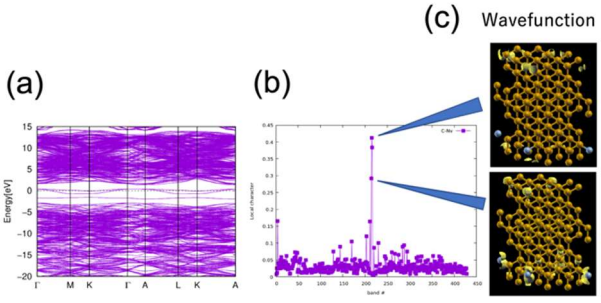

Fig. 1 (a) Electronic band structure of the calculation system with a point defect. (b) An indicator showing the localization of each wavefunction. (c) Wavefunctions corresponding to the peaks of the localization indicator.

Next, we started to develop the infrastructure for developing noise reduction protocols in quantum sensors. To achieve noise reduction in quantum sensors, we apply a pulse sequence protocol that extends the spin coherence time (T2), where the spin coherence time T2 is an important indicator of how robust the quantum sensor is to noise. Therefore, we first worked on the development of a computational scheme to calculate the spin coherence time T2 from first principles. Based on the Cluster Correlation Expansion (CCE) method, we can successfully calculate the spin coherence time T2 by generating a large number of clusters for the input localized spin distribution and calculating their contribution to the coherence function (Fig. 2.(c)). There, we can calculate the spin coherence time T2 when the pulse sequence, a noise reduction protocol, was given. In fact, Fig. 2(b) shows a typical pulse sequence, the Hahn echo, and Fig. 2(d) shows the result of the calculation, where you can see the change of the spin coherence time T2 when the time to give the π pulse is changed. Thus, we have prepared the basic simulation technology necessary to efficiently search for noise-reducing pulse-sequence protocols. In the future, we will search for protocols that extend the spin coherence time T2.

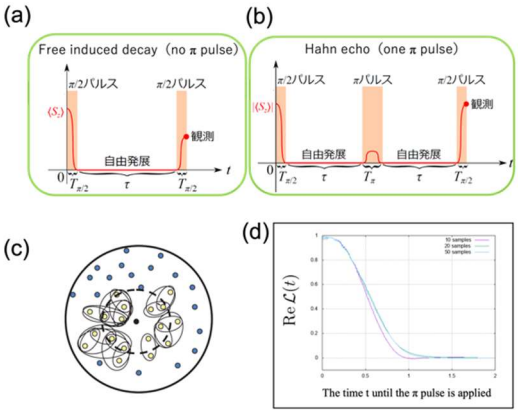

Fig. 2 (a)(b) Various types of pulse sequences for noise reduction. (c) Schematic showing the generation of a large number of clusters and compute the contribution to the coherence function. (d) Calculated spin coherence time T2 by the Hahn echo.

Theoretical discovery of skyrmions in two-dimensional layered matter

We have searched for novel skyrmion materials, which are also attracting attention as qubit materials for quantum computers. We have developed a simulation software for magnetic materials based on first-principles calculations. Using the simulation software, the properties of magnetic materials under finite temperature and external magnetic field can be calculated from first principles. In fact, we have applied the software to a two-dimensional layered material MCl_3 (M=Cr, V, Fe). As a result, we theoretically found the existence of a vortex texture of spin, so called skyrmion phase, in the two-dimensional layered material $CrCl_3$ [1]. Investigation of the physical origin of the skyrmion revealed that local spatial inversion symmetry breaking in the crystal structure of the two-dimensional layered material $CrCl_3$

generates a finite Dzyaloshinskii-Moriya interaction between the spins, which in turn manifests as a skyrmion. We also found that the skyrmion radius is the smallest in the world, and that replacing Cr with V causes the skyrmion vortex (helicity) to be in the opposite direction. This is the first reported case of predicting a skyrmion phase in a material without heavy elements and in a two-dimensional material.

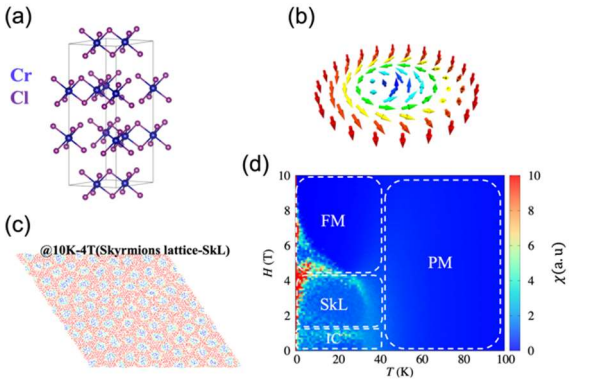

Fig. 3 (a) Crystal structure of the two-dimensional layered material $CrCl_3$. (b) Spin vortex structure of skyrmion. (c) Skyrmion texture appeared in $CrCl_3$. (d) Magnetic phase diagram of $CrCl_3$, where FM denotes ferromagnetic phase, PM denotes paramagnetic phase, SkL denotes skyrmion phase, and IC denotes incommensurate phase.

Reference

[1] H. Tran and Y. Matsushita, Scripta Materialia **239**, 115799(2024). DOI: 10.1016/j.scriptamat.2023.115799

P1-6 Rare-Earth Quantum Device Project

Chief : SATO Shin-ichiro

Rare-Earth Quantum Device Project aims to develop quantum devices based on gallium nitride (GaN), which has high quality and advanced microfabrication and device technologies, and rare-earth ions (RE^{3+}), which have excellent characteristics as qubits and single photon sources. RE:GaN quantum devices have the potential to realize "electrically controlled single photon sources in the optical communication wavelength band at room temperature," "on-chip quantum entangled light sources," and "real-time diagnostics inside GaN devices by quantum sensing," which have not been achieved to date. Currently, our project studies ion implantation and post thermal annealing for high efficiency optical activation of implanted RE ions in GaN, local atomic structure of implanted RE ions, development of quantum sensing using RE ions in GaN, and enhancement of spontaneous emission of implanted RE ions in GaN by coupling to photonic crystal.

Enhancement of near-infrared photoluminescence of neodymium ions in gallium nitride coupled to photonic crystal L3 cavity

Neodymium (Nd)-doped GaN (Nd:GaN) exhibits near-infrared (NIR) emission from the 4f-4f transition that is temperature insensitive, sharp, and stable. The photon emission is electrically controllable [1], and the well-developed GaN platform allows integration into more complex devices. These superior optical and optoelectronic properties are suitable for single photon sources (SPSs) which is a key technology for quantum computing and quantum communication. However, in order to realize Nd:GaN SPS, it is necessary to increase the photon emission rate for the optical detection of isolated single Nd ions. Our project studies the photon emission rate enhancement of Nd ions in GaN coupled to photonic crystal (PhC) L3 cavity based on the Purcell effect.

A resist film with 400 nm diameter holes was deposited as an ion implantation mask on a GaN epilayer on Si substrate, and 100 keV Nd ions were implanted at the dose of 1×10^{14} cm^{-2} at room temperature. Post-implantation thermal annealing was performed at 1200 °C for 2 mim in N_2 atmosphere to optically activate the Nd ions. PhC-L3 cavity structures were then fabricated on the Nd-implanted regions using nanofabrication techniques such as electron beam lithography and plasma etching. The optimal design parameters (hole spacing *a*, and hole radius *r*) were determined by FDTD simulation. As shown in Figs. 1(a) and 1(b), strong photoluminescence (PL) was observed from the Nd ions implanted in the center of PhC-L3 cavity. The emission peak at 916 nm resulting from the $^4F_{3/2}$ - $^4I_{9/2}$ transition in the 4f-shell [2] was significantly enhanced when compared to the PL from Nd ions without L3 cavity (Fig. 1(c)). This fact indicates that the spontaneous emission of Nd ions is enhanced by the Purcell effect. The Q value ($\Delta\lambda/\lambda$) was estimated to be about 400, which was slightly lower than the value obtained by the FDTD simulation (Q = 535). This is thought to be due to the deviation from the designed value (hole radius, circularity of holes, etc.) and thus the further improvement is possible by optimizing the nanofabrication process.

This work was supported by JST FOREST Program (Grant No. JPMJFR203G, Japan), JSPS KAKENHI (Grant No. JP18H01483, Japan), and the Foundation for Promotion of Material Science and Technology of Japan. Part of this study was conducted at the NIMS Nanofabrication Platform, supported by "Advanced Research Infrastructure for Materials and Nanotechnology in Japan (ARIM)" of the Ministry of Education, Culture, Sports, Science and Technology (MEXT), Proposal No. JPMXP1222NM0001.

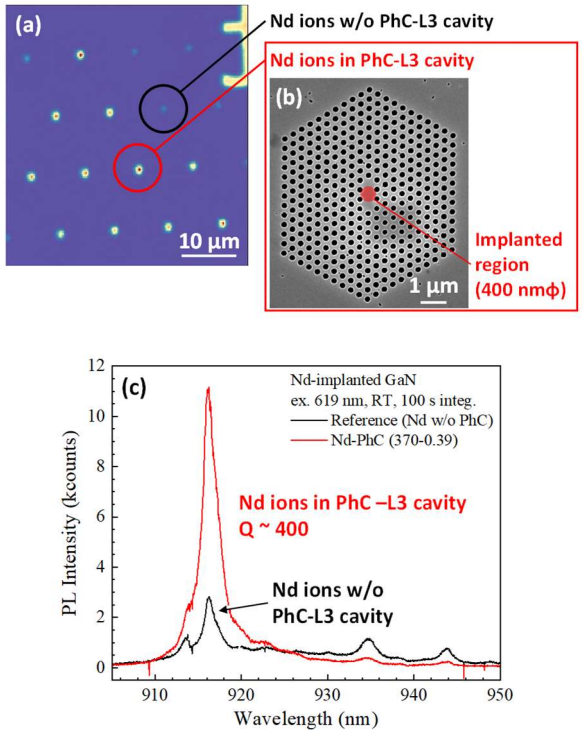

Fig. 1 (a) A two-dimensional PL map of implanted Nd ions. Bright spots are PL from Nd ions coupled to PhC-L3 cavity. (b) A SEM image of Nd-implanted PhC-L3 cavity (r = 370 nm, a/r = 0.39). (c) PL spectra of Nd ions coupled to PhC-L3 cavity (red) and Nd ions without cavity (black).

References

[1] J.H. Kim, P.H. Holloway, Adv. Mater. **17**, 91-96 (2005). DOI: 10.1002/adma.200306402

[2] S.-I. Sato *et. al.*, Opt. Mater. Express **10**, 2614-2623 (2020). DOI: 10.1364/OME.401765

P1-7 Quantum Materials Ultrafine Fabrication Project

Chief : YAMAMOTO Hiroki

Project “EUV Ultra-fine Fabrication” has been developing the functional polymer materials such as high-performance resist materials for extreme ultraviolet (EUV) and next generation EUV lithography. We have investigated dependence of dissolution kinetics of main-chain scission type resists on molecular weight and transient swelling during development of resist materials such as poly(methyl methacrylate) resist by using quantum beams such EUV and electron beam (EB). We aim to develop resist materials for EUV lithography and conduct fusion between top-down and bottom-up nanofabrication for next generation EUV lithography. We report herein two recent study: dependence of dissolution kinetics of main-chain scission type resists on molecular weight and transient swelling during development of poly(methyl methacrylate) resist.

Dependence of dissolution kinetics of main-chain scission type resists on molecular weight [1]

The dissolution kinetics and molecular weight in main-chain scission type resists such as poly(methyl methacrylate) (PMMA) and ZEP520A were investigated using a quartz crystal microbalance (QCM) method and a Gel Permeation Chromatography (GPC) to clarify the effects of the molecular weight after polymer degradation on the dissolution kinetics.

Fig.1 shows the relationship between dissolution rate and number average molecular weight in (a) PMMA and (b) ZEP520A. The dissolution rates were estimated from QCM charts. The number average of molecular weight (M_n) of PMMA was estimated from GPC charts. The dissolution kinetics of PMMA and ZEP520A are compared. Dissolution rate of PMMA and ZEP520A depend on molecular weight after main chain scission. There are three molecular weight regions from QCM results in case of PMMA. In small molecular weight region, only dissolution occurs. In middle molecular weight region, PMMA firstly swells and then dissolved into developer. In large molecular weight region, only swellings are observed. By these results, dissolution kinetics of PMMA depends on its molecular weight after irradiation. On the other hand, there are two molecular weight regions in ZEP520A. In small molecular weight region, only dissolution occurs. In large molecular weight region, only swellings are observed. We couldn’t observe the middle molecular weight region, where swelling and dissolution occur simultaneously. This region affects lithographic performance. The dissolution behavior depends on molecular weight after polymer degradation in both PMMA and ZEP 520A. These results indicate that ZEP520A is better to be better lithographic performance.

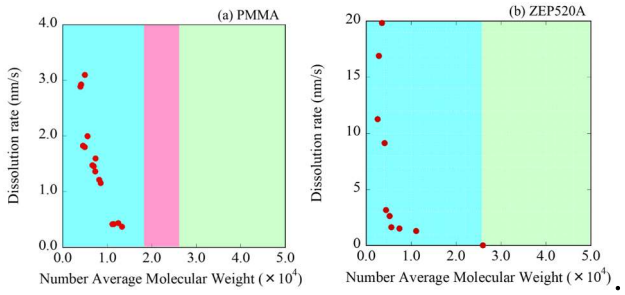

Fig.1 Relationship between dissolution rate and number average molecular weight in (a) PMMA and (b) ZEP520A.

Transient swelling during development of poly(methyl methacrylate) resist [2]

For the realization of further miniaturization at scales of 10 nm and below in semiconductor devices, it is essential to understand the dissolution kinetics of resist films in developer. In this study, the changes in molecular weight and dissolution kinetics induced by ionizing radiation in PMMA resist films were studied using a QCM method and GPC. The weight-averaged molecular weight M_w was changed from 50000 to 996000. Three types of developers were examined.

Fig. 2 shows the relationship between development rate and M_n of PMMA in methyl isobutyl ketone （MIBK）: isopropyl alcohol（IPA）=1:3, MIBK:IPA=1:7, and *o*-xylene developers. The dissolution behavior of PMMA was divided into three molecular weight regions from QCM results. The dissolution rate was determined by the molecular weight after polymer degradation, irrespectively of the initial molecular weights. Long PMMA chains are anchored deeply into the polymer. Consequently, the swelling should be large for the dissolution. The kinetic factors involved are the diffusion of the solvent in the polymeric film, the subsequent relaxation response of the polymer, and the diffusion of the polymer molecules into the developer. There are three regions in PMMA; (only dissolution, both swelling and dissolution, and only swelling.) It is important for the improvement of resist performance to control the relationship between swelling and dissolution.

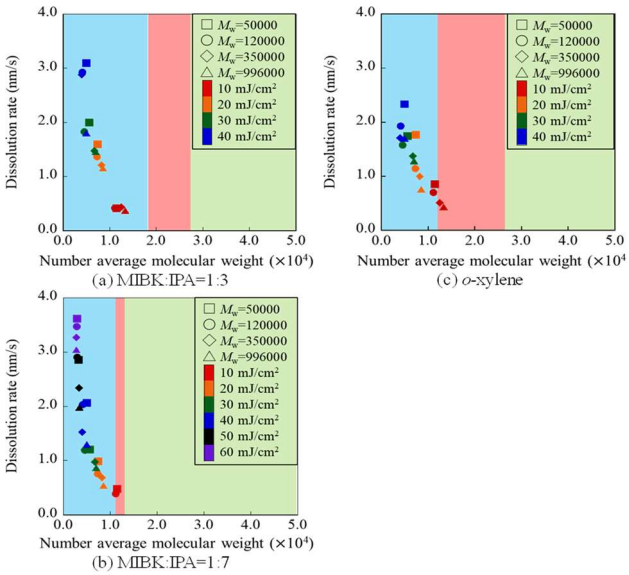

Fig. 2 Relationship between development rate and M_n of PMMA in (a) MIBK:IPA=1:3, (b) MIBK:IPA=1:7, and (c) *o*-xylene

References

[1] A. Konda *et al.*, J. Photopolym. Sci. Technol. **35**, 1 (2022). DOI: 10.2494/photopolymer.35.1

[2] A. Konda *et al.*, J. Photopolym. Sci. Technol., in press.

Part Ⅰ

2. Materials Science

P2-1 Functional Polymer Project

Leader : ZHAO Yue

Functional Polymer Project has been developing advanced functional polymer materials, such as polymer electrolyte membranes, separation membranes and ionomers for high-performance fuel cells and hydrogen production systems by quantum beams. We have synthesized the proton- and anion-conducting electrolyte membranes (PEM and AEM) and the hydrogen permselective membranes using γ-rays and electron beams, and characterized the nanostructures using X-ray and neutron scattering. We report herein the development of a new structural analysis technology to precisely elucidate the hierarchical structure of polymer membranes.

Unique structural characteristics of graft-type PEMs using SANS partial scattering function analysis

Radiation-grafted PEMs made of poly(styrenesulfonic acid)-grafted poly(ethylene-co-tetrafluoroethylene) (ETFE-g-PSSA), are promising alternatives to the benchmark material Nafion® for electrochemical applications such as electrodialysis and fuel cells. They offer the advantages of a potentially low-cost fabrication technique, and the adaptability of both improving membrane ionic conductivity by PSSA graft polymers and maintaining the excellent mechanical/thermal properties of ETFE base polymer. To the current stage of research, challenges remained to overcome are the relatively low proton conductivity of ETFE-g-PSSA under reduced relative humidity and long-term stability, which need thorough understanding of structure-property relationships.

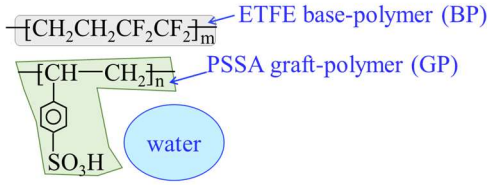

Fig. 1. An illustration of the three-component system of the hydrated ETFE-g-PSSA PEMs composed of ETFE base polymer (BP), PSSA graft polymer (GP) and water (W).

In a hydrated ETFE-g-PSSA PEM, the sulfonic acid groups absorb water and form hydrophilic ionic channels that phase segregate from the hydrophobic polymer matrix. Thus, the proton conductivity is strongly controlled by the morphology and connectivity of ion channels. Small-angle neutron scattering (SANS) technique is one of the most essential techniques to understand the nanostructure of PEMs. However, the conventional analysis is based on the intensity profile that contains information of all components such as the hydrophobic polymer, hydrophilic polymer, ions, and water, and fails to provide the detailed structure of the individual components. This undesirable data problem was recently solved by us using partial scattering function (PSF) analysis, which is the quantitative decomposition of a series of intensity profiles obtained through contrast-variation SANS experiments [1-2]. Here we applied PSF analysis to explore the detailed structure of ETFE-g-PSSA membrane with an ion exchange capacity of 2.0 mmol/g, which is defined as a three-component system consisting of ETFE base polymer (BP), PSSA graft polymers (GP) and water as illustrated in Figure 1 [2].

PSF analysis gave quantitative knowledge of the role of individual components in the entire structure. The self-term analysis revealed the detailed structure of each component, whereas the cross-terms gave the correlation between two components, leading to the location determination of the components. The entire structure patterns of the hydrated ETFE-g-PSSA were constructed in Figure 2. Polymer grains with a cutoff size of ~150 nm are formed by the aggregates of GP/water domains in a mass fractal structure with a fractal dimension of 2.4 that are well phase-separated and dispersed in the BP matrix. Each GP/water domain is made of homogeneously incorporated GP and water with an average radius of 9.5 nm. In each GP/water domain, both GP and water show a bicontinuous-like local structure, demonstrating the formation of a well-connected ion channel network. Additionally, PSF cross-term analysis shows that GP and water are repulsive at the molecular length level <3 nm, resulting in a lower hydration number but higher conductivity compared to Nafion membranes.

Note that a high PEM conductivity at low water content is of great scientific interest. This study shows that PSF analysis is capable of providing mechanistic insights concerning structural correlations over a range of length scales, from microscopic to molecular level. In particular, the structural guidelines at the molecular level are significant and relevant for establishing superior design rules for fuel cell membranes.

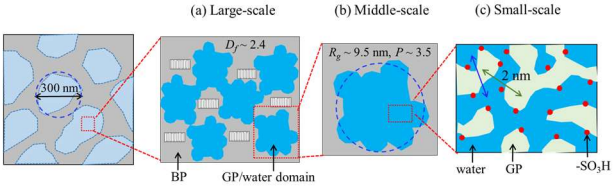

Fig. 2. Schematic of the hierarchical structure of the ETFE base polymer, PSSA graft polymer, and water domains in the fully hydrated ETFE-g-PSSA PEMs at (a) large-scale; (b) middle-scale; and (c) small-scale.

References

[1] Y. Zhao *et al.*, Macromolecules, **54**, 4128-4135 (2021). DOI: 10.1021/acs.macromol.1c00587

[2] Y. Zhao *et al.*, Macromolecules, **55**, 7100-7109 (2022). DOI: 10.1021/acs.macromol.2c00333

P2-2 Advanced Catalyst Project

Leader : YAMAKI Tetsuya

Our primary research target has been development of catalytic materials for next-generation energy devices in future H_2 society by effective use of electron and ion beams. The advantage of our overarching strategy is that these quantum beams can lead to high-energy defect creation, active-site formation via non-equilibrium chemical reactions, and nano-to-micro fabrication. This report deals with R&Ds of new nanoparticle (NP) catalysts for an O_2 reduction reaction (ORR) in polymer electrolyte fuel cells (PEFCs).

O_2 adsorption states on an active Pt catalyst developed by ion beam-induced defects in a carbon support [1]

We recently developed Pt/carbon catalysts with improved ORR activity utilizing ion-beam-induced defects in a carbon support [2,3]. The Pt NPs were deposited on a glassy carbon (GC) substrate irradiated with 380 keV Ar^+ at a fluence of 7.5×10^{15} ions/cm^2. The specific activity of the obtained catalyst (referred to as Pt/irrad. GC) became higher than that of Pt NPs on a non-irradiated GC substrate (referred to as Pt/GC). To clarify an origin of such high activity, the O_2 adsorption states of Pt NPs were examined by X-ray absorption near edge structure (XANES) measurements at the Pt L_3-edge at BL14B1 of SPring-8.

The XANES was measured *in situ* in the following two conditions: (i) after removal of surface oxide species (initialization) in a gas mixture of H_2 and He for 10 min at 1 atm and 100°C and (ii) after exposure to O_2 at 1 atm and room temperature. We obtained a difference spectrum between conditions (i) and (ii), *i.e.*, a $\Delta\mu$ spectrum to observe O_2 adsorption states directly.

Figure 1 shows the $\Delta\mu$ spectra for the Pt/irrad. GC and Pt/GC together with the results of peak fitting by the Lorentzian function. These represented the positive absorption only at energies of 11550-11575 eV around Pt L_3 peak, suggesting the formation of new Pt electronic states by the O_2 adsorption. The spectrum of the Pt/GC was fitted with one peak (denoted as peak 1), which can be assigned to the Pt-O* antibonding states because its energy position is lower than that for the oxide peak. On the other hand, the Pt/irrad. GC exhibited another peak in the higher energy range (denoted as peak 2) maybe due to the surface oxide-like layer of Pt involving the vacancies in GC.

More importantly, the position of peak 1 was 0.7 eV lower for the Pt/irrad. GC than for the Pt/GC. This shift indicates that the Pt-O* antibonding level were lowered in energy and became close to the Fermi level; thus, the Pt-O bond in the Pt/irrad. GC would be weakened.

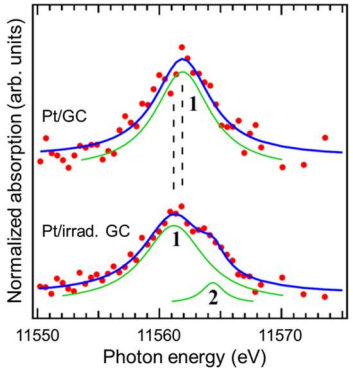

Fig. 1. $\Delta\mu$ spectra for the Pt/irrad. GC and Pt/GC samples.

High durability of Pt NP electrocatalysts prepared by ion implantation [4,5]

Improved durability as well as activity of ORR catalysts is an urgent issue for commercialization of PEFCs. Our previous finding [2,3] of the active Pt NPs on the carbon support irradiated with the Ar-ions motivated the present study. We prepared Pt NPs by Pt-ion implantation in the GC substrate and then found them to exhibit high durability. This method can introduce ion-beam-induced defects simultaneously with the Pt NP formation; thus, Pt-carbon interfacial interactions are expected to occur efficiently.

The GC substrate was implanted with 100 keV Pt^+ at 1.5×10^{16} ions/cm^2 and electrochemically etched at 1.9 V for 30 s to expose the ca. 40-nm deep implanted layer, followed by a heat treatment at 400°C for 1 h in an N_2 atmosphere for NP agglomeration (referred to as an implanted sample). For comparison, Pt NPs with approximately the same size were deposited by rf magnetron sputtering (referred to as a deposited sample). Cyclic voltammograms were recorded in an N_2-saturated 0.1 M $HClO_4$ solution at 25°C in the potential range of 0.05-1.25 V (vs. RHE). The electrochemical surface area (ECSA) of the samples was determined from the H_2 adsorption region using a conversion factor of 210 μC/cm^2.

An accelerated durability test was performed in the potential range of 1.0-1.5 V (vs. RHE) at a potential scan rate of 500 mV/s for 52000 cycles. A change in the ECSA of both the samples is plotted against the number of cycles in Fig. 2. By comparing the rate of an ECSA decrease, the durability of the implanted sample was found to be about 3.5 times higher than that of the deposited sample.

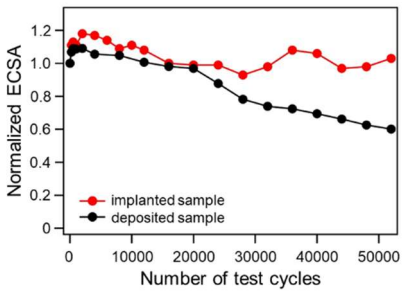

Fig. 2. ECSA change for the implanted and deposited samples.

References

[1] H. Okazaki *et al.*, J. Phys. Chem. C, in press.
[2] T. Kimata *et al.*, Phys. Rev. Mater., **6**, 035801 (2022). DOI: 10.1103/PhysRevMaterials.6.035801
[3] (in Japanese) T. Yamaki, Clean Energy, pp. 37-43 (Sep. 2022).
[4] T. Kimata *et al.*, APL Mater. **11**, 061115 (2023). DOI: 10.1063/5.0148263
[5] T. Kimata *et al.*, J. Appl. Phys., **132**, 175303 (2022). DOI: 10.1063/5.0103520

P2-3 Environmental Polymer Project

Leader : SEKO Noriaki

In our Environmental Polymer Project, we are developing highly functional adsorbents by radiation-induced graft polymerization using electron beams and gamma rays. The developed adsorbents are functional materials for the removal of harmful metals in industrial wastewater and the recovery of rare metals from seawater. We are also developing biodegradable polymers with thermal stability and processability by radiation-induced crosslinking for use in packaging material and agriculture.

Aminophosphonate functional adsorbents prepared by radiation grafting and subsequent Kabachnik-Fields three-component reaction [1]

The Kabachnik-Fields three component reaction can synthesize polymeric materials containing special functional groups, which are difficult to introduce by ordinary methods. As shown in Figure 1, a lignin monomer of vanillin methacrylate (VM) was radiation grafted onto a nonwoven fabric (PNWF) composed of pineapple fibers and polylactic acid by radiation-induced graft polymerization using the gamma ray preirradiation method. The grafted material (PNWF-g-PVM) has the aldehyde groups. The gamma ray preirradiation dose for the grafting was 50 kGy and the degree of grafting of the obtained grafted materials increased with the increase of reaction time and monomer concentration. The introduction of amiophosphonate functional structures into the fabrics through the reaction of aldehyde groups with amine and phosphite compounds allows the development of new adsorbents. The amiophosphonate groups readily bind to metal ions in aqueous solution, thereby removing or recovering them from the water.

In general, the fabrication of amiophosphonate from aldehyde proceeds in two steps, a fast reaction step that the aldehyde attached with the amine to form a Schiff base imine, and a slow addition step that the phosphite reacted with the imine. In this study, we developed a simplified and rapid one-step method. That is, we directly immersed the grafted fabrics into a dioxane solution containing amine and phosphite compounds, where a Kabachnik-Fields three-component reaction (KF3CR) of amine, phosphite and aldehyde occurred in the solution, resulting in the new aminophosphonate functional groups. After the reaction, the structure of the fabrics before and after modification were analyzed in detail. The results indicated that KF3CR did proceed and new aminophosphonate functional groups appeared on the fabrics. Furthermore, the modified fabrics exhibited enhanced thermal stability without significant radiation degradation effects. The aminophosphonate functional fabrics can be used as adsorbents for the selective removal and recovery of metal ions from water solutions such as industrial wastewater and seawater.

Development of Radiation crosslinked Biodegradable Mulch Film for Agricultural Application [2]

Most common plastic mulch films are not easy to biodegrade and will remain in the soil for a long time, resulting in increased salt content and reduced water and nutrients in the soil. In this study, as shown in Figure 2, we developed a biodegradable mulch film for agricultural applications. The polyhydroxyalkanoate (PHA) and polycaprolactone (PCL) are biodegradable materials, but when used alone, their biodegradation rate is too fast to be practically used. We prepared a dual-layer composite mulch film by compounding PHA and PCL resins. By complementing each other with their advantages and disadvantages, we expected to develop a practical mulch film with high biodegradability for agricultural application. We used PHA film as the first layer and PHA/PCL blend film as the second layer, and then hot-pressed the two layers to form a dual-layer mulch film. The hot-pressed film was then radiation crosslinked by electron beam irradiation. Thus, a dual-layer mulch film with high transparency and good adhesion between the two layers was obtained.

Soil burial biodegradability tests were carried out on the obtained dual-layer mulch films as well as PHA and PCL pristine films. After five weeks of testing, the pristine films of PHA and PCL lost more than 40% of their weight in soil. Such a fast biodegradation is not suitable for the practical use. The biodegradability of the radiation crosslinked dual-layer mulch film was reduced with a certain degree, and the weight loss was about 10% after five weeks in soil. Radiation crosslinking and the interaction of the two polymers resulted in a modest degradation rate of the dual-layer mulch films compared to the pristine films. In addition, the dual-layer mulch films were more transparent than the PHA and PCL pristine films. Therefore, the radiation crosslinked and compounded dual-layer mulch film had a modest biodegradation rate and was suitable for the agricultural applications.

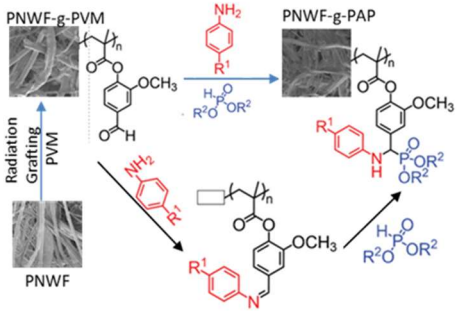

Fig. 1 Schematic diagram for the radiation grafting of PVM onto the PVWF and the one-step/two-step functionalization of the grafted materials.

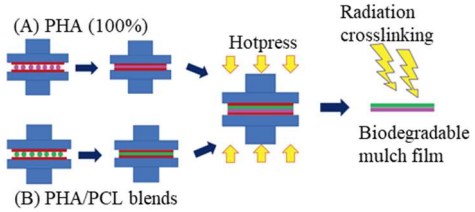

Fig. 2 Process for the preparation of the dual-layer mulch films.

References

[1] B. Barba *et al.*, J. Nat. Fibers, **19**(16), 13550 (2022). DOI: 10.1080/15440478.2022.2114980
[2] N. A. Othman *et al.*, Energy Nexus, **8**, 100137 (2022). DOI: 10.1016/j.nexus.2022.100137

P2-4 Biocompatible Materials Project

Leader : TAGUCHI Mitsumasa

Biocompatible Materials Project has been developing the functional biocompatible materials based on the crosslinking reaction induced by quantum beams. The obtained materials could be used in bio-devices for diagnosis, treatment, and regenerative medicine.

Peptide nanogels for pancreatic cancer diagnosis

Among cancers, which are the leading cause of death in Japan, the survival rate of pancreatic cancer patients is less than 10%, and the importance of early diagnosis and treatment of pancreatic cancer is increasing. Although the size of pancreatic stromal permeability varies with individual patients and the degree of cancer progression, nanoparticles of several 10 nm could reach cancer cells. In addition, pancreatic cancer cell membranes are positively charged, so nanogels must be negatively charged to enhance intracellular accumulation. This research aims to develop negatively charged smaller nanoparticles made of biopolymers for pancreatic cancer diagnosis using quantum beam cross-linking technology [1].

Three types of peptides consisting of histidine (His: involved in radiation crosslinking) and glycine (Gly: not involved in radiation crosslinking) with different chain lengths, His-Gly-His-Gly-His(H5), His-Gly-Gly-Gly-His-Gly-Gly-Gly-His(H9), and His-Gly-Gly-Gly-Gly-Gly-His-Gly-Gly-Gly-Gly-Gly-His(H13), were designed from the standpoint of conventional peptide reaction analysis. And these peptides were synthesized using a solid-phase column in the same manner as the previous work [2]. Aqueous peptide solutions were irradiated with γ-rays under aerated conditions at 25 °C at the doses of 5–15 kGy (Gy = J kg^{-1}) using a ^{60}Co γ-ray source at the Takasaki Institute for Advanced Quantum Science, QST. Nanogels were produced by the irradiation and the average diameters of the nanogels after 5 kGy irradiation were 53, 49, and 30 nm for H5, H9, and H13 nanogels, respectively, at 5 kGy (Fig. 1). The sizes of these nanogels decreased with increasing γ-ray absorption above 5 kGy. Among the three nanogels, the H9 nanogels had extremely high stability in phosphate-buffered saline solution for over six days. The peptide nanogel stability was attributed to their surface potential and oxidation resistance. H5 was less hydrophilic than others, and H5 nanogels became larger-sized particles due to aggregation. H13, which was more hydrophilic than others, had a lower particle density and was likely oxidized by dissolved oxygen in the solution.

Fluorescence staining of the peptide nanogel solution was performed using a Hi-Lyte Fluor 555 Labeling Kit-NH2. PANC-1 human pancreatic cancer cells (RCB2095, Bioresource Center) were cultured in RPMI 1640 medium supplemented with 10 vol% fetal bovine serum, 100,000 U L^{-1} penicillin, and 100 mg L^{-1} streptomycin. Cells were seeded in glass-bottom dishes and incubated in the

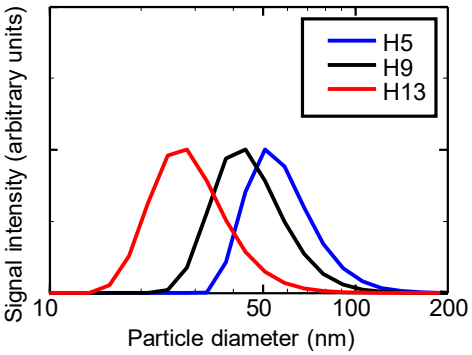

Fig. 1 Number-weighted distribution of 0.1 wt.% H5, H9 and H13 aqueous solutions at 5 kGy.

medium containing fluorescently labeled peptide nanogels. Fluorescent H9 nanogels accumulated in the human pancreatic PANC1 cancer cells (Fig. 2). No significant changes in cell morphology were observed, indicating the low toxicity of the nanogels. The observed bright spots were larger than the size of individual nanogels, suggesting that the nanogels entered the cells via endocytosis and accumulated in intracellular vesicles such as endosomes and lysosomes. The negative surface potential of the H9 nanogels enhances adhesion to pancreatic cancer cells, and a particle size of less than 100 nm allows accumulation inside pancreatic cancer cells via endocytosis. The nanogels accumulated in only 2 h, which is faster than their half-life when degraded by a protease. These properties would be useful to improve the efficacy of MRI or PET imaging of intractable cancers.

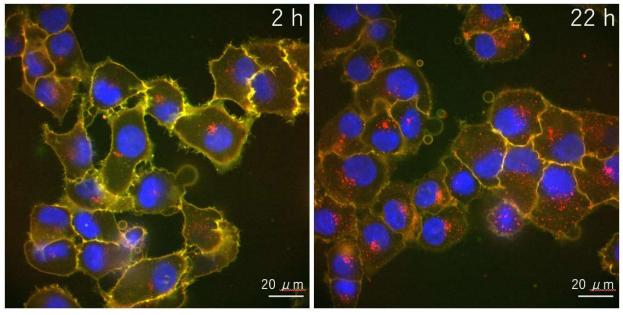

Fig. 2 Confocal images of fluorescent H9 nanogels (red) accumulated in PANC1 cells after incubation for 2 and 22 h. Plasma membranes and nuclei are shown in yellow and blue, respectively.

References

[1] A. Kimura *et al*., Pharmaceutics. **44**, 2400 (2022). DOI: 10.3390/pharmaceutics14112400

[2] A. Kimura *et al*., Nanomaterials. **11**, 714 (2021). DOI: 10.3390/nano11030714

P2-5 Element Separation and Analysis Project

Leader: OHBA Hironori

Quantum beams are versatile sources for materials processing. Our project explores the basic process of the laser-matter interaction to recover valuable elements from industrial wastes and to analyze elements in solid and liquid without pre-treatment. Specially, we have developed laser-induced particle formation (LIPF) technique for the elemental separation and laser-induced breakdown spectroscopy (LIBS) for the in situ elemental analysis. Moreover, in the development of LIPF, the particle formation mechanism has been studied by time-resolved X-ray absorption fine structure (XAFS) spectroscopy and theoretical calculation. The recent achievements in our project are introduced as follows.

Reaction pathways for reduction of the $PdCl_4^{2-}$ complex in LIPF: An ab initio molecular orbital study [1–3]

When a nano-second pulsed UV laser (266-355 nm) is irradiated to the aqueous/ethanol solution including precious metals (PM^{n+}: Pd^{2+}, Rh^{3+}, Au^{3+} and so on), the photo-excited PM^{n+} ions react with alcohols (ethanol and methanol) and are reduced to PM neutrals. The PM neutrals can form particles in the solution because electronic repulsion forces between the ions are lost in the neutrals (Fig. 1). In previous studies, we showed that LIPF can selectively recover Pd from the solution of a spent nuclear fuel [4], and investigated the LIPF mechanism by the time-resolved XAFS with an interval of 1 min [5]. However, there has not been information on the early stage in the LIPF, where the photo-excited PM^{n+} ions are reduced to PM neutrals. Thus, we started ab initio molecular orbital study to investigate the reaction in the early stage of LIPF.

The existence form of Pd^{2+} in the HCl solution is the $Pd(II)Cl_4^{2-}$ complex, which was confirmed by extended XAFS. We thus theoretically investigated the photodissociation of $Pd(II)Cl_4^{2-}$ using the multi-reference configuration interaction (MRCI) method [1,2]. We calculated excited potential energy surfaces for single and double Cl losses from $Pd(II)Cl_4^{2-}$. It was suggested, as a result, that the photoexcitation of $Pd(II)Cl_4^{2-}$ may be followed by a single Cl loss:

$$Pd(II)Cl_4^{2-} \rightarrow Pd(II)Cl_3^- + Cl^-, \quad (1)$$

and/or by a double Cl loss:

$$Pd(II)Cl_4^{2-} \rightarrow Pd(I)Cl_2^- + Cl + Cl^-. \quad (2)$$

We should note that reaction **2** corresponds to the one-electron reduction from Pd(II) to Pd(I).

The XAFS result suggests that the photoreduction of Pd(II) → Pd(0) is one-photon process [5], whereas the theoretical consideration expects that one-photon absorption of $Pd(II)Cl_4^{2-}$ results in Pd(II)→Pd(I) through reaction **2**. To solve this contradiction, assuming that the Cl radical in reaction **2** reacts with the alcohol solvent, such as methanol MeOH, we theoretically investigated two reaction pathways [3]. Both reactions are initiated with

$$CH_3OH + Cl \rightarrow CH_2OH + HCl, \quad (3)$$

which is followed by

$$Pd(I)Cl_2^- + CH_2OH \rightarrow Pd(0)Cl^- + CH_2ClOH \quad (4)$$

in pathway A and

$$Pd(I)Cl_2^- + CH_2OH \rightarrow Pd(0)HCl_2^- + CH_2O \quad (5)$$

in pathway B. Fig. 2 shows potential energy diagram for pathways A and B. Potential diagram for reaction **5** (pathway B, blue) strongly suggests that $Pd(0)HCl_2^-$ is easily generated in water. Although reaction **4** (pathway A, red) has a small potential barrier (3.0 kcal/mol), it may also occur to generate $Pd(0)Cl^-$ in water.

In conclusion, the present study has shown that the reduction Pd(II) → Pd(0) can be completed through the photodissociation of $Pd(II)Cl_4^{2-}$ followed by the alcohol reaction with the dissociation product; the products $Pd(0)Cl^-$ and $Pd(0)HCl_2^-$ are candidates for precursors of the Pd-Pd bond formation in the early stage of LIPF.

Fig. 1 Recovery of precious metals using LIPF.

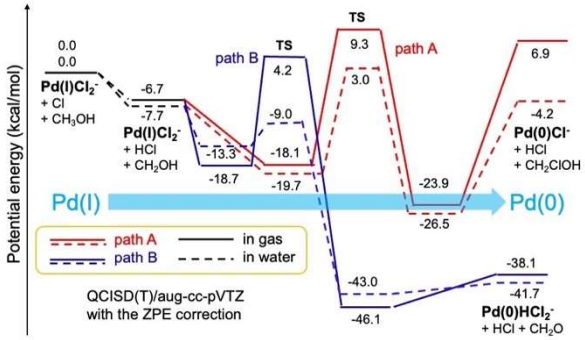

Fig. 2 Potential energy diagram for pathways A and B.

References

[1] Y. Kurosaki et al., Chem. Phys. Lett. **746**, 137288 (2020). DOI: 10.1016/j.cplett.2020.137288

[2] Y. Kurosaki et al., Chem. Phys. Lett. **764**, 138247 (2021). DOI: 10.1016/j.cplett.2020.138247

[3] Y. Kurosaki et al., Chem. Phys. **569**, 111857 (2023). DOI: 10.1016/j.chemphys.2023.111857

[4] S. Asai et al., Anal. Chem. **88**, 12227 (2016). DOI: 10.1021/acs.analchem.6b03286

[5] M. Saeki et al., J. Phys. Chem. C **123**, 817 (2019). DOI: 10.1021/acs.jpcc.8b09532

P2-6 Advanced Functional Polymer Materials Research Group

Leader : SEKO Noriaki

The research of "Advanced Functional Polymer Materials Group" has been focused on efficient development technique for advanced functional polymer materials, which are widely used in advanced devices and construction materials. The technique includes materials informatics such as machine learning and neural network in addition to the established radiation techniques regarding to the radiation-induced graft polymerization and the X-ray/neutron structure analysis. This group has been conducting mainly the R&D for "Advanced functional polymer materials alliance" under QST innovation hub program in collaboration with participant companies.

Research results of "Advanced functional polymer materials alliance "

On the alliance project of the 6th year, the main achievements in three research subjects are as follows.

(1) Grafting yields prediction: To find quickly optimal experimental conditions for the graft polymerization of chloromethyl styrene with polyetheretherketone (PEEK), we performed statistical analysis such as frequency analysis. From the results, it was predicted that the conditions for obtaining high grafting ratio were using a low molecular weight annealing solvent and a dose of more than 300 kGy.

(2) Structural data accumulation and property prediction: We proceeded with the simulation of the hierarchical structure of polymer electrolyte membranes (PEM). The simulation parameters were optimized by matching the scattering spectrum calculated by the simulation with the scattering spectrum obtained from contrast-modulated small-angle neutron scattering. Machine learning was performed using the structure data obtained from the simulation as explanatory variables, and it was found that hierarchical structure data is as important as water content in predicting ionic conductivity.

(3) Database preparation: We have developed the application for members to efficiently view the database concerning the graft-type polymer materials.

Direct observation of hierarchical structures in graft-type polymer electrolyte membranes using AFM [1]

For the above topic (2), structural measurements using the following new analysis methods were performed to construct a structural database. Polymer electrolyte membrane (PEM) is a key material for next-generation energy devices such as metal-air batteries and fuel cells and is desired to have both high mechanical strength and high ion conductivity. However, not only the chemical composition (molecular design) but also the polymer association state (hierarchical structure) in the micron to nano range affects the material functions has hindered the progress of material creation. We performed structural measurements by atomic force microscopy (AFM) on PEMs prepared by radiation-induced graft polymerization, which does not require a film-forming process that affects the hierarchical structure.

We analyzed the graft-polymer regions (hydrophilic ion-conducting regions) in ethylene tetrafluoroethylene (ETFE)-PEMs with different grafting degree (GD) of 16, 26, 39, and 46%, which correspond to ion-exchange capacities of 1.2, 1.7, 2.1, and 2.4 mmol/g, respectively. In particular, AFM phase images can image surface adsorption and hardness, and directly measure phase-separated structures caused by differences in polymer properties. We quantify the size and shape of hydrophilic regions by the following approaches: (1) observation of surface and cross-sectional structures; (2) theoretical division of hydrophobic and hydrophilic phases in phase images; and (3) the comparison of surface area in phase image to the volume fraction of hydrophilic graft-polymer/water and hydrophobic ETFE matrix. The direct measurement for the mesoscopic structure of PEM has been limited due to difficulty of the preparation of a clear surface by cutting the soft materials. It is especially useful to show the abovementioned methodology, consisting of measurement of cross-sectional surface of the bulk polymer functional materials, semi-quantitative analysis of the phase structures and the comparison of these results with those obtained by scattering methods.

In the AFM phase images of cross-sections of ETFE-PEM with different GD, the structure derived from hard polystyrene sulfonic acid (PSSA) graft chains was observed, and the area increased with increasing GD. The size (radius from the center of mass) of the PSSA-derived structures contributing to ionic conduction was calculated from image analysis, and it monotonically increases up to 39% GD to about 12 nm, whereas it significantly increases at 46% GD (Fig. 1a, ■). As shown in Fig. 1b, this result indicates that above the GD threshold (here about 40%), adjacent PSSA-derived structures fuse, affecting, for example, the connectivity of ion conduction paths. Above 39% GD, the change in water uptake is decreased due to the lower connectivity of the ionic conduction paths (Fig. 1a, ○). The structural properties of PEMs can be visualized and semi-quantitatively characterized by AFM [1]. The unnoticed hydrophilic domains of a few tens of nm are expected to enable the design of the functions of PEM.

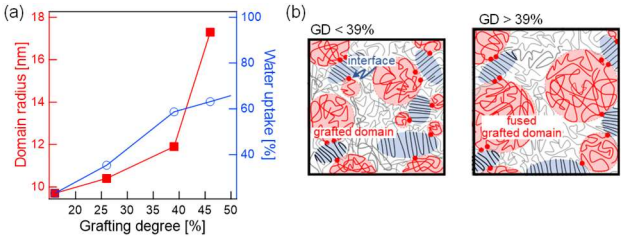

Fig. 1 (a) Plot of size of PSSA-derived structures (■, left axis) and water content of PEM (○, right axis) against GD. (b) Schematic diagram of ETFE-PEM at low GD ~39% where each grafted domain is separate from the others, and ETFE-PEM at high GD where several domains are grown and fused together to create a larger domain. Reprinted with permission from [1]. Copyright 2022 American Chemical Society.

Reference

[1] T. Motegi *et al.*, Langmuir **38**, 9992 (2022). DOI: 10.1021/acs.langmuir.2c01398

Part Ⅰ

3. Life Science

P3-1 Microbeam Radiation Biology Project

Leader : FUNAYAMA Tomoo

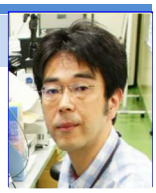

The Microbeam Radiation Biology Project had developed a technology to irradiate biological samples with heavy ion microbeams and conducted research to elucidate the radiation response mechanisms using the developed irradiation technology.

The higher biological effects of heavy ions are believed to be due to the concentrated energy deposition of heavy ions on organisms, which causes severe damage to their DNA. However, this concentrated energy deposition is difficult to elucidate because it causes non-uniformity in the spatial distribution of energy deposition at the micrometer scale. Therefore, as a way to solve this problem and elucidate the heavy ion response of cells and individuals, the project had developed a technology to target and irradiate a part of a cell or an individual organism under a microscope using a micrometer-scale beam spot, which is smaller than the size of a cell [1, 2].

The developed microbeam irradiation technique enables precise and flexible heavy ion irradiation of biological samples, such as single-point irradiation inside a cell or irradiation of specific organs of an organism. Using this technology, we have advanced the elucidation of the response of locally irradiated organisms, as well as research aimed at the application of the technology derived during the development process of microbeam technology.

Responses of hematopoietic cells after ionizing-irradiation in anemic adult medaka (*Oryzias latipes*) [3]

Hematopoietic tissues are highly sensitive to radiation and their response is highly complex. However, histological analysis of the radiation response in hematopoietic tissue is technically difficult in mammals because hematopoietic tissue is located in the bone marrow.

Therefore, we examined the effects of irradiation on hematopoiesis histologically using medaka, whose hematopoietic function is mediated by the kidneys, which are easy to observe for histological changes, rather than the bone marrow. In the experiment, we used medaka with hemolytic anemia induced by phenylhydrazine treatment in addition to medaka in the normal state. The kidneys of these medaka were locally irradiated with protons and carbon beams from the TIARA cyclotron.

In untreated medaka, proton irradiation of the kidneys caused a temporary decrease in hematopoietic cells, followed by recovery in 21 days. In contrast, no recovery was observed in carbon-irradiated fish. In addition, hematopoietic cell proliferation was observed after 7 days in medaka treated with phenylhydrazine to induce anemia, both with and without irradiation. These results suggest that medaka hematopoietic stem cells did not undergo a proliferative arrest after being damaged by radiation, but preferentially proliferated to eliminate anemia and increase peripheral blood cells. Thus, this study demonstrates that the medaka is a promising model for elucidating the complex and dynamic radiation response of the hematopoietic system.

Effects of γ-irradiation as phytosanitary treatment on the quality of Japanese fruits and the survival of their regulated pests [4]

The use of irradiation of living organisms is not limited to diagnosis and treatment in medicine, but is also used in the agricultural industry. For example, the use of irradiation is expanding in international standard for phytosanitary measures (ISPM) for regulated pests. The Japanese apples and mandarins are exported according to bilateral agreements about the quarantine, such as methyl bromide fumigation, against peach fruit moth and Japanese orange fly. Recently, irradiation treatments in quarantine have been approved in annexes of ISPM No. 28.

Therefore, we conducted a study to confirm the effectiveness of this irradiation treatment, the quarantine dose for the peach fruit moth and the generic dose for the family Tephritidae, in preventing adult emergences. In addition, the effect of irradiation on fruit quality was studied in 11 apple cultivars and 3 mandarin cultivars.

The larvae of peach fruit moth and Japanese orange fly were irradiated and the adult-emerging inhibition ability was evaluated. As a result, it was confirmed that adult emergences were prevented by irradiation at the effective doses of ISPM and that the quarantine doses of irradiation had sufficient ability to prevent adult emergences. In addition, we irradiated fruits at twice the effective dose and tested the change in taste to verify the change in quality by tasting test among volunteers. As a result, no quality change was observed in the irradiated fruits and it was confirmed that the fruit quality was maintained.

This study showed that irradiation is an effective means of quarantine for apples and mandarins without quality degradation.

References

[1] T. Funayama *et al.*, Quantum Beam Sci. **3**, 13 (2019). DOI:10.3390/qubs3020013
[2] T. Funayama *et al.*, Nucl. Instr. Meth. Phys. Res. B. **465**, 101 (2020). DOI:10.1016/j.nimb.2019.12.028
[3] K. Nagata *et al.*, Int. J. Radiat. Biol. **99**, 663 (2023). DOI:10.1080/09553002.2022.2110328
[4] M. Kikuchi *et al.*, Radiat. Phys. Chem. **208**, 110918 (2023). DOI:10.1016/j.radphyschem.2023.110918

P3-2 Ion Beam Mutagenesis Project

Leader : OONO Yutaka

Ion beams are useful mutagens for improving characteristics of plants and microbes because ion beams are thought to cause mutations via a mechanism distinct from those of chemical mutagens or gamma rays. Our project aims to understand feature of ion-beam-induced mutations and to develop applications in the realms of basic biology and biotechnology. We are investigating the ion-beam- and gamma-ray-induced mutations through both genome-wide and gene-specific approaches. In addition, we are trying to establish various valuable mutants of plants, algae, yeasts, fungi, and bacteria under collaborations with academic or industrial research organizations. Revealing molecular bases of biological response against ionizing radiations is also major business in our project.

Genome wide analysis of quantum beam-induced mutations in bacteria [1]

In the past few years, we have investigated genome wide distribution of the quantum beam-induced mutations in Arabidopsis and rice. As opposed to higher plants, overall picture of quantum beam-induced mutations in microorganisms was not well characterized although we have used ion beams to improve industrially important microorganisms [2]. In this fiscal year, the final year of this 7-year project, we have conducted whole-genome sequencing analysis of practically important bacterium, *Bacillus subtilis*, irradiated by radiations with different linear energy transfer (LET).

Freeze-dried spore samples of the *B. subtilis* strain 168 were irradiated with various doses of ion beams (48 MeV $^{4}He^{2+}$ [surface LET: 24 keV/μm], 311 MeV $^{12}C^{6+}$ [111], 208 MeV $^{12}C^{5+}$ [156], or 177 MeV $^{12}C^{6+}$ [179]) or ^{60}Co gamma rays (0.2). After irradiation, the spore suspensions were spread on LB agar and incubated at 37 ºC for 1 day, and the surviving fraction (SF) was determined. For whole genome sequencing analysis, 13 single colonies were randomly selected from the surviving colonies at a dose resulting in an SF of around 1% for each radiation. Then, genomic DNA was extracted from the overnight culture of the colonies. Five colonies were also randomly selected from the mock-irradiated sample.

From 70 colonies, 194 single base substitutions (SBSs), 78 insertions and deletions (INDELs), and 12 inversions were detected in the circular genome of *B. subtilis* (Fig. 1). No significant biases was observed in the distribution of SBSs and INDELs. The mutation frequencies (MFs) of five radiations are ranged from 52.9 to 124.1 × 10^{-8} / bp. These frequencies were 5 to 13 times higher than that in the mock-irradiated spores (9.5 × 10^{-8} / bp). The MFs of gamma rays and $^{12}C^{6+}$ (111) ion beams were significantly higher than those of $^{12}C^{5+}$ and $^{12}C^{6+}$ (179) ion beams. Regarding the mutation type, the gamma rays, $^{4}He^{2+}$, and $^{12}C^{6+}$ (111) ion beams induced SBSs that account approximately 69.0% to 74.2% of the total mutation events. The proportion of SBS mutations of $^{12}C^{5+}$ was 37.1% and significantly lower than the three irradiations. Together with SF analysis with different doses of the radiations, the results suggested that the lower LET radiations (gamma and $^{4}He^{2+}$) showed low lethality and high MF, resulting in the major induction of SBSs. Whereas higher LET radiations ($^{12}C^{5+}$ and $^{12}C^{6+}$ [179]) showed high lethality and low MF, resulting in the preferential induction of deletion mutations. In addition, $^{12}C^{6+}$ (111) ion beams likely possess characteristics of both low- and high-LET radiations simultaneously. The results indicate that type and frequency of induced mutations in bacteria could be controlled by selecting an ionizing radiation of an appropriate LET in accordance with the intended purpose.

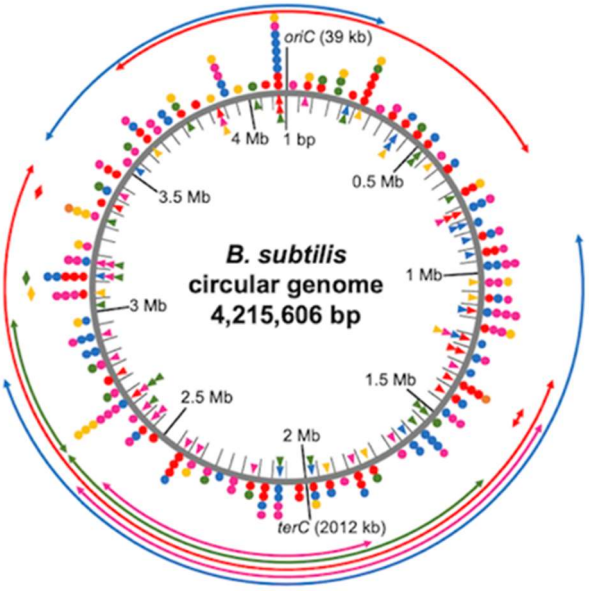

Fig. 1 Distribution of mutations on the circular genome of the *B. subtilis strain* 168. Mutations induced by different LET radiations were indicated by different color (mock, orange; gamma, red; $^{4}He^{2+}$, blue; $^{12}C^{6+}$ [111], pink; $^{12}C^{5+}$, green; and $^{12}C^{6+}$ [179], yellow) and plotted as mutation counts per 50 kb against the position of the reference genome. Circular and triangular symbols and the two-headed arrows indicate SBSs, INDELs, and inversions, respectively.

References

[1] K. Satoh *et al.*, Mutat. Res. **827**, 111835 (2023). DOI: 10.1016/j.mrfmmm.2023.111835

[2] K. Satoh and Y. Oono, Quant. Beam Sci. **3**, 11 (2019). DOI: 10.3390/qubs3020011

P3-3 Medical Radioisotope Application Project

Leader : ISHIOKA Noriko S.

Based on various RI manufacturing technologies using quantum beams, we develop basic technologies that contribute to the development of radiopharmaceuticals useful for the diagnosis and treatment of diseases. In particular, our research focuses on the elucidation of the key mechanisms that maximize the therapeutic effect of radiation and the development of new RI compounds that enhances the cell-killing effect by simultaneously irradiating multiple targets.

Organic cation transporter 3 mediates the non-norepinephrine transporter driven uptake of meta-[^{211}At]astato-benzylguanidine.

Meta-[^{211}At]astato-benzylguanidine ([^{211}At]MABG) accumulates in pheochromocytoma via norepinephrine transporter (NET) and leads to a strong antitumor effect, but it also distributes in normal tissues non-specifically. Therefore, the reduction of the non-specific accumulation of [^{211}At]MABG is important to avoid possible adverse effects. The intracellular transport pathway of [^{211}At]MABG other than via NETs remains unclear, however. *Meta*-[^{131}I]iodo-benzylguanidine ([^{131}I]MIBG), an iodine-labeled analog of [^{211}At]MABG, is known to be transported by not only NET but also organic cation transporter (OCT). Among 3 subtypes of OCTs, OCT3 is widely expressed in organs such as the brain, heart, liver, skeletal muscle, prostate, and adrenal gland, OCT3 is thus speculated to be the major transport system of MIBG (other than NET). Here, we conducted the present study to investigate the involvement of OCTs in [^{211}At]MABG uptake in order to elucidate the non-NETdriven uptake of [^{211}At]MABG both *in vitro* and *in vivo* [1].

In this study, 4 cell lines, PC-12 (rat pheochromocytoma cell line), NIH/3T3 (mouse fibroblasts cell line), ACHN (human renal cancer cell line), and BxPC-3 (human pancreatic cancer cell line) were used to investigate [^{123}I]MIBG and [^{211}At]MABG uptake. The uptake of both [^{123}I]MIBG and [^{211}At]MABG was significantly inhibited by NET-selective inhibitor, desipramine in PC-12 cells but not the other cell lines, indicating possible involvement of other transport systems. The expression of OCT3 was relatively higher than those of the other OCT subtypes in ACHN and BxPC-3 cells. The expression of OCTs was not observed in NIH/3T3 cells. The uptake of both [^{123}I]MIBG and [^{211}At]MABG in ACHN and BxPC-3 cells was significantly inhibited by OCT3-specific inhibitors, hydrocortisone (HDC) and prednisolone. The [^{211}At]MABG uptake was also reduced in OCT3-knockdown cells (Fig. 1, $p<0.001$). These results indicate that mainly OCT3 was involved in the uptake of [^{123}I]MIBG and [^{211}At]MABG in ACHN and BxPC-3 cells.

We further investigated the biodistribution of [^{211}At]MABG in PC-12 tumor-bearing mice after a preloading of phosphate-buffered saline (PBS) or HDC solution. The radioactivity of [^{211}At]MABG was significantly reduced in normal tissues by the preloading of HDC (Table 1). In contrast, there was an increasing trend of [^{211}At]MABG uptake in the PC-12 tumors. The tumor-to-normal tissue ratio was significantly increased by the preloading of hydrocortisone compared to that of PBS. OCT3 inhibition could therefore be useful to suppress the non-specific uptake of [^{211}At]MABG without affecting its accumulation in pheochromocytomas.

In conclusion, our results suggest that OCT3 is involved in non-NET-driven [^{211}At]MABG uptake. The preloading of HDC selectively reduced [^{211}At]MABG accumulation in normal organs *in vivo*. OCT3 inhibition may therefore be beneficial for a reduction of the radiation risk in healthy organs in the treatment of malignant pheochromocytomas.

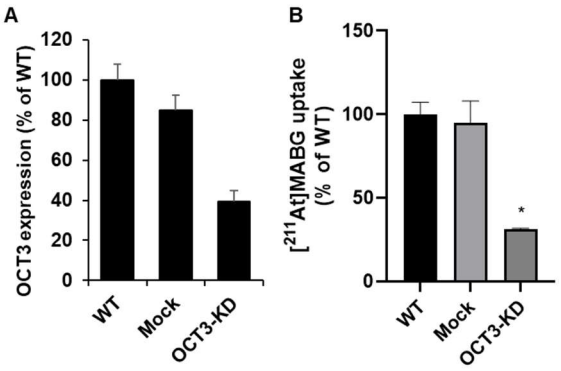

Fig. 1 The expression of OCT3 protein at 48 h after the transfection of siRNAs. The density ratio between OCT3 and β-actin (A, n=2). [^{211}At]MABG uptake in wildtype (WT), siRNA-NC-treated (Mock), and siRNA-OCT3-treated cells (OCT3-KD) (B) (n=4 each). *p < 0.001 vs. WT.

Table 1
The biodistribution of [^{211}At]MABG in tumor bearing mice.

	Control	HDC (8 mg/kg)	HDC (80 mg/kg)	Control vs HDC (8 mg/kg) P value	Control vs HDC (80 mg/kg) P value
Blood	0.44 ± 0.07	0.29 ± 0.08	0.24 ± 0.05	0.009	< 0.001
Liver	2.98 ± 0.54	2.00 ± 0.64	1.59 ± 0.23	0.021	0.002
Kidney	1.42 ± 0.36	0.92 ± 0.15	0.82 ± 0.28	0.045	0.016
Adrenal	21.67 ± 6.90	17.92 ± 9.54	15.82 ± 4.02	0.671	0.396
Intestine	3.59 ± 0.71	1.24 ± 0.49	0.90 ± 0.08	< 0.001	< 0.001
Spleen	5.04 ± 1.67	2.37 ± 0.41	2.47 ± 0.70	0.012	0.016
Pancreas	2.17 ± 0.39	1.65 ± 0.35	1.60 ± 0.63	0.175	0.136
Stomach	5.41 ± 1.19	2.51 ± 1.27	2.23 ± 0.66	0.003	0.001
Heart	7.16 ± 1.43	5.32 ± 1.25	5.55 ± 0.78	0.080	0.133
Lung	2.90 ± 0.99	1.75 ± 0.67	1.93 ± 0.76	0.118	0.205
Muscle	0.94 ± 0.30	0.64 ± 0.19	0.54 ± 0.12	0.147	0.048
Tumor	33.48 ± 18.91	45.19 ± 17.52	57.40 ± 30.15	0.662	0.209

Reference

[1] Y. Ohshima *et al.*, Nucl. Med. Biol. **112-113**, 44-51 (2022). DOI: 10.1016/j.nucmedbio.2022.06.005

P3-4 Radiotracer Imaging Project

Leader : KAWACHI Naoki

The aim of Radiotracer Imaging Project is to measure, visualize the radiation sources quantitatively, and characterize the biological processes and functions, using radioisotopes and imaging devices such as PETIS, PET, and Gamma Camera. We will establish systematized the most advanced techniques for live imaging using radiotracers and these production methods, nuclear imaging apparatus, imaging techniques using each apparatus, and kinetic analytical methods for understanding the elements and molecules transport functions related to agriculture, environmental problems and medicine within living systems.

Rice adjusts photosynthate translocation to roots in response to changes in soil water environment

Rice, a staple for over half of the world's population, faces challenges like drought stress and decreasing yields due to global warming. A detailed understanding of the response of rice to drought is essential to improve crop production. Roots play a vital role in this by adapting their architecture and function to acquire water and nutrients. To assess root structure and function accurately, Miyoshi et al., 2021 have developed the three-dimensional analysis technique that combined high-throughput X-ray computed tomography (CT), which allows high-throughput 3D structural analysis of plant roots, and open-type positron emission tomography, which utilizes ^{11}C-photosynthates enabling repeated in vivo measurements [1]. This system quickly analyzes root structure and photosynthate translocation dynamics in rice roots without harming the plants. In this study, we evaluate the dynamics of photosynthate translocation to rice roots grown in a pot replicating the intermittent drought stresses, i.e., drought stress and recovery from drought stress due to water influx by using this newly constructed.

Rice plant was sown in plastic pots and irrigated to a water level of 4 cm from the bottom of the pot for two weeks after sowing. The water was then drained, and the rice was grown under drought conditions for an additional two weeks and subjected to PET imaging. For the PET, about 35 MBq of $^{11}CO_2$ gas was supplied to the aboveground part of rice under drought conditions, and 30 min later, the pot was set in the PET detector ring. The above-ground part was placed outside the ring. The translocation of ^{11}C-photosynthates to the rice roots were then imaged for 120 min. After the PET imaging, the bottom 4 cm of the pot of the same plant was irrigated to recover from drought conditions, and 4 hours after the start of irrigation, about the $^{11}CO_2$ gas was again supplied to the aboveground part, and the translocation of ^{11}C-photosynthates to the rice roots were imaged by PET. In addition, the pot area of the same plant was imaged by an X-ray CT to obtain three-dimensional images of root system structures in the soil.

The short half-life of ^{11}C (20.39 min) afforded us the opportunity to conduct multiple experiments using the same plant. Consequently, we were able to visualize the translocation of photosynthates as the plant underwent cycles of drought stress and subsequent re-irrigation for recovery (Fig.1). Our findings unveiled a distinct pattern of photosynthate translocation in response to varying soil water conditions. Under drought conditions, ^{11}C-photosynthates were actively translocated from the base of rice to the seminal root extending downward to the bottom of the pot (red arrow in Fig.1b). It was considered that under the drought conditions, the photosynthates were actively transferred to the seminal roots, which develop in a downward direction to absorb nutrient water deep in the soil. In contrast, under well-watered conditions, photosynthates translocation to seminal roots was not observed, and the translocation to crown roots extending diagonally downward from the base became active (blue arrow in Fig.1c). This was considered to be the result of the active translocation of photosynthates to the crown roots to promote the growth of the entire root system under well-watered conditions.

These results suggest that re-irrigation of rice plants undergoing drought conditions immediately switches the photosynthates translocation from seminal roots to crown roots. We reveal that rice plants differentially adapts the dynamics of photosynthates translocation depending on soil water conditions [2]

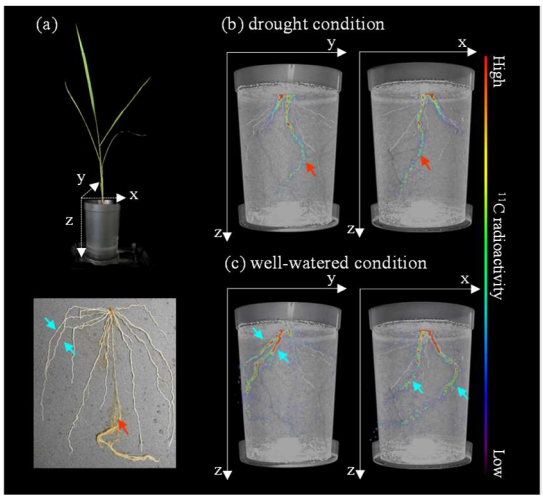

Fig. 1. (a) Photographs of the rice plant and roots, and distribution of ^{11}C-photosynthates (RGB) and root structure (B&W) under (b) drought and (c) well-watered conditions.

References

[1] Y. Miyoshi *et al.*, JINST. **16**, C12018 (2021). DOI: 10.1088/1748-0221/16/12/C12018

[2] Y. Miyoshi *et al.*, Front. Plant Sci. **13**, 1024144 (2023). DOI: 10.3389/fpls.2022.1024144

P3-5 Generation of Radioisotopes with Accelerator Neutrons Project

Chief : NISHINAKA Ichiro

In our project, we have developed the production of medical radioisotopes (RI) for cancer diagnosis and therapy such as ^{99}Mo/^{99m}Tc, ^{90}Y, ^{47}Sc, ^{64}Cu, and ^{67}Cu using fast neutrons from a cyclotron accelerator. The neutrons were obtained by irradiating 40-50 MeV deuterons to beryllium or carbon. A separation and purification method of aimed radioisotope from the target materials and radioactive impurities has also been developed. We also investigate the production of medical RI such as ^{211}At and $^{95, 96}$Tc by the tandem accelerator in Tokai (Japan Atomic Energy Agency, JAEA). Our final goal is to build a domestic production system of medical radioisotopes using accelerator driven neutrons.

Estimated Isotopic compositions of Yb in enriched ^{176}Yb for producing ^{177}Lu with high radionuclide purity by ^{176}Yb(d, x)^{177}Lu [1]

Recently, great interest has arisen concerning ^{177}Lu as one of the most important therapeutic radionuclides for treating neuroendocrine tumors. This has driven demand for ^{177}Lu with high radionuclide purity produced in accelerators, by using highly enriched ^{176}Yb samples to develop a variety of ^{177}Lu-labelled radiopharmaceuticals.

We developed a method for estimating the isotopic compositions of enriched ^{176}Yb samples required to produce a carrier-free ^{177}Lu with high radionuclide purity by the ^{176}Yb(d,x)^{177}Lu reaction. Here, we derived the excitation function of individual reactions for producing a radionuclide of Lu isotopes, such as ^{169}Lu, ^{170}Lu, ^{171}Lu, ^{172}Lu, ^{173}Lu, ^{174g}Lu, ^{174m}Lu, ^{176m}Lu, and ^{177}Lu, using the latest measured excitation functions of the ^{nat}Yb(d,x)Lu reactions. Note that we demonstrated that our measured integral yields of a variety of Lu radionuclides produced by the ^{nat}Yb(d,x)Lu reaction agree with the calculated integral yields of Lu radionuclides (Table 1) using the derived excitation functions.

Table 1
Calculated integral yields of Lu radionuclides at the EOI that will be generated by irradiating a ^{nat}Yb sample with 25 MeV deuteron beams are compared with the measured ones. Here, ^{174g}Lu (T1/2= 3.31 y) should be noted to be produced not only by the ^{173}Yb(d,n), ^{174}Yb(d,2n), and ^{176}Yb(d,4n) reactions but also from an isomeric decay of the isomeric state at 171 keV of ^{174m}Lu (T1/2 = 142 d). Since in this study, the yield of ^{174g}Lu was measured 37 days after the EOI, it is compared to the calculated yield corresponding to the yield at 37 days after the EOI.

Nucleide	$T_{1/2}$	E_γ (keV)	Yield (Bq)	
			Meas.	Cal.
^{177g}Lu	6.65 d	208.4	8.61E+04	8.83E+04
^{176m}Lu	3.66 h	88.4	1.36E+06	2.41E+06
^{174g}Lu	3.31 y	1241.8	2.21E+03	2.02E+03
^{173}Lu	1.37 y	272.1	1.56E+04	1.49E+04
^{172g}Lu	6.70 d	900.7	8.23E+05	8.93E+05
^{171g}Lu	8.24 d	739.8	8.96E+05	7.23E+05
^{170g}Lu	2.0 d	1280.3	1.13E+06	1.48E+06
^{169g}Lu	34.1 h	191.2	2.68E+05	2.95E+05

Our results demonstrate that the estimated radionuclide purity of ^{177}Lu for the 99.90 and 97.60% enriched ^{176}Yb samples at 2.5 days after the end of irradiation (EOI) is >98 and >99% at E= 20 and 15 MeV.

We also evaluated an integral yield of the carrier-free ^{177}Lu that is obtained by irradiating a ^{176}Yb sample of 0.25 mm thickness with a 100 μA, 25 MeV deuteron beams for 24 h. The yield is calculated to be 28 GBq using the measure yield of ^{177}Lu, 8.61 × 10^4 Bq as given in Table 1, that was obtained by irradiating the thick ^{nat}Yb sample (the abundance of ^{176}Yb is 13.0%) with 0.338 μA deuteron beams for 10 min. This yield is compared with a typical carrier-free ^{177}Lu activity of about 8 GBq; that is produced in a reactor with a typical thermal neutron flux of 1.0 × 10^{14} n/cm^2/sec for a neutron irradiation time of 24 h using an enriched ^{176}Yb sample of 100 mg. Here, we note a typical dose of therapeutic radiation of ^{177}Lu-radiopharmaceuticals that is delivered to tumor cells. The recommended dosage of a ^{177}Lu-radiopharmaceutical, ^{177}Lu-dotatate, is 7.4 GBq/patient every 8 weeks four intravenous infusions [2]. Therefore, the present yield of 28 GBq/day encourages us to produce ^{177}Lu by the ^{176}Yb(d,x)^{177}Lu reaction using enriched ^{176}Yb samples. The production method of ^{177}Lu by the ^{176}Yb(d,x)^{177}Lu reaction will play an important role in promoting the widespread use of ^{177}Lu for a variety of therapeutic applications. In addition, the present method would play an important role in determining the isotopic compositions of enriched samples for producing medical radionuclides with high radionuclide purity from measured excitation functions of nuclear reactions of natural samples in accelerators.

Production of an α-emitting radionuclide At-211 for medical use at JAEA tandem accelerator [3]

Experimental studies concerning the production of a medical α-emitting radionuclide ^{211}At have been conducted at the JAEA tandem accelerator under a research subject of the development of a ^{211}Rn-^{211}At generator system since 2011. In addition, research subjects related to the ^{211}Rn-^{211}At generator system, e.g., production of At and I radioisotopes, At chemistry as well as the analytical method of ^{211}At using an α-scintillation camera have been studied.

References

[1] Y. Nagai *et al*., J. Phys. Soc. Jpn. **91**, 044201 (2022). DOI: 10.7566/JPSJ.91.044201
[2] A. Abbott, *et al*., J. Nucl. Med. Technol. **46**, 237 (2018).
[3] I. Nishinaka, Proceedings of the 2021 Symposium on Nuclear Data, JAEA-Conf 2022-001, 75 (2022).

Part Ⅰ

4. Quantum-Beam Technology

P4-1 LCS Gamma-ray Project

Leader : HAJIMA Ryoichi

The research objective of LCS Gamma-ray Project is developing the technologies of high-brilliance γ-ray generation and exploring its scientific and industrial applications such as nuclear physics, nuclear astrophysics and non-destructive measurement of nuclear material. The γ-ray source is based on laser Compton scattering (LCS), which enables one to generate energy-tunable mono-energetic γ-rays. In the research project, we are developing critical components for electron accelerators to achieve small-emittance and high-average current beams, γ-ray optics and a Monte Carlo simulation code.

Low-lying dipole strength distribution in ^{204}Pb [1]

Low-lying electric dipole (E1) excitation in atomic nuclei has attracted considerable interest during the past decades, caused by significant progress in experimental and theoretical studies of its properties. It has been observed as a local accumulation of the E1 strength at the low-energy tail of the giant dipole resonance (GDR) in both stable and unstable nuclei over a broad range of nuclei. This structure is commonly denoted as the pygmy dipole resonance (PDR), because the E 1 strength is weak relative to that of the GDR.

The stable lead isotopes including ^{204}Pb are suitable for studying the PDR since they exhibit an appreciable amount of low-lying dipole strength. So far, the low-lying dipole distribution below 6.75 MeV in ^{204}Pb has been measured in nuclear resonance fluorescence (NRF) experiments with bremsstrahlung. In the present work, the information was extended up to the neutron separation energy of 8.395 MeV by using higher-energy bremsstrahlung from an electron beam at a kinetic energy of 10.5 MeV at the linear accelerator ELBE of the Helmholtz-Zentrum Dresden-Rossendorf.

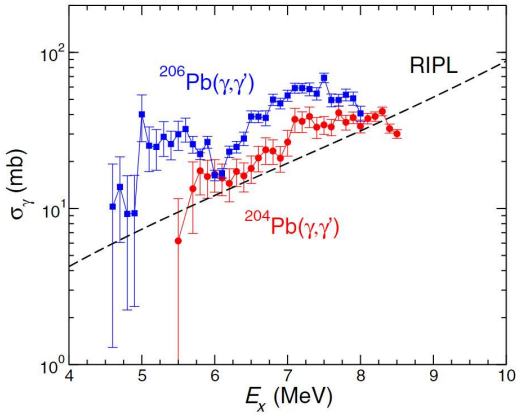

Fig. 1 Photoabsorption cross section of ^{204}Pb resulting from the present experiment (red circles) in comparison with that of ^{206}Pb (blue squares) as taken from Ref. [2]. Also shown is the Lorentz curve from the database Reference Input Parameter Library (RIPL) [3] (black dashed line) [1].

The experimental data of ^{204}Pb obtained in the present experiment shows unique character of the low-lying dipole strength distribution. In Fig. 1, the photoabsorption cross section of ^{204}Pb deduced from the quasicontinuum analysis is compared with that of ^{206}Pb [2] and a Lorentz curve taken from the database Reference Input Parameter Library (RIPL) [3]. It can be seen that the cross sections include extra strength with respect to the RIPL curve, which might be considered as the PDR. The cross section values in ^{204}Pb is approximately 60% of that in ^{206}Pb in the energy range from 6 to 8 MeV. This difference is consistent with the total strengths obtained from the analysis of the resolved peaks, which may support that there are stronger single-particle excitations in ^{206}Pb than ^{204}Pb.

We also confirmed that the gross properties of the E1 strength observed below the neutron separation energy in ^{204}Pb are consistent with theoretical predictions from the self-consistent energy density-functional (EDF) theory and the three-phonon quasiparticle-phonon model (QPM).

Generation of primary photons through laser Compton scattering using a Monte Carlo simulation code [4]

Photon sources based on laser Compton scattering are emerging as quasimonochromatic energy-tunable sources either as compact alternatives to synchrotron facilities for the production of low-energy (10–100 keV) x rays or to reach the 1–100 MeV photon energy range, which is inaccessible at synchrotrons. A reliable tool for the simulation of the radiation produced is essential for the design, the commissioning, and, subsequently, the study and optimization of this kind of source. In the present study, we developed a novel Monte Carlo code based on GEANT4 for the simulation of laser Compton scattering in the linear regime.

The developed code is based on the algorithm described in our previous work [5] to simulate LCS in GEANT4, which was limited to a head-on geometry. We extended the original LCS algorithm to overcome its limitations and gain generality, so as to be able to simulate a variety of LCS sources in GEANT4.

In order to assess the performance of the developed code, we calculated the photon spectrum of BriXS, which is a proposed source devoted to x-ray imaging in the energy range 10–100 keV and is based on an energy recovery linear accelerator coupled with a Fabry-Pérot cavity [5]. A complete simulation with both CAIN [6] and our GEANT4 code was carried out, using the parameters of BriXS. For each case, the same number of uncollimated photons (about 10^7) was simulated. Figure 2 shows the energy spectra considering three different collimations (one couple of curves refers to uncollimated spectra). It is possible to note that the general agreement is excellent. Comparison

of the calculation time required to obtain collimated spectra between our GEANT4 code and CAIN suggested that our code is about 200 times faster than CAIN.

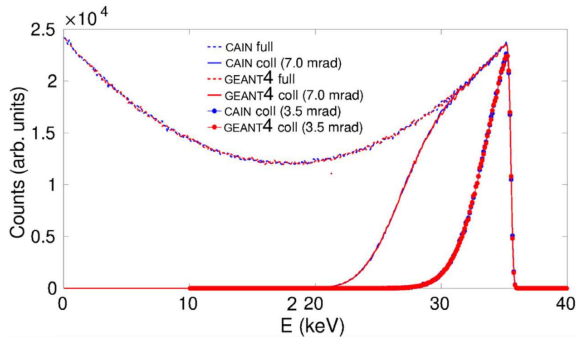

Fig. 2 Full and collimated spectrum of the BriXS photon beam simulated with CAIN and GEANT4 [4].

Non-destructive inspection of water or high-pressure hydrogen gas in metal pipes by the flash of neutrons and x rays generated by laser [7]

The thermal and epithermal neutrons are powerful probes to inspect water or high-pressure hydrogen gas because of their large scattering cross-sections with protons. Laser-driven neutron source, which is able to simultaneously emit different types of radiations such as x rays, can be used for neutron and x-ray radiography in the same laser shot. We demonstrated non-destructive inspection for H_2O contained within a stainless steel pipe using a laser-driven thermal neutron source, where water and stainless containers were detected by neutrons and x rays, respectively.

The experiment was conducted by using the LFEX laser facility at Osaka University. The primary target of a 5-mm-thick deuterated polystyrene (CD) foil was irradiated by the LFEX laser (~10^{19} W/cm^2, ~1.5 ps) to accelerate protons and deuterons via the boosted-TNSA (Target Normal Sheath Acceleration) mechanism. The energies of the protons and deuterons are up to 30 and 20 MeV, respectively. The secondary target was a beryllium (Be) block (ϕ5 × 10 mm). When ions accelerated from the CD foil bombard the Be target, fast neutrons with energies of several MeV are generated via the ^{9}Be(d, n)^{10}B and ^{9}Be(p, n)^{9}B reactions. The Be target was embedded in a circular truncated cone polyethylene (top diameter: 3.4 cm, bottom diameter: 7.4 cm, and height: 4 cm) with a density of 0.96 g/cm^3 to decelerate immediately fast neutrons to low energies. The fast neutrons are decelerated to thermal energies with a peak at ~50 meV and the yield is ~10^5 n/cm^2 at 10 cm downstream from the moderator. Although the average energy is slightly higher than the typical thermal energy of 25 meV, the energies of most neutrons are lower than the cadmium cut-off energy of 0.5 eV.

The radiography samples used in this experiment are two stainless steel pipes, where one is filled with water and the other is empty. The neutron and x-ray images for these pipes are shown in Fig.3. Note that these images are snapshots in a single laser shot with a moderated neutron pulse of few μs and x-ray with a width of ps. The spatial resolution is ~0.2 cm, and it can be improved by using a collimator in front of the samples. Due to low transmittances of thermal and epithermal neutrons for hydrogen, we can distinguish whether there is water in the pipe in the neutron image. On the other hand, since x-ray is not sensitive to low-atomic number elements, we can only see the shadows of the stainless pipes in the image.

In the coming hydrogen society, the inspection of hydrogen gas and its container is frequently needed for maintenance. Therefore, LDNSs, emitting neutrons, and x-rays, simultaneously, are expected to be used for non-destructive measurements of water or high-pressure hydrogen gas inside of transport metal tubes in factories or hydrogen stations. The experimental result suggests that the non-destructive inspection system based on high repetition-rate ultra-intense power lasers is expected to be available in factories and hydrogen stations.

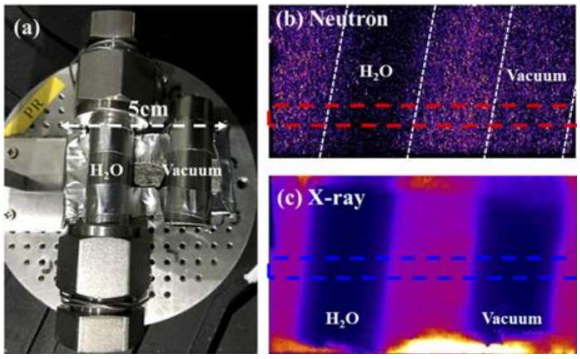

Fig. 3 (a) Picture of the radiography samples of the stainless steel pipes, of which one is full with H_2O and the other is opened in a vacuum chamber. A dysprosium plate and an imaging plate are placed under the two pipes. (b) Measured neutron radiograph. (c) X-ray image [7].

References

[1] T. Shizuma *et al*., Phys. Rev. C. **106**, 044326 (2022). DOI: 10.1103/PhysRevC.106.044326

[2] T. Shizuma *et al*., Phys. Rev. C. **98**, 064317 (2018). DOI: 10.1103/PhysRevC.98.064317

[3] R. Capote *et al*., Nucl. Data Sheets **110**, 3107 (2009). DOI: 10.1016/j.nds.2009.10.004

[4] G. Paternò *et al*., Phys. Rev. Acc. Beams, **25**, 084601 (2022). DOI: 10.1103/PhysRevAccelBeams.25.084601

[5] I. Drebot *et al*. Proc. IPAC2018, pp.4196-4198 (2018). DOI: 10.18429/JACoW-IPAC2018-THPMF057

[6] P. Chen *et al*., Nucl. Instrum. Meth. A **355**, 107-111 (1995). DOI: 10.1016/0168-9002(94)01186-9

[7] T. Wei *et al*., AIP Advances **12**, 045220 (2022). DOI: 10.1063/5.0088997

P4-2 Beam Engineering Section

Section Manager : ISHII Yasuyuki

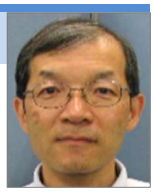

The research objectives in our section are development of various accelerator-related-techniques including ion-beam-irradiation-techniques and ion-beam-analyses. Each member has been engaged in individual research more than one. Recent remarkable study is “Characterization of hourly-collected airborne particulate matters from an automated sampling unit of the atmospheric environmental regional observation system by in-air micro-PIXE analysis”.

Characterization of hourly-collected airborne particulate matters from an automated sampling unit of the atmospheric environmental regional observation system by in-air micro-PIXE analysis [1]

Transboundary air pollution propagations are a global environmental issue affecting the human quality of life. Particulate matter (PM) is an essential indicator for such phenomena, providing information on the global atmospheric environment and long-term health care and human risks. PM concentrations are often monitored to indicate air pollution worldwide. Moreover, the elemental composition of PM is one of the most important key factors in estimating the origin of such air pollution. Often, atmospheric conditions are differed from time to time, and PMs from different origins or events are mixed rapidly and form a complex within a short period. Thus, Elemental composition analysis on PM sampled with high time resolution is desirable; however, it is sometimes hardly accomplished to characterize the elemental composition of PMs with limited concentrations with general-purpose analytical technologies. Namely, the expected amount of PM collected in an hour is approximately less than a few μg, and extraction of trace elements poses a challenge in terms of the sensitivity of the techniques. Several highly sensitive general-purpose analytical methods exist, such as ion chromatography and inductively coupled plasma mass spectrometry. We have tackled this issue by demonstrating PIXE analysis on hourly-collected PMs from Atmospheric Environmental *Regional Observation System (AEROS)* automated sampling unit and successfully revealed its elemental compositions. The micro-PIXE analysis technique can visualize the distribution of elemental compositions even at low concentrations in the air. In this case, micro-PIXE had envisioned elemental aggregation in a PTFE (Polytetrafluoroethylene) membrane tape filter from the AEROS. We can continue the investigation to obtain consecutive datasets of elemental composition for better understanding and characterization of PM collected in the short-term from the atmosphere.

We investigated element composition ratios in two sets of sequentially collected airborne particulate matter (PM) samples obtained through the automatic sampler of the Atmospheric Environmental Regional Observation System (AEROS). A series of micro-PIXE analyses and imaging were performed as shown in Fig.1 on a PTFE (Polytetrafluoroethylene) membrane tape filter corresponding to two hourly time slots through a high-concentration air pollution event from 26th to 27th March 2020 sampled at Ota, Japan (36.290◦ N, 139.381◦ E) by utilizing an external 3 MeV proton microprobe. Latent variables of sequentially collected PM samples were analyzed by the non-linear least square method and classified by those clustering driven by house-made data analysis software. Micro-PIXE imaging effectively confirmed the presence of large elemental agglomerations on the PTFE membrane tape filter of AEROS that often appeared as outliners in data analysis.

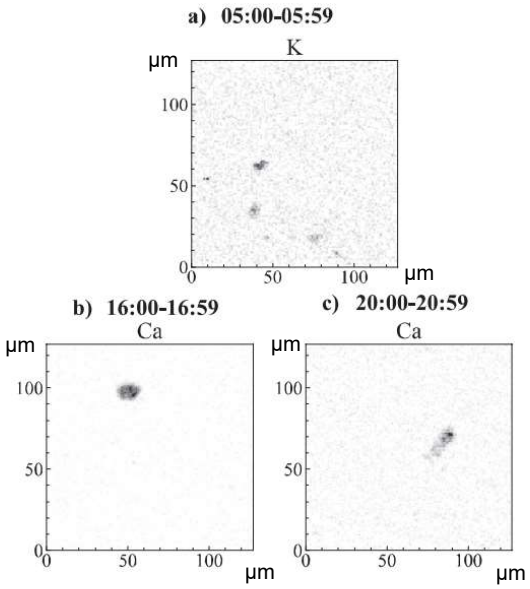

Fig. 1 Elemental aggregations on PTFE membrane tape filter visualized by Micro-PIXE imaging.

Reference

[1] K. Usui *et al*., Nucl. Instr. Meth. Phys. Res. B **544**, 165106 (2023). DOI: 10.1016/j.nimb.2023.165106

Part Ⅱ

Part Ⅱ

1. Quantum Materials and Applications

1 - 01 Generation of entanglement state between NV centers created by molecular ion implantation

K. Kimura[a,b], S. Onoda[a], W. Kada[b], K. Yamada[c],
T. Teraji[d], J. Isoya[e], O. Hanaizumi[b], and T. Ohshima[a]

[a]Quantum Materials and Applications Research Center, TARRI, QST
[b]Faculty of Science and Technology, Gunma University
[c]Department of Advanced Radiation Technology, TARRI, QST
[d]Research Center for Functional Materials, NIMS
[e]Faculty of Pure and Applied Science, University of Tsukuba

Introduction

Generating quantum entanglement states is one of the most important steps in quantum technologies such as quantum information processing and quantum sensing. The entanglement state between dipolar coupled Nitrogen-Vacancy (NV) centers in diamond has a potential to realize quantum sensors beyond the standard quantum limit. However, the techniques to create dipolar coupled NV centers have some issues. For example, N^+ ion implantation via nanohole [1], which is known as one of the techniques to create dipolar coupled NV center, has the issue about distribution of the implanted nitrogen atoms. These issues lead to reduce the fidelity of quantum entanglement state and prevent the application of quantum sensing. In our previous research, we developed molecular ion implantation technique [2,3] that overcomes the issue of nanohole implantation technique. Our technique allowed to create strongly dipolar coupled NV centers, since multiple nitrogen atoms could be implanted into the diamond at single point. It is expected that strongly dipolar-dipolar interactions lead to generate entanglement state between NV centers with high fidelity. In this study, we report the generation of quantum entanglement state between NV centers created by molecular ion implantation and discuss about fidelity.

Experimental

To create dipolar coupled NV centers, $C_5N_4H_n$ ions were accelerated at 65 keV and implanted into diamond using 400 kV ion implanter at TIARA. $C_5N_4H_n$ ion decomposes into individual atoms by collision with diamond lattice, and each nitrogen atom is implanted 9±4 nm apart. The implanted nitrogen atom was combined with a vacancy by annealing (1000°C, 2h) to create NV centers.

The created NV centers were observed using confocal fluorescence microscopy (CFM). The measurement of electron spin states of NV centers was performed with a 532 nm pulsed laser and pulsed microwaves at room temperature in the static magnetic field. Fig.1 (a) shows the pulse sequences for generation of entanglement state. Preparing both NV centers showed by NV_A and NV_B in state $|m_S^A = 0, m_S^B = 0\rangle$ by optical pumping, the Hahn Echo measurement was carried out on both NV_A and NV_B, respectively. We calculated the free evolution times ($2\tau_{ent}$) for maximum entanglement state from the fluorescence.

Results and Discussion

Fig.1 (b) shows the measured result of fluorescence signals. The black dots show the measured values, and the black solid line indicates the result of fitting with the cosine wave $\cos(2\pi\nu_{dip}\tau)$, where ν_{dip} is the strength of dipolar-dipolar interactions. The ν_{dip} was calculated to be 98.4 kHz. The maximum entanglement state appears at $\tau_{ent} = 1/4\nu_{dip}$, and the free evolution time $2\tau_{ent}$ is calculated to be 5.08 μs.

Since the electron spin state of NV center relaxes exponentially to the mixed state. The free evolution time $2\tau_{ent}$ is required to be shorter than coherence time, which is time constant tied to the process of dephasing. $2\tau_{ent}$=5.08 μs obtained in this result is short compared to the coherence time of both NV_A and NV_B (109.3 μs and 66.9 μs), respectively. It is expected to be generated entanglement state with high fidelity. The simulated fidelity from coherence time and $2\tau_{ent}$ was 0.95. This is no doubt that molecular ion implantation is technique to realize quantum sensing used entanglement state.

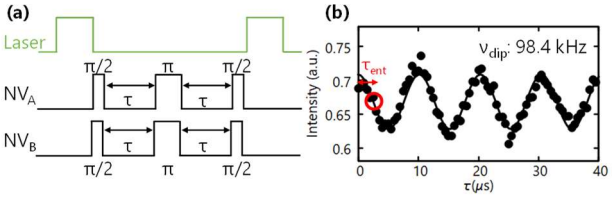

Fig. 1 (a) The pulse sequence for entanglement state. (b) The result of fluorescence signals.

Acknowledgments

This work was supported by JST Support for Pioneering Research Initiated by the Next Generation JPMJSP2146, JSPS KAKENHI No. 21H04646, 20H02187, 20H05661, JST moonshot R&D Grant Number JPMJMS2062, MIC R&D for construction of a global quantum cryptography network JPMI00316, and MEXT Q-LEAP Grant Number JPMXS0118067395 and JPMXS0118068379.

References

[1] I. Jakobi *et al.*, J. Phys. **752**, 012001 (2016). DOI: 10.1038/1742-6596/752/1/012001
[2] M. Haruyama *et al.*, Nat. Commun. **10**, 2664 (2019). DOI: 10.1038/s41467-019-10529-x
[3] K. Kimura *et al.*, Appl. Phys. Express **15**, 066501 (2022). DOI: 10.35848/1882-0786/ac7030

1 - 02 Development of super radiation-hard triple-junction solar cells: PHOENIX

Y. Murakami [a)], T. Nakamura[a)], T. Okumura[a)], S.-I. Sato[b)] and T. Ohshima[b)]

[a)]Research and Development Directorate, JAXA,
[b)]Quantum Materials and Applications Research Center, QST

We are developing a mechanically stacked InGaP/GaAs//CIGS 3-junction solar cell, named PHOENIX cell [1], as a next-generation space solar cell and planning on-orbit demonstration experiment using SDX [1] to evaluate its space environment resistance. PHOENIX aims to improve initial efficiency and radiation tolerance by using

have clarified that CIGS solar cells are extremely radiation tolerant [2]. Therefore, the radiation tolerance of PHOENIX cell is mainly dominated by a top InGaP/GaAs 2-junction (top-2J) solar cell. In the SDX radiation environment, trapped high-energy protons significantly degrade solar cells. Hence, in this study, we performed proton irradiation tests on the top-2J cells and evaluated their radiation tolerance. Furthermore, we compared the degradation curve of top-2J cells with that of conventional space solar cells to reveal the advantages of PHOENIX cells.

The top-2J cells were irradiated with proton at National Institutes for Quantum Science and Technology (QST). Energies of protons were 30 keV, 200 keV, 380 keV, 1 MeV, 3 MeV, and 10 MeV. We evaluated the change in current-voltage characteristics under air mass zero (AM0) light illumination due to proton irradiation and calculated the relative damage coefficient (RDC). RDC is one of the indicators to evaluate the degradation of cell's output on-orbit. RDC for proton means the degree of damage caused by protons of various energies compared to 10 MeV protons. For example, if RDC is 2, half the fluence cause the same degradation as 10 MeV protons irradiation.

RDCs of open-circuit voltage (V_{oc}) and maximum power point (P_{max}) are shown in Figure 1. Short-circuit current (I_{sc}) was almost not degraded by 10 MeV protons irradiation. Figure 1 indicates that 200 keV protons caused maximum degradation of V_{oc} and P_{max}. In this case, protons stop within the GaAs layer and cause damage to GaAs layer, which has lower radiation tolerance than InGaP [3].

Figure 2 shows a comparison of the remaining factor of P_{max} of top-2J cells with a conventional InGaP/GaAs/Ge 3-junction (503) cell and an IMM InGaP/GaAs/InGaAs 3-junction (IMM-3J) cells [4]. IMM-3J solar cells are much more radiation tolerant than 503 solar cells. This is due to the reduction in thickness of IMM-3J solar cells compared to 503 solar cells, which leads to reduction in the influence of diffusion length reduction. Top-2J solar cells are much more radiation resistance than IMM-3J solar cells at higher fluence region since top-2J solar cell is designed to be thinner than IMM-3J solar cell.

In future work, we will obtain RDC for electron to investigate PHOENIX's radiation tolerant in various environments in more detail.

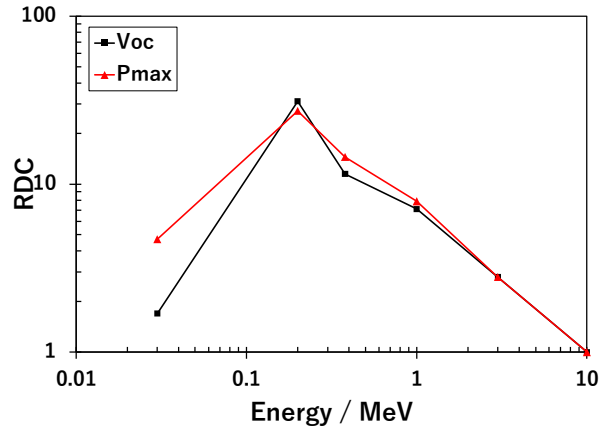

Fig. 1. RDC of top-2J cells (V_{oc} and P_{max}).

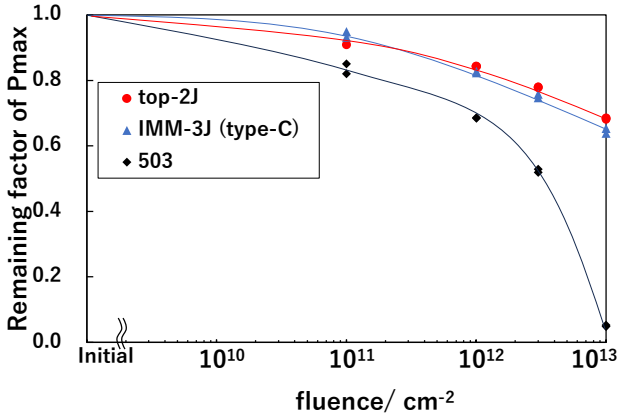

Fig. 2. Remaining factor of P_{max} as a result of 10 MeV proton irradiation.

Acknowledgments

The authors thank the kind assistance of M. Sugai and Y. Mori of the AES Corporation.

References

[1] M. Imaizumi *et al.*, IEEE 49th Photovoltaics Specialists Conference (PVSC), Philadelphia, PA, USA, 1257-1257 (2022).
[2] T. Hisamatsu *et al.*, 2nd World Conference on Photovoltaic Energy Conversion (WCPEC), 3568 (1998).
[3] M. Imaizumi *et al.*, Prog. Photovolt: Res. Appl. 25:161–174 (2017).
[4] T. Takamoto *et al.*, IEEE 40th Photovoltaic Specialist Conference (PVSC), Denver, CO, USA,1-5, (2014).

1 - 03 TIARA AVF cyclotron first revealed the cosmic-ray reliability of oxide semiconductor and new reaction

T. Makino[a)], T. Ohshima[a)], D. Kobayashi[b)], A. Ikuta[b)], H. Takahashi[c)], Y. Okamoto[c)], T. Hamada[c)], Y. Komura[c)], S. Watanabe[c)], K. Tsuda[c)], H. Sawai[c)], T. Matsuzaki[c)], Y. Ando[c)], T. Onuki[c)], H. Kunitake[c)], and S. Yamazaki[c)]

[a)]Quantum Materials and Applications Research Center, QST
[b)]ISAS and TansaX, JAXA
[c)]NOS Development and CAD Divisions, Semiconductor Energy Laboratory, Co., Ltd.

Introduction

Today's Information Technology (IT) society relies on semiconductor devices. As represented by Internet on Things (IoT), people's demands for using semiconductor devices anywhere and anytime call for further reduction in their power consumption. This purpose brings new materials into device structures, such as Wide-band Gap (WG) semiconductors.

The TIARA AVF cyclotron has been revealed various new features of WG semiconductors, for example an anomalous reaction of SiC diodes to cosmic rays (radiation heavy ions) [1]. Here, we show our recent findings in a new type WG semiconductor device, which is drawing attention for ultra-low power operation. The cyclotron has revealed its superior reliability in comparison with standard Si devices and a new reaction unable to be explained in the standard theory established in Si devices [2].

Experimental

The tested WG semiconductor device was an Oxide Semiconductor (OS) memory, which was fabricated in a process developed by Semiconductor Energy Laboratory Co. Ltd. The memory consisted of *c*-axis-aligned crystalline OS filed-effect transistors. This transistor provides off-current down to 10^{-24} A/μm, which is extremely lower than typical range from 10^{-10} to 10^{-8} A/μm for Si transistors.

We exposed the OS memory to the cocktail-5 (M/Q=5) beam from the TIARA *K*=110 AVF cyclotron. The memory was prepared as a fully functional chip with a memory capacity of *M*=228 KB. Two chips were in total tested. We programmed the memory cells on a chip with predetermined data and exposed the chip to a beam for one minute (t = 60 s). We then read out data from the memory and compared them with the original data to identify memory cells failed to keep their memory. From the number of failed (upset) cells n [bits], we calculated a single-event upset (SEU) cross section $\sigma = n/(\varphi t M)$ [cm^2/bit], where φ represents the flux of the beam (cm^{-2} s^{-1}). This number (σ) corresponds to an error probability and should be lower for higher reliability.

Results and Discussion

The cocktail-5 heavy-ion beam successfully revealed the superior reliability of the tested OS memory (Fig. 1). The SEU cross sections of the OS memory were all smaller than standard Si SRAMs, which were fabricated in a bulk or a silicon-on-insulator (SOI) process with a design rule similar to that used for the OS memory (60 nm).

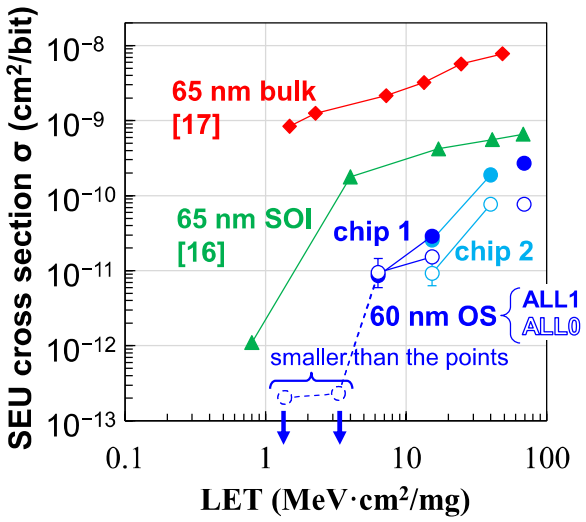

Fig. 1 Measured SEU cross sections of the tested OS memory, compared with bulk- and SOI-Si SRAMs, reprinted from [2] (©2023, IEEE). See [2] for the references [17] an [16].

The tested two chips (chips 1 and 2 in Fig. 1) exhibited the statistically same SEU cross sections, as expected from the maturity of the fabrication process. They also revealed a clear dependence on the programmed data (ALL1 or ALL0). In ALL1 test all the memory cells were programmed with binary logic 1 whilst ALL0 to logic 0. The revealed dependence is interesting because it is different from our expectations. We expected that the OS memory showed a pattern dependence, but the difference revealed between the ALL1 and ALL0 tests was smaller than that we expected. From an analogy between the operational principle of the OS memory and Si ones, we expected that the OS memory preserved the ALL0 pattern and exhibited no upset (i.e., σ = 0). The experimental results, however, have shown $\sigma > 0$ and close to the ALL1 case (roughly 0.5X). The theory established in Si semiconductors cannot explain this finding.

References

[1] T. Makino *et al.*, IEEE Trans. Nucl. Sci., 2647 (2013). DOI: 10.1109/TNS.2013.2243469
[2] H. Takahashi *et al.*, in Proc. IRPS, 7C.1 (2023). DOI: 10.1109/IRPS48203.2023.10118302

1 - 04 Efficient creation of NV centers in HPHT type-Ib diamonds by electron irradiation with in-situ annealing

S. Ishii, S. Saiki, S. Onoda, H. Abe, T. Ohshima

Quantum Materials and Applications Research Center, QST

Introduction

Negatively charged nitrogen-vacancy (NV^-) center, one of defects in diamond, acts as a quantum sensor at room temperature (RT) for magnetic field [1]. The magnetic field sensitivity for ac signals has been realized to be subpicotesla-level [2]. Improving the sensitivity would lead to a new class of scientific and industrial applications e.g. real-time magnetic imaging of neuronal circuit dynamics [1,3].

The magnetic field sensitivity is proportional to the reciprocal of $\sqrt{NT_2}$, where N is the number of NV centers and T_2 is the spin coherence time. The sensitivity can be enhanced by increasing the number of NV^- center and extending spin coherence time [1,4]. To obtain high concentration of NV^- center, electron beam irradiation into type-Ib diamond containing high concentration of isolated substitutional nitrogen (P1 center) is effective [1]. The electron beam irradiation can introduce a plenty of vacancies into diamond, and subsequent annealing over 600°C enables vacancies to diffuse in diamond lattice. When the diffused vacancy is trapped by P1 center, NV center is created. Recently, M. Capelli et al. reported that NV center was created more efficiently by irradiation with in-situ annealing at 740°C compared to RT irradiation [5]. In this study, irradiation with in-situ annealing at higher temperature (800-1000°C) was performed for efficient creation of NV^- center.

Experimental

Type-Ib diamonds synthesized by HPHT method were purchased from Sumitomo Electric Industries, Ltd (Osaka, Japan). The samples have initial P1 concentration of 67, 57, 63 ppm for irradiation at RT, 800°C and 1000°C, respectively. Electron beam irradiation with energy of 2 MeV was carried out with irradiation fluence up to 5.0×10^{18} e/cm^2 at Takasaki Institute for Advanced Quantum Science. Irradiation with in-situ annealing at 800°C and 1000°C was performed in vacuum with custom-built chamber. Then, all irradiated samples at each fluence step were subsequently annealed at 1000°C for 2 hours in vacuum (~ 1.0×10^{-4} Pa).

The concentration of P1 center and NV^- center was calculated from the sample volume and the number of spins, obtained from the double integration of ESR spectra measured by continuous-wave X-band ESR spectrometer (JES-X330, JEOL Ltd., Tokyo, Japan).

Results and Discussion

The P1 center concentration was plotted against irradiation fluence in Figure 1A. As irradiation fluence increased, the concentration of P1 center decreased at all irradiation temperature. P1 concentration changed from 67, 57, 63 ppm at unirradiated to 40, 33, 35 ppm at 5.0×10^{18} e/cm^2 for RT, 800°C and 1000°C, respectively.

Next, the NV^- concentration was plotted against irradiation fluence in Figure 1B. At the irradiation fluence of 5.0×10^{18} e/cm^2, the concentration of NV^- center reached ~7.6 ppm, ~10.3 ppm, ~8.3 ppm for RT, 800°C and 1000°C, respectively. NV^- centers were created 1.4 times at 800°C as many as RT. In this fluence range, the concentration of NV^- centers monotonically increased with increasing irradiation fluence.

The conversion efficiency from initial P1 center to created NV^- center, which is defined as the ratio of NV^- concentration to the concentration of all nitrogen atoms, was enhanced by irradiation with in-situ annealing at 800°C and 1000°C compared to RT irradiation. Furthermore, NV^- centers were created more efficiently at 800°C than at 1000°C. Irradiation with in-situ annealing at 800°C seems to be more appropriate temperature for efficient creation of NV^- center compared to RT and 1000°C.

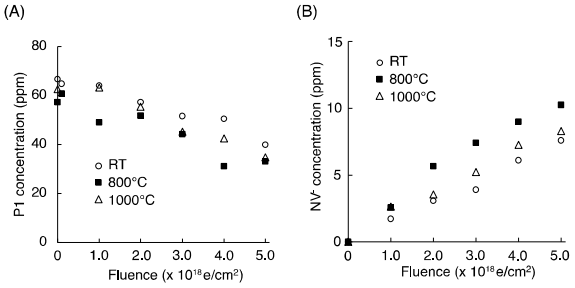

Fig. 1 Irradiation fluence dependence of NV^- and P1 concentration. (A) Irradiation fluence vs P1 concentration at RT, 800°C and 1000°C are shown, respectively. (B) Irradiation fluence vs NV^- concentration at RT, 800°C and 1000°C are shown, respectively.

Acknowledgments

This study was supported by Quantum Leap Flagship Program (Q-LEAP: JPMXS 0118067395) of MEXT.

References

[1] J.F. Barry et al., *Rev. Mod. Phys.,* **92**, 015004(68) (2020). DOI: https://doi.org/10.1103/RevModPhys.92.015004.

[2] T. Wolf et al., *Phys. Rev. X.,* **5**, 041001 (2015). DOI: https://doi.org/10.1103/PhysRevX.5.041001.

[3] J.F. Barry et al., *Proc. Natl. Acad. Sci. USA.,* **113**, 14133 (2016). DOI: https://doi.org/10.1073/pnas.1601513113.

[4] D. Budker et al., *Nat. Phys.,* **3**, 227 (2007). DOI: https://doi.org/10.1038/nphys566.

[5] M. Capelli et al., *Carbon*, **143**, 714 (2019). DOI: https://doi.org/10.1016/j.carbon.2018.11.051.

1 - 05 Experimental design for manipulating quantum states of trapped Ba^+ isotopes with various nuclear spin values

H. Shimada[a)], K. Hosaka[a)], H. Kashiwagi[a)], S. Hosoya[a)], Y. Yuri[a)], R. Nakanishi[a)], K. Tamura[a)], K. Ogura[a)], H, Ohba[b)], and K. Narumi[a)]

[a)]Quantum Materials and Applications Research Center, QST
[b)]Collaborative Laboratories for Advanced Decommissioning Science, JAEA

The use of trapped ions as qubit carrier for quantum information processing is one of the promising candidates for realizing a high-fidelity scalable quantum computer.

Various schemes for encoding a single qubit onto electronic states of an ion has been proposed, among which the hyperfine qubit is known to be rather robust to environmental noise and easy to handle. In this scheme, a pair of levels in the ground-state hyperfine manifolds of an ion with non-zero nuclear spin (I) is used as a qubit.

Among various ion species with non-zero nuclear spin trapped and cooled so far, special attentions have been paid for those having I = 1/2 in the context of the information processing. This is because they have the smallest non-zero nuclear spin; the hyperfine structure is simplest, having the minimum number of levels. This special feature of ions having I =1/2 makes them appropriate for information processing. Due to their smallness in the number of levels, the fidelity of population transfer is expected to be higher than other species having I > 1/2. In addition, the initialization and readout processes can become quite simple due to the special properties of selection rules of electronic transitions.

Until recently, the trapped and cooled species having nuclear spin I = 1/2 have been limited to $^{111}Cd^+$, $^{171}Yb^+$, and $^{199}Hg^+$. These ions are, however, rather difficult to handle because of their complicated electronic structure or the requirement for short-wavelength laser radiation in the UV range for driving the electronic transitions.

In 2020, Campbell's group at UCLA succeeded in trapping, cooling, and manipulating a new I = 1/2 ionic species, $^{133}Ba^+$ [1]. The Ba^+, compared with the other ions above mentioned, has rather simple electronic structure, with the wavelengths of the electronic transitions in the visible range, which greatly simplifies the optical setup. One disadvantage of $^{133}Ba^+$ is that it is radioactive isotope (RI), requiring special care for its handling.

Fully utilizing our capability of handling RI in QST Takasaki campus, we have started studying this new laser-cooling capable $^{133}Ba^+$ having I = 1/2. We are designing and constructing the experimental setup for trapping, cooling, and manipulating various isotopes of Ba^+ including $^{133}Ba^+$. The whole system is roughly divided into the following subsystems: (1) a vacuum subsystem, (2) an ion source subsystem (for both RI and non-RI), (3) a trap and driver subsystem, and (4) an optical subsystem (this is further divided into the laser part and the observation part). In this report, we describe the laser part of the optical subsystem in detail.

For cooling Ba^+, two frequency-stabilized external-cavity diode lasers (ECDL) in the visible range (493 nm and 650 nm) are used. For the Doppler cooling of zero nuclear spin isotopes ($^{138}Ba^+$ and other even isotopes), thus having no hyperfine structure, these two optical frequencies are enough to establish a closed system of cycling transitions. For odd isotopes (I = 1/2: $^{133}Ba^+$, and I = 3/2: $^{137/135}Ba^+$), due to the presence of the hyperfine splitting, it is necessary to drive the electronic transitions from all the lower sublevels so as to complete the transition cycles. This is achieved by generating additional frequency components using two broadband electro-optic modulators (EOMs). In addition, schemes for sub-Doppler cooling for these isotopes have been designed.

For the manipulation of a qubit, this is most easily achieved for ions with nuclear spin I = 1/2. In this special case, the initialization and readout of a qubit can be done with the basically same optical setup for the Doppler cooling described above. For other cases (I = 0 and I = 3/2), we have designed the initialization and readout setup using three additional ECDLs based on the scheme give in [2], which does not necessitate the use of narrow-linewidth laser, simplifying the implementation.

One complication is that we can handle $^{133}Ba^+$ only in the RI-controlled area. On the other hand, the optical setups are almost common for both RI (A = 133) and non-RI (others) Ba^+ experiments. Therefore, we decided to construct a single system of the light sources and locate it in the non-RI experimental room, from which the lights for $^{133}Ba^+$ are delivered to the RI experimental room. A fiber cable for this purpose is in preparation.

The whole conceptual design and the most part of the technical design for the whole experimental system, including the laser part described here, has been finished. The implementation is in progress.

Acknowledgments

This work was supported by the JST Moonshot R&D Grant Number JPMJMS2063 and by QST President's Strategic Grant QST Advanced Study Laboratory.

References

[1] JE Christensen *et al*., npj Quantum Inf 6, 35 (2020). DOI: 10.1038/s41534-020-0265-5

[2] A. H. Myerson et al., Phys. Rev. Lett. 100, 200502 (2008). DOI: 10.1103/PhysRevLett.100.200502

1 - 06 Calculation study of selective ion extraction from a linear-Paul-trap

N. Miyawaki[a)], Y. Ishii[a)], Y. Yuri[a)], K. Narumi[a)], K. Muroo[b)], K. Ito[a, b)] and H. Okamoto[a, b)]

[a)]Quantum Materials and Applications Research Center, QST
[b)]Graduate School of Advanced Science and Engineering, Hiroshima University

Introduction

We are developing a single ion implantation system that combines a linear-Paul-trap (LPT) and a two-stage electrostatic acceleration lens (TAL) to create arrays of nitrogen-vacancy (NV) centers, which have recently attracted attention as qubits. Nitrogen (N) atoms must be spaced within a few tens of nanometers to allow electron spins of NV centers to interact. In addition, because it is necessary to create arrays of NV centers at depths of several tens of nanometers or less, which are not affected by the diamond surface, N ions must be accelerated to energies on the order of 10 keV and implanted. A TAL focused 47-keV hydrogen ions to a diameter of 115±10 nm with a conventional ion source [1], but the beam emittance (ε) in the ion source limited further focusing. The LPT has been used as a N_2^+ source that can deterministically control individual ions with low ε [2]. N_2^+ is cooled with the Coulomb interaction with $^{40}Ca^+$ which is Doppler-laser-cooled in the LPT, and a mixed Coulomb crystal of Ca^+ and N_2^+ is formed. Therefore, we have performed a computational study using a multi-particle simulation code on how to extract a single low-ε N_2^+ from the mixed Coulomb crystal state formed in the LPT.

LPT and Simulation

The LPT treated here is a conventional one consisting of four rod electrodes and two end-plate electrodes, as shown in Fig. 1. Ions are confined in the *x*-*y* plane by a quadrupole electric field generated by an RF voltage applied to four parallel rod electrodes. Confinement of ions in the *z*-axis direction uses an electrostatic field generated by applying a DC voltage to the end-plate electrodes, and the volume enclosed by the rods and end-plate electrodes are the trap region. By irradiating this region with a cooling laser (397 nm) from outside of the LPT, the trapped $^{40}Ca^+$ can be cooled to 0.54 mK, the Doppler limit temperature. The procedure for extracting a single N_2^+ from the LPT is based on the timing of the two end-plate electrode voltages as shown in Fig. 2. The potential distribution produced by an

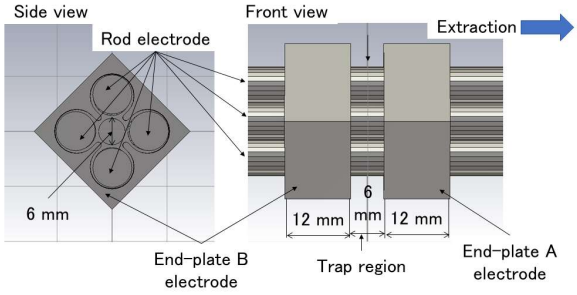

Fig. 1 Schematic view of the LPT.

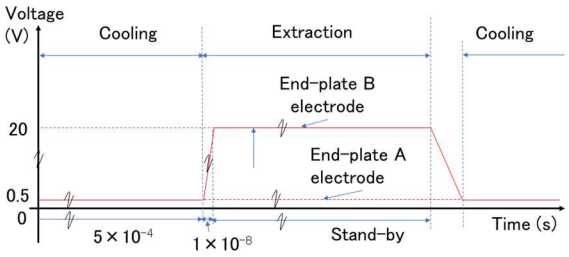

Fig. 2 Timing diagram of the two end-plate electrodes potentials.

LPT electrode geometry was calculated with the CST STUDIO SUITE code. A multi-particle simulation code, imported with data of the calculated potential distribution, analyzes the three-dimensional trajectories and Coulomb interactions of ions confined in an arbitrary LPT system, allowing the simulation of complex procedures to extract ions from the LPT. The effect of the arrangement of ions in the mixed Coulomb crystal on the ε of N_2^+ was investigated in this simulation.

Results and Discussion

The ε of N_2^+ as a beam in the extraction procedure from the LPT was calculated by repeating the simulation 100 times for each of the following four types of arrays: 1 (N_2^+, Ca^+, Ca^+, Ca^+), 2 (Ca^+, N_2^+, Ca^+, Ca^+), 3 (Ca^+, Ca^+, N_2^+, Ca^+), and 4 (Ca^+, Ca^+, Ca^+, N_2^+). The ε of N_2^+ in the array 4, which is closest to the end-plate A in the extraction direction, was 6.5×10^{-16} m·rad, the smallest of the four arrays. This was almost the same as ε = 5.5×10^{-16} m·rad for N_2^+ in the Coulomb crystalline state. In the other three arrays, the ε of N_2^+ degraded by more than three orders of magnitude from that of the array 4, as the N_2^+ collided with Ca^+ during acceleration and the lighter N_2^+ overtook the Ca^+. The ε of N_2^+ was calculated with simulation for the case of two N_2^+ in an array (Ca^+, Ca^+, N_2^+, N_2^+). Since the leading N_2^+ in the array was tracked by the latter N_2^+, ε was 4.8×10^{-15} and 4.7×10^{-15} m·rad, respectively. These were an order of magnitude worse than ε of the single N_2^+ in the array 4. Thus, it was found that for the extraction of low-ε N_2^+ from the LPT N_2^+ must be single and leading in an array of a mixed Coulomb crystal.

Acknowledgments

This work was supported by the JST Moonshot R&D Grant Number JPMJMS2062, and the JSPS KAKENHI Grant Numbers JP 20H00145 and JP 20H02673.

References

[1] Y. Ishii *et al.*, Nucl. Instr. and Meth. B 420 12 (2018). DOI: 10.1016/j.nimb.2018.01.013
[2] K. Groot-Berning *et al.*, New J.Phys. 23 (063067) 1 (2021). DOI: 10.1088/1367-2630/ac0753

1 - 07 Laser-cooled ion source for an ultrahigh-precision single-ion implanter

K. Hosaka[a)], S. Hosoya[a)], H. Kashiwagi[a)], Y. Yuri[a)], N. Miyawaki[a)], Y. Ishii[a)], H. Shimada[a)], R. Yamagata[a)], T. Sato[a)], Y. Saito[a)], S. Onoda[a)], K. Narumi[a)], K. Muroo[b)], K. Ito[b)], and H. Okamoto[b)]

[a)]Quantum Materials and Applications Research Center, QST
[b)]Graduate School of Advanced Science and Engineering, Hiroshima University

Deterministic ion implantation methods at the nanometer scale provide a route towards scalable quantum information processing [1,2]. For this purpose, we have started the development of an inherently deterministic method for single-ion implantation based on a linear Paul trap (LPT) as a single-ion source since the laser-cooling technique can be applied to the trap system to obtain ultralow-emittance ions and manipulate single ions one by one [2]. As a first step, Coulomb crystals of laser-cooled Ca^+ ions were observed with a test LPT system.

Schematic view of the test LPT system combined with the laser-cooling setup are shown in Fig. 1. The Paul trap consists of four cylindrical rods and two end plates with a hole. The distance from the trap center axis to the surface of the electrodes is 3.0 mm and the distance between two end plates is 6.0 mm. An atomic oven is located below the center of the LPT. Neutral gases produced by the oven are ionized by an electron beam coming from an electron gun placed above the LPT. The LPT utilizes an rf quadrupole field to confine charged particles transversely. The rf frequency and amplitude are 2 MHz and 33 V, respectively. The axial ion confinement is achieved by applying DC voltages to the two end plates $V_A = V_B = +1.0$ V. The trapped $^{40}Ca^+$ are Doppler cooled with cooling (397nm) and repumping (866nm) lasers. Laser-induced fluorescence (LIF) photons are divided with a half mirror and are detected both with a photomultiplier tube (PMT) and a CCD camera.

Figure 2 shows an example of LIF images obtained with the CCD camera, where each spot represents a single $^{40}Ca^+$. This crystal-like structure is called a “Coulomb crystal”, where the translational motion of ions is negligibly small, and each ion stays at its own position as the result of the balance between Coulomb repulsion and focusing electric field. The structure of a Coulomb crystal depends on the total ion number and the transverse and longitudinal focusing forces. Under the experimental conditions outlined above, a 1D “string” crystal consisting of 14 ions was observed.

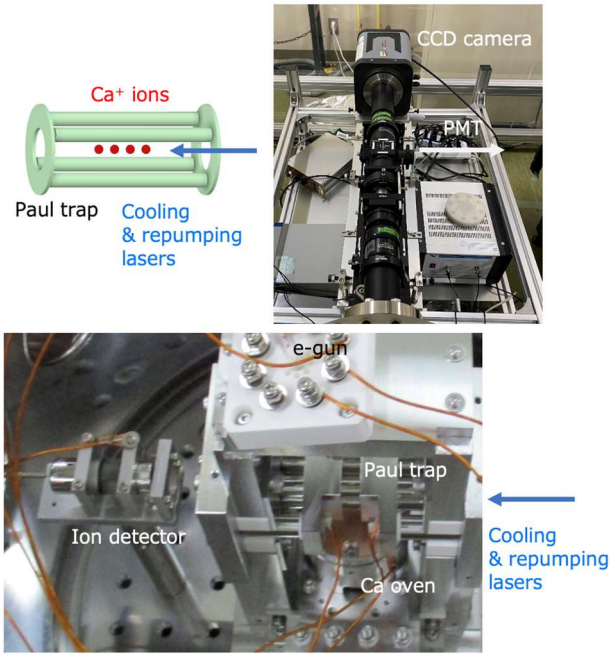

Fig. 1 Schematic view of the test LPT system combined with the laser-cooling setup.

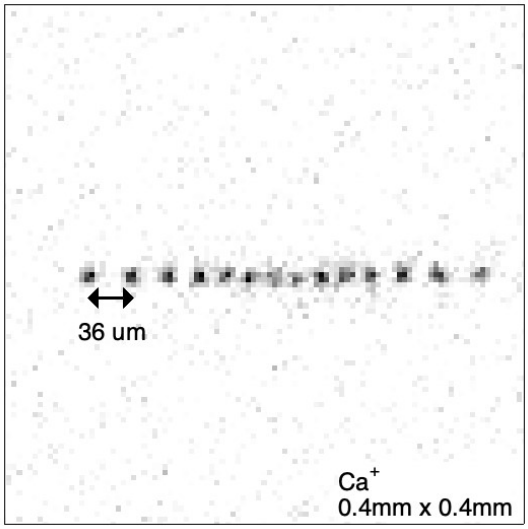

Fig. 2 LIF images of $^{40}Ca^+$ detected by the CCD camera.

Acknowledgments

This work was supported by the JST Moonshot R&D Grant Number JPMJMS2062, the JSPS KAKENHI Grant Number JP 20H00145, and QST President's Strategic Grant QST Advanced Study Laboratory.

References

[1] K. Groot-Berning, *et al.*, Phys. Rev. Lett. **123**, 106802 (2019). DOI: 10.1103/PhysRevLett.123.106802
[2] K. Izawa *et al.*, J. Phys. Soc. Jpn.**79**, 124502 (2010). DOI: 10.1143/JPSJ.79.124502

1 - 08 Numerical feasibility study on an ultrahigh-precision single-ion implanter based on laser-cooled ions

Y. Yuri[a)], N. Miyawaki[a)], K. Hosaka[a)], S. Hosoya[a)], Y. Ishii[a)], H. Kashiwagi[a)], H. Shimada[a)], R. Yamagata[a)], T. Sato[a)], Y. Saito[a)], S. Onoda[a)], K. Narumi[a)], K. Muroo[b)], K. Ito[b)], and H. Okamoto[b)]

[a)]Quantum Materials and Applications Research Center, QST
[b)]Graduate School of Advanced Science and Engineering, Hiroshima University

Ion implantation is an indispensable accelerator technique for creating defects and introducing impurities in materials. Especially, deterministic single-ion implantation is necessary for the precise creation of diamond nitrogen vacancy centers, applied to state-of-art quantum metrology and communication.

For this purpose, we have started the research and development study of an ultrahigh-precision single-ion implanter system to achieve the requirement of an irradiation precision of a few tens of nm. A linear Paul trap (LPT) has been adopted as a single-ion source since the laser-cooling technique can be applied to the trap system to obtain ultralow-emittance ions and manipulate single ions one by one. An electrostatic focusing lens system is connected to the LPT, where single ions extracted from the LPT can be strongly focused down to a spot size of the nm scale with an energy of the order of 10 keV. Recently, the dynamics on the single-ion extraction from an LPT was studied [1] and a two-stage electrostatic bipotential lens system was designed [2]. According to these results, a systematic simulation study has been conducted to show the feasibility of the whole implanter system.

We here adopt nitrogen molecular ions $^{14}N_2^+$ as an implantation ion species for the above-mentioned application. To make them ultralow-emittance, sympathetic cooling with laser-coolable $^{40}Ca^+$ (Doppler limit: 0.54 mK) is employed. A two-component string Coulomb crystal where the leading ion is N_2^+ is prepared in the LPT for the selective extraction of N_2^+ without significant deterioration of its emittance [1]. Only the leading N_2^+ ion can be extracted from the LPT by properly controlling the voltage and its timing of the end-plate electrode. Then, the extracted ion is accelerated in the two-stage lens and focused onto a target sample. The acceleration energy of N_2^+ is chosen as 14 keV for the implantation at a depth of 10 nm in diamond.

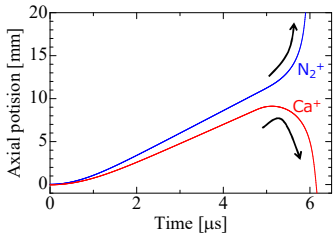

Fig. 1 Temporal evolution of the axial position of the two laser-cooled ions during the extraction from the LPT. The origin of the abscissa is the time when the prompt voltage switching of the upstream end-plate electrode is initiated.

Detailed molecular dynamics simulations were conducted to explore the behavior of laser-cooled ions. The electrostatic potential was obtained from the modeled configuration of the implanter system using the software CST Studio Suite.

As an example, the case of a two-ion (one Ca^+ and one N_2^+) crystal, confined with the voltage of the two end-plate electrodes of 0.5 V in the LPT, is discussed here. The temporal evolution of the two ions in the extraction process is shown in Fig. 1. They start to move downstream by switching the voltage of the upstream end-plate electrode from 0.5 V to 20 V and then reach the downstream end-plate electrode. If the voltage of the downstream end-plate electrode is increased from 0.5 V to 1.8 kV promptly in a proper timing (e.g., at 4.7 μs in Fig. 1), the N_2^+ ion is pre-accelerated to 0.7 keV toward the lens system while the following Ca^+ is reflected backward to the LPT. The ion-selective extraction can be achieved in this way.

The final distribution of N_2^+ ions after acceleration and focusing is shown in Fig. 2. The normalized emittance and spot size of the 14-keV ions are of the order of 10^{-16} m·rad and 1 nm, respectively. The working distance is about 16 mm in the present condition. It is thus numerically shown that sympathetically-cooled ions extracted from the LPT can be focused well below 10 nm.

Acknowledgments

This work was supported by the JST Moonshot R&D Grant Number JPMJMS2062, and the JSPS KAKENHI Grant Number JP 20H00145.

References

[1] N. Miyawaki *et al.*, Nucl. Instr. Meth. B **542**, 183 (2023). DOI: 10.1016/j.nimb.2023.06.015
[2] Y. Ishii *et al.*, Nucl. Instr. Meth. B **541**, 200 (2023). DOI: 10.1016/j.nimb.2023.05.021

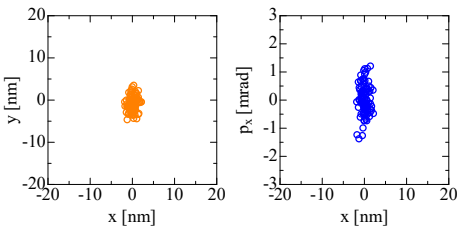

Fig. 2 Transverse cross-sectional and phase-space distribution of focused N_2^+ ions near the waist position. The results of 100 independent simulation runs are plotted to take the average.

1 - 09 Spin property improvement of boron vacancy defect in hexagonal boron nitride by thermal treatment

Y. Yamazaki[a)], T. Suzuki[a,b)], T. Taniguchi[c)], K. Watanabe[c)], Y. Nishiya[d)], Y. Matsushita[a,d)], K. Harii[a)], Y. Masuyama[a)], Y. Hijikata[b)] and T. Ohshima[a)]

[a)]Quantum Materials and Applications Research Center, QST
[b)]Department of Electrical Engineering, Saitama University
[c)]Research Center for Functional Materials, NIMS
[d)]Institute for Innovative Research, Tokyo Institute of Technology

Introduction

Quantum sensors based on spin defects in wide-gap semiconductors, such as nitrogen-vacancy complex defect in diamond (NV center) and silicon vacancy in SiC, have attracted much attention as promising sensors that can detect magnetic-, electric-fields and temperature with high sensitivity and spatial resolution.

Recently, spin defects in two-dimensional material, hexagonal boron nitride (hBN), have been discovered [1, 2]. In general, when spin defects are formed by energetic particle irradiation, unwanted defects are also introduced. The unwanted defects degrade the optical and spin properties of the spin defects. It is known that unwanted defects, which have lower thermal stability than spin defects, can be removed by post-annealing, and the optical and spin properties of spin defects are improved [3]. In this study, we investigate the changes in optical and spin properties of hBN-V_B by thermal treatment.

Experimental

The samples used in this study were hBN flakes exfoliated on SiO2 (90 nm)/Si substrates by a tape peeling method. V_B ensemble was formed by N_2 ion irradiation with ion energy of 40 keV (fluence = 1×10^{15} cm^{-2}). In order to investigate the effect of thermal stability on the formation of V_B ensemble, we compared two methods: high-temperature ion irradiation (HTI) and room-temperature irradiation followed by post-annealing (PA). The processing temperature was varied from room temperature to 800 °C. Photoluminescence (PL) and optically detected magnetic resonance (ODMR) were used for characterizing optical and spin properties, respectively.

Results and Discussion

Figure 1 shows the PL spectra of hBN flakes and substrates before and after room temperature irradiation. After irradiation, two peak signals were obtained from the hBN flakes. The signal from the short wavelength side is similar to that from the substrate. Considering this, the long wavelength peak is estimated to be located at 700-900nm.

The dependence of PL intensity on processing temperature is shown in Fig. 2. For PA, the PL signal disappears at 600 °C, while a slight PL signal can be observed even at 700 °C for HTI. These results show that V_B can be formed at higher temperatures than those for PA,

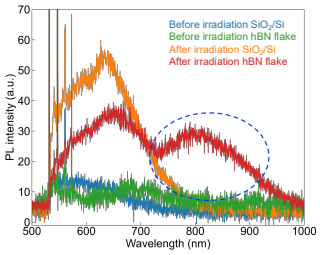

Fig. 1 the PL spectra of hBN flakes and substrates before and after room temperature irradiation.

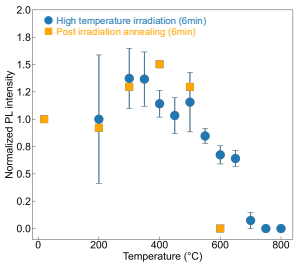

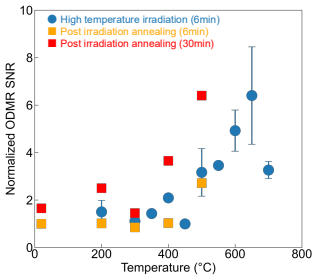

Fig. 2 (left) The dependence of PL intensity on processing temperature.
Fig. 3 (right) The dependence of the signal-to-noise ratio.

because defect formation and thermally structural change occur simultaneously for HTI. Figure 3 shows the dependence of the S/N ratio of the ODMR signal, indicating sensor sensitivity, on the processing temperature. Both treatments improved the S/N ratio by about 4. This result indicates that sensor sensitivity is improved by thermal treatment. The treatment is an easily applicable method, and is an important finding for the future practical application of hBN-V_B-based quantum sensors.

Acknowledgments

This research has been supported by the QST President's Strategic Grant QST Creative Research and JSPS KAKENHI No. 20K05352.

References

[1] A. Gottsholl *et al.*, Nat. Mater. **19**, 540 (2020). DOI: 10.1038/s41563-020-0619-6.
[2] N. Mendelson *et al.*, Nat. Mater. **20**, 321 (2020). DOI: 10.1038/s41563-020-00850-y.
[3] Y. Chiba *et al.*, Mater. Sci. Forum **1004**, 337 (2020). DOI: 10.4028/www.scientific.net/MSF.1004.337.
[4] N.-J. Guo *et al.*, ACS Omega **7**, 1733 (2022). DOI: 10.1021/acsomega.1c04564.

1 - 10 Chlorine doping into single-layer graphene film by high-energy ion irradiation

S. Entani[a)], M. Honda[b)], M. Mizuguchi[c)], H. Watanabe[d)] M. Kohda[a,e)] and T. Ohshima[a,e)]

[a)]Quantum Materials and Applications Research Center, QST
[b)]Sector of Nuclear Science Research, JAEA
[c)]Institute of Materials and Systems for Sustainability, Nagoya University
[d)]Research Institute for Applied Mechanics, Kyushu University
[e)]School of Engineering, Tohoku University

Introduction

Heteroatom-doping into graphene has attracted wide attention for tailoring electronic, physical and chemical properties of graphene. Although studies on the synthesis and analysis of graphene hydrides (graphane) and fluorographene are widely available, studies on the synthesis of graphene with heavier halogen functional groups such as graphene chlorides and bromides are less well reported due to their chemical instability. In this study, a non-chemical technique toward synthesizing an intrinsic chlorographene (graphene chloride) film under high-energy ion irradiation was demonstrated for the KCl/graphene/SiO_2 heterostructure [1].

Experimental

Graphene was grown by conventional thermal chemical vapor deposition on a polycrystalline Cu foil. After the growth, the graphene sheet was transferred on SiO_2 by etching the Cu foil with a $FeCl_3$ solution [2]. Graphene/SiO_2 was then introduced to an ultrahigh vacuum chamber and a 100 nm-KCl was deposited at room temperature. The specimen was irradiated with 3.0 MeV Ni^+ ions at Takasaki Ion Accelerators for Advanced Radiation Application (TIARA), TARRI, QST and at Research Institute for Applied Mechanics (RIAM) in Kyushu University. The Ni ion fluence was varied from 10^{13} to 10^{15} ions·cm^{-2}. The ion irradiations were performed at room temperature. After the ion irradiation, the KCl overlayer was removed by water-rinsing. The atomic and electronic structure of ion-irradiated KCl/graphene/SiO_2 were characterized using Raman spectroscopy, near edge X-ray absorption fine structure (NEXAFS) and X-ray photoelectron spectroscopy (XPS). NEXFS measurements were performed at the BL-27A station of the Photon Factory in High Energy Accelerator Research Organization (KEK-PF). Finite difference method (FDM) within full potential was used to simulate Cl *K*-edge NEXFS by FDMNES program [3].

Results and Discussion

Figure 1 shows Cl *K*-edge NEXAFS spectra of 10^{15} ions·cm^{-2} ion-irradiated KCl/graphene/SiO_2. Two prominent peaks are observed at 2815 eV (α) and 2819 eV (β). The peak α is assigned to the transition from 1*s* to empty states of p_x- and p_y-like characters, whereas the peak β is assigned to 1*s* to p_z transitions. It should be noted that the significant angle dependence of the intensity of the α and β peaks is observed, which indicates that most Cl atoms take place on the basal plane of graphene (see Fig.1 (b)). In general, defects on the edges of graphene sheets are more reactive than the basal plane of graphene. It can be considered that the energy transfer by the high-energy ion irradiation promotes homogeneous chlorination of graphene by the formation of Cl-C bonds at all regions of the interface between KCl and graphene. With the consideration of the results of the chemical state analysis by XPS (not shown here), we can conclude that high-energy ion irradiation of KCl/graphene/SiO_2 has enabled the synthesis of the chlorographene film. We propose that the high-energy ion irradiation can be useful as a novel tool for synthesis of new graphene compounds.

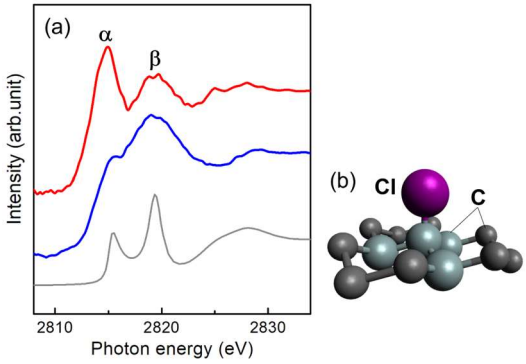

Fig. 1. (a) Cl *K*-edge NEXAFS spectra of 10^{15} ions·cm^{-2} irradiated Cl/graphene/SiO_2 (red and blue). The incident angle of X-ray beams to the surface is set to 90° (red) and 30° (blue). For comparison, the Cl *K*-edge NEXAFS spectrum calculated by the full-potential FDM simulation is included in the figure (grey). The KCl layer was removed by water-rinsing before NEXAFS measurements. (b) The model of the atomic structure using the simulation. First and second proximity C atoms (light grey) and Cl atom (purple) were used for the calculation.

Acknowledgments

XAFS experiments were performed as part of the projects accepted by the Photon Factory Program Advisory Committee (PF-PAC No. 2020G589, 2022G633).

References

[1] S. Entani *et al.*, RSC Adv. **6**, 68525 (2016). DOI: 10.1039/c6ra09631j, S. Entani *et al.*, Nanotech. **31**, 125705 (2020). DOI: 10.1088/1361-6528/ab5bcc
[2] S. Entani *et al.*, Surf. Sci. **704**, 121749 (2021). DOI: 10.1016/j.susc.2020.121749
[3] O. Bunău and Y. Joly, J. Phys.: Condens. Matter., **21**, 345501 (2009). DOI: 10.1088/0953-8984/21/34/345501

1 - 11 Room temperature photoluminescence of Pr ions implanted in GaN after ultra-high pressure annealing

S. Ito[1,2], S.-I. Sato[2], M. Bockowski[3], M. Deki[4], H. Watanabe[5], S. Nitta[5], Y. Honda[4,5], H. Amano[4,5], N. Hagura[1]

[1] Cooperative Major in Nuclear Energy, Tokyo City University
[2]Quantum Materials and Applications Research Center, QST
[3]Institute of High Pressure Physics, Polish Academy of Sciences
[4]Deep Tech Serial Innovation Center, Nagoya University
[5]Institute of Materials and Systems for Sustainability, Nagoya University

Introduction

Single photon sources (SPSs) are one of the key devices for the development of quantum technologies such as quantum computing, quantum communication, and quantum sensing. Isolated single lanthanoid (Ln) ions in gallium nitride (GaN), whose photon emission properties are stable and narrow even at room temperature (RT), are expected to be used in electrically controlled SPSs operating at RT. Although the ion implantation technique allows the deterministic placement of Ln ions with high precision, the recovery from ion implantation damage is necessary for their optical activation. However, annealing of GaN is challenging because of the material decomposition (preferential evaporation of nitrogen from the surface) at temperature above 800 °C at 1 atm. Here we show that the optical activation implanted praseodymium (Pr, one of Ln elements) ions in GaN was achieved by ultra-high pressure annealing (UHPA) [1] at the temperature up to 1480 °C. The optical properties of Pr ions in GaN after UHPA were investigated.

Experimental

700 keV praseodymium (Pr) ions were implanted into GaN epitaxial films at the doses of 3.4×10^{14} cm^{-2} at RT using the 400 kV Ion Implanter at TIARA. After implantation, UHPA at 1 GPa in N_2 atmosphere was performed to optically activate implanted Pr ions. The annealing temperatures varied from 1200 °C to 1480 °C. The optical activation of implanted Pr ions were analyzed by photoluminescence (PL) measurement with the excitation laser wavelength of 266 nm (above bandgap excitation). The recovery from ion implantation damage was investigated by X-ray diffraction (XRD) and Raman spectroscopy.

Results and Discussion

Figure 1 shows the RT-PL spectra of 700 keV-Pr implanted GaN with different annealing temperatures. Emission peaks at 650 and 652 nm were attributed to the $^3P_0$-$^3F_2$ transition in 4f shell of Pr^{3+} ions, according to the Dieke's diagram [2]. The PL intensity increased with increasing annealing temperature and was highest at 1400°C, then decreased at 1480°C. No significant change in spectrum due to annealing temperature was found. The

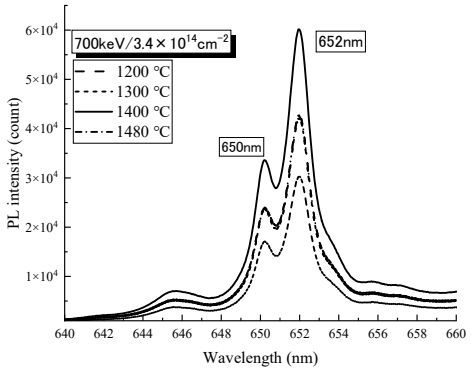

Fig. 1 RT-PL spectra of Pr-implanted GaN after UHPA.

reduction of PL intensity at 1480 °C is thought to be due to the thermal diffusion and/or complex formation of implanted Pr ions.

On the other hand, almost comparable XRD and Raman spectra to the unirradiated GaN was obtained from all the annealed samples regardless of the annealing temperature. These results indicates that the almost full recovery of implantation damage was achieved by the annealing at 1200 °C. Therefore, the increase in PL intensity at temperatures above 1200 °C could not simply be interpreted as the recovery of implantation damage. It would appear that the change in atomic configuration of neighboring Pr ions contributes to the enhancement of optical activation.

Acknowledgments

This work was supported by the JST FOREST Program (JPMJFR203G), JSPS KAKENHI (JP18H01483 and JP22H03880), the Foundation for Promotion of Material Science and Technology of Japan, and the joint research program of the Institute of Materials and Systems for Sustainability (IMaSS), Nagoya University.

References

[1] S. Porowski, *et al.*, J. Phys. Condens. Mat. **14**, 11097 (2002). DOI: 10.1088/0953-8984/14/44/433
[2] R. Birkhahn, *et al.*, Appl. Phys. Lett. **74**, 2161 (1999). DOI: 10.1063/1.124686

Part Ⅱ

2. Materials Science

2 - 01 A preparation of anion conducting electrolyte membranes based on polyetheretherketone

A. Hiroki, S. Hasegawa, K. Yoshimura, Y. Zhao, and Y. Maekawa

[a)]Department of Advanced Functional Materials Research, QST

Introduction

We have developed an anion conducting electrolyte membrane (AEM) for fuel cells based on poly(ethylene-co-tetrafluoroethylene) (ETFE) [1, 2]. AEM is expected to be used not only in fuel cells, but also in metal-air batteries and water electrolysis. For this purpose, improvements in mechanical strength are required as well as ionic conductivity. Poly(ether ether ketone) (PEEK) is a super engineering plastic with high breaking strength and excellent heat resistance, but it is difficult to chemically modify it. In this study, we investigated pretreatment conditions on preparing PEEK-based AEM.

Experimental

Before the grafting reaction, PEEK membranes (a thickness of 16 μm) were immersed in organic solvents such as 1,4-dioxane (DOX), triethylene glycol (TEG), etc, and then vacuum-dried. The pretreated PEEK membrane under Ar atmosphere was irradiated with 160 kGy of gamma rays at a ^{60}Co source (QST Takasaki). The irradiated PEEK film was immersed in a mixed solution (50/50 vol%) of chloromethyl styrene (CMS) monomer and organic solvent, and a graft polymerization reaction was performed at 80 °C for a predetermined time. The grafting ratio was calculated from the weight of the membrane before and after the grafting reaction. By immersing the CMS-grafted PEEK membrane in a trimethylamine/DOX aqueous solution, trimethylamine was introduced into the CMS-grafted chains. And then, an PEEK-based AEM (PEEK-AEM) in OH- form was obtained by immersing the membrane in 1M KOH aqueous solution (Scheme 1).

Results and Discussion

Figure 1 shows the grafting ratios of CMS-grafted PEEK membrane as a function of the reaction time. In the case of DOX as the solvent, the grafting ratio was approximately 20% at maximum. In the case of TEG, the grafting ratio increased rapidly up to 80% in 20 hours and reached approximately 100% in 48 hours. The ion exchange capacity and ionic conductivity of PEEK-AEM obtained with the grafting ratio of 106% were 1.57 mmol/g and 16 mS/cm, respectively. The water uptake of it was 30%. Theoretically, when Cl groups in CMS-grafted chains are completely substituted with trimethylamine, the ion exchange capacity should be 2.96 mmol/g. Therefore, the degree of substitution was estimated to be only 53%. Thus in the future, we will review the conditions of the ion exchange reaction in order to improve the degree of substitution, and hence to increase the ionic conductivity.

Acknowledgments

This work was partially supported by the JSPS KAKENHI Grant Number 20K05625 and the JST Adaptable and Seamless Technology transfer Program through Target driven R&D (A STEP) Grant Number JPMJTM22AW.

References

[1] K. Yoshimura *et al*., J. Membr. Sci., **573**, 403 (2019). DOI: 10.1016/j.memsci.2018.12.002

[2] Y. Zhao *et al*., Macromolecules, **55**, 7100 (2022). DOI: 10.1021/acs.macromol.2c00333.

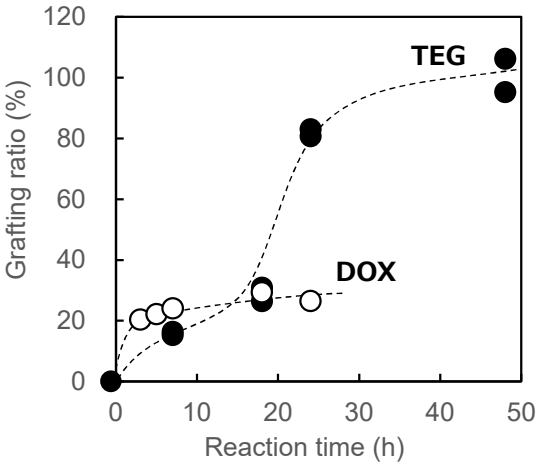

Fig. 1 The grafting ratio of CMS-grafted PEEK membranes as a function of the reaction time.

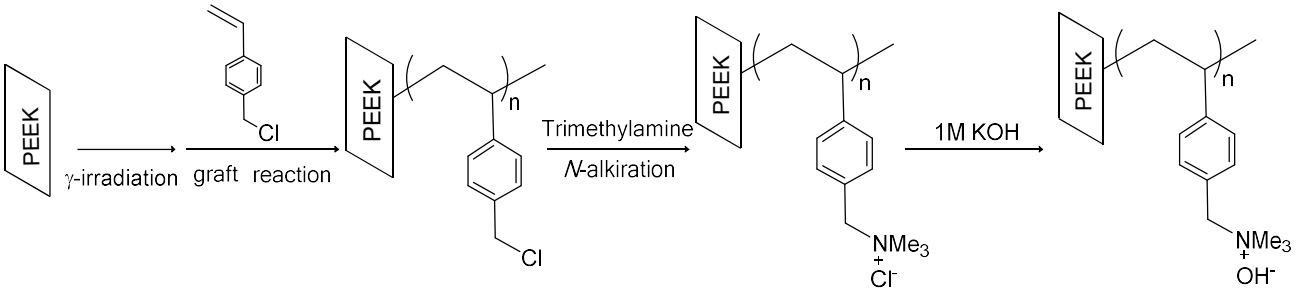

Scheme 1 Reaction scheme for the preparation of PEEK-AEM

2 - 02 Modification of polymeric materials by quantum beam irradiation (3)

A. Idesaki, A. Hiroki, S. Hasegawa and Y. Maekawa

Department of Advanced Functional Materials Research, QST

According to the Basic Hydrogen Strategy, efforts for popularization of fuel cell vehicles (FCVs) and hydrogen refueling stations (HRSs) are declared as one of the most important issues in the field of mobilities. Especially, the costs of FCVs should be reduced in order to realize the popularization. For example, the cost of current high pressure-hydrogen tank installed in the FCVs is ¥700,000; the cost is required to be reduced to around ¥300,000. The common high pressure-hydrogen tank for FCVs, type IV tank, is composed of plastic liners and carbon fiber reinforced plastics (CFRPs). It is effective to reduce the amount of expensive carbon fiber in order to realize the low cost-tank, therefore, novel high performance-polymeric materials which can be alternative to the CFRPs have been strongly desired.

The materials in the type IV tank are exposed repeatedly to severe conditions such as high pressure of 70 MPa, wide temperature range of -40°C to 85°C. Especially, the materials must retain sufficient durability against the high pressure-hydrogen; the materials with low hydrogen gas permeability and high mechanical properties are desirable as shown as “TARGET ZONE” in figure 1. Referring to the fig. 1, we have been examined radiation crosslinking of polymeric materials such as polyethylene (PE), polyamides (PA), and lately, polymer blends [1, 2]. In this work, polymer blends of PA and PE were irradiated by gamma-rays to investigate change of gel fraction (weight ratio of insoluble components) of the blends. Figure 2 shows the change of gel fraction of PA/PE blends after gamma-ray irradiation with dose of 72 kGy. The gel fraction for PA, PA/PE(90/10), PA/PE(80/20), PA/PE(70/30), and PE was 0%, 0%, 8.5%, 14.0%, and 6.5%, respectively. The pure PA requires the dose of several hundreds kGy to form insoluble components. Assuming that no reactions occurs between PA and PE, the gel fraction of PA/PE(90/10), PA/PE(80/20), PA/PE(70/30) samples can be estimated as 0.7%, 1.3%, and 2.0%, respectively, from the value of pure PE. The obtained values for PA/PE(80/20) and PA/PE(70/30) were much greater than that of estimation. This suggests that the insoluble components were increased by crosslinking reaction between PA and PE. In other words, PA and PE reacted to form crosslinking at the interface by the irradiation.

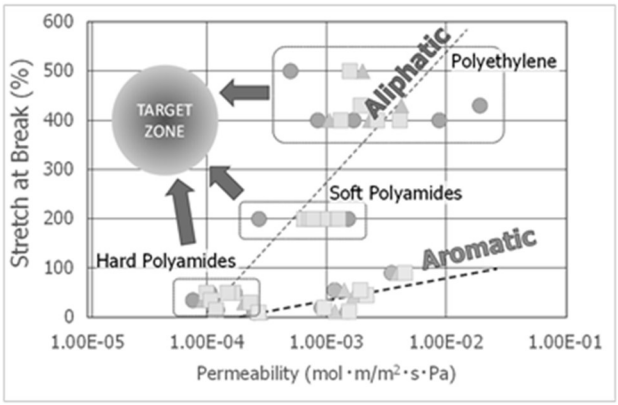

Fig. 1 Relationship between H_2 permeability and tensile property for various polymeric materials presented by Prof. Nishimura at Kyushu University.

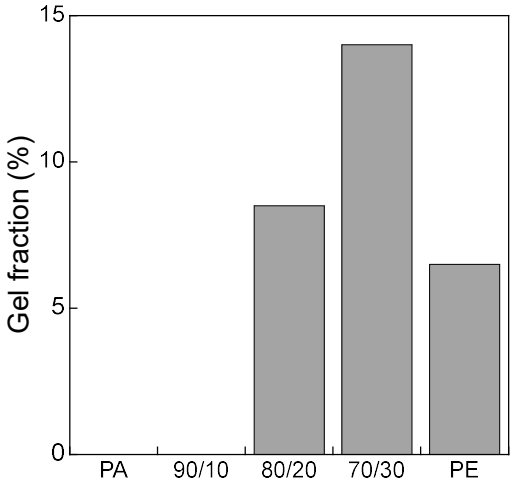

Fig. 2 Change of gel fraction of PA/PE blends after gamma-ray irradiation.

Acknowledgments

This work is based on results obtained from a project, JPNP20003, commissioned by the New Energy and Industrial Technology Development Organization (NEDO). This is a collaboration work with Prof. Shin Nishimura at Kyushu University and Prof. Katsuhisa Tokumitsu at The University of Shiga Prefecture.

References

[1] A. Idesaki *et al*., QST Takasaki Annu. Rep. 2020, **QST-M-33** 27 (2021).

[2] A. Idesaki *et al*., QST Takasaki Annu. Rep. 2021, **QST-M-39** 34 (2022).

2 - 03 Development of metal oxide-catalysts utilizing quantum beam irradiation technique (3)

A. Idesaki and S. Yamamoto

Department of Advanced Functional Materials Research, QST

Popularization of fuel cell vehicles (FCVs) is one of the most important tasks to realize the carbon neutrality. In order to realize popularization of FCVs, the cost of polymer electrolyte fuel cells (PEFCs) for the FCVs should be reduced; the cost of about 20,000 yen/kW for the current PEFCs is required to be reduced to about 5,000 yen/kW. In the PEFCs, platinum of several tens grams is used as a catalyst to enhance the reaction at the cathode as shown in Fig. 1. Therefore, non-precious metal catalysts have been desired to reduce the cost of the PEFCs. An oxygen reduction reaction (ORR; $O_2 + 4H^+ + 4e^- \rightarrow 2H_2O$) occurs at the cathode in the PEFC. This ORR proceeds through production of some intermediates (*OOH, *O, *OH) as shown in Fig.1. The adsorption energy of the intermediates on the catalyst surface dominates the performance of the catalysts, therefore, appropriate adsorption energy of each intermediate should be controlled to achieve the highest performance. However, theoretical calculation has revealed that the equilibrium potential (E^0 = 1.23 V vs. RHE) cannot be achieved in the case of platinum catalysts because the adsorption energy of the intermediates is independently uncontrollable on the platinum catalysts [1]. On the other hand, another theoretical calculation has predicted that titanium oxide (TiO_2) with oxygen defects and/or doped heteroatoms exhibit the possibility to realize the equilibrium potential of 1.23 V vs. RHE [2]. Here, we examined electron beam (EB) irradiation to form catalytically active sites in TiO_2 powder. A mixture of TiO_2 powder, polyacrylonitrile (PAN), and carbon nanotube (CNT) was irradiated by 2 MeV EB with dose of 5 MGy under N_2 atmosphere and subsequently heat-treated at 1000 °C under N_2 atmosphere. The PAN and CNT were added as the binder and electron conductive path. The EB-irradiated sample showed the onset potential of ORR of 0.78 V vs. RHE which is higher than that of unirradiated sample. This result indicated that the EB irradiation and subsequent heat treatment are useful to form catalytically active sites and electron conductive path for TiO_2 powder. It is expected that the catalytic activity of TiO_2 will be modified by controlling the composition of TiO_2/PAN/CNT and conditions of EB irradiation and subsequent heat treatment.

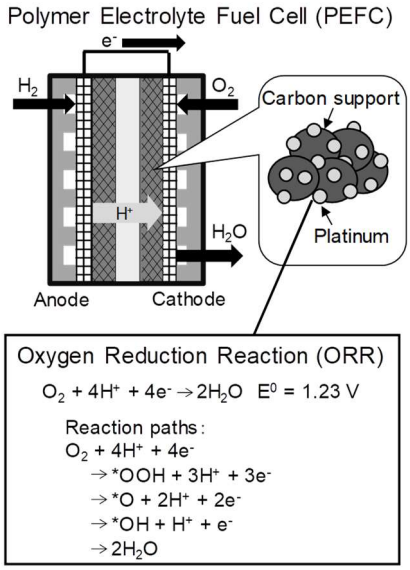

Fig. 1 Scheme of the polymer electrolyte fuel cell (PEFC) and oxygen reduction reaction (ORR) at the cathode.

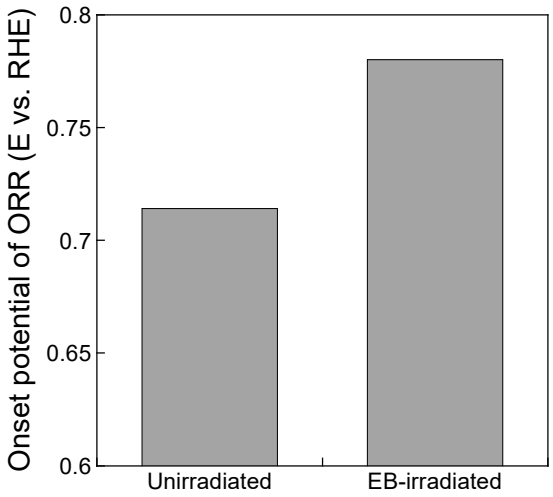

Fig. 2 Comparison of onset potential of ORR between unirradiated and EB-irradiated TiO_2 catalyst.

Acknowledgments

This work is based on results obtained from a project, JPNP20003, commissioned by the New Energy and Industrial Technology Development Organization (NEDO). This is a collaboration work with Fukuoka University, Chiba University, Osaka University, Kyushu University, Oita University, Kochi University of Technology, and Utsunomiya University.

References

[1] A. Kulkarni et al., Chem. Rev. 118, 2302 (2018). DOI: 10.1021/acs.chemrev.7b00488

[2] Y. Yamamoto et al., J. Phys. Chem. C 123, 19486 (2019). DOI: 10.1021/acs.jpcc.9b03398

2 - 04 The durability improvement of Pt catalyst by ion irradiation into carbon support

H. Okazaki, H. Koshikawa, A. Idesaki, S. Yamamoto and T. Yamaki

Department of Advanced Functional Materials Research, QST

Introduction

There is the most critical barrier to the commercialization for Pt catalysts in fuel cells because of the intrinsic high cost due to its scarcity. Therefore, the improvement of activity in oxygen reduction reaction (ORR) and durability of the Pt nanoparticles (NPs) is required. Our previous study shows that the Pt NPs on an Ar^+-irradiated glassy carbon (GC) substrate exhibits a higher ORR activity than those on the non-irradiated GC substrate [1]. We have reported the mechanism of the improvement of ORR activity due to the ion irradiation by XAFS studies [2] but have not revealed the change of the electrochemical durability. In this report, in order to reveal how the ion irradiation affects the durability of Pt NPs on GC substrates, we observed the change of the electrochemical durability of Pt NPs on the GC substrate by the ion irradiation into GC substrates.

Experimental

The GC plates with the size of 1 cm×1 cm and the thickness of 1 mm (Tokai Carbon Co. Ltd.) were used for the substrates. The ion irradiations were performed using an Ar^+ beam with an energy of 380 keV at the fluence of 7.5×10^{15} ions/cm^2 in the ion implanter at the Takasaki Ion Accelerators for Advanced Radiation Application (TIARA).

The electrochemical durability is estimated by cyclic Voltammetry (CV) measurements before and after accelerated aging tests. The CV measurements were performed in an N_2-saturated 0.1 M $HClO_4$ electrolyte. The accelerated aging tests were performed by the process repeating the potential cycling between 1.0 and 1.5 V at a rate of 0.5 V/s in accordance with the Fuel Cell Commercialization Conference of Japan (FCCJ) recommendations [3].

Results and Discussion

We compared electrochemical surface area (ECSA) between the Pt NPs on the pristine GC and those on the Ar^+ irradiated GC. The ECSA was calculated from the hydrogen adsorption region during the CV using a conversion factor of 210 μC/cm^2 [4]. Figure 1 shows the cycle number dependence of ECSA ratio for the pristine and irradiated GC substrates with the fluence of 7.5×10^{15} ions/cm^2. At 50,000 cycles, the reduction of ECSA for the irradiated GC is about 10% while the reduction for the pristine is about 40%. The smaller reduction in the irradiated GC indicates that the ion irradiation into the carbon support enhances the durability for Pt catalysts. In order to elucidate the origin of improvement of the durability, we compared the CV curves before and after the accelerated aging test with the 50,000 cycles for Pt NPs on the pristine and irradiated GC substrates, as shown in Fig. 2. Comparing the CV curves before (broken line) and after the aging test (solid line), the capacity in the double layer region significantly increases after the aging test for the pristine GC. The increase of capacity in the pristine GC indicates that the area surface of GC increases due to the carbon corrosion. On the other hand, we observed little increase of the capacity for the irradiated GC. Thus, we concluded that the ion irradiation can improve the durability of Pt catalysts by the suppression of the carbon corrosion.

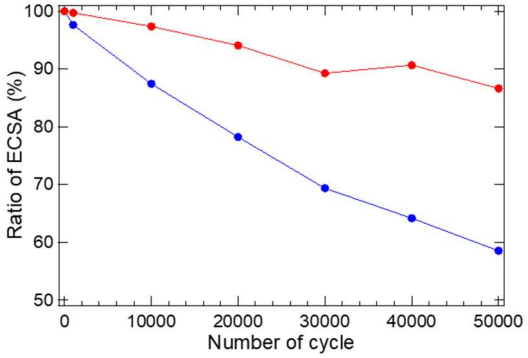

Fig. 1. Cycle number dependence of ECSA ratio for the pristine (blue) and the irradiated GC (red).

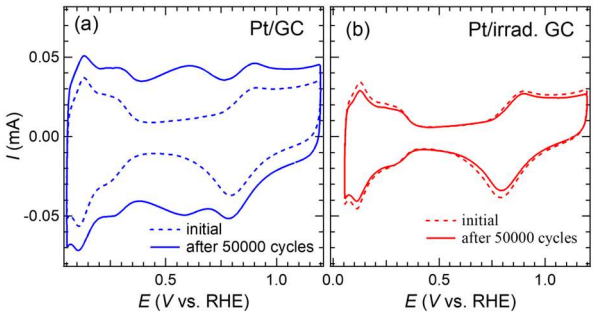

Fig. 2. Comparison of CV curves before and after the aging test for (a) the pristine and (b) the irradiated GC.

Acknowledgments

This work is partially supported by a Grant-in-Aid for Scientific Research (KAKENHI) Grant Numbers 18H01923 and 21H04669.KAKENHI is funded by the Ministry of Education, Culture, Sports, Science and Technology (MEXT), Japan.

References

[1] T. Kimata *et al.*, Phys. Rev. Materials 6, 035801 (2022).
[2] H. Okazaki et al., J. Chem. Phys. 152, 124708 (2020).
[3] A. Ohma *et al.*, ECS Trans. 41, 775–784 (2011).
[4] S. A. Sheppard *et al.*, Analyst 123, 1923 (1998).

2 - 05 Structural characterization of Pt nanoparticles on Ar^+ irradiated glassy carbon substrates

S. Yamamoto, T. Taguchi, H. Koshikawa and T. Yamaki

Department of Advanced Functional Materials Research, QST

Proton exchange membrane fuel cells (PEMFCs), which directly convert chemical energy to electrical energy, have attracted attention as one promising power source. Platinum nanoparticles (Pt NPs) supported on carbon materials are generally used as electrocatalysts for the oxygen reduction reaction (ORR) in the PEMFCs. However, there a need to improve ORR activity and durability in Pt-carbon electrocatalysts. In our previous work, we found the enhancement of the ORR activity in Pt NPs on glassy carbon (GC) substrates irradiated with 380 keV Ar^+ ions [1]. This activity enhancement would be due to the ion-beam-induced defects in GC substrates. However, the detailed ion irradiation effects on GC substrates, such as the incident energy of Ar^+ ions, are still unclear. Here we structural characterized Pt NPs on GC substrates irradiated with 3 keV Ar^+ ions.

Mirror polished 1-mm-thick GC substrates (GC-20SS, Tokai Carbon Co., Ltd.) with the size of 10 mm ×10 mm were irradiated with 3 keV Ar^+ using an ion gun (ACIG-3, AVC) at fluences up to 6.7×10^{15} ions/cm^2. The Ar^+ beam (0.45 μA/cm^2) was incident perpendicularly to the substrate surface. The Ar^+ irradiated GC samples were characterized by transmission electron microscope (TEM) operating at 200 kV, Raman spectroscopy with 532 nm wavelength laser and Rutherford backscattering spectroscopy (RBS) using a 2.0 MeV $^4He^+$ beam from a 3 MV single-stage-accelerator at TIARA. Cross-sectional TEM samples were prepared with ion slicer (IB-090600CIS, JEOL) using Ar ion. The sample surface was coated with an epoxy to prevent Ar ion sputtering. Pt NPs were deposited on the GC substrates by a magnetron sputtering (JEC-3000FC, JEOL).

Figure 1 (a) show a cross-sectional TEM image of 3 keV Ar^+ irradiated GC substrate. The TEM image indicated the GC substrate was composed of graphitic crystallites (un-irradiated region) and the graphitic crystallites became disorder in a region with a depth of 15 nm on the sample by Ar^+ irritation. The fluence of Ar in the irradiated region was 6.7×10^{15} ions/cm^2 evaluated by RBS. The results of the Raman spectroscopy indicated that the irradiated region was disordered due to the characteristic peaks (the D and G bands) broadening after the irradiation. Figure 1 (b) show a cross sectional HAADF-STEM (high-angle annular dark-field scanning transmission electron microscopy) image of the Ar^+ irradiated GC substrate. The HAADF-STEM suggested the density of the Ar^+ irradiated region was higher than that of the un-irradiated region due to higher contrast image in the Ar^+ irradiated region. Furthermore, TEM-EELS (electron energy-loss spectroscopy) measurements, evaluation from the plasmon peak shift of carbon, indicated the mean density of the irradiated region was increased 1.03 times than that of the un-irradiated region. TEM analysis suggested Ar^+ irradiation caused disorder and densification in the irradiation region. Figure 1 (c) show a cross-sectional TEM image of Pt (2.5×10^{15}/cm^2) deposited on the Ar^+ irradiated (4.7×10^{15}/cm^2) GC substrate. The Pt NPs with an average particle diameter of 2.6 nm were formed on disordered GC surface. Preliminary electrochemical testing suggested the ORR activity of Pt NPs on Ar irradiated GC is enhanced. Thus, we plan to investigate the ORR activity of Pt NPs on Ar irradiated GC substrates with various incident energy and fluence.

Acknowledgments

The authors thank Ms. C. Suzuki for her help with the TEM observations.

References

[1] T. Kimata *et al*., Phys. Rev. Mater. **6**, (2022) 035801. DOI:10.1103/PhysRevMaterials.6.035801

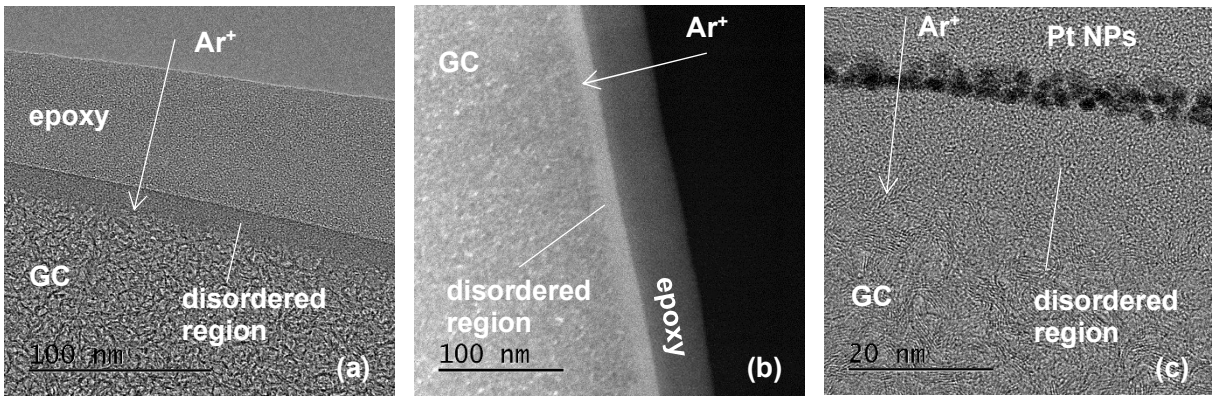

Fig. 1 (a) cross-sectional TEM image of 3 keV Ar^+ irradiated GC substrate, (b) HAADF-STEM mage of the Ar^+ irradiated GC substrate, (c) cross-sectional TEM image of Pt deposited on the Ar^+ irradiated (4.7×10^{15}/cm^2) GC substrate.

2 - 06 Modified methanol oxidation activity of a composite electrode catalyst with TiO_2 by ion beam irradiation

N. Nakagawa [a)], H. Gao [a)], H. Ishitobi[a)], H. Koshikawa[b)], H. Okazaki[b)], S. Yamamoto[b)] and T. Yamaki[b)]

[a)]Graduate School of Science and Technology, Gunma University
[b)]Department of Advanced Functional Materials Research, QST

Introduction

Direct methanol fuel cells are expected to be a compact power source with high energy density. However, the slow methanol oxidation reaction (MOR) at the anode is one of the issues for their commercialization, and research on the development of highly active catalysts to accelerate this reaction has been actively conducted. So far, it is known that the addition of transition metal oxides such as CeO_2 and TiO_2 to PtRu nanoparticles in conventional catalysts increases the catalytic activity [1], and some reports suggest that oxygen vacancies and other defects in the oxide are responsible for this [2]. In order to increasing oxygen defects in the oxide particles, the authors irradiated high-energy ion beams to carbon nanofibers (CNFs) embedded with CeO_2 nanoparticles (CECNF) and then reported that the irradiation had the effect of increasing the MOR reaction activity of PtRu/CECNF [3]. The effect of ion beam irradiation has not been investigated for other than CECNF , and it is unclear whether a similar effect can be obtained for TiO_2-based catalyst support. Therefore, in this study, a composite catalyst with TiO_2, carbon nanofibers coated with fine anatase TiO_2 nanoparticles (TCCNF), was used and investigated the effect of the irradiation on the MOR activity of the catalyst, PtRu/TCCNF.

Experimental section

TCCNF sheets were prepared by applying a titanium tetraisopropoxide solution to CNF sheets obtained by electrospinning followed by carbonization [4]. TCCNF sheets were irradiated with high energy ion beams, $^{12}C^{3+}$, 75 MeV electron beam and $^{40}Ar^{10+}$, 250 MeV electron beam, using AVF cyclotron at TARRI. The ion fluence was calculated to be approximately 1×10^{11} ions/cm^2 for each irradiation. TCCNFs with and without irradiation were pulverized and then loaded with PtRu by chemical reduction method using $NaBH_4$ to obtain PtRu/TCCNFs. The irradiated catalysts are denoted as PtRu/TCCNF-NI and the irradiated ones as PtRu/TCCNF-C75 and PtRu/TCCNF-Ar250. XRD measurements were performed on each catalyst to determine the crystal structure and crystallite size. XPS measurements were also performed for PtRu/TCCNF-NI and PtRu/TCCNF-C75.

For each of the prepared catalysts, a three-electrode cell was constructed with a glassy carbon electrode coated with the catalyst (1 mg$_{\text{-cat}}$ cm^{-2}) as the working electrode, and electrochemical active surface area (ECSA) was measured by CO stripping method. The MOR activity was evaluated in methanol aqueous solution with H_2SO_4 by cyclic voltammetry between 0~1.2 V vs. RHE; the current density at 0.7 V vs. RHE was used as the mass activity of the catalyst.

Results and discussion

Comparison of the XRD patterns among the catalyst with and without irradiation showed a similar pattern with anatase TiO_2 and Pt peaks. The peak shift due to ion irradiation, as observed for CeO_2 [3], was not detected for anatase TiO_2 in this experiment. Table 1 shows ECSA and MOR activity for the catalysts as well as the Pt crystal diameter calculated from the XRD peak. ECSA was lower for the ion beam irradiated catalysts, while the crystallite diameter of Pt was similar to each other, 5-6 nm. The reason of the altered ECSA by the irradiation is currently unknown. The MOR activity was higher in the case of C75 irradiation and lower in the case of Ar250 irradiation than in the case of no irradiation. The XPS results, not shown here, revealed that the C75 irradiated sample had an increase in the existence percentage of zero-valent Pt to that of divalent Pt as well as an increase in the ratio of tetravalent Ti, compared to the unirradiated sample. The irradiation at higher energies would have altered the electron structure of TiO_2 in TCCNF, which in turn changed the MOR activity of Pt. The ion beam irradiation altered ECSA and the methanol oxidation activity of the PtRu/TCCNF.

Table 1. Pt size by XRD, ECSA and MOR mass activity for the catalysts with and without irradiation.

Catalyst (PtRu/TCCNF)	Pt crystal diam. [nm]	ECSA [m^2 g$_{\text{-PtRu}}^{-1}$]	MOR activity [A g$_{\text{-PtRu}}^{-1}$]
NI (No irrad.)	4.7	80.2	61.3
C75	6.2	73.8	77.8
Ar250	5.8	48.6	45.4

References

[1] Y. Ito *et al*., J. Power Sources **242**, 280 (2013). DOI: 10.1016/j.jpowsour.2013.05.064
[2] C-H. Chung *et al*., Chem. Letters **50**, 856 (2021). DOI: 10.1246/cl.200845
[3] N. Nakagawa *et al*., Catalysis Today **364**, 118 (2021). DOI: 10.1016/j.cattod.2019.12.017
[4] H. Ishitobi *et al*., Int. J. Hydrogen Energy **44**, 30743 (2019). DOI: 10.1016/j.ijhydene.2018.03.108

2 - 07 Preparation of polystyrene with through-pores by using ion-track

H. Koshikawa, S. Yamamoto, M. Sugimoto, S. Sawada and T. Yamaki
Department of Advanced Functional Materials Research, QST.

Introduction

There have been numerous studies on the ion-track membranes for poly (ethylene terephthalate) (PET) and polycarbonate because the tracks of these materials are easily dissolved in an alkaline solution. The characteristics of ion-track membranes are that the etching time can be controlled to control the pore diameter to any size from several tens of nanometers to several micrometers, and the irradiation time can be controlled to control the number per unit area. Therefore, to create through-pores in a polystyrene membrane, which is a biocompatible material, it can be expected to be applied to biocompatible materials. However, very few studies have been reported for ion-track membranes of radiation-resistant polystyrene (PS); to our knowledge, only one proceeding report was published by J. Kaewsaenee et al. [1]. They reported the conditions of irradiation and the subsequent chemical etching, but they did not mention the information regarding the depth direction of the prepared pores, i.e., whether or not the pores penetrated through the PS film. In this study, we report the first successful preparation of PS ion-track membranes with through-pores by a sensitization technique of UV-visible light irradiation [2].

Experimental

Figure 1 (a) shows the preparation process of PS ion-track membranes. 25-μm-thick PS films (Asahi Chemicals Co., Ltd., OPS) were irradiated with 560 MeV ^{129}Xe ions at a fluence of 3.0×10^7 and 3.0×10^6 ions/cm^2 from the TIARA cyclotron of the QST/Takasaki and were exposed to a xenon lamp (USIO, UXL-500SX2) with an illuminance of 3.0 mW/cm^2 through the filter (UV-290, Asahi Techno Glass) that cuts UV light with wavelengths of < 290 nm. The PS membranes were then etched in a mixture of 40% H_2SO_4 and 1.2 mol/L $K_2Cr_2O_7$ at 80°C without stirring. The etched samples were washed with a large amount of water and dried for 4 h in air. The etched samples were cut leaving part of the membranes, cooled sufficiently in liquid nitrogen, and then cleavage using tweezers, to make a clean cross section. The surface and cross-section of the membranes were observed with an SEM after their Au coating.

Results and Discussion

Figure 1 (b, c) shows the cross-sectional and surface SEM images of the PS ion-track membranes prepared with the UV-visible light exposure for 24 h. The cylindrical through-pores with a diameter of 380 nm appeared to be formed by the chemical etching for only 3.4 h. For comparison, the PS ion-track membrane was prepared without the sensitization process (fig. 2(a)). As seen in its cross-sectional SEM image of fig. 2(b, c), we obtained conical pores with a surface diameter of 2.3 μm and a depth of 5.7 μm by the etching even for 24 h. Normally, PS is transparent to UV-visible light with wavelengths of > 290 nm and does not decompose; however, fragmented PS chains with unsaturated end-groups in the ion track can absorb the UV-visible light and thus undergo further decomposition. This would lead to effective sensitization of the ion tracks for preparing through-pores.

References

[1] J. Kaewsaenee *et al.*, 31st Congress on Sci. and Technology of Thailand at Suranaree University of Technology, 18-20 (2005).
[2] Z. Zhu *et al.*, Nucl. Instr. and Meth. in Phys. Res. **B217** (2004) 449-456.

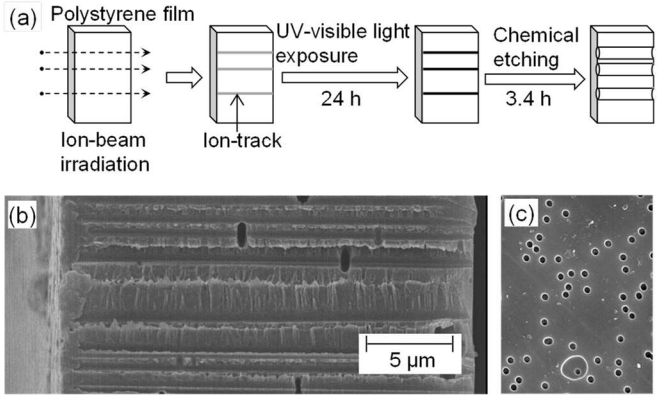

Fig. 1. (a) The preparation process of PS ion-track membranes with UV-visible light exposure. (b, c) The cross-sectional and surface SEM images of the PS ion-track membranes prepared with the sensitization process of UV-visible light irradiation.

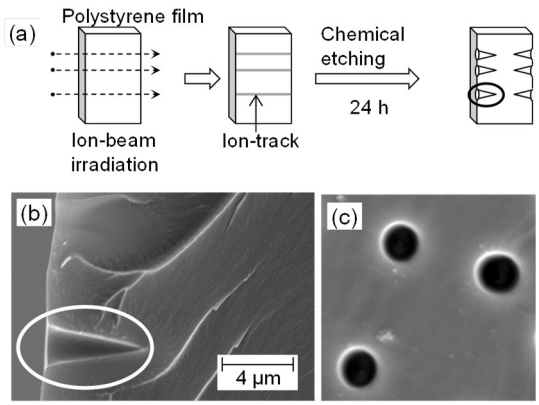

Fig. 2. (a) The preparation process of PS ion-track membranes without light exposure. (b, c) The cross-sectional and surface SEM images of the PS ion-track membranes prepared.

2 - 08 Effect of 310 keV proton irradiation on superconducting properties in $YBa_2Cu_3O_y$ films

T. Ozaki[a)], H. Okazaki[b)], H. Koshikawa[b)], S. Yamamoto[b)] and T. Yamaki[b)]

[a)]School of Engineering, Kwansei Gakuin University,
[b)]Department of Advanced Functional Materials Research, QST

Introduction

High-temperature superconductors based on $REBa_2Cu_3O_y$ (REBCO, RE = rare earth) have become powerful materials for high-field applications such as generators for wind turbine and magnet use in medical imaging machines. For these applications, it is very important to raise the critical current density J_c in magnetic fields. The in-field J_c can be enhanced by the introduction of precipitates and defects with nano-meter size, which can pin the vortices. The desirable pinning structures could be provided by ion irradiation which enable the creation of a variety of defects, such as points, clusters and tracks. Therefore, ion irradiation would be a promising approach to realize high performance REBCO films. We have introduced pinning defects in iron-chalcogenide $FeSe_{0.5}Te_{0.5}$ superconducting films to enhance J_c in magnetic field by ion irradiation.[1,2] In this study, we report the effect of 310 keV proton irradiation on superconducting properties in $YBa_2Cu_3O_y$ (YBCO) films.

Experimental

The samples were 0.7-μm thick YBCO superconducting layers on metal substrates. The irradiation experiment was carried out using 400kV ion implanter at TIARA. A beam of 310 keV proton at fluences of 2.1×10^{15} and 4.3×10^{15} ions/cm^2 was directed to the film surface at normal incidence. The superconducting properties were measured using a Physical Property Measurement System (Quantum Design PPMS DynaCool).

Results and Discussion

Figure 1(a) and 1(b) show the temperature dependence of resistivity for a pristine (prior to irradiation) film and a film irradiated at fluences of 2.1×10^{15} and 4.3×10^{15} ions/cm^2, respectively. The superconducting transition temperature T_c decrease from 90.9 K to 88.6 K and from 91.2 K to 86.1 K after the proton irradiation, respectively. The degradation of the T_c would arise from structural damages produced by the irradiation.

Figure 2 shows a critical current density J_c as a function of magnetic fields for a pristine film and a film irradiated at a fluence of 2.1×10^{15} ions/cm^2. We found that the J_c decrease at both 65 and 77.3 K after the irradiation. This indicate that the fluence of 2.1×10^{15} ions/cm^2 produce the irradiation damage excessively in the GdBCO films. We expect that the decrease of the fluence would lead to increase of J_c in the magnetic fields.

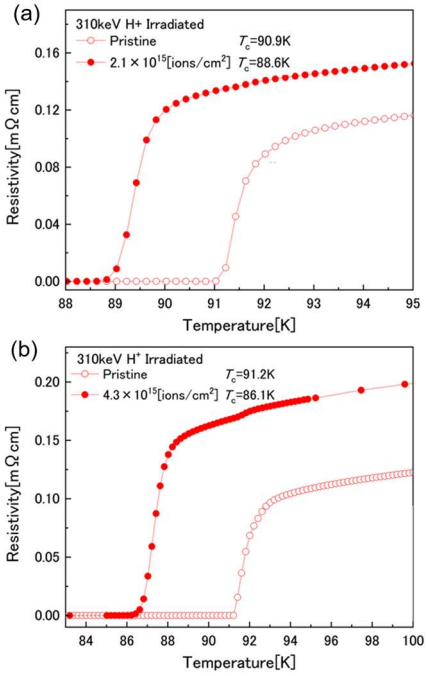

Fig. 1 Resistivity as a function of temperature for a pristine GdBCO film and a film irradiated at fluences of 2.1×10^{15} and 4.3×10^{15} ions/cm^2, respectively.

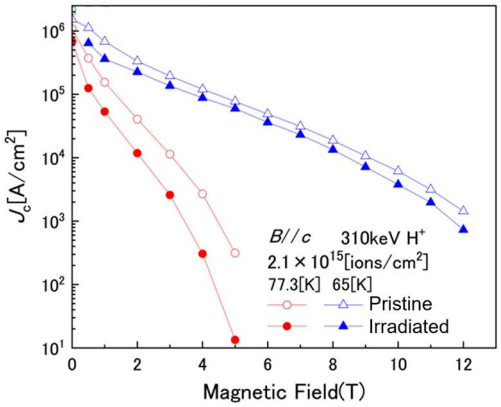

Fig. 2 Critical current density J_c as a function of magnetic field for a pristine GdBCO film and a film irradiated at a fluence of 2.1×10^{15} ions/cm^2 of 310 keV protons at 30 an 65K.

References

[1] T. Ozaki et al., Nat. Commun. 7, 13036 (2016). DOI: 10.1038/ncomms13036
[2] T. Ozaki et al., Supercond. Sci. Technol., 33, 094008 (2020). DOI: 10.1088/1361-6668/ab9f66

2 - 09 Development of powdered boron adsorbent using radiation induced graft polymerization

H. Hoshina, H. Amada, Y. Ueki, M. Omichi and N. Seko

Department of Advanced Functional Materials Research, QST

Introduction

The boron concentration in water discharged into public waters is regulated to be less than 10 mg/L because excessive intake of boron has adverse effects on the human health. However, there is no efficient method to remove boron, and new methods need to be developed.

In this research, N-methyl-D-glucamine (NMDG), which is effective for boron adsorption, was introduced into a cellulose powder with radiation induced graft polymerization (RIGP), and its adsorption properties for boron were evaluated.

Experimental

1. Preparation of boron adsorbent

The cellulose powder with a diameter of 40 - 200 μm was packed into a polyethylene bag. It was purged with nitrogen gas to make a nitrogen atmosphere, which was irradiated with γ-rays at 20 kGy (5 kGy/h × 4 h) under a dry-ice temperature of approximately -80 °C. The irradiated cellulose powder was placed into a glass ampoule and was evacuated with a vacuum line. Monomer solutions was prepared by adding glycidyl methacrylate (GMA) to deionized water with Tween 20. After the monomer solutions were degassed by bubbling with nitrogen gas, it was transferred into an ampoule containing the irradiated cellulose powder. The grafting was carried out at 40 °C up to 60 minutes. Finally, the grafted cellulose powder was washed with methanol to remove the residual monomer and homopolymer. The amount of GMA introduced by RIGP onto the cellulose powder was evaluated by calculating the degree of grafting (Dg) and the monomer density on the grafted cellulose powder using the following equations:

$$\text{Degree of grafting (Dg) [\%]} = (W_1 - W_0) / W_0 \times 100$$

where W_0 and W_1 correspond to the weights of cellulose powder before (W_0) and after (W_1) RIGP.

To introduce NMDG as a functional group for boron adsorption, the GMA-grafted cellulose powder was immersed into an 10 % of NMDG solution at 80 ◦C to bring about a reaction between the epoxy group and NMDG. Thus, a powdered boron adsorbent with NMDG was obtained.

2. Batch adsorption tests

The adsorption capacity of powdered boron adsorbent was evaluated by batch adsorption test using 0.1 – 100 mg/L of boron solution. The effect of adsorption time on amount of adsorbed boron was investigated using 10 mg/L of boron solution (pH 5.5) for 5 to 60 minutes. The amount of adsorbed boron was obtained by measuring the concentrations of boron in the solution before and after the adsorption tests with an inductively coupled plasma optical emission spectrometer (ICP-OES).

Results and Discussion

In the RIGP of GMA into the cellulose powder using 5 % of GMA emulsion solution (0.5 % Tween 20), the Dg was increased with increment of reaction time. The Dg reached higher than 100% only 15 minutes of reaction time, and Dg 150% was obtained on 60 minutes. A powder adsorbent having 2.3 mmol/g of NMDG was prepared by immersing the GMA grafted powder with Dg 150% in a 10% NMDG solution at 80°C for 30 minutes.

Figure 1 shows the results of evaluation the dependence of boron adsorption on boron concentration. In the adsorption test using the lowest concentration of 0.1 mg/L boron solution, the adsorption amount was 6 mg/g. While the adsorbent showed very high boron adsorption of 18 mg/g in the test using the 100 mg/L solution.

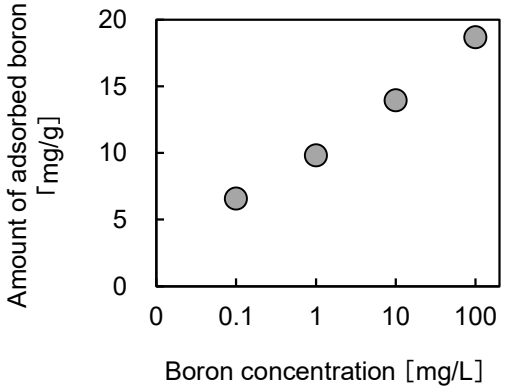

Fig. 1 The Effect of boron concentration on adsorption amount

As a result of adsorption test using 10 mg/L boron solution, the amount of adsorbed boron was 3 mg/g in just 5 minutes of adsorption time. The adsorption amount increased as the adsorption time increased, and the adsorption amount reached 10 mg/g at 60 minutes.

These results indicates that the adsorbent introduced NMDG in cellulose powder, which is hydrophilic and has large specific surface area, can efficiently adsorb boron.

Acknowledgments

This research was performed by the Environment Research and Technology Development Fund (JPMEERF20221G02) of the Environmental Restoration and Conservation Agency provided by Ministry of the Environment of Japan.

2 - 10 Electrodialysis with membrane/extractant/membrane sandwich separator for lithium recovery from saltlake brine

J. Chen, N. Seko

Department of Advanced Functional Materials Research, QST

The recent rapid increase in the production and use of electric vehicles using lithium-ion batteries has led to rapid increases in lithium prices due to its limited supply. In addition, the current proven recoverable lithium resources are only about 20 million tons, and the distribution is limited to some areas such as South America and Australia. On the other hand, lithium in seawater worldwide exceeds 200 billion tons, which is an inexhaustible resource for applications. However, despite the presence of lithium in seawater in large quantities, its concentration (0.17 ppm) is too low to establish economical harvesting technologies. As a leading technology for recovering lithium from seawater, we propose an electrodialysis system for recovering lithium from saltlake brine where the lithium concentration is relatively high (about 1000 ppm).

However, saltlake brine contains high concentrations of other metal ions such as Na^+ and K^+. To collect and concentrate Li^+ from brine, as shown in Figure 1, we designed an electrodialysis system consisting of an anode, a cathode, and a membrane/extractant/membrane sandwich separator between the anode and cathode. Under the loaded direct electric current, Li^+ in the anode is forced to move to the cathode through the sandwich separator, while the other metal ions could not move through the separator and remained in the anode. Thus, the Li^+ was selectively collected in the cathode.

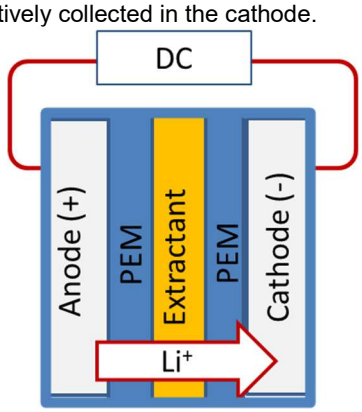

Fig.1 Electrodialysis using a PEM/extractant/PEM sandwich separator designed for the selective recovery of Li^+ from aqueous solutions.

Here, the extractant is 0.13 M $FeCl_3$ solution of tributyl phosphate (TBP), and the membranes were prepared by radiation grafting of styrene onto polyvinylidene fluoride (PVDF) films and subsequent sulfonation [1]. In brief, the styrene was grafted onto PVDF by a gamma-ray pre-irradiation method. The grafted films were then sulfonated to prepare a polymer electrolyte membrane (PEM). The degree of grafting of polystyrene on PVDF films was 23%. After sulfonation and hydrolysis, the PEMs were obtained. The PEMs were immersed in an aqueous lithium chloride solution to obtain the Li^+ conductive membranes. The Li^+ conductivity of the resulting membranes was detected by impedance method and was 0.03 S/cm in water saturated state at room temperature.

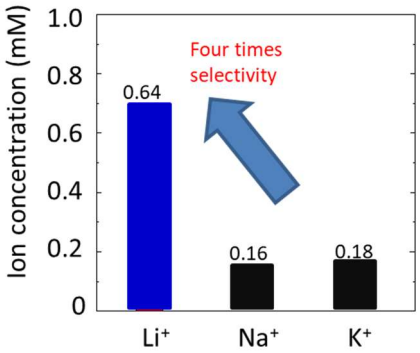

Fig. 2 Concentration of metal ions in the cathode after running for 0.5 h. Direct current; Voltage, 1.5V.

Figure 2 shows the results of the electrodialysis for lithium recovery. A test solution (50 ml) containing Na^+, K^+ and Li^+ at the same concentration (0.1 M) was circulated through the anode, and 0.1 M HCl aqueous solution (50 ml) was circulated through the cathode. The loaded DC voltage is 1.5 V. After running for 0.5 h, the ion concentration in the cathode was detected with an ion chromatography. As shown in Figure 2, the concentrations of Na^+ and K^+ are about 0.16 and 0.18 mM, respectively, while the concentration of Li^+ is 0.64 mM, the latter is 4 times higher than the former, indicating the high lithium selectivity of the designed electrodialysis.

The high Li^+ selectivity is attributed to the TBP/$FeCl_3$ extractant between the two PEMs. That is, at the PEM/extractant interface near the anode side, Li^+ is extracted by TBP/$FeCl_3$ as follows: $LiCl_{aq}$ + $nTBP/FeCl_{3\,org}$ ⇆ $[Li(TBP)_n][FeCl_4]_{org}$; while at the interface near the cathode side, Li^+ can be stripped in the form of $[Li(TBP)_n][FeCl_4]_{org}$ + HCl_{aq} ⇆ $[H(TBP)_n][FeCl_4]_{org}$ + $LiCl_{aq}$. In contrast, other metal ions could not bind to TBP/$FeCl_3$ and were remained in the anode. Therefore, the newly designed electrodialysis can be used to selectively recover lithium from saltlake brine.

References

[1] J. Chen, N. Seko. Polymers, 11, 1098-1-17 (2019). DOI: 10.3390/polym11071098

2 - 11 An impact of solvents on graft polymerization of biomass-derived vinyl monomers from PE/PP substrates

K. Matsubara[a)], T. Nirazuka[a)], R. Kakuchi[a)], M. Omichi[b)] and N. Seko[b)]

[a)]Division of Molecular Science, Faculty of Science and Technology, Gunma University
[b)]Department of Advanced Functional Materials Research, QST

Introduction

Surface modification of polymeric materials is one of the most important research topics for synthesizing functional polymers due to its versatility. Among various surface modification methods, radiation-induced graft polymerization (RIGP) has unique characteristics and is attracting attention as a method that can easily impart various properties to polymeric materials without harming their physical properties. In this regard, we have achieved RIGP of methacrylated vanillin (MV), which can be synthesized from the lignin derivative vanillin, from the surface of materials such as polyethylene-coated polypropylene (PE/PP) and cellulose. [1,2] Of note here, the graft polymerization of MV needed to be carried out in organic solvents, such as DMSO, in order to secure the homogeneity during graft polymerization conditions. However, under the conditions of graft polymerization using DMSO as a solvent, the MV conversion resulted in a rather limited conversions, corresponding to ca. 10 %, and this low reactivity was therefore regarded as a major issue. In addition, unnecessary contact to DMSO solution containing reactants would be potentially dangerous due to the skin penetration to the DMSO solutions in general.

Considering these backgrounds, we attempted to optimize the polymerization conditions by varying the polymerization solvents to improve the MV conversion in RIGP. In this study, PE/PP substrate was selected, and the influence of the solvent used in the reaction on the grafting ratio was systematically evaluated (Fig. 1).

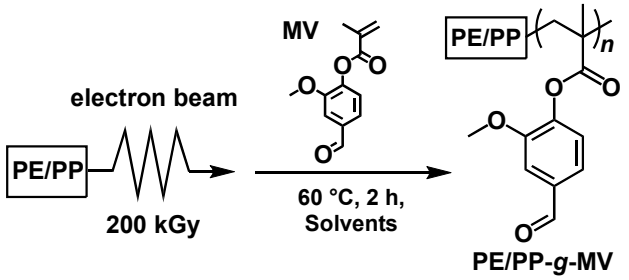

Fig. 1. Radiation-induced Graft polymerization of MV from PE/PP substrates.

Results and Discussion

As mentioned in the introduction, an impact of solvents on the radiation-induced graft polarization of MV was detailed with a wide range of organic solvents. For this, we selected the following six solvents (Dimethyl Sulfoxide (DMSO), Toluene, *N,N*-Dimethylformamide (DMF) , Cyclopentyl methyl ether (CPME) , Bromobenzene, Chlorobenzene). The MV graft polymerization is briefly described here. MV (0.60 g) was dissolved in a solvent (3.6 mL) and the resulting reaction solution was degassed with Ar gas. PE/PP substrates irradiated with 200 kGy electron beam were immersed in the reaction solutions and allowed to react for 2 hours at 60 ºC. After the reaction completion, the resulting PE/PP substrate was washed with the solvent used in the reaction and methanol to afford MV-grafted PE/PP substrate (PE/PP-*g*-PMV).

The results showed an increase in GD in the case of aromatic solvents such as Toluene and bromobenzene, as well as in the case of an ether-based solvent, CPME. In particular, the MV conversion in the case of chlorobenzene dramatically increased to 42.3%, which is several times higher than the conversion in DMSO. On the other hand, when DMF or DMSO was used as a solvent, the GD decreased significantly, revealing a significant solvent dependence of RIGP.

Table 1 Results of RIGP with different solvents.

Solvent	GD (%)	Conv. (%)
DMSO	175.9±2.5	10.9±0.1
DMF	77.2±1.9	4.6±0.1
Toluene	211.0±11.2	12.4±0.7
CPME	305.3±6.6	17.9±0.4
Bromobenzene	587.3±34.0	32.9±1.9
Chlorobenzene	763.9±14.7	42.3±0.8

Conclusions

In this study, we investigated solvents in RIGP, and found that halobenzene solvents and ether solvents achieved significantly enhanced MV conversions and succeeded in increasing the MV conversion compared to conventional experimental conditions.

Acknowledgments

R. K. gratefully acknowledges the Leading Initiative for Excellent Young Researchers (LEADER) for the financial support. R. K. also acknowledge the S-Membrane Project and the F-Materials Project at Gunma University for the financial support.

References

[1] R. Kakuchi *et al*., Polym. J. **53**, 523 (2021).
[2] T. Hamada *et al*., ACS Sustainable Chem. Eng. **7**, 7795 (2019).

2 - 12 Suppression of silicone rubber bleed-out by electron beam crosslinking

Y. Ueki[a)], M. Oshida[b)], H. Sando[b)] and N. Seko[a)]

[a)]Department of Advanced Functional Materials Research, QST
[b)]Research & Technical Development Department, MITSUBA Corporation

Automobile wipers are an essential equipment for wiping off raindrops and dirt from the windshield and ensuring safe visibility for the driver on rainy days. Currently, natural and synthetic rubbers with excellent wiping and friction properties are commonly used as wiper blade rubbers. However, the wiper blade rubber has a short lifespan because it is constantly exposed to a harsh environment of rain and ultraviolet rays. Therefore, silicone rubber wipers with better weather, heat, and chemical resistance than natural and synthetic rubbers are eagerly awaited for development. However, conventional silicone rubber has the disadvantage that water-repellent components such as plasticizers and low-molecular-weight siloxane, which are added to maintain its flexibility as rubber, tend to bleed-out from the silicone rubber surface. When water-repellent components adhere to the windshield during wiper use, a water-repellent film is formed, causing poor visibility. The objective of this study is to verify the effect of electron beam (EB) crosslinking on silicone rubber surfaces to suppress the bleed-out of water-repellent components. [1]

A silicone rubber sample with a highly crosslinked surface layer was synthesized by a two-step crosslinking reaction involving thermal processing and subsequent EB-irradiation. The silicone rubber, which consisted of 100 g of KE-571-U, 1 g of C-25A, 4 g of C-25B, and 2 g of trimethylolpropane trimethacrylate, was thoroughly mixed. After mixing, the silicone rubber was cured at 120°C for 10 min using a thermal compression molding machine to form thermally crosslinked structures throughout the interior of the silicone rubber. Subsequently, the thermal-compression molded silicone rubber sheet was irradiated with EB to create EB-crosslinked structures only on the surface layer of the silicone rubber.

Figure 1 shows the effects of EB-irradiation dose on the swelling rate and surface hardness of silicone rubber. As the EB irradiation dose increased, the swelling rate decreased, while the surface hardness increased. This is due to the effect of the EB-crosslinked surface layer formed on the silicone rubber, and the crosslinking density increased as the EB-irradiation dose increased. Additionally, the thickness of the EB-crosslinked surface layer could be easily controlled by changing the acceleration voltage of the EB. In particular, using an EB of 90 keV, the penetration depth of the EB was about 100 μm. Therefore, a new type of silicone rubber with a soft rubber interior and a hard surface was successfully synthesized.

The bleed-out suppression effect of the silicone rubber with a highly crosslinked surface layer was evaluated indirectly by transferring the water-repellent components exuding from the silicone rubber to a glass surface, and then measuring the water contact angle of the glass surface. As shown in Figure 2, the water contact angles decreased gradually with the increase in EB-irradiation dose. The decrease in water contact angle occurs as the finer crosslinked structure of the silicone rubber surface layer formed by the EB-irradiation behaves as a leak-proof filter, preventing the low-molecular-weight siloxane inside the silicone rubber from bleeding out. These results demonstrate that the EB-crosslinked layer formed on the surface of the silicone rubber had a bleed-out suppression effect. Furthermore, the effect of the EB-crosslinking agent type on the bleed-out suppression was investigated, and it was found that the EB-crosslinking agent with more crosslinking points (vinyl group numbers) had a higher bleed-out suppression effect. The thermally and EB-crosslinked silicone rubber successfully reduced the bleed-out ratio by approximately 60%, compared to the conventional silicone rubber.

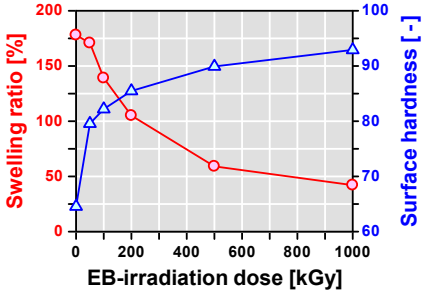

Fig. 1 Effect of EB-irradiation dose on swelling rate and surface hardness of silicone rubber.

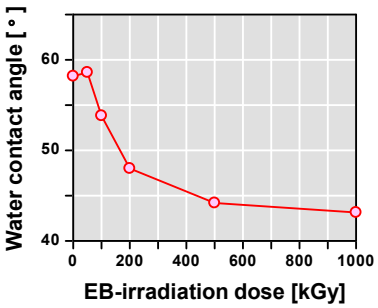

Fig. 2 Effect of EB-irradiation dose on the glass surface water contact angle of surface crosslinked silicone rubber.

References

[1] Y. Ueki *et al.*, Radiat. Phys. Chem. **193**, 110002 (2022). DOI: 10.1016/j.radphyschem.2022.110002

2 - 13 Development of grafted catalyst for biodiesel fuel production using cellulose fabric

M.Harada[a, b], Y.Ueki[a] and N.Seko[a]

[a]Department of Advanced Functional Materials Research, QST
[b]Department of **Science and Engineering**, Gunma University

Introduction

Biodiesel fuel (BDF) which is produced from waste cooking oil is attracting attention as a carbon-neutral biomass fuel from the perspective of the SDGs. We have attempted to develop a grafted catalyst for BDF production that can convert waste cooking oil into BDF and succeeded in synthesizing the grafted catalyst via a three-step reaction using three chemicals (chloromethyl styrene: CMS, trimethylamine: TMA, sodium hydroxide: NaOH) as shown in Figure 1 [1]. However, since this synthetic method has to use the TMA which is a specific malodorous substance, it is difficult to apply to large-scale production sites. Then, it is necessary to find out a new synthetic method to replace TMA due to realize mass production of the grafted catalysts. In this study, we investigated a one-step graft polymerization method using vinyl benzyl trimethyl ammonium chloride (VBTAC) which has both CMS and TMA functions and evaluated the catalytic performance of the prepared grafted catalysts for BDF production with the aim of developing the grafted catalyst suitable for mass production.

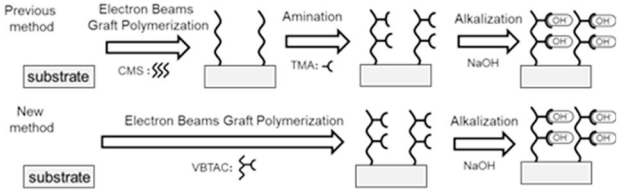

Fig. 1 Improvement of grafted catalyst synthesis method for BDF production

Experimental

The cellulose nonwoven fabric of substrate(fiber diameter: 15 μm) was irradiated with electron beams under a nitrogen atmosphere (Irradiation dose: 10～100 kGy). Then, graft polymerization with 0.5 MVBTAC solution(temperature: 40℃, time: 24 h) and alkalization with 1 M NaOH solution (temperature: 25℃, time: 20 h) were sequentially performed to obtain grafted catalysts for BDF production. The catalytic performance of the grafted catalyst was evaluated by transesterification of triglyceride (TG) and alcohols according to the reaction conditions of Ueki et al [1]. The composition of the reaction samples was analyzed by high-performance liquid chromatography (HPLC) and the BDF conversion of TG was calculated from the analysis results.

Results and Discussion

Figure 2 shows the results of one-step graft polymerization of VBTAC. When polyethylene was used as the base material, graft polymerization did not proceed. The reason for this was thought to be the repulsion between the hydrophilic monomer VBTAC and the hydrophobic polyethylene. Therefore, instead of polyethylene, we performed graft polymerization that it was adopted cellulose fabrics as the base material to reduce the hydrophobicity. As a result, the grafting rate (Dg: degree of grafting) after 24 h of graft reaction reached 131% (VBTAC group density: 2.67 mmol/g) which was sufficient as a grafted catalyst.

Although the graft polymerization of VBTAC was possible by using cellulose, cellulose has the disadvantage of low radiation resistance. Therefore, the mechanical strength of the catalyst was evaluated, and it was confirmed that the catalyst retained the mechanical strength necessary for a grafted catalyst module, although there was a slight reduced by electron beam irradiation and graft polymerization.

Using the prepared grafted catalyst, BDF was produced by the transesterification between TG and ethanol. As a result, TG was converted to BDF as the reaction time progressed. As shown in Fig. 3, 97% of TG was converted to BDF in 4 h. The catalytic performance of the VBTAC-type catalyst in the BDF production reaction was comparable to that of the conventional CMS-TMA-type catalyst in terms of TG conversion to BDF, indicating that the catalyst functions well as a BDF production catalyst.

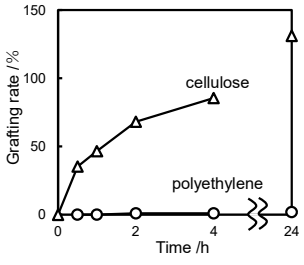

Fig. 2
Effect of the reaction time on the Grafting rate

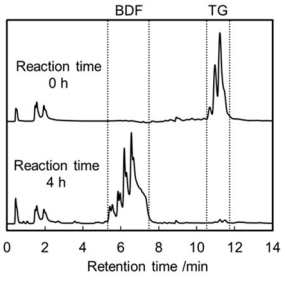

Fig. 3
Results of BDF measurement by HPLC

References

[1] Y. Ueki *et al*., International Journal of Organic Chemistry. Vol 4, 91-105 (2014). DOI: 10.4236/ijoc.2014.42011

2 - 14 Hydrogels for reduction of peripheral neuropathic pain

N. Natori[a)], Y. Shibano[a)], A. Hiroki[b)], M. Taguchi[b)], A. Miyajima[c)], K. Yoshizawa[a)], Y. Kawano[a)], T. Hanawa[a)]

[a)] Faculty of Pharmaceutical Sciences, Tokyo University of Science
[b)] Department of Advanced Functional Materials Research, QST
[c)] Faculty of Pharmaceutical Sciences, Meiji Pharmaceutical University

Introduction

Neural disturbance, which occurs in the central neural system, peripheral neural system, and so on, develops in one-third of patients receiving anticancer agents. Peripheral neuropathies are side effects of anticancer drugs. Although some clinical trials have been carried out to address this issue, no method has been established to prevent or treat peripheral neuropathy. Tramadol hydrochloride (TRA) is effective for peripheral neuropathy, but considering the viewpoint of ingestibility, it needs to develop topical preparations to apply directly to the affected area as an alternative oral dosage. This study aimed to find the possibility of a new dosage form to replace the existing oral therapeutic agent for peripheral neuropathy.

Experimental

Hydroxypropyl methylcellulose (HPMC) and purified water were kneaded and sandwiched by polyethylene terephthalate film. The samples were irradiated with 2 MeV electron beams with doses from 10 kGy to 50 kGy (kGy = J/g) at room temperature. The irradiated samples were washed with distilled water at 25 °C for 48 h to remove non-crosslinked contents, and then dried to xerogel. Tramal® injection was diluted in purified water to prepare TRA solutions (10 mg/mL). Xerogels were immersed in a TRA solution for 24 h to prepare TRA-containing hydrogels [1].

Eight-week-old male mice were injected intraperitoneally with a 0.7% (v/v) acetic acid solution (10 mL/kg of body weight) as a stimulus. The number of writhes was recorded for 10 min. Writhe was defined as stretching of the hind limbs accompanied by a contraction of the abdominal muscles. The HPMC hydrogels irradiated at 50 kGy containing TRA or saline were pasted on the back of the mouse 2 h before the injection of acetic acid.

Results and Discussion

Transparent and resilient HPMC hydrogels were obtained by electron beam irradiation. The swelling degree of the HPMC hydrogel was 15 and the water content was greater than 90% at 50 kGy. Since oxygen diffuses through the water which is the main component of the hydrogel, the oxygen permeability of the hydrogel is considered to be almost equal to that of water. Regarding wound dressings, oxygen permeation is a key parameter for rapid epidermal regeneration.

The concentrations of TRA were 0.11 and 0.09 mg/mg in the 30 and 50 kGy irradiated hydrogels, respectively. No change in transparency was observed by the spectrophotometer. The skin permeation behavior of TRA from TRA-containing hydrogels through the dorsally extracted skin of hairless mice is shown in Fig. 1. The released amount increased with time and the hydrogels irradiated at 50 kGy exhibited greater release than those irradiated at 30 kGy.

The effects of TRA on acetic acid-induced writhing behavior in mice are shown in Fig. 2. The number of writhes induced by acetic acid reduced dose-dependently and significantly. The transdermal administration using hydrogel would result in higher doses than oral administration (26 mg/kg), which is expected to be as effective as oral administration.

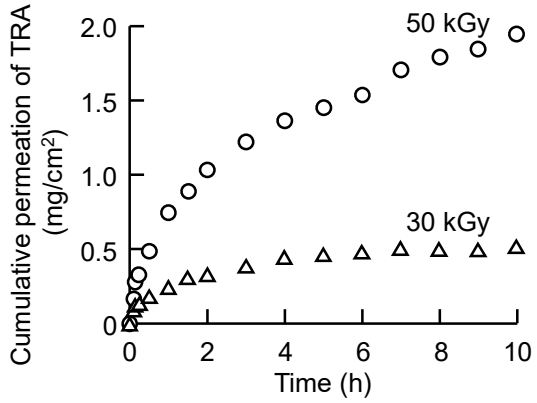

Fig. 1 Effect of irradiation doses on permeability profile of TRA from hydrogels.

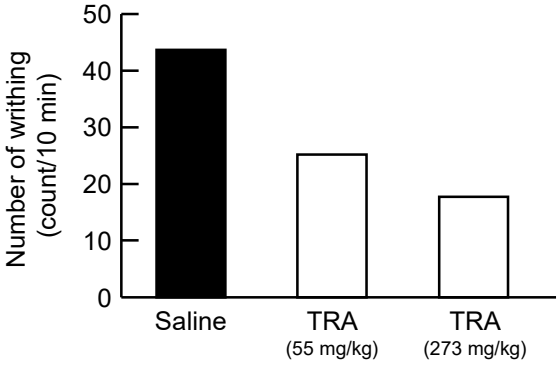

Fig. 2 Effects of the hydrogel containing TRA on the acetic acid-induced writhing test in mice.

Acknowledgment

This work was partially supported by JSPS (KAKENHI 17K08466).

Reference

[1] N. Natori *et al*., J. Pharm. Sci. **112**, 132 (2013). DOI: 10.1016/j.xphs.2022.05.013

2 - 15 Effect of radiolysis in gas phase on the corrosive environment in liquid phase

K. Hata[a)], A. Kimura[b)], T. Sato [c)], C. Kato [c)] M. Taguchi[b)]

[a)]Materials Evaluation Research Group, Nuclear Safety Research Center, JAEA
[b)]Department of Advanced Functional Materials Research, QST
[c)]Research Group for Corrosion Resistant Materials, Nuclear Science and Engineering Center, JAEA

Radiolysis of contaminated water of the Fukushima Daiichi Nuclear Power Station (1F) is a critical issue to evaluate the corrosion behavior of structural components in the containment vessels. A large volume of gas phase space exists in the 1F containment vessels and is constantly exposed to ionizing radiation. Although the gas phase is generally less sensitive to ionizing radiation than the liquid phase, the effect of radiolysis of chemical species in the gas phase may not be negligible under the large volume and the long irradiation time. Especially, nitrogen oxides (NO_x), which are dominant species produced from gas-phase radiolysis, are known as strong oxidants. These nitrogen oxides are mainly produced by the reaction of excited nitrogen and oxygen in the air. In this study, to estimate the corrosive environment in the 1F containment vessels, the effect of radiolysis of gas phase was evaluated. Gamma-ray irradiation experiments under gas-liquid coexistence conditions and radiolysis calculations were carried out to quantify the radiolytic products.

The ^{60}Co γ -ray irradiation facility, TARRI, QST was used for the irradiation. Glass vials of 20 ml containing 10 ml of pure water were sealed with a cap and a butyl rubber septum. The samples were saturated with air or mixed gas of N_2 and O_2. The concentrations of nitrate ion (NO_3^-) and nitrite ion (NO_2^-) in the liquid phase were measured by an ion chromatograph after irradiation. The production yields of nitrogen oxides produced in the gas phase (G(NOx)) were estimated as the sum of the apparent yields of NO_3^- ($G'(NO_3^-)$) and NO_2^- ($G'(NO_2^-)$), which are calculated from these concentrations in the liquid phase according to the equations shown in Fig. 1. In this estimation, all NOx produced in the gas phase radiolysis is assumed to be dissolved in the liquid phase.

Radiolysis calculations were carried out using FACSIMILE [1]. Primary yields of chemical species and chemical reaction sets were determined by reference to the previous reports [2, 3]. In the calculations, the interfacial mass transfer of volatile species produced in the liquid phase (H_2 and O_2) and NO_2 produced in the gas phase is taken into account according to the previous works [4, 5].

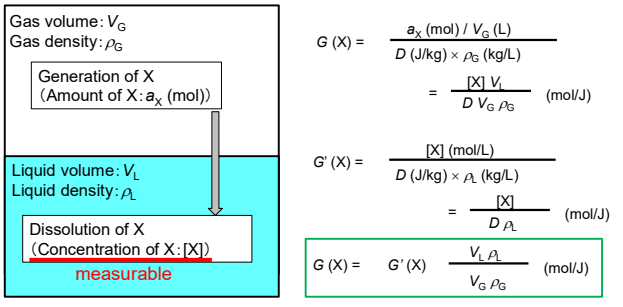

Fig. 1. Calculation of the production yield in the gas phase from the concentration in the liquid phase.

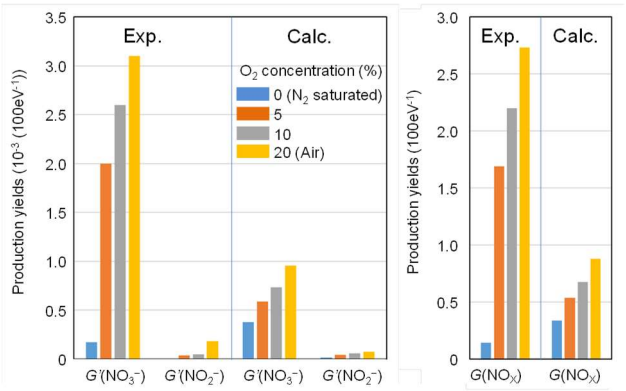

Fig. 2. The apparent production yields (G') of NO_3^- and NO_2^- in the liquid phase and the production yields (G) of NOx in the gas phase obtained by experiment and radiolysis calculation.

Fig. 2 shows $G'(NO_3^-)$, $G'(NO_2^-)$ and G(NOx) obtained by the experiments. It was found a small amount of O_2 (5%) strongly affected the NOx formation in the gas phase. Although the production yields obtained by radiolysis calculation were about one-third as small as those obtained by experiment, the qualitative trend, such as the ratio between $G'(NO_3^-)$ and $G'(NO_2^-)$, was well simulated. The improvement of the radiolysis calculation method should be tried in future work.

Acknowledgments

This research was supported by the Nuclear Energy Science & Technology and Human Resource Development Project JPJA20P20333127.

References

[1] E.M. Chance, AERE-R 8775 (1977).
[2] A.M. Bulearcă, et al., U.P.B. Sci Bull., Series B, **72**, 101 (2010).
[3] A.J. Elliot and D.M. Bartels, AECL 153-127160-450-001, (2009).
[4] P.A. Yakabuskie, et al., Radiat. Phys. Chem. A, **79**, 777 (2010).
[5] R. Talviste, et al., Plasma Chem. Plasma Process, **42**, 1101 (2022).

2 - 16 Ion irradiation induced deviant volumetric change behavior of silicon carbide nanotubes

T. Taguchi[a)], S. Yamamoto[a)], M. Saeki[a)] and H. Ohba[a, b)]

[a)]Department of Advanced Functional Materials Research, QST
[b)]Collaborative Laboratories for Advanced Decommissioning Science, JAEA

Introduction

Silicon carbide (SiC) is a promising non-oxide ceramic material used in a wide range of applications. SiC has been expected to be utilized as structural materials for fusion reactors, owing to its attractive chemical, physical, and mechanical properties. Meanwhile, nanomaterials may possess excellent and novel properties that differ from those of their bulk materials. In particular, we succeeded in synthesizing nanometer-sized single-phase SiC nanotubes with engrossing geometries [1, 2]. SiC nanotubes may have novel properties relative to bulk SiC materials. It has been reported that the volume of SiC material swells under the neutrons and ions irradiation conditions. Here, we report the ion irradiation induced deviant volumetric change behavior of SiC nanomaterials such as SiC nanotubes compared to bulk SiC materials.

Experimental

The multi-walled carbon nanotubes (MWCNTs: GSI Creos Corporation, Tokyo, Japan) were heated with Si powder (The Nilaco Corporation, Tokyo, Japan) at 1,200 °C for 30 h in a vacuum. The samples were then heated at 800 °C for 4 h in air in order to remove unreacted MWCNTs and carbon layers. The polycrystalline SiC nanotubes were synthesized by immersing the sample heated in air in a 5 M NaOH and then a 0.2 M HCl solutions to eliminate the thin SiO_2 layers. The chemical vapor deposition (CVD) SiC substrate (Ferrotec Material Technologies Corporation, Japan) was used as a SiC bulk material in this study. The CVD SiC substrate for TEM observations was thinned with a thickness of approximately 100 nm by using 2 keV Ar^+ beam (JEOL Cryo Ion Slicer IB+09060CIS). The molybdenum grid holder, which deposited the polycrystalline SiC nanotubes, and the thinned CVD SiC specimens were irradiated with 200 keV Si^+ ions from 400 kV ion implanter at room temperature. The ion irradiation was performed at the Takasaki Ion Accelerators for Advanced Radiation Application (TIARA) facility in the National Institutes for Quantum Science and Technology. The irradiation damage (in terms of displacement per atom; dpa) for the SiC was estimated by SRIM 2008 to be 47.8 dpa. The circumstantial microstructural developments to the SiC nanotube and CVD SiC before and after ion irradiation were observed by TEM (Model 2100F, JEOL Ltd., Akishima, Japan) operating at 200 kV. Electron energy-loss spectroscopy (EELS, Enfinium spectrometer, Nippon Gatan, Nishi-Tokyo, Japan) was carried out to measure the plasmon energies of SiC nanotube and CVD SiC before and after the ion irradiation.

Results and Discussion

The volumetric changes of SiC nanotube and CVD SiC were estimated by the difference between their plasmon energies before and after the ion irradiation. Figure 1 shows the volumetric change behavior of SiC nanotube and CVD SiC bulk material. The amount of volumetric change in CVD SiC bulk material by the ion irradiation at room temperature increases up to the irradiation dose of around 1 dpa, and almost saturates afterwards. The saturated amount of volumetric change is measured to be approximately 15 %. It is well consistent with previous studies [3]. On the other hand, the amount of volumetric change in SiC nanotube increases up to the irradiation dose of around 3 dpa, which is the irradiation dose of their completely amorphization, and decreases rapidly afterwards. Furthermore, the maximum amount of volumetric change in SiC nanotube is measured to be approximately 10 %. It is smaller than that of CVD SiC bulk material. These results suggest that the SiC nanotubes have the deviant volumetric change behavior compared to CVD SiC bulk materials.

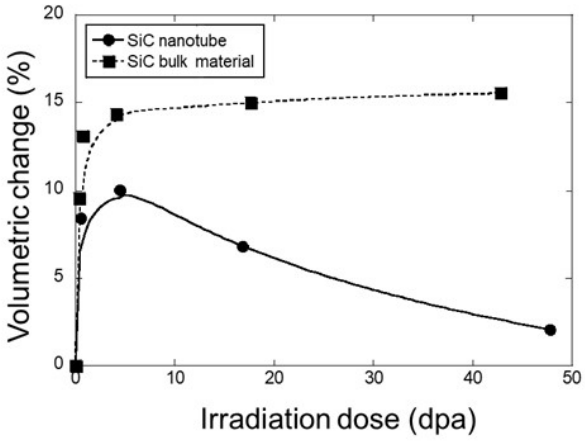

Fig. 1 Volumetric change behavior of SiC nanotube and CVD SiC bulk material.

References

[1] T. Taguchi *et al*., J. Am. Ceram. Soc. **88**, 459 (2005). DOI: 10.1111/j.1551-2916.2005.00066.x
[2] T. Taguchi *et al*., Physica E **28**, 431 (2005). DOI: 10.1016/j.physe.2005.05.048
[3] L. L. Snead *et al*., J. Nucl. Mater. **273**, 213 (1999). DOI: 10.1016/S0022-3115(99)00023-9

2 - 17 Radiation tolerant laser-induced breakdown spectroscopy system using a single crystal micro-chip laser for remote elemental analysis

K. Tamura[a)], R. Nakanishi[a)], H. Ohba[a,b)], T. Karino[b)], T. Shibata[b)], T. Taira[c,d)] and I. Wakaida[b)]

[a)]Foundational Quantum Technology Research Directorate, QST
[b)]Collaborative Laboratories for Advanced Decommissioning Science, JAEA
[c)]Division of Research Innovation and Collaboration, IMS
[d)]Laser-Driven Electron-Acceleration Technology Group, RSC

Introduction

By the accident at the TEPCO Fukushima Daiichi Nuclear Power Station, the fuel debris was generated and left inside the reactor vessel. Since retrieval and storage of the debris are necessary for the decommissioning, it is crucial to develop a method for a remote elemental analysis for searching the debris in a radiation environment. For the analysis, laser-induced breakdown spectroscopy (LIBS) system utilizing the micro-chip laser (MCL) of an Nd:YAG/Cr:YAG composite has been developed [1].

This report describes the radiation dose rate effects on the laser properties of the MCL, and gadolinium (Gd) LIBS spectra in composite oxides simulating fuel debris for the development of the remote elemental analysis system operatable in harsh radiation environment based on LIBS.

Experimental

Radiation effects were measured for a monolithic Nd:YAG/Cr:YAG composite, where Nd:YAG is a laser gain medium and Cr:YAG is a saturable absorber. The YAG composite was set in a holder in an irradiation area at the gamma-ray irradiation facility and was irradiated using ^{60}Co source. The MCL properties of single crystal (SC) (II-VI Incorporated, USA) and ceramics (Konoshima Chemical/Baikowski-Japan, Japan) were measured and compared.

For Gd spectrum measurements, an echelle spectrograph (EMU-120/65 VIS/NIR, Catalina Scientific, USA) was used. The sample was synthesized from powder mixtures of Gd_2O_3, CeO_2, ZrO_2 and Fe_2O_3 to simulate the nuclear fuel debris. The Gd concentrations was 0 and 0.87 wt%. The LIBS measurement was triggered at a delay of 1 μs from the laser irradiation. The exposure time was 2 μs, and each LIBS spectrum was acquired for 100 laser shots. The gamma-ray irradiation time during LIBS measurement was 25 minutes and ten spectra were recorded for each sample.

Results and Discussion

Radiation effects on the laser properties were investigated. Various parameters including pump energy for oscillation, laser output energy, build-up time (BUT), number of pulses, and pulse energy were measured as a function of dose rate. The results show that the detrimental radiation effects on SC were significantly smaller than those observed in ceramics. It was concluded that the radiation effects on LIBS signal using SC were negligibly small, which shows that the SC LIBS system is a highly radiation tolerant for remote element analysis.

Figure 1 illustrates the LIBS spectra of the simulated debris using SC MCL system before and during gamma-ray irradiation at a dose rate of 5 kGy/h. In this figure, Gd emission peaks were clearly observed. These results demonstrate that the radiation effect on the spectra was negligible as expected from the radiation effects on laser properties. This characteristic enables effective quantitative analysis using the developed SC LIBS system.

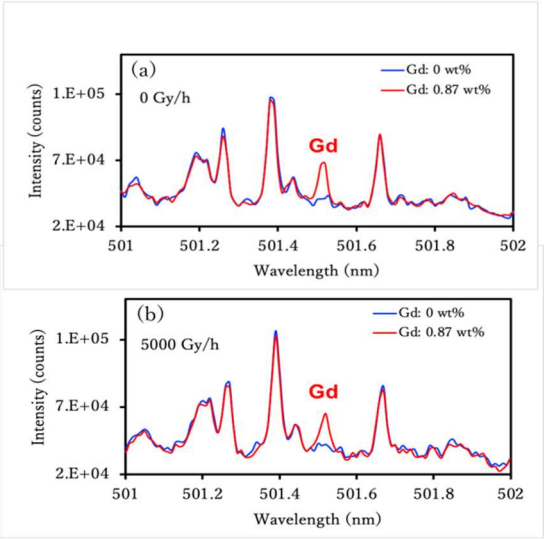

Fig. 1. LIBS emission spectra of simulated debris including Gd line at a dose rate of (a) 0 kGy/h and (b) 5 kGy/h.

Acknowledgments

The authors wish to thank Dr. M. Saeki and Dr. T. Taguchi (QST) for their support. This study includes a part of the results of “Project of Decommissioning and Contaminated Water Management”, the Japanese Ministry of Economy, Trade and Industry as The Subsidy Program, Japan.

References

[1] K. Tamura et al. J. Nucl. Sci Tech. **57**, 1189–1198 (2020).

2 - 18 Study on fusion neutron irradiation effects using multiple ion-beam irradiation

M. Ando, J. Yu and T. Nozawa

Department of Fusion Reactor Materials Research, QST

Introduction

Reduced activation ferritic steels (RAFM) such as F82H and EUROFER97 are candidates for DEMO blanket structural materials. Many reactor irradiation studies have shown neutron irradiation effects on RAFM, however the details of the 14 MeV fusion neutron effect are still unknown since a fusion neutron irradiation facility is currently unavailable. Instead, several simulated fusion neutron irradiation damage experiments are used to understand their effects. Ion irradiation experiments using multiple accelerators can partially simulate the characteristics of fusion neutron irradiation, i.e., displacement damage and helium production at a certain rate, however unfortunately the evaluation volume is very small and only limited evaluation methods can be applied.

In the past, as ion irradiation experiments and post-irradiation examinations, evaluation of void swelling (mainly cavity microstructure analysis) has been conducted mainly by electron microscope observation, and strength for irradiated materials (irradiation hardening/softening) has been conducted by micro-hardness tests. In particular, the effect of helium on swelling is significant, and contributes to the judgment (critical point) of how far the fission reactor irradiation data (almost no helium) can be used. In terms of strength, there is concern that helium accelerates embrittlement, and more information on fracture characteristics is needed. In order to obtain this fracture-related information from ion-irradiated materials, we modified the μ-tensile test method and attempted to evaluate fracture strength as a new indicator.

Experimental

The materials used in this study were F82H IEA. The irradiations were carried out with 10.5 MeV Fe^{3+} ions and 1.05 MeV He^{+} ions. In multi-ion irradiation, He implantation rate was fixed to be 15 appm/dpa. The irradiation temperature was selected near 300°C, where strong irradiation-hardening is occurred in F82H, and the irradiation dose was up to 80 dpa. A μ-tensile specimen has notches in middle gauge section as shown in Figure 1.

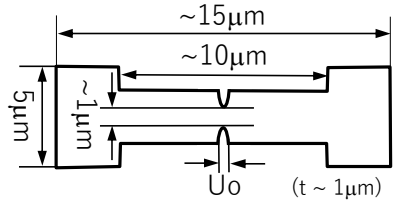

Fig. 1. Dimension of μ-tensile specimen

It is considered that a kind of fracture stress (μ-FS) for a single-block F82H can be obtained by using μ-tensile specimens with notches because the local deformation constraint occurs around notches. The μ-tensile tests were performed in a focused ion beam (FIB) processing device. Each μ-tensile specimen was prepared and fixed to the micro-probe attached to the FIB device, and μ-tensile tests were performed. The test load was estimated from the deflection of the SiC micro-beam to which the specimen was fixed [1]. The indicator of fracture strength was defined as the maximum stress just before fracture.

Results and Discussion

Figure 2 shows the results of μ-tensile test for unirradiated and ion- irradiated F82H at 300°C up to 80 dpa. The unirradiated F82H steel slightly deformed after maximum strength and then fractured. The fracture surface after broken is a pyramid-shaped fracture surface, similar to the so-called chisel point fracture surface with good ductility. On the other hand, it is known that irradiation hardening occurs significantly in the irradiated F82H to 80 dpa at 300°C with or without helium [2]. In the same way, it tends to fracture with little deformation by micro-tensile test. The fracture stress was higher in the ion-irradiated F82H, and most of the fracture surfaces tended to be flat-like with little deformation. This method has shown the potential to be used as a new indicator to evaluate the ductility and brittleness of ion irradiated F82H steel. Additionally, the dispersion in fracture stress was obvious in irradiated F82H with helium. We will continue to investigate the relationship between the fracture stress and the amount of helium.

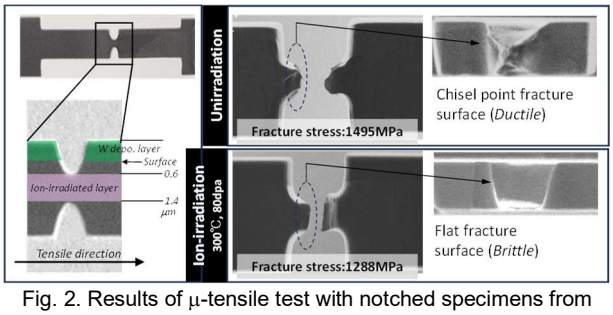

Fig. 2. Results of μ-tensile test with notched specimens from unirradiated and ion-irradiated F82H

References

[1] Juhyeon Yu et al., Nucl. Mater. Energy, 30, 101145, (2022), DOI:10.1016/j.nme.2022.101145.

[2] M. Ando et al., J. Nucl. Sci. Tech., 60, 1116–1124 (2023).

2 - 19 Irradiation tests of radiation hardness components and materials for ITER blanket remote handling system

M. Saito, Y. Kawai, K. Nakata, Y. Noguchi and N. Takeda

Department of ITER Project, QST

Introduction

The ITER blanket remote handling system (BRHS) will replace the first walls in a gamma radiation environment having a dose rate of 250 Gy/h to 500 Gy/h. We set a radiation hardness target value of 3 MGy to increase the availability of the system. In this study, we investigated the radiation hardness of magnetic sensor, which will be used for detecting movable limit, and SUS630H900/1150 which are structural materials of rail's rack and pinion.

Irradiation tests

The samples were irradiated at γ-ray irradiation facility as shown in Table 1. Samples of SUS630H900/1150 were irradiated with humidity control. The atmosphere around the samples was kept at 30 °C and 43.2% relative humidity by using a thermostatic chamber where a K_2CO_3 saturated salt solution was placed. After irradiation, transmission test with 1 m and 30 m cables, and insulation resistance test (more than 100 MΩ at DC 500 V) were performed for sensors. The transmission was tested by detecting the signals of the sensors with 1 m / 30 m cables. The surface observation and SEM-EDX analysis were performed on SUS630H900/1150 samples.

Table 1
Irradiation conditions for each sample.

Component	Dose rate [Gy/h]	Total [MGy]
Sensor (M9 x 43mm)	800-1950	1, 2, 3, 5, 10 (N=2)
Structural material (SUS630H900,30×30×t5mm)	1100	1, 2, 3, 5 (N=2)
Structural material (SUS630H1150,30×30×t5mm)	1100	1, 2, 3, 5 (N=1)

Results

The sensors have been irradiated up to 10 MGy and confirmed transmission and insulation resistance. At 1 MGy of irradiation, signals were correctly detected, and the insulation resistance was within the criteria. After 2 MGy and 3 MGy of irradiation, detection error occurred. Moreover, after 3 MGy, 5 MGy and 10MGy of irradiation, insulation resistance decreased below criteria. Although this magnetic sensor achieved 1 MGy radiation hardness, we will research the degraded part of this sensor and other candidate of magnetic sensors.

Both SUS630H900 and SUS630H1150 had no corrosion on the surface even after 5 MGy of irradiation. SEM-EDX analysis was also performed. Although oxygen on the surface increased slightly with irradiation up to 5 MGy, no change was observed on the surface. Therefore, we considered that SUS630H900/1150 are applicable to the BRHS parts.

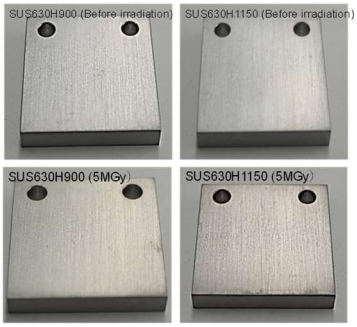

Fig. 1 Sample surface of before and after irradiation

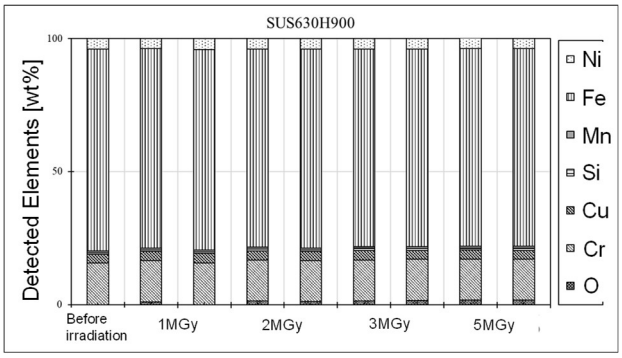

Fig. 2 EDX element mass concentration for SUS630H900.

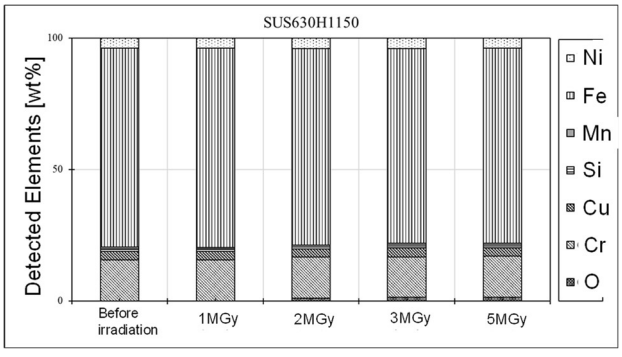

Fig. 3 EDX element mass concentration for SUS630H1150.

Acknowledgments

The authors would like to acknowledge Beam Operation Co., Ltd. and Takasaki Advanced Radiation Research Institute's Irradiation Facilities Section who supported the irradiation experiments.

2 - 20 Gamma-ray irradiation experiment for ITER diagnostic systems in JADA V

S. Kitazawa, Y. Nunoya, M. Ishikawa, R. Imazawa, E. Yatsuka, K. Nojiri, T. Ushiki, S. Kono, K. Torimoto, M. Inamine, T. Kikuchi, T. Yokozuka, H. Murakami, K. Shimizu, and T. Sugie

Department of ITER Project, QST

JADA (ITER project Japan Domestic Agency) is developing to procure five diagnostic systems, microfission chamber (MFC), poloidal polarimeter (PoPola), Edge Thomson Scattering (ETS), divertor impurity monitor (DIM) and divertor infrared thermography (IRTh).

The reliability under the ITER radiation conditions of relevant equipment to be installed in the vacuum vessel, in the interspaces (IS) between the vacuum boundary and the biological shield and in the port cells (PC) outside the biological shields should be evaluated. In this project, we launched gamma-ray irradiation experiments in QST Takasaki Advanced Radiation Research Institute from 2018. The results obtained in the experiments are used important basses for showing that components can maintain its their performances under the ITER radiation environment in the design review for each diagnostic system.

The gamma-ray irradiation experiments on optical components for plasma diagnostics have mainly been conducted by measuring optical density or reflectance before and after irradiations [1, 2, 3]. Regarding electronic equipment for diagnostic systems, we have conducted gamma-ray irradiation durability tests on piezo elements and electrical equipment, observing their characteristics before and after irradiation. As the ITER construction procurement activities progressed and the design has been solidified, implementation verification became necessary, so we have lunched in-situ experiments in which gamma rays were irradiated while the current was turned on.

For MFC, in-situ experiments for the preamplifier were performed again, because the circuit of the preamplifier was improved against an oscillation phenomenon [4]. The preamplifier was placed at the position of intended radiation dose in 3rd Cell at Co-60 1st Building, while the other equipment, including a signal generator, measurement instruments, and a power supply were placed outside the cell. Coaxial cables for input signal, output signal, and low voltage power supply were connected to the preamplifier through feedthroughs. High voltage power supply cables were not used because no MFC detectors were connected. The irradiation sequence was a dose rate of 20 Gy/h up to 100 Gy. Pulse signals with different amplitudes and sine signals with different frequencies were input into the preamplifier during the irradiation to investigate the effects of gamma-rays on the pulse counting mode and Campbelling mode, respectively. Output signals from the preamplifier were compared with the input signals to calculate the gain change by the irradiation. The result suggests that the changes in the gain in both pulse counting mode and Campbelling mode are small enough to withstand use during the operation period of ITER. The details will be published elsewhere [5].

For ETS, the radiation-resistant glass (SF6G05) used to correct chromatic aberration of the ETS signal light was irradiated with gamma-ray of up to 10 MGy. In past tests, the degree of degradation of transmittance varied depending on the individual sample. At that time, samples without anti-reflection coating showed significant degradation. This time, three samples were tested: two without the anti-reflection coating and one with the anti-reflection coating removed by polishing. Although discoloration was observed in all three sheets, the decrease in transmittance occurred at wavelengths below 600 nm and did not significantly affect ETS performance. It is remained unclear why some samples had significant transmittance degradation in the past. Additional trials are planned in the future.

For IRTh, gamma-ray irradiation tests were conducted on ZnSe and ZnS samples, both non-AR and AR-coated, to examine their impact on the infrared optical properties. Gamma-ray irradiation at 100 kGy had no significant effect on all samples. However, at 5.6 MGy, non-AR ZnSe and ZnS exhibited induced absorption bands. AR coating partially mitigated this effect, but ZnS, even with AR coating, showed up to 2.5% degradation over the wide wavelength range of 1.5-4.5 μm, whereas ZnSe was less affected. Both materials exhibited a modest 2% absorption around 3 μm. Surface analysis by SEM, laser microscope and XPS linked the 3 μm degradation to gamma-ray irradiation-induced $Zn(OH)_2$ formation, but it was confined to the surface. The details will be published in elsewhere [6].

For PoPola and DIM, gamma-ray irradiations were not conducted in 2022, but preparations are underway for some additional tests to be carried out in the coming years.

Acknowledgments

We would like to thank Naotsugu Nagasawa, Hajime Seito, Hiroyuki Okazaki, Shunya Yamamoto and Hiroshi Koshikawa (TARRI) for their cooperation in the irradiation and observation.

References

[1] S. Kitazawa *et al.*, J. Plasma Fusion Res., **14** 3405089 (2019).
[2] E. Yatsuka *et al.*, Fusion Eng. Des., **160** 111846 (2020).
[3] T. Ushiki *et al.*, Rev. Sci. Instrum., **93** 84905 (2022).
[4] S. Kitazawa *et al.*, J. Plasma Fusion Res., **18** 2405014 (2023).
[5] M. Ishikawa *et al.*, *to be submitted*
[6] T. Ushiki *et al.*, *to be submitted*

2 - 21 Radiation resistance test of insulation for JT-60SA in-vessel coils

M. Takechi, S. Nakamura, D. Tsuru, H. Murakami, A. Sukegawa and A. Isayama

Naka Fusion Institute, Fusion Energy Directorate, QST

JT-60SA is a satellite tokamak in the Broader Approach activity under the international collaboration between Japan and EU [1]. It has three types of in-vessel coils, i.e., Error Field Correction Coil (EFCC), Fast Plasma position Control Coil (FPCC) and Resistive Wall Mode Coil (RWMC), as shown in Fig. 1. Glass fibre reinforced resin will be employed for the insulation material of these in-vessel coils. High heat resistance performance is required for RWMC insulation material because there will be no cooling for RWMC during 200°C baking. In addition, the insulation is required to withstand the irradiation of 9 MGy through the lifetime. We looked for the heat-resistant organic insulator for JT-60SA RWMC and performed the heat resistant test for several resins which passed the irradiation tests. However, no resin passed the heat resistant test [2]. We again performed the heat resistant test of several organic insulator in the circumstances without air and finally found that the some Bismaleimide-Triazine (BT) resin has enough heat resistance without air, as shown in Fig. 2. The RWMC was manufactured with the BT resin [3].

In this study, radiation resistance tests were carried out for four candidate insulation materials as follows.

(1) 70wt% BT resin (BT2160) +30wt% Bisphenol F type Epoxy (jer807) cured with 170ºC.
(2) 70wt% BT resin (BT2160) +30wt% Bisphenol F type Epoxy (jer807) cured with 220ºC.
(3) 100% BT resin (BT3309) cured with 220ºC.
(4) 100% BT resin (BT6070) cured with 230ºC.

100% BT resin (BT2160) was employed as the RWMC insulation material. In addition to these, other BT resins were tested. Also, the BT resin mixed with the Epoxy was tested taking the productivity of coils into account. Dumbbell shaped tensile samples were produced using the three candidate materials. Two samples were manufactured under the different curing conditions. The tensile samples were irradiated at the Gamma-ray irradiation facility in QST Takasaki Institute up to 9 MGy. The number of samples is 12 in total; four candidate insulation materials and three samples for each.

No change was observed between before and after irradiation test, as shown in Fig. 3. Tensile tests will be carried out before the manufacturing other in-vessel coils.

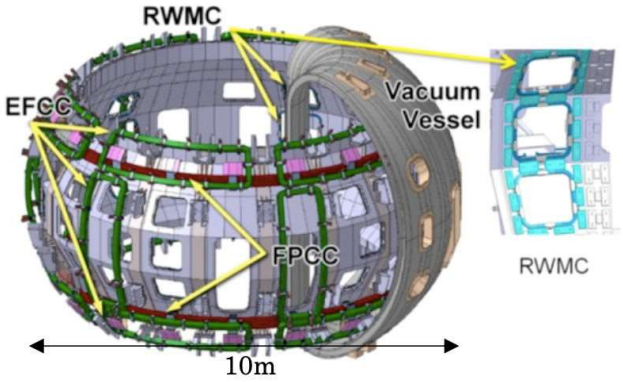

Fig. 1 In-vessel coils for JT-60SA (1)

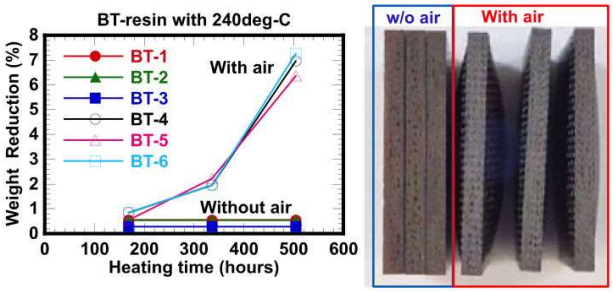

Fig. 2 Weight reduction plots of BT resin at 240ºC with/without air. (b) Photo of BT resin at 240ºC

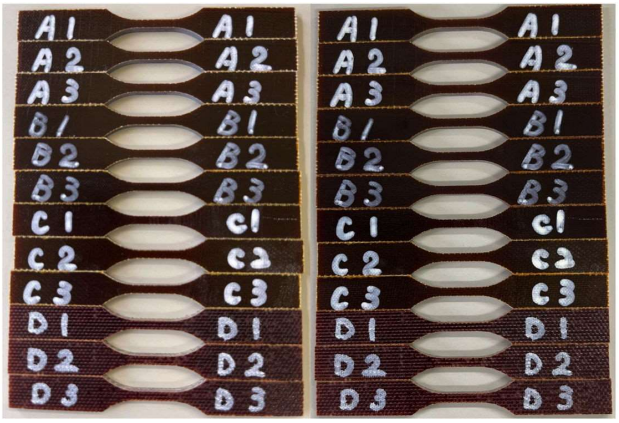

Fig. 3 Samples before (left) and after (right) irradiation test.

References

[1] S. Ishida et al., Nucl. Fusion **51** (2011) 094018, DOI 10.1088/0029-5515/51/9/094018.
[2] M. Sukegawa, et al, Fusion Eng. Des. **98-99** (2015) 2076–2079.
[3] M. Takechi, et al, submitted to Fusion Eng. Des. (2022).

2 - 22 Study on material evolution by ion-irradiation at fuel cladding coating layer and interface

I. Ioka, E. Suzuki, A. Mohamad and S. Yamashita

Fuels and Materials Engineering Division, Nuclear Science and Engineering Center, JAEA

Introduction

After the accident at Fukushima Daiichi Nuclear Power Plant caused by the 2011 Great East Japan Earthquake, benefit to use an Accident Tolerant Fuel (ATF) has been focused among the utilities, industries and regulatory bodies. Then the development of ATF has been accelerated around the world. In Japan, Cr-coated Zr alloy (Cr-coated Zry), improved stainless steel by the dispersion of fine oxide particle (FeCrAl-ODS), and SiC/SiC composite materials are being developed as an ATF. Cr-coated Zry cladding tube is expected to be introduced earlier than other ATFs. The corrosion resistance of Cr-coated Zry cladding tube in high-temperature water, mechanical properties, and resistance to accidents have already been reported [1].

The purpose of this research is to investigate the irradiation resistance of the Cr-coated Zry cladding tube under development, focusing on the coating layer and Cr/Zry interface, and to confirm its applicability to existing light water reactors.

Experimental

The Cr-coated Zry cladding tube used in the ion irradiation experiment was a Zr alloy tube with a diameter of approximately 10 mm and a wall thickness of approximately 0.6 mm, with a Cr coating of approximately 10 μm coated on the outer surface by PVD. Specimens for irradiation cut out from this cladding tube was curved with a width of 6 mm, a length of 3 mm, and a thickness of 0.6 mm. After buffing the irradiated surface with 0.5μm Al_2O_3 particles, ion milling was performed to remove processing distortion. Fig.1 shows the results of cross-sectional observation of the irradiation specimen. Approximately

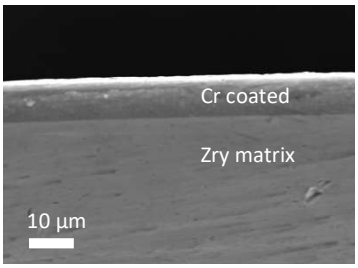

Fig.1 Cross-sectional observation of the irradiation specimen

10μm of Cr is densely coated. In order to confirm the interfacial properties against irradiation, the specimen was irradiated at 10 dpa (at a depth of 1 μm from the surface) using 10.5 MeV $^{56}Fe^{3+}$ from the cross-sectional direction of the specimen using the 3MV tandem accelerator at TIARA of QST. The irradiation temperature was approximately 350°C, and the irradiation holder was water-cooled to prevent overheating. The temperature of specimen was monitored with a thermocouple and an infrared thermometer during irradiation. The damaged area of the specimen was processed using a focused ion beam (FIB). In order to remove defects introduced into the observation surface by FIB processing, the surface was treated with a 2kV gentle mill, and the microstructure was observed using a transmission electron microscope (TEM).

Results and Discussion

Fig.2 shows a TEM specimen is collected by FIB processing from a Cr-coated Zry cladding that has been irradiated with Fe ions from the cross-sectional direction. Although no peeling was observed at the Cr/Zry interface, numerous cracks were observed within the grains and along grain boundaries in the Zry base material, and cracks

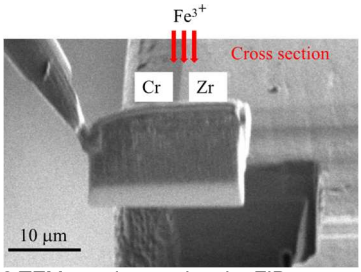

Fig.2 TEM specimen taken by FIB processing

along grain boundaries were observed in the Cr coating layer. Similar cracks were confirmed in other TEM specimens taken from the same irradiated material. Since cracks were observed even at the microstructure observation position 1 to 1.5 μm from the surface (an area unaffected by the implanted Fe ions and only exposed to irradiation damage), it is difficult to achieve the intended purpose. As a result, microstructure observation of this ion-irradiated material was discontinued. Similar cracks were not observed in the TEM specimen of non-irradiated material. It is considered that cracks may occur due to excessive force being applied to the specimen when the specimen was set in the irradiation holder.

In the future, when preparing specimens for ion irradiation, we will be careful not to apply excessive force to the specimens. We plan to perform 10 dpa ion irradiation again and observe the microstructure using TEM.

Acknowledgments

We would like to thank Mr. D.Sato and Mr. Y.Okada for preparing the Cr-coated Zry cladding tubes.

References

[1] N.Murakaami, et.al.," 10th Annual EPRI/DOE/INL Joint Workshop on Accident Tolerant Fuel, March 30-April 1,2021(WebEx meeting).

2 - 23 Simulating α-ray degradation of the TEHDGA adsorbent by the He^{2+} ion beam irradiation experiment

Y. Miyazaki[a)], S. Watanabe[a)], M. Nakamura[a)], M. Koka[b)], Y. Yuri[c)], T. Yuyama[c)], T. Ishizaka[c)] and H. Hanaya[c)]

[a)]Nuclear Fuel Engineering Lab, JAEA
[b)]Beam Operation Co., Ltd.
[c)]Department of Advanced Quantum Beam Technology, QST

Introduction

For the carbon neutral society of 2050, advanced spent nuclear fuel reprocessing technology is required to reduce the volume of radioactive waste and radiotoxicity by separating minor actinides (MA^{3+}: Am^{3+}, Cm^{3+}) from the liquid waste. One of the candidates is extraction chromatography that adapts the use of an adsorbent packed in a column. The adsorbents impregnating the extractants of *N,N,N',N'*-tetra(2-ethylhexyl)diglycolamide (TEHDGA) and *N,N,N',N',N'',N''*-hexaoctylnitrilotriacetamide (HONTA) on the silica-based support are proposed for the two-step MA separation [1-2]. Figure 1 shows these molecular structures. In this study, the radiation resistance of the TEHDGA-impregnated adsorbent was investigated by the He^{2+} ion at 5.5 MeV to simulate the α-ray of the MA nuclides. The degradation is evaluated by the distribution coefficient of Eu^{3+} as a complexing ability.

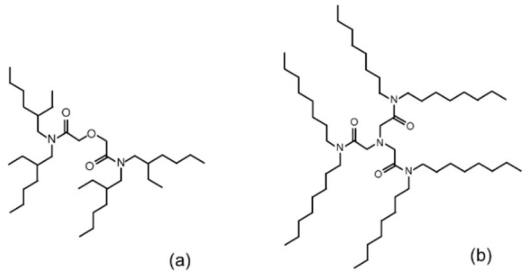

Fig. 1 Molecular structures of (a)TEHDGA and (b)HONTA

Experimental

The He^{2+} ion beam irradiation experiments were performed using the large-area uniform beam irradiation system (LB2) at the Takasaki Institute for Advanced Radiation Application (TIARA). The TEHDGA-impregnated adsorbent was prepared by coating the porous silica with styrene-divinylbenzene copolymer with the particle size of 50 μm and pore size of 50 nm, and impregnated with the extractant of TEHDGA at the weight ratio of 20%. It was immersed in 3 M nitric acid solution with a solid-liquid ratio of 1 : 2, placed in the sample holder (5×5×0.02 cm^3) and sealed with aluminium plate (165 μm thickness). After loading into the vacuum chamber, the sample holder was irradiated with the cyclotron-accelerated He^{2+} ion beams (20 MeV, 6 ×6 cm^2) and decelerated to 5.5 MeV by the aluminium plate.

The distribution coefficient (K_d) was obtained by shaking the mixture of the adsorbent and feed solution (10 mM Eu^{3+} in 3 M nitric acid solution) at a solid-liquid ratio of 1:20 for 3 hours, filtration and ICP analysis of the filtrate.

Results and Discussion

Based on the experimental conditions, the irradiation doses were estimated to be 1, 2 and 4 MGy at the exposure times of 400, 780 and 1560 s, respectively. The distribution coefficients of Eu^{3+} obtained on the adsorbent after irradiation are shown in Figure 2. The adsorption performance decreases with increasing irradiation dose, and a certain threshold K_d value was found at 13. The former indicates the reduced number of complex formation that stems from the radiolysis of TEHDGA, while the latter is the reach of the He^{2+} ion beam into the adsorbent layer. Assuming that α-rays penetrate the depth of 50 μm, 24% of TEHDGA would be degraded at a dose of 1 MGy. Therefore, to suppress the degradation and ensure long use, MA adsorbed on the column would be eluted immediately after adsorption.

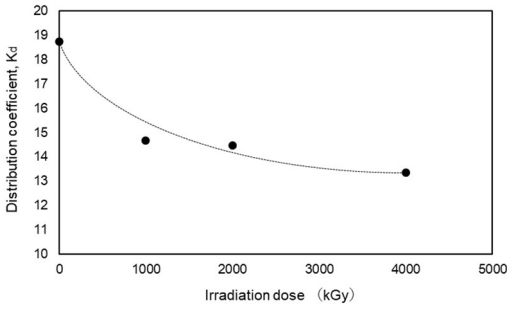

Fig. 2 Distribution coefficients of the TEHDGA adsorbent with respect to the irradiation dose

Acknowledgements

This work was carried out as a part of the research project "Basic Research Programs of Vitrification Technology for Waste Volume Reduction (JPJ010599)", commissioned by the Ministry of Economy, Trade and Industry (METI), in FY2022.

References

[1] Y. Horiuchi et al., *J. Radioanal. Nucl. Chem.* **330**, 237-244 (2021).
DOI: https://doi.org/10.1007/s10967-021-07940-4

[2] T. Akuzawa et al., *J. Radioanal. Nucl. Chem.* **331**, 5851-5858 (2022).
DOI: https://doi.org/10.1007/s10967-022-08658-7

2 - 24 Ion beam induced luminescence measurements of porous silica adsorbents containing europium complexes by argon ion beam irradiation

M. Nakahara[a)], S. Watanabe[a)], T. Yuyama[b)], T. Ishizaka[b)], Y. Yuri[b)], Y. Ishii[b)], R. Yamagata[b)], N. Yamada[c)], M. Koka[c)], W. Kada[d)] and N. Hagura[e)]

[a)]Nuclear Fuel Cycle Engineering Laboratories, JAEA
[b)]Department of Advanced Quantum Beam Technology, QST
[c)]Beam Operation Co., Ltd.
[d)]Faculty of Science and Technology, Gunma University
[e)]Faculty of Science and Engineering, Tokyo City University

Introduction

In the study on radioactive waste treatment, trivalent minor actinides (MA) such as Am and Cm have been attempted to be recovered in high-level radioactive liquid waste in a solvent extraction and an extraction chromatography methods after U, Pu, and Np are recovered from dissolver solutions derived from irradiated nuclear fuels [1]. In these methods, an extractant is used to extract MA from high-level radioactive liquid waste. MA forms complexes with the extractant and is extracted into an organic phase. Various extractants have been developed to recover MA from high-level radioactive liquid waste efficiently in the world. It is important to understand the structures of MA complexes with extractant for separating and recovering MA efficiently. Recently, the structures of complexes have been generally evaluated using X-ray absorption fine structure and quantum chemical calculation. On the other hand, our research group has tried to evaluate the structure of complexes with ion beam induced luminescence (IBIL) analysis [2]. In this study, the IBIL measurements were performed in Takasaki Ion Accelerators Radiation Application (TIARA), QST.

Experimental

To extract MA from high-level liquid waste, bis(2-ethylhexyl) hydrogen phosphate (HDEHP) was synthesized [3]. In the experiments, HDEHP was used as an extractant, and an adsorbent used for the extraction chromatography method was prepared as measuring samples for the IBIL spectra. Styrene-divinylbenzene copolymer-coated porous SiO_2 particles (SiO_2-P) were impregnated with HDEHP solvent. In the experiments, Eu was selected as simulated material of MA. This is because Eu exhibits similar behavior to trivalent MA in the solvent extraction and the extraction chromatography processes. $Eu(NO_3)_3 \cdot 6H_2O$ powder was dissolved to a HNO_3 solution, and Eu nitrate solution was mixed with the HDEHP/SiO_2-P adsorbent to adsorb Eu into the HDEHP/SiO_2 adsorbent. A 107 MeV Ar^{8+} ion beam was derived from the beam line for large-area uniform irradiation at an azimuthally varying field cyclotron for the IBIL measurements. The IBIL spectra of Eu complexes in the adsorbent were measured with 1 s of exposure time.

Results and Discussion

Fig. 1 shows the IBIL spectra of Eu complexes in the HDEHP/SiO_2 adsorbent [4]. The IBIL measurements repeated five times at intervals of 5 s. Some peaks were observed due to the Eu transition in the complexes [5]. The dominant peak was observed at 592 nm assigned to the $^5D_0 \rightarrow {}^7F_1$ transition. Two peaks were present at 610–617 nm due to the $^5D_0 \rightarrow {}^7F_2$ transition. The weak peaks were confirmed at 653 nm assigned to the $^5D_0 \rightarrow {}^7F_3$ transition and 685-703 nm assigned to the $^5D_0 \rightarrow {}^7F_4$ transition. The intensity of all peaks decreased with increasing the measurement cycle number. It is reported that polymer network is damaged due to the radiation [6]. The phenomenon would be caused by breaking the chemical bond of Eu complexes in the adsorbent by Ar^{8+} ion beam irradiation.

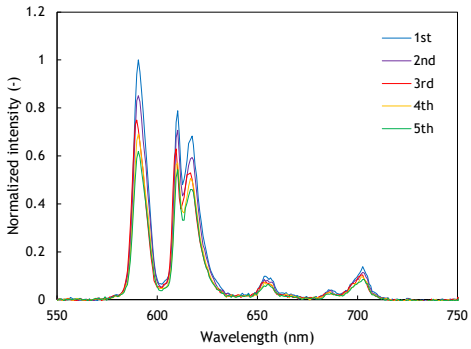

Fig. 1 IBIL spectra of Eu complexes in HDEHP/SiO_2 adsorbent

References

[1] P. Baron *et al.*, Prog. Nucl. Energy **117**, 103091 (2019).
[2] S. Watanabe *et al.*, Nucl. Instrum. Methods Phys. Res. B **477**, 60 (2020).
[3] B. Weaver *et al.*, ORNL-3559 (1964).
[4] M. Nakahara *et al.*, Nucl. Instrum. Methods Phys. Res. B **542**, 144 (2023).
[5] K. Binnemans, Coord. Chem. Rev., **295**, 1 (2015).
[6] A. Quaranta *et al.*, Nucl. Instrum. Methods Phys. Res. B **191**, 680 (2002).

2 - 25 Thermodynamic evaluation of Ti1-xAlxN thin film growth on monocrystalline AlN by reactive CVD

Y. Kasukabe [a), b)], H. Shimoda [b)] and S. Yamamoto [c)]

[a)] Global Learning Center, Tohoku University,
[b)] Department of Metallurgy, Tohoku University,
[c)] Department of Advanced Functional Materials Research, QST

Introduction

Films of $Ti_{1-x}Al_xN$ have been known as the material which exhibits superior mechanical and thermal properties, and those are widely used as coatings for industrial applications such as cutting tools. Irrespective of those attracting performance, little is studied on the growth mechanism as well as the chemical process. In this work, $Ti_{1-x}Al_xN$ thin films have been prepared by reactive Chemical Vapor Deposition (CVD) and analyzed by Field Emission Gun Scanning Electron Microscopy (FEG-SEM), Transmitting Electron Microscope (TEM) [1], and X-ray Diffraction (XRD).

Experimental

Films of $Ti_{1-x}Al_xN$ have been grown by use of the titanium tetra chloride, $TiCl_4$, and c-plane (0001) monocrystalline hexagonal aluminum nitride, AlN, precursors [2]. The AlN has been prepared at 1500°C with the gas mixture of NH_3 and $AlCl_3$ on c-plane (0001) monocrystalline hexagonal sapphire. During the $Ti_{1-x}Al_xN$ growth, hydrogen (H_2) gas is used as carrier gas of $TiCl_4$. The growth has been performed on the 100-nm-thick monocrystalline AlN on sapphire.

Results and Discussion

As a result of analyzing the compound grown by reactive CVD method by using TEM, FEG-SEM and XRD, it was revealed that H_2 carrier gas promotes the growth of $Ti_{1-x}Al_xN$ film, and that more H_2 carrier gas leads to the growth of of Ti-rich $Ti_{1-x}Al_xN$ films. In order to evaluate the composition of the $Ti_{1-x}Al_xN$ non-stoichiometric compound grown by introducing $TiCl_4$ gas using H_2 carrier gas onto a monocrystalline AlN substrate at 1200 °C, a thermodynamically phase diagram was simulated at 0.01 atm and 1200°C for the AlN-$TiCl_4$-H_2 ternary system as shown in Fig. 1. This simulation was calculated in a closed equilibrium state, and the actual experiment was performed in an open system with a gas flow rate. Therefore, it is considered that there is a large amount of H_2 in the vicinity of the AlN substrate surface compared to $TiCl_4$ and AlN, and the H_2-rich state shown in Fig. 1 is realized, which leads to the growth of $Ti_{1-x}Al_xN$ films. The affinity of N for Ti is stronger than that of N for Al, and in the initial stage of the reaction, TiN non-stoichiometric compounds are preferentially formed on the AlN substrate, and then Al is incorporated into the TiN non-stoichiometric compounds by the diffusion. Therefore, Al atoms of the AlN substrate are classified into those that eventually become $Ti_{1-x}Al_xN$ and those that become gases such as aluminum chlorides ($AlCl_3$, $AlCl_2$, AlCl) and leave the substrate. Fig. 2 indicates the thermodynamic simulation showing the relationship between the amounts of H_2 gas and the content of Al in $Ti_{1-x}Al_xN$ at the condition of temperature at 1200°C with 1 mol AlN and 1 mol TiCl4 in the atmosphere at 0.01 atm. This thermodynamic simulation revealed that much amounts of H_2 gas in this system produces more Al gas compounds such as AlCl and AlH. It can be concluded from thermodynamic simulations that H_2 carrier gas produces the atmosphere in which Al is likely to be vaporized, leading to decrease the content of Al in $Ti_{1-x}Al_xN$.

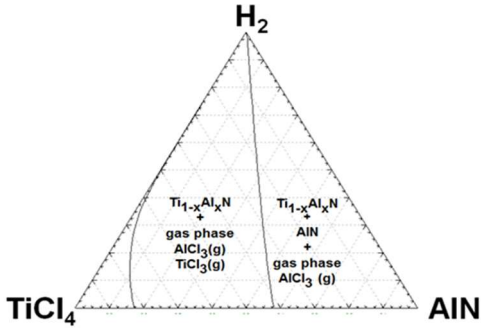

Fig. 1. AlN-$TiCl_4$-H_2 ternary phase diagram simulated at 1200°Cat 0.01 atm. Note that $Ti_{1-x}AlxN$ lattice structure is cubic system, and AlN is hexagonal system. Main compounds existing in the gas phase are noted.

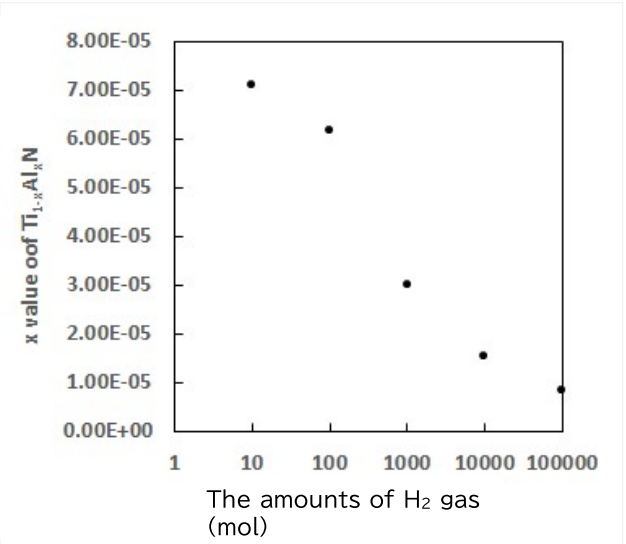

.Fig. 2. The relationship between the amounts of H_2 gas and the content of Al in $Ti_{1-x}Al_xN$ calculated by thermodynamic simulation.

References

[1] H. Abe et al., JAERI-Research 96-047 (1996) 1.
[2] R. Boichot *et al*., Surf. Coat. Technol. 205 (2010) 1294.

2 - 26 γ-ray irradiation effect on ammonia radical derived from hydrothermally altered potassium feldspar: A physical basis for the application to fault dating

T. Fukuchi

Faculty of Education, Graduate Faculty of interdisciplinary Research, Univeristy of Yamanashi

Introduction

For the purpose of earthquake disaster prevention, it is important to determine the absolute ages of unrecognized active faults and to assess their fault activity during the Quaternary period. The ESR (electron spin resonance) dating technique is available in estimating the absolute age of fault movement using radical centers derived from hydrothermally altered minerals subjected to frictional heat by faulting [1]. Previous studies showed that the Mo quartet signals with the signal intensity ratio of 1:3:3:1, which are often detected from montmorillonite and are applicable to fault dating [2], were detected from the hydrothermally altered potash feldspar (orthoclase) in natural fractured granite [3]. The formation mechanism of the Mo quartet signals has not been yet clarified.

Experimental

I carried out hydrothermal reaction experiments (for 2 weeks at 250°C) under pure H_2O and an aqueous solution of 10%NH_4Cl (pH4.7) , using the powder sample of fresh potash feldspar extracted from the fractured granite at the Hakushu fault outcrop of the Itoigawa-Shizuoka Tectonic Line Active Fault System. The hydrothermal reaction samples were irradiated with ^{60}Co sources in the γ-ray irradiation facilities (No.1 bld., No.1 cell and Food irrad., No.2 cell), and measured by an ESR spectrometer (JEOL RE-3X) in Yamanashi University.

Results and Discussion

According to the ESR spectra obtained from the hydrothermal reaction samples after γ-ray irradiation, the quartet signals with the signal intensity ratio of 1:3:3:1 are not detected from the natural sample (Fig.1A) and the hydrothermal reaction sample under pure H_2O (Fig.1B), but from that under an aqueous solution of 10%NH_4Cl (Fig.1C). The signal at g=1.997 in the spectra of Figs.1A and 1B is derived from the Ge center in quartz [1], which is included as an impurity in the potash feldspar samples.

ESR analyses indicate that the quartet signals (A, B, C and D signals) have the same g-values and hyperfine splitting parameters (A=2.4mT) as the Mo quartet signals and are attributed to the ammonia ($\cdot NH_3^+$) radical. Since hydrothermal reactions involving NH_4^+ ions may lead to the substitution of K^+ or Na^+ ions in potash feldspar with NH_4^+ ions, γ-ray irradiation may result in the knock-on of H atoms in the substituted NH_4^+ ions and then generate the $\cdot NH_3^+$ radical. The quartet signals regularly increase with increasing radiation dose, so that they are applicable to the dating of hydrothermal alteration associated with faulting.

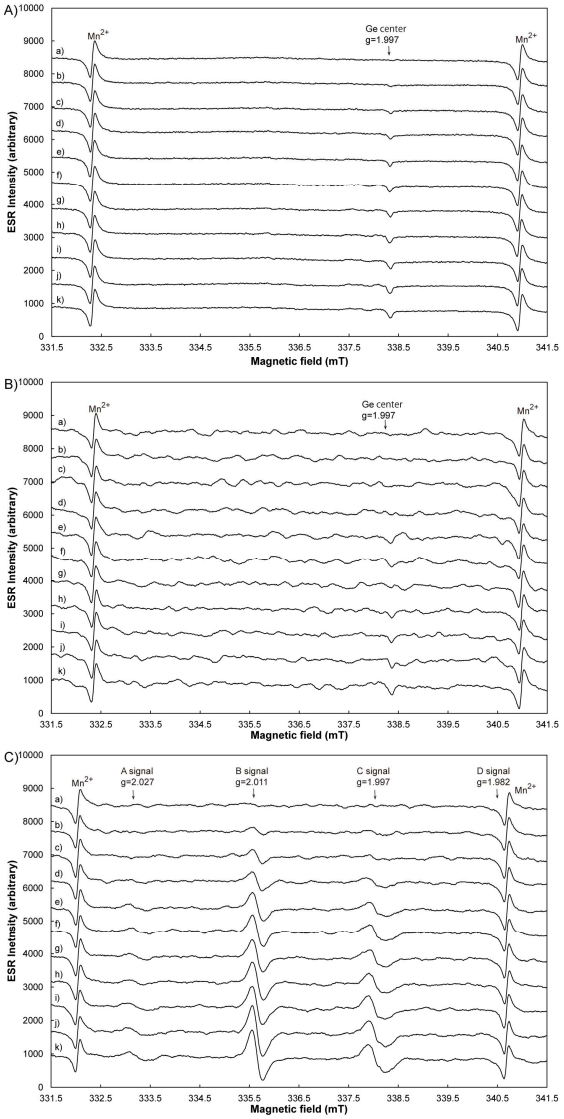

Fig. 1 γ-ray irradiation effect on radical centers detected from the natural and hydrothermal reaction samples. A) natural potash feldspar, B) hydrothermal reaction sample under pure H_2O, C) hydrothermal reaction sample under an aqueous solution of 10%NH_4Cl. The ESR spectra were measured at a microwave power of 1 mW under room temperature (20°C). The irradiation dose rate is 277.8 Gy/h (A &B) and 312.8 Gy/h (C). Irradiation time: a) 0h, b) 1h, c) 2h, d) 3h, e) 4h, f) 5h, g) 6h, h) 7h, i) 8h, j) 9h, k) 10h

References

[1] T. Fukuchi, Radioisotopes, **70**, 131 (2021). Doi: 10.3769/radioisotopes.70.131

[2] T. Fukuchi, Jpn. J. Appl. Phys., **35**, 1977 (1996).

[3] T. Fukuchi, QST Takasaki Annual Report 2020, **1-41**, 66 (2022).

2 - 27 Oxidative coupling reaction between diamine and naphthol (Nadi reaction) for visualization of γ irradiation

T. Tachikawa and M. Yoshioka

Faculty of Engineering, Graduate School of Science and Engineering, Saitama University

Introduction

The color formers have been developed [1-2] to visually detect radiation that is harmful to the human body but cannot be detected by the human senses. In this study, the dye formation by oxidative coupling between diamines and naphthols (Nadi reaction), which has been applied to the detection of hydrogen peroxide, was applied to the visualization of γ-ray irradiation. This paper presents the coloration of aqueous solutions of 1 as phenylenediamine and 2 as naphthol after γ-ray irradiation.

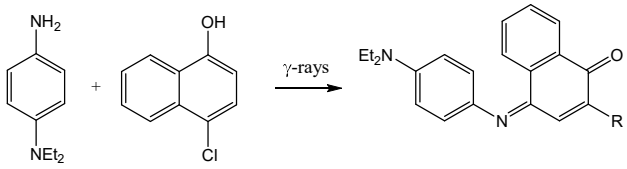

1 2 3

Scheme 1. Reaction of diamine 1 and naphthol 2 to produce dye 3

Results and Discussion

In oxidative coupling reactions, diamines are oxidized to quinodiimines, and the quinodiimines (QDI) attack the aromatic rings electrophilically to form dyes, so the reaction rate depends on the pH of the solution. In the reaction of naphthols, the basicity of the solution increases the rate of electrophilic substitution reaction for the naphthol becomes the naphthoxide ion. The neutral aqueous solution ($[\mathbf{1}]_0$ = 0.72 mM, $[\mathbf{2}]_0$ = 0.32 mM, $[POD]_0$ = 0.40 μM), and the basic aqueous solution solution ($[\mathbf{1}]_0$ = 0.72 mM, $[\mathbf{2}]_0$ = 0.32 mM, $[POD]_0$ = 0.40 μM, $[NaHCO_3]_0$ = 0.32 mM) of the color former was prepared and hydrogen peroxcide ($[H_2O_2]_0$ = 100 μM) was added to the solutions. As a result, in the neutral aqueous solution, **1** was oxidized to QDI immediately after the addition, and the solution turned red (Fig. 1), but in this solution, the coupling reaction between GDI and **2** was slow, so little dye **3** was produced and the solution turned pale blue.

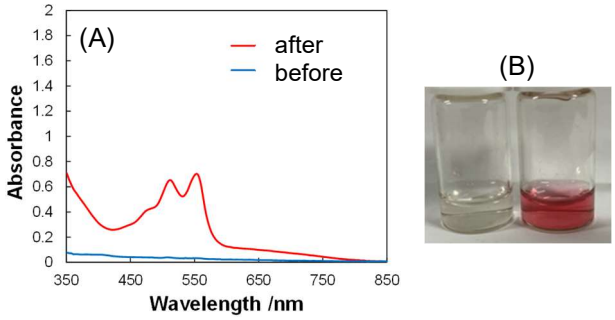

Fig. 1. Spectral change (A) and color changing image (B) of colorformer aqueous solution before and after H_2O_2 addition .

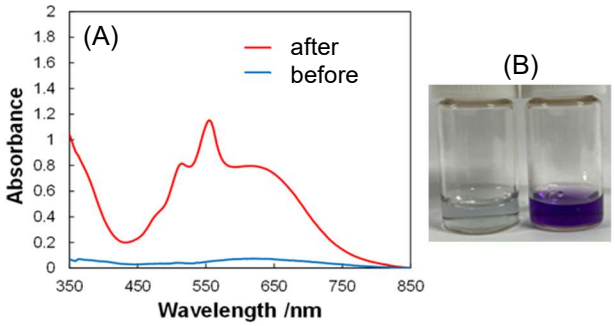

Fig. 2. Spectral change (A) and color changing image (B) of colorformer basic aqueous solution before and after H_2O_2 addition .

For the solution made weakly basic with sodium bicarbonate, the coupling reaction by hydrogen peroxide proceeded quickly and the solution turned dark blue (Fig. 2). The aqueous basic solution of **1** and **2** were prepared and irradiated with 10-70 Gy of γ-rays at a dose rate of 100 Gy/h at the γ irradiation facility at QST.

The basic aqueous solutions of **1** and **2** developed a blue color from irradiation with 10 Gy of γ-rays, and the absorption of the dye **3** was observed in the spectra (Fig. 3).

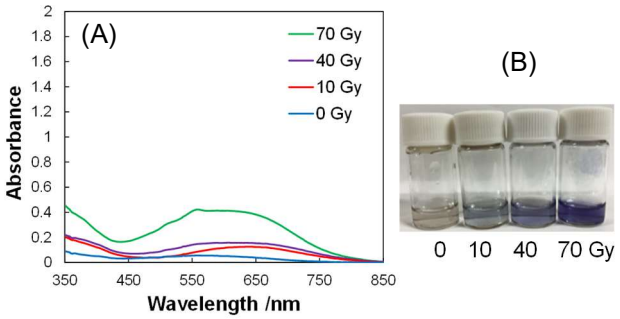

Fig. 3. Spectral change (A) and color changing image (B) of colorformer basic aqueous solution before and after γ irradiation.

The Gel dosimeters containing **1** and **2** will be prepared and irradiated with carbon ion beams in the same way as the phenoxazine-type color former [3].

References

[1] H. Itoi, *et. al.,* Chem. Lett., **38**, 1002 (2009). DOI: 10.1246/cl.2009.1002

[2] T. Tachikawa, *et. al.,* Isotope News, **731**, 7(2015).

[3] T. Tachikawa and K Yamada, QST Takasaki Annual Report 2021, 66, (2022).

Part Ⅱ

3. Life Science

3 - 01 Development of user interface for defining targeting areas for microbeam paint irradiation of individual organs

T. Funayama and M. Suzuki

Department of Quantum-Applied Biosciences, QST

Heavy ion microbeam irradiation technologies for biological samples have been developed at TIARA, QST-Takasaki. The developed technology is now being used to elucidate the effects of heavy ion irradiation on cells and the mechanisms of biological response to localized irradiation of individual organisms [1].

We have succeeded in developing heavy-ion microbeam irradiation technologies that use very small beam spots of a focused microbeam device to target specific locations in cells and specific cells in the nematode *Caenorhabditis elegans* [2]. In addition, we are developing a technology that allows us to irradiate specific organs of individual organisms [3]. Using this technology, we are delivering localized heavy ion irradiation to specific organs of *C. elegans* and elucidating their responses to irradiation.

The development of microbeam paint irradiation technology required the development of features that did not need to be developed in conventional microbeam targeted irradiation techniques. Until now, irradiation using microbeams has been carried out by delivering ions precisely to a single point specified at a specific coordinate on the target sample to be irradiated. On the other hand, paint irradiation, in which the specified area is uniformly irradiated by beam spot scanning, requires a user interface to select and specify the area to be irradiated on the observed image of the target viewed under a microscope. Conventional microbeam devices do not require the ability to specify an area, because it has been sufficient to specify a point to be irradiated. Therefore, it does not have such a function. Thus, we incorporated a user interface for specifying an irradiating region into the irradiation control software, and developed a function to execute localized irradiation smoothly to the individual organ observed under a microscope.

Fig. 1a shows how the terminal bulb region of the pharynx for chewing and swallowing in *C. elegans* was selected using the developed user interface. By selecting a point along the contour of the area to be irradiated in the microscopic image with a mouse click, the user can specify a region surrounded by a curve that smoothly connects the specified points. When the contour is closed and the area is specified, the area on the image is filled by blue color, so that the irradiated area can be clearly identified as it will be paint-irradiated (Fig. 1b). Paint irradiation of individual organs is implemented by specifying the coordinates of each ion destination and scanning the beam spot so that the number of ions corresponding to the dose to be irradiated is uniformly distributed within this specified area. This interface allows the user to select multiple regions for a single microscopic image and to deliver different doses to each of the specified regions. Localized irradiation with focused microbeams using this paint irradiation technique made it possible to analyze how each tissue of the pharynx is involved in the pumping motion of chewing and swallowing in *C. elegans*.

In the future, we intend to develop more efficient microbeam targeting technology, such as automatic recognition of the individual organs to be irradiated, by utilizing machine learning technology.

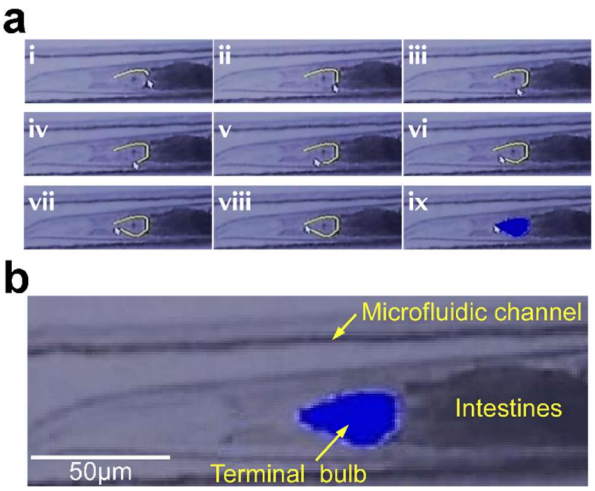

Fig. 1 Animated captured images of selecting operation of targeted area of the pharynx in *C. elegans*. **a.** Example of the situation during the target area selection operation. The view during the selection of the terminal bulb shown in Fig. 6a. Clicking with the mouse draws the boundaries of the target area (indicated by a yellow line) and fills in the interior with blue after the target area is selected. The drawing of each mouse click was captured from a video of the target area selection process from behind. **b.** The targeted area selected (blue). Only the terminal bulb is selected.

Acknowledgments

We thank the Caenorhabditis Genetic Center of the Univ. of Minnesota for providing strains of *C. elegans*. This work was carried out in part with a JSPS KAKENHI (JP21K12247) to T.F. and the 61th research grant from the radiation effects association to M.S.

References

[1] T. Funayama, Quantum Beam Sci. **3**, 13 (2019). DOI: 10.3390/qubs3020013

[2] T. Funayama *et al*., Nucl. Instr. Meth. Phys. Res. B. **465**, 101 (2020). DOI: 10.1016/j.nimb.2019.12.028

[3] T. Funayama *et al*., QST Takasaki Annu. Rep. 2021, **QST-M-39** 74 (2022).

3 - 02 Optimization of the depth-controlled irradiation for silkworm eggs at the cleavage stage

N. Miyasaka[a)], T. Funayama[b)], M. Suzuki[b)] and K. Shirai[a)]

[a)] Faculity of Textile Science and Technology, Shinshu University
[b)] Department of Quantum-Applied Biosciences, QST

Introduction

Checkpoint systems of animal eggs at early development are considered to be absent or incomplete. Therefore, the development of early embryos usually continues even if the genome DNA is damaged. However, we have reported a dose-dependent developmental arrest of the silkworm (Bombyx mori) eggs at the cleavage stage by heavy ion irradiation. These results indicate that the silkworm eggs at early development have the mechanisms for developmental arrest by checkpoints.

During the cleavage stage (until about 12 hours after oviposition), the silkworm egg is a polynuclear cell (syncytium). We observed that the developmental arrest of the egg at the cleavage stage is probably determined by the ratio of damaged and normal nuclei by targeted irradiation experiments using the HZ1 port. The mechanism of cell cycle arrest in syncytium during early development will provide significant knowledge about the developmental mechanisms during the early development of insect eggs. However, the targeted irradiation using the microbeam of the HZ1 port cannot process many eggs. Last year, we attempted to construct an irradiation method by depth-controlled irradiation by HY-1 port using stacked Mylar films. As a result, we revealed that depth-controlled irradiation for the silkworm eggs at the cleavage stage (8 hours after oviposition) was possible by shielding them with a thickness of 200 μm to 300 μm of the stacked Mylar films.

In the studies, we optimized the depth-controlled irradiation with heavy ions to half of the nuclei of silkworm egg at 8 hours after oviposition.

Experimental

The silkworm (*Bombyx mori)* strain used in the experiments was the non-diapause strain, N4. The silkworm eggs were collected and irradiated with 100 Gy of carbon ions ($^{12}C^{6+}$, 190 MeV, HY1 port) 8 hours after oviposition. The optimization of depth-controlled irradiation using stacked mylar films was carried out by varying the thickness in 25 μm increments with a thickness of 200 μm to 300 μm. The irradiated eggs were incubated at 25°C, then some of the eggs were fixed by Carnoy's solution at 4 hours after irradiation, and the effects of irradiation were observed. Two weeks after oviposition, the unhatched eggs were fixed in hot water, and then the eggshells were removed for morphological observation of unhatched embryos.

Results and Discussion

Depth-controlled irradiation was performed on silkworm eggs 8 hours after oviposition using Mylar films varying in thickness from 200 μm to 300 μm in 25 μm increments. Last year, we revealed that the effects of irradiation only appeared on some nuclei by shielding with 300 μm thickness. In the eggs with irradiation shielding with a 200 μm thick film, all nuclei are irradiated and cannot develop. However, with 225 μm thick shielding, some nuclei on the non-irradiated side were spared from irradiation, and cellularization of the nuclei was observed at the blastula stage (Figure 1A). These cells ultimately formed part of the unhatched larva (Fig. 2A). The experiment with 250 μm shielding revealed the effect of irradiation, even on the non-irradiated side of the egg, then failure to form thoracic limbs in lethal embryos (data not shown). It was predicted that more than half of the nuclei would be abnormal on this irradiation condition. In the egg with irradiation using 275-μm shielding, cellularization by some normal nuclei was confirmed on the irradiated side (Figure 1B), and thoracic legs were formed on the only half side of the unhatched larva (Figure 2B).

The results revealed that irradiation using 225 - 275 μm of thickness film was optimal for the silkworm egg.

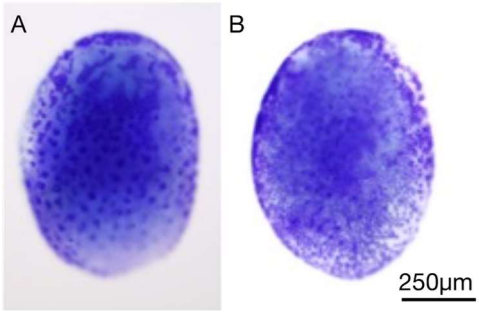

Fig. 1 The irradiated egg at the cellular blastoderm stage (irradiation side).

The egg shielding with Mylar films was irradiated with carbon ions at the cleavage stage. A: irradiation with 225 μm of film. The nuclei at the side are abnormal. B: irradiation with 275 μm of film. Some nuclei seemed to be non-damaged.

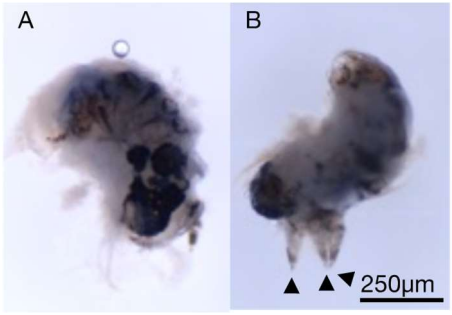

Fig. 2 Unhatched larva that developed from the egg irradiated with depth control.

A : Unhatched larva of the irradiated egg shielded with 225 μm of film. The larva has only part of its body formed.

B: Unhatched larva of the irradiated egg shielded with 275 μm of film. The larva has three thoracic legs (arrowhead), and over half of the body has formed.

3 - 03 Microbeam and immune cell-labeled transgenic medaka are promissive combination to investigate the early processes of inflammation

S. Oda[a], M. Suzuki[b] and T. Funayama[b]

[a]Department of Integrated Biosciences, The University of Tokyo
[b]Department of Quantum-Applied Biosciences, QST

In tissues undergoing inflammation, neutrophils and macrophages are activated and migrate from blood vessels to the interstitial spaces. They phagocytize bacteria that have invaded from the outside and necrotic cells, defending the tissues. Inflammatory responses can be divided into acute inflammation, which promptly resolves, and chronic inflammation, which persists for an extended period. Investigation of the behavior of immune cells such as neutrophils and macrophages is crucial for understanding the mechanisms and developing treatment strategies for inflammation.

In brain tissue protected by blood-brain barrier, microglia is the main residential immune cell, of which main function is the phagocytosis and removal of damaged cells. We have been using the microbeam device in Ion Irradiation Research Facility (Takasaki Ion Accelerators for Advanced Radiation Application ; TIARA) at QST Takasaki Advanced Radiation Research Institute to selectively irradiate a portion of medaka embryo brains and have investigated the radiation responses of microglia.

Gamma-ray irradiation induces apoptosis cell death in the midbrain (optic tectum) of medaka embryo, where microglia express apolipoprotein E (apoeb) and phagocytize apoptotic bodies to repair damaged brain tissue (Yasuda et al., 2015). In our laboratory, the transgenic medaka, SK2-TG(pApoEb-Kaede), that express a fluorescent protein (Kaede) under the control of the apoeb promoter was generated and the dynamics of microglia following radiation exposure was successfully visualized (Peh, 2019).

On the other hand, the microbeam device installed in TIARA enabled us to irradiate collimated carbon-ion microbeams into the area of 70 μm in diameter (Funayama te al., 2008; Yasuda et al., 2020). We found that the carbon ion microbeam irradiation induced cell damage only in the irradiated area, when right lobe of optic tectum (OT) of 3 days post-fertilization embryo was irradiated with the microbeam, and only microglia present in the irradiated area were activated. On the 2nd day, activated microglia were present also in the left lobe of OT and activation of microglia continued through several days after the irradiation (Yasuda et al., 2017), suggesting a process of enhancement of microglial activation. Furthermore, gamma-ray irradiation markedly suppresses the induction of apoptotic cell death, but activates almost as many microglia as the wild type in the tp53 deficient medaka embryo, indicating a dynamic response of microglia to irradiation (Yasuda et al., 2015).

Conventionally, inflammatory tissues are chemically fixed and tissue sections are prepared to investigate the behavior of immune cells, such as neutrophils, macrophages, and microglia, by immunostaining using antibodies specific for each immune cells. However, this method analyzes the inflammatory response at a certain moment in time, and it is very difficult to elucidate the time course of a dynamically changing inflammatory response. In this study, we have visualized the behavior of microglia in live medaka embryos by restricted irradiation with the microbeam onto transgenic medaka embryo expressing fluorescent protein in microglia, and are confirming the findings in the histological analysis described above. The combination of microbeam irradiation and live imaging of microglia in transgenic medaka is a powerful method to elucidate the early inflammatory response exhibited by immune cells: how inflammation is initiated and how it develops, and the dynamics of the inflammatory response.

The medaka strain (SK2), that we employed to develop the transgenic medaka, lacks pigmentation due to multiple mutations, making it highly suitable for live imaging. This strain exhibits a remarkably high transparency even in adult fish (Fukamachi et al., 2008), and it is expected to accelerate research in adult fish, where conventional live imaging has been previously challenging.

Acknowledgments

We thank the crew of the cyclotron of TIARA at QST-Takasaki for their kind support for providing fine beams.

References

[1] T. Yasuda et al., PLoS One **10**, e0127325 (2015). DOI: 10.1371/journal.pone.0127325
[2] A. C. G. Peh, Master thesis, Univ. Tokyo (2019).
[3] T. Funayama et al., JRR. **49**, 71 (2008). DOI: 10.1534/genetics.107.073387
[4] T. Yasuda et al., biology **9**, 447 (2020). DOI: 10.3390/biology9120447
[5] T. Yasuda et al., Int J Mol Sci. **18**, 1428 (2017). DOI: 10.3390/ijms18071428
[6] S. Fukamachi et al., Genetics **178**, 761 (2008). DOI: 10.1269/jrr.07085

3 - 04 Effect of plant residue extracted components on DNA damage induced by heavy ion beam

T. Suzuki[a)], T. Oizumi[a)], T. Funayama[b)], and A. J. Nakamura[a)]

[a)]College of Science, Ibaraki University
[b)]Department of Quantum-Applied Biosciences, QST

Introduction

Radiation exposure is a growing concern in today's society as the opportunities for radiation use increase. For example, radiation therapy, which is effective in cancer treatment, affects not only cancer but also normal tissue, resulting in radiation damage such as fatigue, loss of appetite, and dermatitis [1]. For this reason, many studies have been conducted on antioxidants to reduce radiation damage. Still, few of them have actually been applied in clinical practice due to their strong side effects on the living body [2]. Therefore, there is a need for new radioprotective agents that have fewer side effects and can reduce health risks due to radiation. This study investigated the radioprotective effects of two plant residue extracts with antioxidant properties.

Experimental

Two types of plant residue extracted components were used: ① and ②. ① is an ethanol-extracted component of a certain plant, which contains various polyphenols. ② is a flavonoid contained in citrus fruits. TIG-3 (human fetal lung fiber cells) were irradiated with helium ion (63 MeV, 13.2 KeV/μm) or carbon ion beams (190 MeV, 124 KeV/μm) at TIARA. Extracted components were treated before 1 hour of irradiation. To evaluate the level of DNA double strand break (DSB) after irradiation, immunofluorescence staining for phosphorylated H2AX (γ-H2AX), a known DSB marker, was performed. In independent experiments, the level of DSB was quantified by counting γ-H2AX focuses in 100 cells and calculating the Mean number of γ-H2AX foci per cell.

Results and Discussion

At 1 hour after helium ion beam irradiation, both extracted components showed a decrease in DSB levels of about 14% compared to DMSO treatment, indicating a significant DSB suppression effect (Fig. 1). At 1 hour after carbon ion beam irradiation, the DSB levels showed a decrease of about 7% in treatment ① and about 9% in treatment ② compared to DMSO treatment, but the difference was not significant (Fig. 1).

The LET of helium ion beam was about 1/10 lower than that of carbon ion beam, suggesting that helium ion beam have a larger contribution from indirect effects. Therefore, the decrease in DSB at 1 hour after helium ion beam irradiation may be attributed to the suppression of the indirect effect by the antioxidant effect of the extracted components. It has been reported that a large γ-H2AX focus is detected in heavy particle beams with relatively high LET, such as carbon ion beam, in which multiple DSBs can be closely produced [3]. This suggests that a significant decrease in slight DSBs may not be detectable by immunofluorescence staining of γ-H2AX.

These results of this study indicate that both of the plant residue-extracted components can suppress the generation of DSBs by heavy ion beam. These components may be used as effective radioprotective agents against exposure to heavy particle radiation used in radiotherapy.

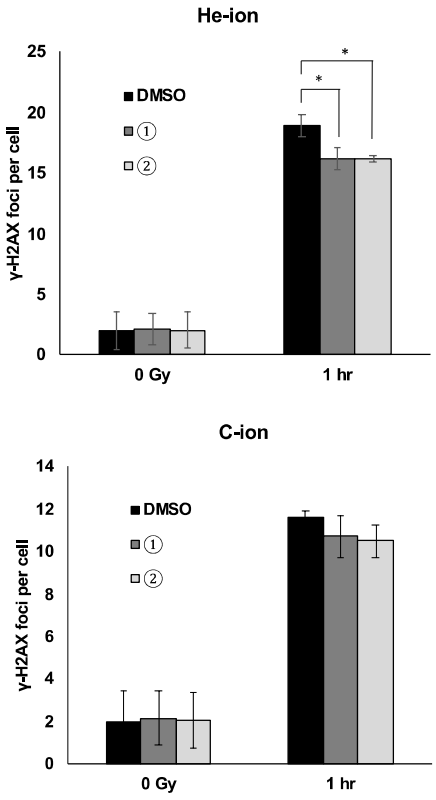

Fig. 1. Mean number of γ-H2AX foci per cell after radiation exposure.TIG-3 cells were exposed to C-ion (1 Gy) or He-ion (1 Gy), and then fixed at 1hr post irradiation. Treatment of the natural components was performed 1 hour prior to irradiation. 100 cells were counted. (error bars: S.D., n=3, student`s t-test; * = p<0.05)

References

[1] L Barazzuol et al., Mol. Oncol. **14**, 1427 (2020) DOI:10.1002/1878-0261.12750

[2] C Soref *et al.*, Int. J. Radiat. Oncol. Biol. Phys. **82**, e701 (2012) DOI:10.1016/j.ijrobp.2011.11.038.

[3] Y Hagiwara et al., J. Radiat. Res. **60**, 69 (2019) DOI:10.1093/jrr/rry096

3 - 05 Bystander effects through gap-junction-mediated cell-to-cell communication between carbon-ion irradiated tumor cells and unirradiated normal cells

M. Suzuki [a)], T. Funayama[b)] and M. Suzuki[b)]

[a)]Department of Charged Particle Therapy, QST
[b)]Department of Quantum-Applied Biosciences, QST

Introduction

We so far have been studying biological cellular effects between the single human cell line with the same origin through gap-junction-mediated cell-to-cell communication or secreted factor(s) from the irradiated cells with the heavy-ion microbeams, such as carbon, neon and argon ions [1]. The results suggested that the bystander cellular effects for cell killing and gene mutation were induced in the same cell system with wild-type *P53* gene, not mutated type *P53* gene.

Communication between heavy-ion irradiated tumor cells and neighboring unirradiated normal cells is one of the major concerns for heavy-ion radiotherapy. This year we examined the bystander cell-killing effect in unirradiated normal human cells affected by carbon-ion irradiated human tumor cells through gap-junction mediated cell-to-cell communication.

Experimental

Human glioblastoma cells (T98G) with mutated type *P53* gene were irradiated with carbon-ion microbeams. Irradiations were carried out by the 256 (16 x 16)-cross-stripe method using Carbon ions ($^{12}C^{6+}$, 190 MeV, 113keV/μm) at the HZ1 port [2]. The beam size was 20 μm in diameter and the irradiation in each point was performed to deliver 7 ions (0.4Gy). Then unirradiated normal human fibroblasts (NB1RGB) with wild-type *P53* gene were co-cultured with the irradiated T98G cells in presence or absence of a gap-junction inhibitor (40 μM of γ-isomer of hexachloro-cyclohexane) using the transwell permeable support system (Fig.1). Cell-killing effect, which was detected a colony-forming assay as a reproductive cell death.

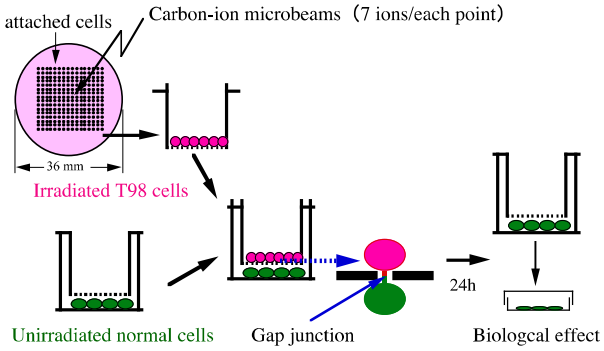

Fig. 1. The co-culture method using the transwell permeable support system for the bystander effect through gap-junction-mediated cell-to-cell communication.

Results and Discussion

Preliminary result was shown in Fig.2. Cell-killing effect was observed in unirradiated co-cultured NB1RGB cells in absence of the inhibitor. However, no biological effect was induced in unirradiated NB1RGB cells in presence of the inhibitor. The results suggested that the bystander cell-killing effect was induced in the unirradiated normal cells being located close to direct irradiated tumor cells through gap-junction-mediated cell-to-cell communication.

We previously reported that the medium from the 220MeV-$^{12}C^{5+}$-ion-microbeam irradiated tumor cells enabled to induce damage in the neighboring unirradiated normal cells through the bystander effect mediated by secreted factor(s), which were scavenged by the ascorbic acid [3]. The present data is consistent with the result, which was induced by the bystander effect through secreted factor(s), and is suggested that the neighboring unirradiated normal cells can be affected by the bystander effects from carbon-ion irradiated tumor cells through gap-junction-mediated cell-to-cell communication as well as secreted factor(s). We believe that the observed effect is one of the important biological effects for highly developing of heavy-ion radiotherapy.

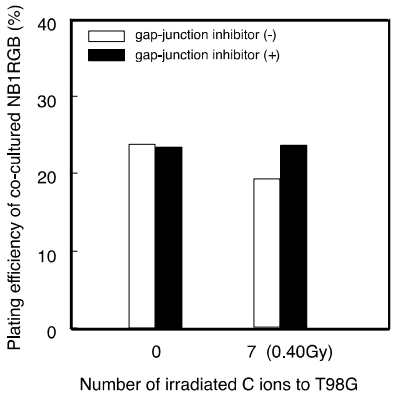

Fig. 2. Bystander cell-killing effect through gap-junction-mediated cell-to-cell communication between 190MeV-$^{12}C^{6+}$-ion-microbeam irradiated tumor cells and unirradiated normal cells.

References

[1] M. Suzuki *et al.*, *J Radiat Res*, (2023). DOI:10.1093/jrr/rrad059.
[2] M. Suzuki *et al.*, JAEA Takasaki Ann. Rep. 2006, **JAEA-Review 2007-060** 107 (2008).
[3] M. Suzuki *et al.*, JAEA Takasaki Ann. Rep. 2018, **QST-M-23** 65 (2018).

3 - 06 Radiosensitivity of cultured canine fibrosarcoma cells to high energy carbon ion beam

T. Funayama[a)], M. Suzuki[a)] and S. Wada[b)]

[a)]Department of Quantum-Applied Biosciences, QST
[b)]School of Veterinary Medicine, Kitasato University

Introduction

Cancer in companion animals has become a societal problem because many cases of cancer are detected when it is too late, even though the cancer can be completely cured if detected and treated at an early stage. Radiotherapy using X-rays has been used to treat cancer in companion animals, but the treatment has not been sufficiently effective. In addition, radiotherapy is sometimes used as an ineffective treatment used primarily to relieve pain, and it is often misunderstood that radiotherapy cannot cure cancer in companion animals. Heavy-ion cancer therapy is becoming increasingly popular as an effective treatment for human cancer. On the other hand, the clinical application of heavy ion radiation in companion animals is still unprecedented worldwide. Furthermore, even research on radiosensitivity analysis using cultured cells of companion animals is currently extremely limited [1]. Therefore, as a first step towards the application of heavy ion cancer therapy in companion animals, a quantitative analysis of the radiosensitivity of canine cancer cells was performed using the carbon ion beam of TIARA.

Materials and Methods

Canine fibrosarcoma (cFS) cells were used as the material for this study. In the experiments, exponentially growing cFS cells were treated with trypsin, made into single-cell suspensions, and then diluted and seeded into 60 mm diameter plastic petri dishes. The concentration of the diluted cell suspension was determined based on preliminary experiments so that the number of viable colonies formed in the Petri dish ranged from 10 to 100. Four to six hours after seeding, the cells were irradiated with carbon ion beams using a heavy ion broad beam irradiation system with a HY1 port of the TIARA cyclotron. Two types of carbon ion beams with different energies, 320 MeV and 220 MeV, were used for irradiation. After irradiation, cells were cultured for 14 days for colony formation. The formed colonies were fixed and stained with crystal violet staining solution, observed under a stereomicroscope, and the survival rate of cFS cells for each carbon ion beam was obtained by counting the number of viable colonies consisting of more than 50 cells.

Results and Discussion

The survival curves of cFS cells obtained in the experiment are shown in Figure 1. The linear quadratic curves that fit the obtained data were calculated, and the values of the 10% survival dose (D10) and the relative biological effectiveness (RBE) at D10 for each type of radiation were calculated based on the obtained curves (Table 1). For the calculation of RBE, ^{60}Co gamma irradiation was used as the standard radiation.

The RBE calculated from the 10% survival dose was 4.42 for the 220 MeV carbon ion beam and 3.44 for the 320 MeV carbon ion beam, which was extremely high, confirming that the carbon ion beam has a high cell killing effect on canine fibrosarcoma cells.

Next, we will quantitatively evaluate the radiosensitivity of canine cancer cells other than fibrosarcoma. The results of our research will provide the basis for achieving heavy particle radiotherapy in companion animals.

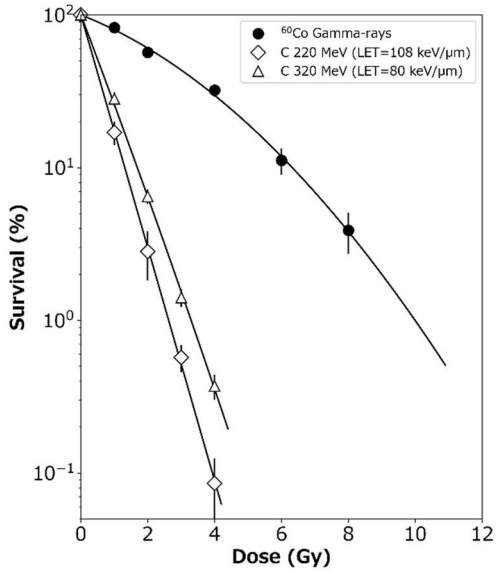

Fig. 1. Survival of canine fibrosarcoma cell to carbon ion beams

Table1. D10 and RBE of cFS cells

Radiation Source	D_{10}	RBE
^{60}Co Gamma-rays	5.81 Gy	1.00
C 220 MeV 108 keV/μm	1.32 Gy	4.42
C 320 MeV 80 keV/μm	1.69 Gy	3.44

Acknowledgement

References

[1] S. Wada *et al.*, J. Vet. Med. Sci. **67**, 1091 (2005). DOI: 10.1292/jvms.67.1089

3 - 07 Induction of cell reprogramming by γ -ray and ion-beam irradiation

N. Gu[a)], M. Suzuki[b)], T. Funayama[b)], Y. Tamada[a)] and A.N. Sakamoto[b)]

[a)]School of Engineering, Utsunomiya University
[b)]Department of Quantum-Applied Biosciences, QST

Introduction

It was known that wounding triggers reprogramming of differentiated plant cells into stem cells. In land plants, the damage or removal of the apical meristem induces the reprogramming of peripheral cells to establish a new stem cell niche. In the moss *Physcomitrium patens*, leaf excision causes differentiated leaf cells to be reprogrammed into stem cells [1]. We have previously shown that applying DNA-damaging reagent such as bleomycin, zeocin or camptothecin to excised leaves enhanced the reprogramming, and transient treatment of the DNA-damaging reagent at critical concentration could trigger the leaf cells reprogrammed into stem cells without wounding [2].

This DNA damage-induced reprograming process was abolished when the DNA-damage checkpoint transducer ATR (ATM and Rad3 related) or the AP2/ERF type transcription factors STEM CELL-INDUCING FACTOR 1 (STEMIN1), STEMIN2, and STEMIN3 were disrupted [2]. These results suggest that DNA strand breaks trigger cellular reprogramming towards stem cells via the activity of ATR and STEMINs.

Since ionizing radiation induces DNA damage, it was expected that irradiation to *P. patens* differentiated tissue induced cell reprogramming. To confirm this expectation, we applied γ-rays and carbon ion beams to wild type plants and analyzed the efficiency of cell reprogramming.

Materials and Methods

P. patens Gransden was used as the wild type. The homogenized protonema tissue was propagated on solid medium at 25 °C under continuous white light to induce gametophores. For γ-irradiation, 3-week-old gametophores were transferred to liquid medium in 35 mm dishes. The gametophores were irradiated with 240-1440 Gy of γ-rays at Co-60 irradiation facility. For ion beam irradiation, the 3-week-old gametophores grown on solid medium were irradiated with 60-480 Gy of $^{12}C^{6+}$ ions (LET: 78 keV/μm) at Takasaki Ion Accelerators for Advanced Radiation Application (TIARA). The images of cell reprograming were captured under a microscope equipped with a CCD camera.

Results and Discussion

To investigate whether γ-ray and ion-beam irradiation can trigger the reprogramming of leaf cells into protonema stem cells, we subjected intact gametophores to γ-ray irradiation across a range of intensities. Notably, at doses between 720 Gy and 1440 Gy, we observed the formation of protonema cells (Fig. 1). However, these γ-ray-induced protonema cells compared to those induced by zeocin treatment, exhibited abnormal shapes and could not sustain continuous growth. These results suggest that both γ-ray irradiation and zeocin treatment are capable of initiating the reprogramming of leaf cells. However, it appears that γ-ray irradiation may cause irreparable damage to the cells, hindering their growth and development.

Regarding ion-beam irradiation, the plants were exposed to doses ranging from 60 Gy to 480 Gy. After two weeks of cultivation, visible cell death was observed in the plants irradiated with 180 Gy and higher doses (Fig. 2). However, no protonema cells emerged from gametophore leaf cells. Similar to γ-ray irradiation and zeocin treatment, it is possible that only a narrow range of ion-beam irradiation doses, that has not yet been tested, can trigger the reprogramming process.

Further experimentation with varying ion-beam irradiation conditions will be necessary in future studies to explore this phenomenon comprehensively.

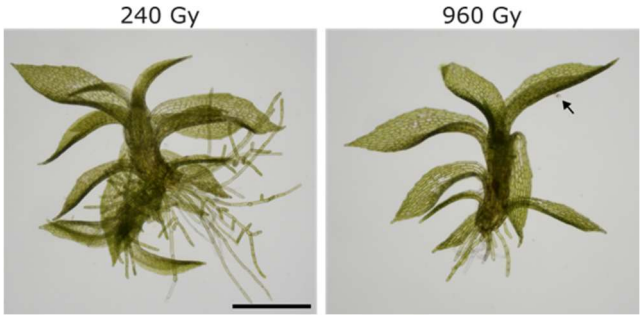

Fig. 1. Reprogramming triggered by γ-irradiation. Bar = 1 mm

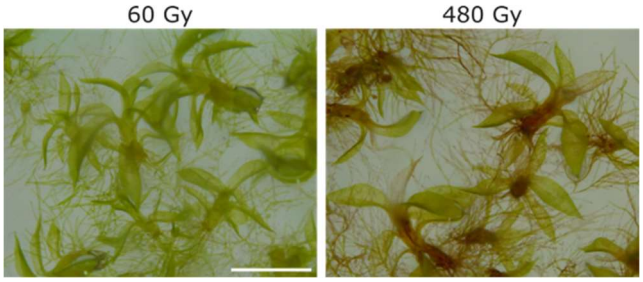

Fig. 2. Ion beam irradiation of wild type gametophores. Bar = 1 mm

References

[1] M. Ishikawa *et al*. Nat. Plants 5, 681 (2019). DOI: 0.1038/s41477-019-0464-2
[2] N. Gu *et al*., Nat. Plants 6, 1098 (2020). DOI:10.1038/s41477-020-0745-9

3 - 08 Investigation of uracil auxotrophic mutants of sake yeast bred by ion-beam mutagenesis technology

T. Watanabe [a)], K. Satoh [b)], Y. Oono [b)], S. Tajima [a)]

[a)] Gunma Industrial Technology Center,
[b)] Department of Radiation-Applied Biology Research, QST

Introduction

For the first time in the world, we have bred sake yeast No. 227 by ion-beam irradiation and successfully put it into practical utilization [1]. Moreover, non-urea producing Gunma KAZE2 yeast (KAZE2-Arg) that is suitable for export were also bred by ion-beam irradiation [2]. Recently, we have developed a new improved technique to prepare sake yeast cells for ion-beam irradiation [3]. In this study, using this new technique and 5-fluoroorotic acid (5-FOA), a reagent that enable positive selection, we tried to obtain uracil auxotrophic yeast mutants from irradiated cells with different nuclides/doses of ion-beams.

Experimental

Following air-dried samples were prepared as described previously [3], sake yeast Kyokai no. 701 (K701) cells were irradiated with ion beams (C220; $^{12}C^{5+}$, 220 MeV, 50 - 350 Gy, C190; $^{12}C^{6+}$, 190 MeV, 100 - 400 Gy, C320; $^{12}C^{6+}$, 320 MeV, 50 - 400 Gy, He50; $^{4}He^{2+}$, 50 MeV, 100 - 350 Gy, Ne350; $^{20}Ne^{8+}$, 350 MeV, 50 - 400 Gy, Ar460; $^{40}Ar^{13+}$, 460 MeV, 50 - 400 Gy) accelerated by the AVF cyclotron at TIARA, TARRI, QST. K701 cells were also irradiated with UV (30, 60 s) at 300 mm distance in the clean bench. After 1 week cultivation on the 5-FOA plate medium (0.67% YNB, 0.05% yeast extract, 0.025% uracil, 0.1% 5-FOA, 2% glucose, 2% agar), uracil auxotrophic candidates were obtained. From these candidates, strains which could not grow on YNB plate medium (0.67% YNB, 2% glucose, 2% agar) incubated for 1 week were selected as uracil auxotrophic mutants. K701 and uracil auxotrophic mutants were pre-cultivated in YM medium (0.3% yeast extract, 0.3 % malt extract, 0.5% peptone, 1% glucose) with shaking at 150 rpm, 30 °C for 24 h. Pre-cultures were inoculated in YM medium containing 0.004% uracil and cultivated on the bio-photorecorder (Advantec, TVS062CA) with shaking at 30 rpm, 30 °C for 24 h. Cell growth (OD_{660}) was automatically measured every 15 minutes.

Results and Discussion

Uracil auxotrophic mutants were obtained by C220, C320, and He50 ion-beam irradiations, while no such mutant was obtained by. C190 and Ne350 (**Table 1**). Only one mutant was obtained by Ar460. Growth time reached at 1.0 OD_{660} of K701 was 8.0 h, while those of mutants were delayed from 10.0 to 24.0 h (**Table 2**). Whole genome analysis to confirm mutation sites of *URA3* and *URA5*, and determine the number of non-target genes mutations is in progress.

Table 1
Summary of uracil auxotrophic mutants of K701.

	Dose, seonds	Viabilitiy (%) Ave.	Std.	candidates (strain)	Appiarance ratio (%)	Mutants (strain)	Proportion (%)
C220	350Gy	74.4	15.6	31	6.4E-06	5	16.1
	300Gy	77.2	8.8	40	8.0E-06	5	12.5
	250Gy	93.8	9.5	14	2.3E-06	2	14.3
	200Gy	93.0	16.7	3	5.0E-07	0	0.0
	150Gy	97.8	6.8	0	0.0	0	-
	100Gy	99.4	3.2	1	1.6E-07	0	0.0
	50Gy	100.0	7.4	24	3.7E-06	2	8.3
C320	400Gy	71.4	14.3	27	2.7E-04	11	40.7
	350Gy	73.8	21.8	7	6.8E-05	2	28.6
	300Gy	78.6	32.7	7	6.4E-05	1	14.3
	250Gy	83.3	23.0	4	3.4E-05	0	0.0
	200Gy	88.1	43.6	1	8.1E-06	0	0.0
	150Gy	95.2	18.0	8	6.0E-05	0	0.0
	100Gy	92.9	31.1	10	7.7E-05	1	10.0
	50Gy	92.9	25.8	1	7.7E-06	0	0.0
He50	350Gy	63.9	31.3	34	1.8E-05	10	29.4
	300Gy	68.9	27.1	51	2.5E-05	17	33.3
	250Gy	78.9	43.6	25	1.1E-05	3	12.0
	200Gy	92.8	5.4	17	6.1E-06	0	0.0
	150Gy	94.4	9.6	24	8.5E-06	3	12.5
	100Gy	80.6	12.3	13	5.4E-06	1	7.7
Ar460	400Gy	47.6	16.9	1	8.7E-06	1	100.0
	350Gy	82.8	16.2	2	1.0E-05	0	0.0
	300Gy	77.9	8.6	0	0.0	0	-
	250Gy	77.2	3.2	0	0.0	0	-
	200Gy	80.7	2.1	0	0.0	0	-
	150Gy	82.1	10.4	0	0.0	0	-
	100Gy	84.8	27.1	2	9.8E-06	0	0.0
	50Gy	111.7	24.4	0	0.0	0	-
UV	30s	87.2	1.1	10	4.6E-09	10	100.0
	60s	93.8	1.1	2	8.5E-10	2	100.0

Table 2
Growth time reached at 1.0 OD_{660}.

	Time (h) Fastest	Ave.	Slowest	Number of strains or traials
K701	7.5	8.0	8.3	17
C220	10.0	11.5	13.3	14
He50	11.0	14.0	24.0	34
C320	11.8	14.8	19.5	16
Ar460	11.5	11.5	11.5	1
UV	10.3	11.3	12.3	12

Acknowledgments

This work was supported by JSPS KAKENHI Grant Number JP21K12528.

References

[1] T. Masubuchi et al., JAEA Takasaki Annu. Rep. 2012, **JAEA-Review 2013-059**, 117 (2014).
[2] T. Watanabe et al., QST Takasaki Annu. Rep. 2018, **QST-M-23**, 81 (2020).
[3] T. Watanabe et al., QST Takasaki Annu. Rep. 2019, **QST-M-29**, 98 (2021).

3 - 09 Inhibition of growth and assessment of damaging bacterial spores by ion beam irradiation

M. Furuta[a)], R. Asada[a)], K. Tatsumoto[a)], H. Den[a)], NHP. Uyen[a)], JJ. Sakamoto[b)], T. Tsuchido[b)], K. Satoh[c)] and Y. Oono[c)]

[a)]Quantum Radiation Engineering, Graduate School of Osaka Metropolitan University,
[b)]Research Center of Microorganism Control, Organization for Research Promotion, Osaka Metropolitan University
[c)]Department of Quantum-Applied Biosciences, QST

Introduction

Controlling spore-forming bacteria of the *Bacillus* genus, which exhibit strong resistance to heat and radiation, is a significant challenge in sterilization processes for food and medical supplies. Understanding how damage incurred by spores due to radiation affects their germination, subsequent growth, and nutritional proliferation, as well as its impact on the occurrence frequency of damaged bacteria and mutants, is essential for advancing radiation sterilization and its integration with other sterilization methods. While heat treatment induces damage in all growth stages, it is observed that, with ^{60}Co γ-ray irradiation, damage appears as an increase of the time for recovery in the post-germination and subsequent nutritional proliferation phases. These results of the increased time required for post-germination growth and a decrease in nutritional proliferation rate, which is presumed to influence the occurrence of damaged bacteria, but this aspect is yet to be extensively studied compared with the lethal and mutagenic effects of the strains [1].

This study aims to gain insights into how changes in resistance of *B. subtilis* spores due to γ-ray irradiation and ion beam irradiation with different Linear Energy Transfer (LET) values affect the recovery and growth processes. We measured survival rates and growth behavior through time using plate assays and monitoring optical density (OD_{650}) changes using a microplate reader. We also evaluated the presence of damaged bacteria using the Differential Viability Staining and Liquid (DiVSaL) method [2].

Experimental

B. subtilis 168 strain *(trpC2*) was used in this study. All spores were formed in Schaeffer's medium, harvested, lysozyme-treated, and repeatedly washed with centrifugation. The obtained spores were suspended in 50 mM potassium phosphate buffer (KPB) containing 0.1% TWEEN and were exposed to ^{60}Co γ-rays (0-6 kGy) at the Radiation Research Center, Osaka Metropolitan University. Furthermore, spores were irradiated (0-4 kGy) with ion beams of different LET values ($^{4}He^{2+}$ [50 MeV; 19.4 keV/μm], $^{12}C^{6+}$ [190 MeV; 148.7 keV/μm], $^{12}C^{5+}$ [220 MeV; 121.8 keV/μm], $^{12}C^{6+}$ [320 MeV; 86 keV/μm], and $^{20}Ne^{8+}$ [350 MeV; 440.8 keV/μm]) accelerated by the AVF cyclotron at TIARA, TIAQ, QST. Spores after each irradiation were appropriately diluted with KPB, plated on LB agar plates, and survival rates were determined using the colony count method. The same irradiated spores were also suspended in liquid LB medium, and the time-dependent change in turbidity was monitored using a microplate reader to observe growth delays. Furthermore, the DiVSaL method was used to detect damaged bacteria by calculating the difference between the calculated survival rate and CFU obtained using the colony count method [2].

Results and Discussion

The survival rates of spores irradiated with ^{60}Co γ-rays and ion beams of different LET values showed variations in Relative Biological Effectiveness (RBE) depending on LET in accordance with the previous results [3]. Additionally, the growth patterns of spores under both ^{60}Co γ-ray and ion beam irradiation exhibited delayed onset of nutritional proliferation as the dose increased. As LET of the ion beam increased, the equivalent survival rate decreased compared to the survival rate determined by the colony count method, suggesting a higher occurrence frequency of damaged bacteria (Table1). Carbon ion irradiations showed the highest lethal effect even at 2 kGy causing no determination of injured cell levels. These results imply that ion beam-induced clustering damage in genomic DNA may have some influence on recovery of the cell damage causing detection of injured bacteria including mutants [4].

References

[1] R. Asada *et al.*, Proceedings of Vietnam conference on nuclear science and technology VINANST-14 485 (2022).
[2] T. Tsuchido, Biocontrol Sci., **22**, 131 (2017). DOI: 10.4265/bio.22.131
[3] Uyen et al., Takasaki Annu. Rep. 2016, **QST-M-8** 104 (2018).
[4] K. Satoh *et al.*, Mutat. Res. **827** 111835 (2023). DOI: 10.1016/j.mrfmmm.2023.111835

Table 1 Appearance of injured cells after 2-kGy irradiation with ^{60}Co γ-rays and ion beams with deferent LET

Irradiation (2KGy)	Inactivated cell fraction (%)	Injured cell fraction (%)
^{60}Co γ-rays	96.4	3.5
$^{4}He^{2+}$ (50 MeV; 19.4 keV/μm)	76.3	20.8
$^{20}Ne^{8+}$ (350 MeV; 440.8 keV/μm)	81.1	16.2

3 - 10 Comparison of mutation frequencies in anthocyanin synthetic genes in irradiated Arabidopsis M1 plants

S. Kitamura[a)], S. Hirata[a,b)], K. Satoh[a)], R. Inamura[a,b)], I. Narumi[b)] and Y. Oono[a)]

[a)]Department of Quantum-Applied Biosciences, QST
[b)]Graduate School of Life Sciences, Toyo University

Ionizing radiations generally interact randomly with target materials such as nuclear DNA. Because radiation-induced mutations are mainly derived from mis-repair of the damaged DNA, they are likely to be formed randomly in the genome. Previously, we showed that the irradiated M1 genomes are favored to detect all types of radiation-induced mutations in Arabidopsis, based on loss of heterozygosity (LOH) in three anthocyanin synthetic genes [1]. However, it was hard to know the mutation responsible for LOH without high-cost next-generation sequencing analysis, because mutants in anthocyanin biosynthetic genes show identical phenotypes (anthocyanin-less) in leaves.

In contrast to the leaf phenotypes, some anthocyanin mutants show unique coloration in seeds. For example, at their mature stage, *tt4* and *tt8* mutant seeds show pale yellow and pale brown, respectively. Thus, double heterozygotes for *TT4* and *TT8* (*TT4/tt4 TT8/tt8*; capital and lower letters mean wild-type and mutant alleles, respectively) produce wild-type brown mature seeds. However, when the *TT4* or *TT8* allele is mutated, these cells would produce pale yellow (*tt4*-type) or pale brown (*tt8*-type) mature seeds, which makes it possible to know mutation frequencies at these two loci very simply (Fig. 1).

The double heterozygous seedlings for *TT4* and *TT8* were irradiated with 15 Gy of 220 MeV $^{12}C^{5+}$ at TIARA, QST. The irradiated M1 seedlings were grown to flowering, and the resultant seed color was observed. All the 430 non-irradiated seedlings produced red immature seeds caused by *ban* homozygous mutation. On the other hand, among 2,588 M1 seedlings, 19 seedlings produced anthocyanin-less immature seeds, indicating the presence of *de novo* mutation in *TT4* or *TT8* (Fig. 1). After maturing these seeds, two showed pale yellow, and the remaining 17 showed pale brown. This unequal distribution of *tt4* and *tt8* was significant (p <0.001), if the two genes were equally mutated.

To obtain molecular evidence for the anthocyanin-less phenotype, seed coat DNA was extracted from four mutants. qPCR analysis indicated that the three *tt8*- and one *tt4*-type seed coats contained reduced quantities of *TT8* and *TT4* fragments, respectively (Fig. 2), suggesting the presence of deletion mutations in these genes. This is consistent with the expectation from the phenotypes and supports our mutation detection system developed in this study.

Acknowledgments

This work was partially supported by JSPS KAKENIH 19K12333.

References

[1] S. Kitamura *et al.*, PLoS Genet. **18**, e1009979 (2022).
[2] S. Kitamura *et al.*, Sci. Rep. **12**, 22467 (2022).

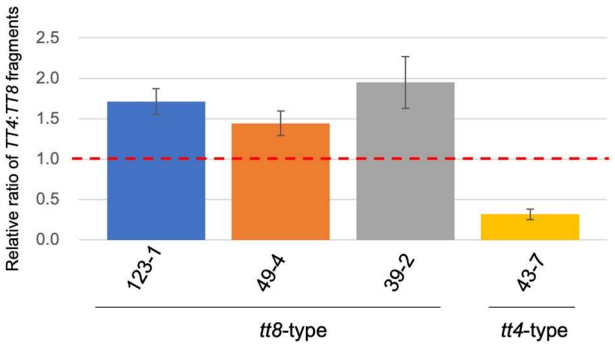

Fig. 2 Quantification of *TT4* and *TT8* fragments in seed coat DNA on the basis of a qPCR analysis [2].

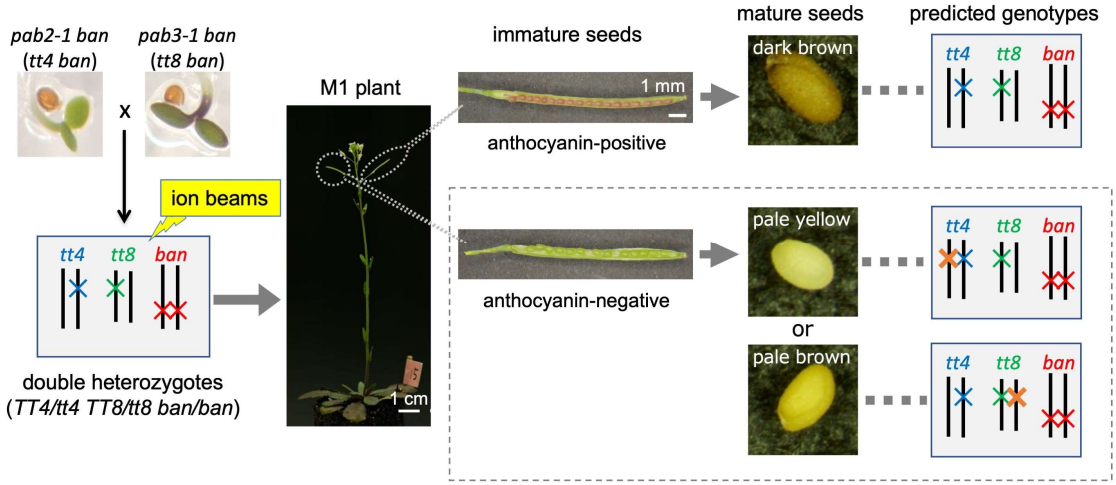

Fig. 1 Strategy for detecting mutations at multiple loci in M1 generation [2].

3 - 11 Induction of mutant seedlings of *CCD4* genes through heavy-ion beam irradiation

K. Ureshino[a)], K. Satoh[b)] and Y. Oono[b)]

[a)]Faculty of Agriculture, University of the Ryukyus
[b)]Department of Quantum-Applied Biosciences, QST

Evergreen azaleas are one of the representative ornamental woody plants. The flower colors of cultivated varieties are mainly variations of white, pink, red, or purple. However, no yellow-flowered cultivar of evergreen azaleas has been produced till date.

R. japonicum f. *flavum* is a yellow-flowered deciduous species belonging to the subgenus Pentanthera [1]. The yellow petals contain carotenoid compounds such as β-carotene and lutein as the main pigments [2]. To create yellow-flowered evergreen azaleas, we have conducted intersubgeneric three-way crosses between an interspecific hybrid of white-flowered evergreen azaleas (‘Miyamasatsuki’) and *R. japonicum* f. *flavum* (a yellow-flowered deciduous species belonging to the subgenus Pentanthera). The petal color of the buds on the progenies was light yellow just before anthesis, and these petals contained carotenoid pigments [3]. However, the light-yellow color of the petals was not stable, and it faded as the flower developed. Carotenoid degradation in the petals of the progeny was mediated by a high *CCD4* gene expression inherited from white-flowered evergreen azalea [2]. Thus, inactivation of *CCD4* gene during petal development is useful to avoid discoloration of petals in the progenies.

Heavy-ion beam irradiation is one of the useful methods for inactivation of target genes. We previously investigated seed germination test with progeny seeds irradiated with various doses (5, 8.3, 15, 25, 30, 50 and 83 Gy) of heavy-ion beam, and obtained green seedlings from each treatment. In the present study, PCR analysis of two intron regions was conducted to find the mutant seedlings of CCD4 gene.

Materials and methods

Seedlings from progeny seeds irradiated with various doses (0, 5, 8.3, 15, 25, 30, 50 and 83 Gy) of heavy-ion beam were used. DNA was extracted from leaves. The 1st and 2nd intron regions of *CCD4* were amplified by PCR using primers designed based on the previously investigated base sequence information [4]. The intron size was determined by electrophoresis of the amplified product.

.

Results

First, we analyzed the intron1 region of parents. Amplicons of two different lengths (4032 and 2310bp) were detected in ‘Miyamasatsuki’, and single amplicon (2702bp) was detected in *R. japonicum* f. *flavum* (Fig. 1). In their progenies, most of seedlings had parental bands （4032/2702 or 2702/2310） following Mendelism. Among them, two seedlings indicated different banded phenotypes (Table 1, Fig. 1). One seedling from 15Gy treatment had a shorter amplicon (2295bp) than that of ‘Miyamasatsuki’ (2310bp). One seedling from 50Gy treatment had a shorter amplicon (2680bp) than that of *R. japonicum* f. *flavum* (2702bp). In intron2 region, single amplicons were detected in parents. The length of ‘Miyamasatsuki’ was 1121bp, and that of *R. japonicum* f. *flavum* was 1954bp. All progenies had both amplicons (Table1, Fig. 1).

In this study, only two seedlings had different banded phenotypes. In current, we are comparing the whole gene size of *CCD4* among seedlings. We will clarify the result in future.

Table 1
Segregation of PCR products of progenies at Intron1 and 2.

	Intron1				Intron2
	4032/2702	2702/2310	2702/2295	4032/2680	1954/1121
0Gy	5	15			20
5Gy	13	18			31
8.5Gy	16	15			31
15Gy	10	9	1		20
25Gy	20	16			36
30Gy	21	19			40
50Gy	26	29		1	53
84Gy	17	16			33

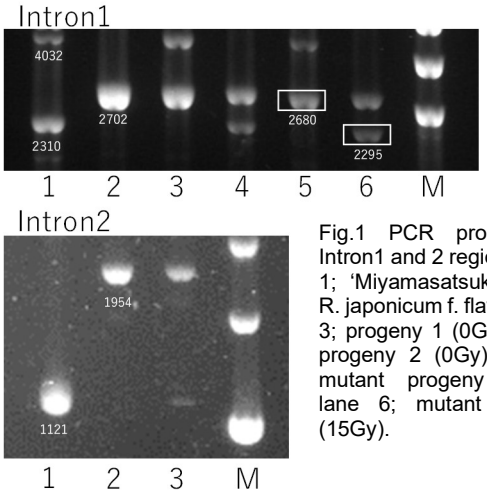

Fig.1 PCR products at Intron1 and 2 regions. Lane 1; ‘Miyamasatsuki’, lane2; R. japonicum f. flavum, lane 3; progeny 1 (0Gy), lane4; progeny 2 (0Gy); lane 5; mutant progeny (50Gy); lane 6; mutant progeny (15Gy).

References

[1] T. Yamazaki, A revision of the genus Rhododendron in Japan, Taiwan, Korea and Sakhalin. Kokusai Bunken Insatsusha, Tokyo. (1996).
[2] K. Ureshino et al., Euphytica. **207**, 401 (2016).
[3] I. Miyajima et al., J. Japan. Soc. Hort. Sci. **69**, 280 (2000)
[4] K. Ureshino et al., J. Japan. Soc. Hort. Sci. **17**(Suppl. 2), 528 (2018)

3 - 12 Crop breeding using ion beams under the mutation breeding project of Forum for Nuclear Cooperation in Asia (FNCA)

Y. Hase[a)], A. Koike[b)], and K. Takemura[b)]

[a)]Department of Quantum-Applied Biosciences, QST
[b)]Nuclear Safety Research Association

The Forum for Nuclear Cooperation in Asia (FNCA) is a framework for the peaceful use of atomic energy led by the Cabinet Office/ MEXT of the government of Japan. At present, ten member countries are participating in the project, namely 'Mutation Breeding of Major Crops for Low-input Sustainable Agriculture under Climate Change (FY2018 – 2023)'. The ion beams from TIARA AVF cyclotron have been utilized to mutagenize the seeds according to the breeding purpose of the member countries [1]. Here, we describe the major achievements and the current situation related to the use of ion beams in the FNCA mutation breeding project.

Three rice varieties, namely BINAdhan-14, -18 and -19, have been released in Bangladesh [1]. The BINAdhan-14 is an early maturing and high yielding variety. The BINAdhan-18 is a high-yielding variety suitable for irrigated cultivation in Boro season (from winter to spring). The BINAdhan-19 is highly drought tolerant, because it derives from NERICA-10, which is an interspecific hybrid between Asian rice (*Oryza sativa*) and African rice (*O. glaberrima*). Furthermore, a new variety, namely Lal Atom dhan 1, was released in 2021 (Fig. 1). The Lal Atom dhan 1 is derived from the indigenous landrace 'B-11'. The indigenous landrace has long been cultivated in the area and is well adapted to the local environment. Therefore, this variety can be cultivated with relatively low fertilizer and low irrigation water. The Lal Atom dhan 1 show high yield (7.8 to 8.0 t/ha) with high amylose content (26.6%) and is suitable for cultivation in Boro season.

Another new rice variety, namely 'DT99', was released in Vietnam in 2020 (Fig. 2). This variety shows higher yield and better resistance to pests and diseases than the original variety. The good grain quality and cooking quality are a major feature of this variety.

Promising mutant lines were obtained from carbon-ion irradiated population in Malaysia. Ten mutant lines have been subjected to yield trial and some of them stably shows high yield in the last several years (Fig. 3 left). Also, mutant screening of wheat and barley is in progress in Mongolia (Fig. 3 right).

In FY2022, we could not irradiate any seeds from FNCA member countries with ion beams, because international shipping service was not available due to the spread of coronavirus infection. Instead, we irradiated dry seeds and seedlings of Nipponbare with carbon ions, in order to examine the characteristics of induced mutation in rice.

Reference

[1] Y. Hase et al., QST Takasaki Annu. Rep. 2017, **2012-QST-M-16** 91 (2019).

Fig. 1 The new rice variety 'Lal Atom dhan 1' released in Bangladesh.

Fig. 2 The new rice variety 'DT99' released in Vietnam.

Fig. 3 (Left) Promising rice mutant lines derived from carbon-ion irradiated population in Malaysia. (Right) Potential wheat mutant lines obtained in Mongolia.

3 - 13 Activation mechanism of DNA damage response protein PprI in *Deinococcus radiodurans*

K. Satoh[a)], Y. Oono[a)] and I. Narumi[b)]

[a)]Department of Quantum-Applied Biosciences, QST
[b)]Faculty of Life Sciences, Toyo University

Introduction

Radioresistance in *Deinococcus radiodurans* is attributed to their highly proficient DNA repair capacity. The previous studies revealed that the expression of a unique DNA repair-related protein, PprA, was up-regulated by a regulatory protein, PprI, following DNA damage in *D. radiodurans* [1]. The radiation/desiccation response (RDR) motif was found in the upstream regions of the radiation-inducible genes (RDR regulons) by comparative genome sequence analysis of *Deinococcus* [2]. The RDR motif is an operator sequence in the unique DNA repair response system [3]. Another regulatory protein, DdrO, binds the RDR motif and acts as a repressor. The PprI consists of three domains, namely metalloprotease, DNA binding, and GAF-like domains. Following DNA damage, the metalloprotease activity of PprI cleaves DdrO, resulting in derepressing the RDR regulon [4]. In contrast to the RDR regulons, the *pprI* gene is constitutively expressed, suggesting that PprI is activated after DNA damage. *In vitro*, the PprI protein has been shown to have metalloprotease activity by coordinating bonds of manganese (Mn) ions [5]. *In vivo*, the functional complementation studies have shown that the metalloprotease activity is crucial for the DNA damage response mechanism [6]. In this study, we investigated the relationship between intracellular Mn accumulation and PprI activation by conducting a reporter assay following gamma irradiation in the presence or absence of Mn ions.

Experimental

The site-directed mutagenesis was performed to introduce the following mutations (E119Q and E149Q in the metalloprotease domain, Y196A in the DNA binding domain, and H260L in the GAF-like domain) into the wild-type *pprI* expression plasmid. The wild-type and mutated *pprI* expression plasmids were introduced into the *pprI*-deleted luciferase reporter strain XDAP (designated DAW, DAM119, DAM149, DAM196, and DAM260). These reporter strains were incubated in TGY or 5 μM Mn/TGY broths at 30 °C for 24 h with agitation. Cells were harvested, washed, and irradiated at room temperature with 2 kGy of ^{60}Co gamma rays at the Gamma-ray Irradiation Facility, TIAQ, QST. After irradiation, the cells were resuspended in TGY or 5 μM Mn/TGY broths and incubated at 30 °C for 2 h with agitation. After incubation, the cells were subjected to the luciferase reporter assay [6].

Results and Discussion

The changes in PprI activation level with Mn following irradiation were compared between the *pprI* mutant and wild-type strains using the luciferase reporter assay (Fig. 1). Like XDAP, DAM119 and DAM149 could not induce the luciferase activity, indicating that *in vivo* activation of the PprI protein required coordinate bond with Mn ions. Under the addition of Mn ions, DAM196 showed an increase in luciferase activity after gamma irradiation, similar to DAW, suggesting that Mn ions compensates for the loss of function of the DNA binding domain. Even with the addition of Mn, DAM260 had lower luciferase activity compared to the wild-type strain. These results indicate that the coordination bonding of Mn ions to the metalloprotease domain has a significant impact on the activation of the PprI protein. Furthermore, it is evident that the GAF-like domain is also involved in the activation of the PprI protein by Mn ions.

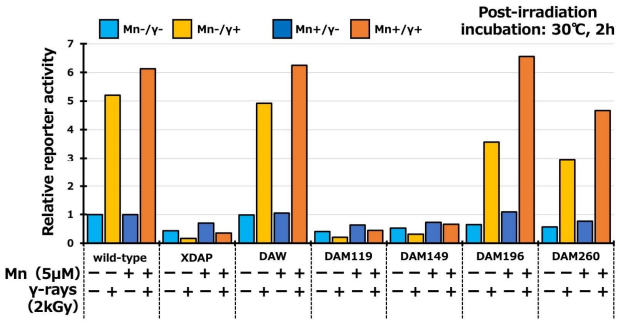

Fig. 1 Changes in intracellular PprI activation level with Mn ions following irradiation.

Acknowledgments

This work was supported by JSPS KAKENHI Grant Number JP21K05356 to K. Satoh.

References

[1] Y. Hua *et al.*, Biochem. Biophys. Res. Commun. **306,** 354 (2003). DOI: 10.1016/s0006-291x(03)00965-3
[2] K.S. Makarova *et al.*, PLoS ONE **2**, e955 (2007). DOI: 10.1371/journal.pone.0000955
[3] M. Ludanyi *et al.*, Mol. Microbiol. **94**, 434 (2014). DOI: 10.1111/mmi.12774
[4] H. Lu *et al.*, DNA Repair **11**, 139 (2012). DOI: 10.1016/j.dnarep.2011.10.013
[5] Y. Wang *et al.*, PLoS ONE **10**, e0122071 (2015). DOI:10.1371/journal.pone.0122071
[6] K. Satoh *et al.*, QST Takasaki Annu. Rep. 2020, **QST-M-33**, 85 (2022).

3 - 14 Mutation spectrum analysis of the *rpoB* gene in *Rubrobacter radiotolerans*

I. Kawasaki[a)], A. Kubo[a)], N. Matsui[a)], H. Otaki[a)], K. Satoh[b)] and I. Narumi[a)]

[a)]Faculty of Life Sciences, Toyo University
[b)]Department of Quantum-Applied Biosciences, QST

Introduction

Rubrobacter radiotolerans is a Gram-positive, rod-shaped bacterium belonging to the phylum Actinomycota with an optimum growth temperature of 45°C isolated from the biofilm of a hot spring in Japan in 1973 [1]. It is known to be highly radioresistant, and its entire genome was sequenced in 2012. Still, no genetic engineering system has been established to date. Installing a genetic engineering system for *R. radiotolerans* is a first step toward elucidating the molecular mechanism of its radioresistance. It is also known that spontaneous mutations in the *rpoB* gene, which encodes the β-subunit of RNA polymerase, cause resistance to rifampicin. Therefore, this study aimed to analyze the mutation spectrum using the *rpoB* gene as an indicator to contribute to the establishment of a gene manipulation system in *R. radiotolerans*.

Experimental

The minimum inhibitory concentration of rifampicin was measured using CYC medium (3.5% Difco Czapek-Dox Broth, 0.2% Difco Yeast Extract, 0.6% Difco Casamino Acids) supplemented with 100 ng/mL cyanocobalamin (CYC-C medium). The spontaneous mutation rate was measured based on the Fluctuation Assay. First, the CYC-C medium was inoculated with 1/100th volume of glycerol stock of *R. radiotolerans* wild strain (JCM 2153) and cultured at 45°C for three days with shaking. A 10-fold dilution series was prepared using phosphate buffer (pH 7.0). Then, 25 µl of the 10^5 diluted solution was inoculated again into 2 ml of CYC-C medium and incubated at 45°C for six days with shaking. The solution was used for the spontaneous mutation rate measurement. The spontaneous mutation rate was calculated by measuring the total number of viable colonies on CYC-C agar and the number of rifampicin-resistant mutant colonies on CYC-C agar supplemented with rifampicin, then substituting the measured values into Drake's formula ($\mu = f$ / ln (Nμ), μ: mutation rate, f: mutant frequency, N: total viable count) [2]. Furthermore, each colony grown on CYC-C agar supplemented with rifampicin was inoculated into CYC-C medium supplemented with rifampicin and incubated at 45°C for five days with shaking. The resulting rifampicin-resistant mutant cells were collected by centrifugation, and genomic DNA was extracted using the FastDNA SPIN Kit. The *rpoB* gene was PCR amplified using the genomic DNA from the rifampicin-resistant mutant strain as a template for DNA sequencing analysis.

Results and Discussion

The minimum inhibitory concentration of rifampicin in the *R. radiotolerans* wild strain was 2.5 ng/mL, which is extremely low compared to other bacteria [3]. When the concentration of rifampicin was varied from 0.05 µg/mL, 1.0 µg/mL, and 5.0 µg/mL, the respective mutation rates were 2.11×10^{-7}, 3.39×10^{-8}, and 2.71×10^{-8}. This suggested that the mutation rate increased with decreasing rifampicin concentration.

Sequence analysis of the *rpoB* gene revealed several characteristic mutations, including deletions of 9 bases and transition mutations for 0.05 µg/mL rifampicin-resistant mutant strains (Table 1).

In the future, we will analyze the mutation spectrum at each rifampicin concentration and investigate the natural transformation ability of *R. radiotolerans* using the genome derived from the rifampicin-resistant mutant strain obtained in this study. We also plan to obtain mutant strains defective in DNA repair by gamma irradiation and identify their mutated sites.

Table 1
Results of *rpoB* sequencing analysis from rifampicin-resistant mutant strains.

Mutant name	Mutation site	Mutation type	Changed base
Rif0.05#1	1211	Transition	C→T
Rif0.05#2	1232	Transition	A→G
Rif0.05#3	1223	Transition	A→G
Rif0.05#4	1232	Transition	A→G
Rif0.05#5	1232	Transition	A→G
Rif0.05#6	1170−1178	Deletion	CTCGCAGCT
Rif0.05#7	1238	Transition	C→T
Rif0.05#8	1232	Transition	A→G
Rif0.05#9	1170−1178	Deletion	CTCGCAGCT
Rif0.05#10	1211	Transition	C→T

References

[1] T. Yoshinaka *et al.*, Agr. Biol. Chem. **37**, 2269 (1973). DOI: 10.1080/00021369.1973.10861003
[2] J. W. Drake, Proc. Natl. Acad. Sci. USA **88**, 7160 (1991). DOI: 10.1073/pnas.88.16.7160
[3] A. Dey and D. Chatterji, J. Bacteriol. Virol. **42**, 87 (2012). DOI: 10.4167/jbv.2012.42.2.87

3 - 15 Preliminary experiments on the culture method and radiation sensitivity of *Bradyrhizobium diazoefficiens* toward mutant screening for high temperature tolerance

Y. Hase, I. Nagafune and K. Satoh

Department of Quantum-Applied Biosciences, QST

Bradyrhizobium diazoefficiens has been utilized as one of the plant growth promoting rhizobacteria for biofertilizer. However, under a high temperature condition, the number of viable cells in biofertilizer products easily decreases and the symbiotic effect is also suppressed after application to the filed. Therefore, the rhizobacterial strain that has a high temperature tolerance is desired. However, the practical strain with high temperature tolerance has not been obtained so far. Single mutant strain with high temperature tolerance, namely M14 strain, has been obtained from carbon-ion irradiated population [1]. This indicates that the high temperature tolerance could be conferred by mutagenesis. However, the M14 strain shows poor growth compared to the wild type and also the underlying mechanism of the high temperature tolerance is unclear. At that time, they continued mutant screening but no other mutant strains were obtained by a conventional mutant screening method under a high temperature condition. In this study, we aimed to obtain high-temperature tolerant mutants of *B. diazoefficiens* by the experimental evolution combined with mutation induction with ionizing radiations. In fiscal year 2022, we performed preliminary experiments to confirm a culture method and examined the sensitivity to gamma rays.

The *B. diazoefficiens* strain USDA110 was used here. The Yeast-Mannitol (YM) broth is a frequently used broth to culture, but the mannitol greatly enhance the production of extracellular polysaccharides and it makes difficult to handle the cultured cells. Therefore, we used the culture media shown in Table 1, which is modified from Peptone-Salt-Yeast extract (PSY) broth [2]. This media (hereafter shown as mPSY) is easy to prepare, the cells grow faster, and only a limited amount of extracellular polysaccharides is produced compared to the case of YM broth.

In order to examine the sensitivity to gamma rays, the cells cultured at 32°C were washed twice with phosphate buffer (PB), resuspended in PB, and irradiated with 0 to 200 Gy at the gamma irradiation facility. At the beginning of this experiment, relationship between the optical density (OD_{615}) measured by the PicoExplorer (Yamato Scientific Co., Ltd.) and the actual colony forming unit (CFU) was unstable and we failed to obtain reproducible results. Therefore, we examined the relationship between the OD_{615} and CFU through the culture period. A linear relationship was seen until the OD_{615} reached around 0.10, but a number of viable cells steeply dropped when the OD_{615} reached 0.15 or higher. When those cells were cultured on mPSY plate, we noticed that a ratio of small colonies increases after prolonged culture (Fig.1). Based on these observations, we performed again the sensitivity check using fresh cells in a logarithmic growth phase. Finally, we obtained reproducible results in two independent experiments (Fig. 2)). The survival fraction decreased to around 0.1 after 100 Gy irradiation.

Our results indicates that the mPSY media is handy for culturing rhizobacteria and the condition of the cells is important to perform further experiments.

References

[1] K. Takeda et al., JAEA-Review **2012-046**, 107 (2012).
[2] B. Regensburger and H. Hennecke, Arch. Microbiol. **135**, 103 (1983). DOI: 10.1007/BF00408017

Table 1
Composition of the culture media used in this study.

3 g/L	Bacto Pepton
1 g/L	Bacto Yeast Extract
0.1 g/L	$MgSO_4$ $7H_2O$
0.1 g/L	NaCl
3 mM	Potassium Phosphate buffer (pH6.8)
(Optional) 1.5%	Bactoagar

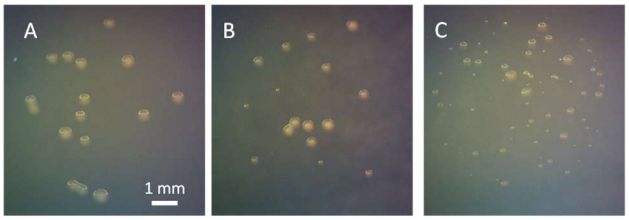

Fig. 1 Representative image of the colonies. Small colonies are frequently seen after prolonged culture.
A: 72h culture, OD_{615} = 0.12
B: 72h culture, OD_{615} = 0.17
C: 120h culture, OD_{615} = 0.15

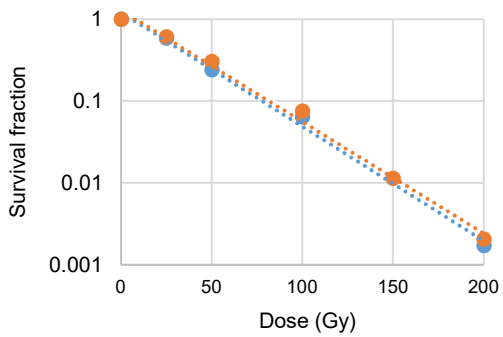

Fig. 2 Survival fraction of *B. diazoefficiens* cells irradiated with gamma rays. Data from two independent experiments are shown.

3 - 16 Highly efficient separation of ultratrace radioactive copper using a flow electrolysis cell

Y. Sugo[a)], S. Ohira[b)], H. Manabe[c)], Y. Maruyama[c)], N. Yamazaki[d)], R. Miyachi[b)], K. Toda[b)], N. S. Ishioka[a)], and M. Mori[c)]

[a)]Department of Quantum-Applied Biosciences, QST
[b)]Department of Chemistry, Kumamoto University
[c)]Faculty of Science and Technology, Kochi University
[d)]Graduate School of Engineering, Gunma University

Introduction

Copper-64 (^{64}Cu) is a useful radionuclide for cancer diagnosis with positron emission tomography (PET) as well as radionuclide therapy. The ^{64}Cu can be produced by the nuclear reaction of ^{64}Ni(p,n)^{64}Cu at high specific activity.

In this study, we developed an effective technique for separating ^{64}Cu from the ^{64}Ni matrix using electrolysis [1] instead of the conventional ion-exchange method.

Experimental

The separation is based on the difference in standard potentials: $E^{\circ}(Cu^{2+}/Cu^{0})$ = +0.340 V, $E^{\circ}(Ni^{2+}/Ni^{0})$ = −0.257 V. A handheld-sized flow electrolysis cell (VF2, EC Frontier) with a working electrode (WE) of carbon felt (effective surface area: 1900 cm^2) was used. By applying a reduction potential, WE adsorbs the zerovalent Cu (Cu^0) and eliminates the Ni^{2+} matrix. In the next step, applying an oxidation potential with flowing dilute HNO_3 eluted the deposited Cu^{2+}.

The experimental conditions were optimized by the preliminary cold test using the stable isotopes. Using the AVF cyclotron of TIARA, ^{64}Cu was produced by irradiating the isotopically enriched ^{64}NiO target with an 11 MeV proton beam. As a tracer of the Ni matrix, ^{57}Ni was also prepared by irradiating the ^{nat}Ni metal with 18 MeV protons. The irradiated targets were each dissolved in HCl with heating.

Results and Discussion

The electrodepositions of Cu and Ni onto the WE were observed in applying a negative potential as shown in Fig. 1. More than 97% of the Cu was adsorbed to the WE in the range of −0.8 to −0.5 V, while all of the Ni^{2+} was excluded from adsorption. The adsorbed Cu was successfully dissolved in 10 mmol/L HNO_3 even without the applied potential. However, the best recovery efficiency of Cu was obtained when +1.0 V was applied. Under the optimal conditions, the. hot test with the radioisotope was performed. During the ^{64}Cu electrodeposition in applied voltage of −0.8 V, ^{57}Ni was quantitatively eluted. By changing the voltage to +1.0 V, ^{64}Cu was quantitatively desorbed from the WE. Figure 2 shows the γ-ray spectra measured with germanium semiconductor detector. These results indicate that the selective and highly efficient separation of ultratrace amounts of ^{64}Cu was successfully achieved.

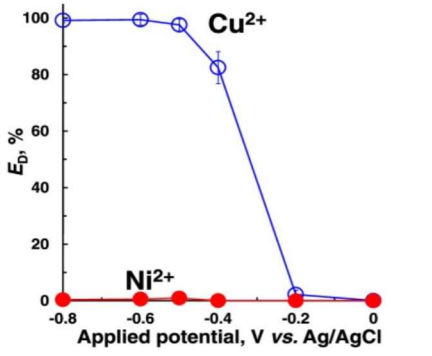

Fig. 1 Effect of applied potential on electrodeposition rate (E_D) of $Ni^{2+}$and Cu^{2+}.

It is concluded that our developed flow electrolysis system can selectively separate ^{64}Cu from the larger amount of ^{64}Ni target by controlling the applied potential to WE.

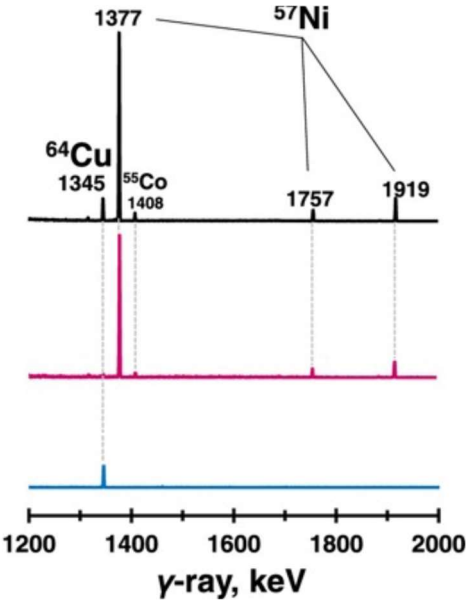

Fig. 2 γ-Ray spectra of the sample before injection (upper), the effluent in applying −0.8 V (middle), and the effluent in applying +1.0 V (lower).

Acknowledgments

This work was supported by JSPS KAKENHI Grant Numbers JP 20H03632 and 17K19137.

Reference

[1] Y. Sugo *et al*., ACS Omega **7**, 15779 (2022). DOI: 10.1021/acsomega.2c00828

3 - 17 Copper-mediated radiobromination via aryl boronic precursor and its application to ^{77}Br-labeled PSMA imaging probes

S. Watanabe[a)], Y. Kondo[b)], I. Sasaki [a)], Y. Ohshima [a)], Y. Yagi[c)], Y. Hattori[d)], M. Koda[b)], H. Kawashima[e)], H. Yasui[b)], H. Kimura[b)] and N.S. Ishioka[a)]

[a)]Department of Quantum-Applied Biosciences, QST
[b)]Department of Analytical and Bioinorganic Chemistry, Kyoto Pharmaceutical University
[c)]Department of Radiological Technology, Kyoto College of Medical Science
[d)]Center for Instrumental Analysis, Kyoto Pharmaceutical University
[e)]Radioisotope Research Center, Kyoto Pharmaceutical University

Introduction

Noninvasive image of prostate-specific membrane antigen (PSMA) expression levels can provide important information regarding disease stage and metastatic lesion location of prostate cancer. Because radiobromines such as ^{76}Br and ^{77}Br have some attractive radionuclides for molecular imaging, radiohalogenated PSMA inhibitors has great potential as novel imaging probes for diagnosis of prostate cancer. Oxidative electrophilic radiobromination using organotin compounds have been widely used for the labeling of radiobromines. However, residual organotin compounds are toxic and oxidative agents such as chloramine-T can arise from side reactions. These backgrounds led us to apply novel radiobromination methods to solve the abovementioned issues. Electrophilic radiohalogenation from a low toxic boronic acid compound is one of the alternative methods for the synthesis of radiobrominated compounds. In this study, we examined synthesis of ^{77}Br labeled PSMA derivatives via boronic acid precursors in the presence of copper catalyst.

Experimental

Synthetic routes of ^{77}Br labeled PSMA derivatives were shown in Scheme 1. Boronic acid PSMA precursors, *m*B-PS and *m*B-PS(^{t}Bu), were synthesized by reported methods [1]. ^{77}Br was produced via the ^{77}Se(p,n)^{77}Br reaction by using AVF cyclotron in QST-Takasaki. Proton beams of 20 MeV irradiated a $Cu_2{}^{77}Se$ target. Produced ^{77}Br was purified using the dry distillation system with some modifications [1]. Radiobromination was carried out using a boronic precursor, $Cu(py)_4(OTf)_2$ (py = pyridine, OTf = triflate) in methanol (0.2 mg each), and an aqueous solution of ^{77}Br (11–23 kBq). The reaction was conducted at room temperature or 90 ◦C for 10 min in Scheme 1A. Trifluoroacetic acid (TFA ,100 μL) was added to the mixture to remove *tert*-butoxy (^{t}Bu) carbonyl group after radiobromination (Scheme 1B). In this case, reaction was conducted at room temperature for 20 min. After removing solvent or TFA with a N_2 gas flow. The mixture in all cases were purified by a reverse-phase high-performance liquid chromatography (RP-HPLC) to yield [^{77}Br]*m*BrB-PS and [^{77}Br]*m*BrB-PS(^{t}Bu).

Results and Discussion

We synthesized [^{77}Br]*m*BrB-PS from the boronic precursor, *m*B-PS. After the labeling reaction at room temperature, the mixture was purified by HPLC to yield [^{77}Br]*m*BrB-PS in 7.4 ± 1.5% of radiochemical yield (RCY). In addition, the labeling reaction was carried out under heating conditions (90 ºC) to improve the RCY (32.2 ± 2.3%). Then, we also tried to synthesize [^{77}Br]*m*BrB-PS using the boronic precursor protected with the ^{t}Bu group . Consequently, the RCY of [^{77}Br]*m*BrB-PS was improved to 95.4 ± 2.5%. We have also confirmed the RCY in the synthesis of [^{77}Br]*m*BrB-PS(^{t}Bu) via *m*B-PS(^{t}Bu). After the labeling reaction, the mixture was purified by HPLC to yield [^{77}Br]*m*BrB-PS(^{t}Bu) (RCY: 96.4 ± 1.0%). During the synthesis of [^{77}Br]*m*BrB-PS using copper-mediated radiobromination via boronic precursors, we confirmed the difference in RCY between Scheme 1A and 1B. These findings suggest that carboxylic acid–protected boronic precursor *m*B-PS(^{t}Bu) should be used to synthesize [^{77}Br]*m*BrB-PS for highly yield-effective synthesis, although two step reaction required in this case.

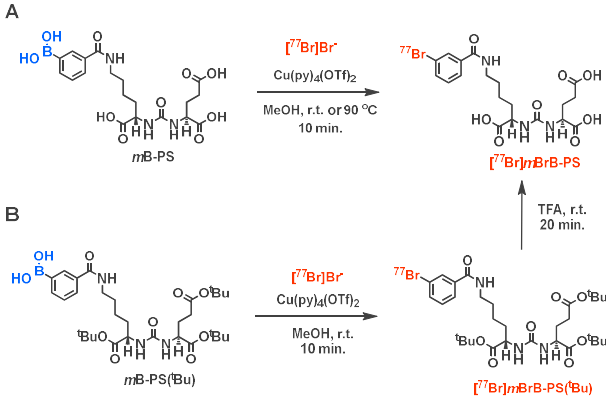

Scheme 1. Synthetic schemes of [^{77}Br]labeled PSMA derivatives.

Acknowledgments

This work was supported by JSPS KAKENHI with grant No. JP20K08061 and JP20K07648

References

[1] Y. Kondo *et al.*, *Bioorg. Med. Chem.*, **69**, 116915 (2022). DOI: 10.1016/j.bmc.2022.116915
[2] S. Watanabe *et al.*, *Trans. Mater. Res. Soc. Jpn.*. 43. 219 (2018) DOI:10.14723/tmrsj.43.219.

3 - 18 Neopentyl glycol as a scaffold to provide radiohalogenated theranostic pairs of high *in vivo* stability

H. Suzuki[a)], Y. Kaizuka[a)], M. Tatsuta[b)], H. Tanaka[b)], N. Washiya[a)], Y. Shirakami[c)], K. Ooe[c)], A. Toyoshima[c)], T. Watabe[c),d)], T. Teramoto[c)], I. Sasaki[e)], S. Watanabe[e)], N. S. Ishioka[e)], J. Hatazawa[f)], T. Uehara[a)] and Y. Arano[a)]

[a)]Graduate School of Pharmaceutical Sciences, Chiba University
[b)]Department of Chemical Science and Engineering, Tokyo Institute of Technology
[c)]Institute for Radiation Sciences, Osaka University
[d)]Graduate School of Medicine, Osaka University
[e)]Department of Quantum-Applied Biosciences, QST
[f)]Research Center for Nuclear Physics, Osaka University

Introduction

Astatine-211 (^{211}At) is an α-emitter of high interest in targeted α-therapy. However, the scaffolds useful to prepare ^{211}At-labeled compounds are limited, restricting the development of radiopharmaceuticals including ^{211}At. A representative astatination scaffold, benzoyl moiety, has been widely used to prepare ^{211}At-labeled compounds. However, they often show low stability against *in vivo* deastatination, especially when labeled for low-molecular-weight (LMW) compounds. Thus, a novel scaffold to produce ^{211}At-labeled LMW compounds with high stability against *in vivo* deastatination. In this study, we focused on the neopentyl glycol structure used for 2-dihydroxymethyl-3-[^{18}F]fluoropropyl-2-nitroimidazole ([^{18}F]DiFA, Fig. 1) [1], and applied it to radioiodine and ^{211}At.

Experimental

Three neopentyl iodide compounds with or without hydroxyl groups ([^{125}I]**1a**, [^{125}I]**2**, and [^{125}I]**3**, Fig. 1) were prepared to investigate the role played by the hydroxyl groups before the study using ^{211}At-labeled compounds. The stability to the nucleophilic attack and cytochrome P450 (CYP)-mediated metabolism was evaluated in a 10 mM glutathione solution and liver microsomes, respectively. The biodistribution was evaluated in normal male mice. Urine samples collected for 6 h after injection were analyzed by a reversed-phase high-performance liquid chromatography (RP-HPLC). Then, [^{211}At]**1b** was prepared and subjected to the same evaluation studies as [^{125}I]**1a**. Some ^{211}At used in this work were produced in the ^{209}Bi(α,2n)^{211}At reaction using the AVF cyclotron in TIARA. He beam of 28–29 MeV irradiated a Bi plate at 5 μA of beam current. Produced ^{211}At was then isolated by dry distillation method.

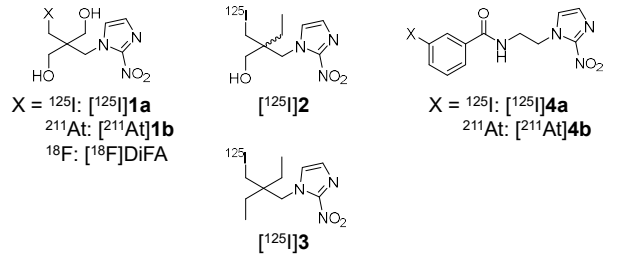

Fig. 1 Chemical structures of radiohalogenated neopentyl and benzoate derivatives evaluated in this study.

Results and Discussion

Although all three neopentyl iodide compounds showed high stability against nucleophilic attack, [^{125}I]**2** and [^{125}I]**3** were deiodinated by CYP-mediated metabolism. Correlated with *in vitro* studies, radioactivity levels in the stomach and neck (thyroid) where free [^{125}I]I^- accumulates were the lowest for [^{125}I]**1a**. When the urine samples collected for 6 h after injection of the neopentyl iodide compounds were analyzed by RP-HPLC, free [^{125}I]I^- was observed for [^{125}I]**2** and [^{125}I]**3**. Whereas, free [^{125}I]I^- was hardly observed for [^{125}I]**1a**, indicating that the C-I bond of [^{125}I]**1a** was stable against *in vivo* deiodination. Thus, [^{211}At]**1b** was prepared and compared with [^{125}I]**1a**. The reference compounds radiohalogenated via a benzoyl moiety ([^{125}I]**4a** and [^{211}At]**4b**) were also prepared. The biodistribution profiles of [^{211}At]**1b** were similar to those of [^{125}I]**1a**. However, [^{211}At]**4b** showed biodistribution profiles different from [^{125}I]**4a** and higher radioactivity levels in the stomach and the neck. In the urine analyses, [^{211}At]At^- was liberated from [^{211}At]**4b** but not from [^{211}At]**1b**, which implies that the C-At bond of [^{211}At]**1b** was stable against *in vivo* deastatination. These findings indicate that the neopentyl derivative with two hydroxyl groups would serve as a useful scaffold to develop ^{211}At-labeled compounds [2].

Acknowledgments

This work was supported in part by a Grant-in-Aid for Scientific Research (C) from the Japan Society for the Promotion of Science, grant number 19K08222. ^{211}At was supplied through the Supply Platform of Short-lived Radioisotopes, supported by JSPS Grant-in-Aid for Scientific Research on Innovative Areas, grant number 16H06278.

References

[1] N. Nakata *et al*., Nucl. Med. Biol. **70**, 39 (2019). DOI: 10.1016/j.nucmedbio.2019.01.008
[2] H. Suzuki *et al*., J. Med. Chem. **64**, 15845 (2021). DOI: 10.1021/acs.jmedchem.1c01147

3 - 19 Visualization of zinc uptake and translocation with positron-emitting ^{65}Zn tracer and gene expression analysis of transport-related gene in two *Lotus japonicus*

Y. Noda[a)], J. Furukawa[b)], N. Suzui[a)], Y.-G. Yin[a)], K. Matsuoka[c)], N. Kawachi[a)], and S. Satoh[b)]

[a)]Department of Quantum-Applied Biosciences, QST
[b)]Faculty of Life and Environmental Sciences, University of Tsukuba
[c)]Graduate School of Life and Environmental Sciences, University of Tsukuba

Zinc (Zn) is an essential element for humans and plants. Soil Zn concentrations are low in many developing countries, making Zn deficiency in crops and humans a serious problem. To overcome this agricultural problem, it is necessary to produce crops that accumulate more Zn in the edible part. The most economically important crops such as rice, maize and soya do not grow well in soils with low Zn concentrations, whereas Lotus japonicus is known to grow well at low Zn concentrations and to accumulate Zn in the edible parts. Therefore, the aim of this study was to elucidate the regulatory mechanisms of Zn uptake and transport in the legume *Lotus japonicus*, with the aim of applying the findings to breeding.

L. japonicus has two natural accessions, MG-20 and B-129, for which genome sequencing has been completed. We first identified differences in the Zn accumulation pattern between the two accessions by mass spectrometry and autoradiography using radioactive Zn (^{65}Zn). Next, to monitor real-time changes in the distribution of ^{65}Zn in both accessions, we then used the positron emission tracer imaging system (PETIS), which is a promising technique for visualizing the distribution of positron-emitting radioisotopes in living plants [1]. Finally, the relationship between Zn transport and gene expression was investigated by observing differences in Zn uptake patterns and analyzing the expression levels of genes known to regulate uptake and transport.

The results of mass spectrometry showed that the shoot Zn concentration in B-129 was higher than that in MG-20. The autoradiography showed that B-129 accumulated high amounts of ^{65}Zn in the root , the shoot and especially in the shoot stem, compared to MG-20. The real-time images of ^{65}Zn distribution by PETIS showed the rapid translocation of ^{65}Zn from the root to the shoot in B-129 (Fig. 1). Furthermore, the increase value calculated from the ^{65}Zn radioactivity in the shoots between 8 and 16 h suggested that B-129 showed a clear tendency towards higher translocation activity than MG-20.

Next, expression analysis of Zn transport-related genes was performed to explore the genetic basis for the difference in Zn efficiency between the two accessions. The Zn uptake and transport pathways from root to shoot were divided into three categories (1; from rhizosphere to root cells, 2; transport in root cell cytoplasm and 3; xylem loading from root cells to xylem vessels). The gene expression levels of relevant genes involved in each process showed that a number of Zn uptake and transport related genes, rather than a single one, are highly expressed in B-129 in these pathways (Fig. 2). Following this result, gene expression levels of known regulatory factors that may regulate Zn transport were examined, but B-129 did not show significantly higher expression levels. These results suggested that Zn uptake and transport in *L. japonicus* B-129 is regulated by an unknown master regulator [2].

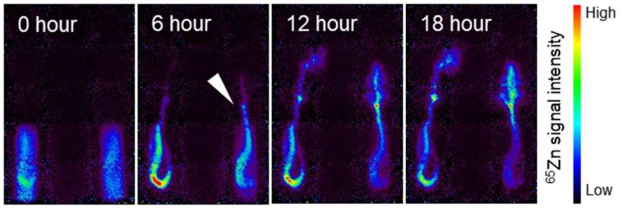

Fig. 1. Real-time PETIS images of the ^{65}Zn distribution in MG-20 (left) and B-129 (right). Radiation intensity is weaker in blue and stronger in red as shown by the color bar. The white arrows indicate that ^{65}Zn began to reach the shoot of B-129.

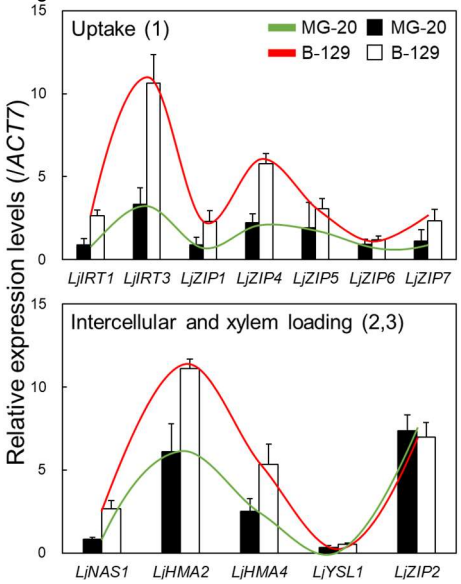

Fig. 2. The graphs compare the expression levels of the uptake-related (upper) and intracellular transport and xylem loading genes (lower) in MG-20 and B-129. The wavy lines represent the gene expression pattern of MG-20 (green) and B-129 (red).

References

[1] N. Suzui *et al*., Quantum Beam Sci. **3**, 18 (2019). DOI: 10.3390/qubs3030018

[2] Y. Noda *et al*., Ann. Bot. **130**, 799-809 (2022). DOI: 10.1093/aob/mcac101

3 - 20 Spatial distributions of strontium and barium in tea leaves evaluated by micro-PIXE analysis

A. Terakawa[a)], K. Ishii[a)], R.Yamagata[b)], Y. Ishii[b)],T. Satoh[b)] and N. Kawachi[c)]

[a)]Cyclotron and Radioisotope Center, Tohoku University
[b)]Department of Advanced Quantum Beam Technology, QST
[c)]Department of Quantum-Applied Biosciences, QST

Introduction

Radioactive contamination of tea plants due to ^{134,137}Cs in tea-growing regions of Turkey [1] and Japan [2] were extensively investigated after the nuclear power plant accidents in Chernobyl and Fukushima. However, few studies have examined ^{90}Sr in tea plants. In this study, we performed particle-induced x-ray emission (PIXE) analysis using a micrometer-sized beam (micro-PIXE) to explore similarities and differences in accumulation of Ca and other alkaline earth elements including Sr on cell and tissue scales.

Experimental

We grew five tea trees [*Camellia sinensis* (L.) Kuntze] in pots with commercial garden soil to obtain tea leaf samples. We transferred stable Sr and Ba into tea leaves via foliar absorption by partially soaking the leaves in mixed aqueous solutions of $SrCl_2$ (57.8 g/L) and $SrCl_2$ (47.5 g/L) for 1 minute. Tea leaves were collected 3, 30, and 90 days after foliar absorption, washed in water for 1 minute, and freeze-dried. We cut away portions of the leaves subject to foliar and non-foliar absorption as samples for a micro-PIXE analysis. We performed the micro-PIXE analysis using a 3-MeV proton beam and an in-air micro-PIXE analysis system at TIARA.

Results and Discussion

X-ray energy spectra obtained by micro-PIXE analysis of the foliar-absorbed samples are shown in Fig. 1. We observed characteristic X-rays of four alkaline earth elements (Mg, Ca, Sr and Ba). Figure 2 presents elemental maps (800×800 μm areas) of Mg, Ca (red), Sr (blue) and Ba (green) in the foliar absorbed potions of the leaf samples. While Mg was distributed throughout the sample, other alkaline earth elements (Ca, Sr and Ba) accumulated mainly in extremely narrow areas of the tea leaves, seen as small dots. Furthermore, we confirmed that Ca, Sr and Ba accumulated in almost exactly the same narrow regions as shown in Fig.3 because when these three elements accumulate in the same location, their distributions appear white in the overlaid image. Therefore, it is strongly suggested that alkaline earth elements other than Mg have common properties in the dynamics and accumulation mechanism within tea leaves.

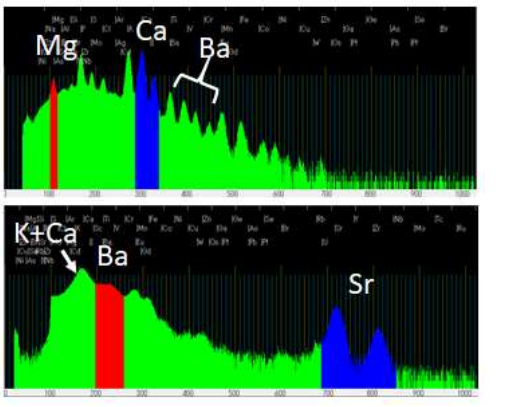

Fig. 1. X-ray energy spectra obtained by micro-PIXE analysis of the tea leaf sample.

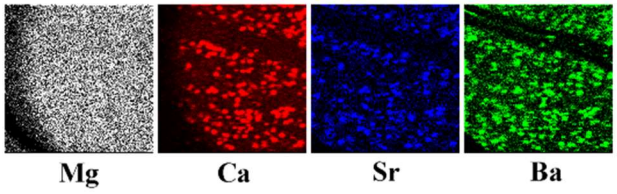

Fig. 2. Spatial distribution of Mg, Ca, Sr and Ba in the foliar-applied region of tea leaf samples collected 30 days after foliar absorption.

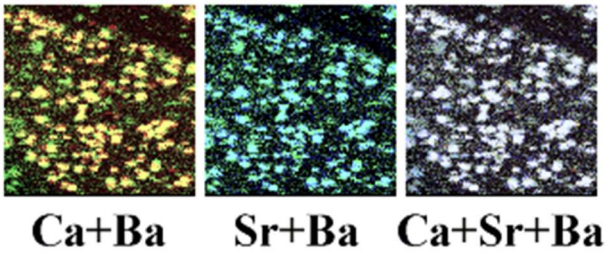

Fig. 3. Overlaid images of the spatial distribution of Ca, Sr and Ba.

Conclusion

The micro-PIXE analysis showed that Ca, Sr and Ba accumulated in almost exactly the same narrow regions, seen as small dots although Mg was almost uniformly distributed throughout the sample, suggesting that alkaline earth elements other than Mg have common properties in elemental accumulation.

References

[1] M. Scott *et al*., Health Phys. **57** 205 (1989)
[2] A. Kamata *et al*., Soil Sci. Plant Nutr. **61** 212 (2015)

3 - 21 In-air micro-PIXE (Particle Induced X-ray Emission) analysis visualized copper distribution in roots of oilseed rape plants

S. Nakamura[a)], K. Suda[a)], Y. Imaizumi[a)], A. Kijima[a)], A. Shinozawa[a)], K. Sato-Izawa[a)], R. Yamagata[b)], Y. Ishii[b)], T. Satoh[b)], Y.-G. Yin[c)], N. Suzui[c)] and N. Kawachi[c)]

[a)]Department of Bioscience, Faculty of Life Sciences, Tokyo University of Agriculture
[b)]Department of Advanced Quantum Beam Technology, QST
[c)]Department of Quantum-Applied Biosciences, QST

Introduction

Copper (Cu) is one of essential elements for plants with various physiological functions [1]. Cu, present in inappropriate amounts in the rhizosphere, is detrimental to plant growth. Soils with high Cu concentrations are one of the factors that reduce plant growth. To make it possible to grow agricultural crops in such soils, plants must be made Cu-tolerant. To elucidate the molecular mechanisms of Cu tolerance in higher plants, it is essential to determine the tissue distribution of Cu in plant roots. In this study, we attempted to visualize the tissue distribution of Cu in roots of oilseed rape plants using in-air micro-PIXE (Particle Induced X-ray Emission) analysis.

In-air micro-PIXE analysis allows us to visualize the two-dimensional distribution of the element of interest in samples [2, 3]. We expect that the experimental results obtained in this study will provide an insight for understanding the molecular mechanisms of Cu tolerance plant roots.

Experimental

Oilseed rape plants (*Brassica napus* L. var. Nourin No.16) were grown hydroponically under fully controlled conditions [4]. In the present study, 100 μM $CuCl_2$ were given to test plants for 2 days prior to harvest in order to visualize tissue distribution of Cu in roots. The Cu treatment concentration followed the experimental method of Zaheer et al. [5]. Harvested plant roots were embedded in a clear resin (Cryomatrix, Epredia) for frozen section preparation and stored at -80°C. Sections were prepared for analysis using a sectioning device (CM1520, Leica Biosystems). Sections were prepared at a thickness of 30 μm. After slicing, the sections were heated on a hot plate (NHP-45N, NISSIN) to remove excessive moisture in sliced sections immediately. Microscopic observations were made to determine the samples to be used in in-air micro-PIXE analysis.

In-air micro-PIXE analysis was performed at TIARA (Takasaki Ion Accelerators for Advanced Radiation Application) in Takasaki Institute for Advanced Quantum Science. Prepared section samples were analyzed for 10 minutes using a 3 MeV proton beam. The specific X-rays generated by proton beam were detected by an X-ray detector. The distribution and intensity of the specific X-ray of Cu determined the Cu distribution in plant roots.

Results and Discussion

Results of in-air micro-PIXE analysis are shown in Figure 1. Tissue distribution of Cu in plant roots was seen in Fig. 1A. Cu was widely distributed in root cells at similar levels (Fig. 1A). We were simultaneously able to visualize tissue distribution of potassium (K) and various other elements in the root tissue of oilseed rape plants. Figure 1B shows K distribution in roots. Cu and K were similarly distributed in the roots under the current treatment conditions (Fig.1). Investigating the tissue distribution of Cu in roots of different Cu-tolerant cultivars or under different growing conditions by in-air micro-PIXE analysis could be a starting point for elucidating Cu-tolerance in plants.

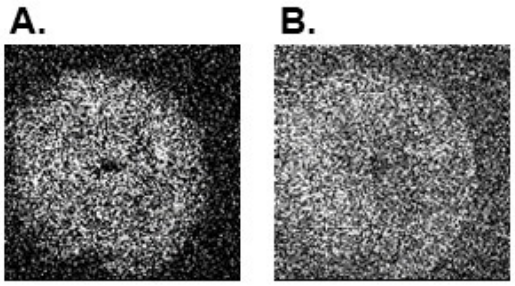

Fig. 1 In-air micro-PIXE analysis of tissue distribution of Cu (A) and K (B) in root cross sections prepared from roots of oilseed rape plants treated with 100 μM Cu for 2 days.

Acknowledgments

This study was supported in part by JSPS KAKENHI Grant Number JP22H02480 to S.N.

References

[1] V. Kumar *et al.*, Chemosphere. **262**, 127810 (2021). DOI:10. 1016/j.chemosphere.2020.127810
[2] T. Sakai et al., Nucl. Instrum. Methods Phys. Res. B. **190**, 271-275 (2002). DOI:10.1016/S0168-583X (02)00469-X
[3] P.M. Kopittke *et al.*, Plant Physiol. **182**, 1869-1882 (2020). DOI:10.1104/pp.19.01306
[4] S. Nakamura et al., Plant Sci. **283**, 424-434 (2019). DOI: 10.1016/j.plantsci.2018.10.018
[5] I.E. Zaheer *et al.*, Ecotoxicol. Environ. Saf. **120**, 310-317 (2015). DOI: 10.1016/j.ecoenv.2015.06.020

3 - 22 A Monte Carlo study of time-of-flight based neutron background reduction in secondary-electron-bremsstrahlung imaging for proton therapy

T. Yabe[a,b], M. Yamaguchi[a], M. Tsuda[a,c], Y. Nagao[a] and N. Kawachi[a]

[a]Department of Quantum-Applied Biosciences, QST
[b]Postdoctoral Research Fellowship, Japan Society for the Promotion of Science
[c]Graduate School of Biomedical Engineering, Tohoku University

In proton therapy, in-vivo range verification is important to monitor the location of the Bragg peak in the patient's body. Secondary-electron-bremsstrahlung (SEB) imaging is a promising method of proton range verification [1,2]. Unfortunately, the SEB images measured by the dedicated low-energy X-ray camera contain neutron-induced backgrounds as well as the SEB counts. To improve the accuracy of range verification for SEB imaging, we proposed to apply the time-of-flight (TOF) method to the SEB imaging [3]. The TOF method can discriminate between SEB and neutron signals by utilizing the differential time characteristics of photons and neutrons.

Monte Carlo simulations were performed using Particle and Heavy Ion Transport code System (PHITS) [4] version 3.26. The SEB and neutron generation and transport were calculated. A total of 10^8 protons of 120 MeV was irradiated to the water phantom. The time spectra and profiles of SEB and neutron were obtained by scoring on a detector placed 150 mm away from the phantom surface.

The SEB, neutron and depth-dose profiles are plotted in figure 1(A). The SEB profile was obtained by accepting only low-energy photons (below 110 keV) crossing on the detector within a collimation angle (90°± 3°). On the other hand, the neutron profiles were obtained by accepting all neutrons crossing the detector. The neutron profiles, represented by the red curves in figure 1(A), were found to be about 10 times higher than the SEB count. The neutron profiles were widely distributed and correlated quite poorly with the depth dose profiles.

Figure 1(B) shows the simulated TOF spectra of SEB and neutron for 120-MeV protons. The TOF value was defined as the time difference between the irradiation start of the proton beam and the arrival of the SEBs and neutrons at the detector. The TOF spectrum of SEB was scored in the collimation angle and integrated over the entire detector area. The SEB spectrum showed a peak at 5.0 ns and the neutron spectrum showed maximum counts around 7.0-8.0 ns. These differences in time spectra were attributed to SEBs arrived the detector earlier than neutrons.

The profiles of SEB and neutron obtained by applying the TOF method are shown in figure 2. The selection of a time width was adopted between 3.0 and 6.0 ns to cover the SEB count from the results of the TOF spectrum in figure 1(B). The total counts and profile shapes of SEB with the TOF method were similar to those without the TOF method. The total SEB counts in the region from the water surface to the proton range (i.e., the location of Bragg peak) were decreased by 6%. In contrast, the total neutron count was dramatically reduced for all proton energies. In the region from the water surface to the proton range, the TOF method reduced neutron background by 99%.

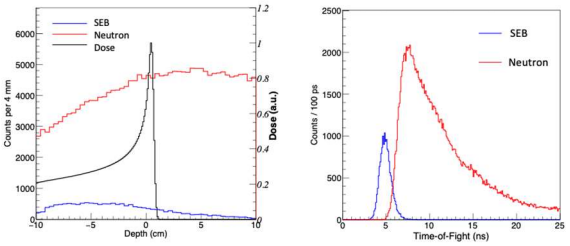

(A) (B)

Fig. 1 (A) Simulated profiles of SEB and neutron scored at the detector as a function of a beam direction with a bin size of 4 mm, and the depth-dose profile in the water phantom for 120-MeV proton beams. (B) The TOF spectra of SEB and neutron arriving at the detector. The figures are reprinted from [3].

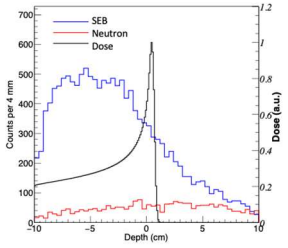

Fig. 2 Profile results of SEB and neutron with a bin size of 4 mm by applying the TOF method to the results of figure 1(A), and the depth-dose profile in the water phantom for 120-MeV proton beams. The figure is reprinted from [3].

Acknowledgments

This work was supported in part by JSPS KAKENHI Grant Numbers JP20H04465 and JP22J01550.

References

[1] M. Yamaguchi et al., Phys. Med. Biol. **57,** 2843 (2012). DOI: 10.1088/0031-9155/57/10/2843
[2] M. Yamaguchi et al., Nucl. Instrum. Methods Phys. Res. A **833**, 199 (2016). DOI: 10.1016/j.nima.2016.07.034
[3] T. Yabe et al., J. Instrum. **18**, C02041 (2023). DOI: 10.1088/1748-0221/18/02/C02041
[4] T. Sato, J. Nucl. Sci. Technol. **55**, 684 (2018). DOI: 10.1080/00223131.2017.1419890

3 - 23 Localization estimation of lesions in DNA produced by $^{40}Ar^{+13}$- irradiation in water and in 0.2M Tris

K. Akamatsu, N. Shikazono and K. Satoh

Institute for Quantum Life Science, QST

Introduction

Ionizing radiation-induced DNA damage can cause mutation and carcinogenesis. In particular, “clustered damage”, that is a DNA region with two or more lesions within a few helical turns, is believed to be hardly repaired. This damage would be induced around high-LET ionizing radiation tracks. However, detail of the damage is unknown. We have already developed a method for estimating localization of apurinic/apyrimidinic sites (APs) on DNA using fluorescence resonance energy transfer (FRET) occurring between different fluorescent dyes (Alexa350 and Alexa 488) (*hetero*-FRET). The FRET efficiency (*E*) was calculated from Alexa350 fluorescence intensities before/after enzymatic digestion of the labeled DNA with APs [1]. We succeeded in estimating qualities of clustered APs produced in $^{4}He^{2+}$-, $^{12}C^{5+}$-, and ^{60}Co γ-irradiated dry DNA film to study “direct” radiation effects using the method [2]. We also applied the method to aqueous DNA solution to study “indirect” radiation effects. However, there are some problems of the complex protocol and of the sensitivity due to the low extinction coefficient of Alexa350. We have, therefore, developed “*homo*-FRET” occurred between two or more Alexa488 molecules. We will obtain magnitude of FRET also from “fluorescence anisotropy” of *homo*-FRET between Alexa488 molecules [3]. The new protocol using *homo*-FRET enables us to estimate DNA damage localization without any enzymes and improves sensitivity to detect a clustered damage. In fact , we found that AP distribution clearly depended on linear energy transfer (LET) in the solid state (dry DNA sample) [4]. This indicates that the higher LET radiation produces more clustered damaged sites by the “direct” effects.

Experimental

●Sample preparation and irradiation

PUC19 digested by Sma I was used (linear formed) for DNA samples to be irradiated. The DNA was dissolved in pure water or in 0.2M Tris-HCl (pH 7.5), to be ~10 g/L. Eight microliters of the DNA solution was mounted on a 10 mmϕ glass plate (thickness: ~0.1 mm), and was irradiated with $^{40}Ar^{13+}$ (LET: 1890 keV/μm) at several doses up to 40kGy.

●Preparation of fluorophore-labeled irradiated DNA and FRET observation [3]

The irradiated DNA (10 μL in water) and 10 μL of 100 mM Tris-HCl (pH 7.5) were mixed in a microtube. Two microliters of Alexa488/DMSO were added to the DNA solution, followed by incubation for 24 h at 37°C. The fluorophore-labeled DNA was purified by ethanol-precipitation and solid phase extraction.

The fluorescence anisotropy was measured at 525 nm (ex. 470 nm). The anisotropy, $< r >$, is defined as follows:

$$< r > = (I_{VV} - G \cdot I_{VH}) / (I_{VV} + 2 \cdot G \cdot I_{VH})$$

where I_{VV} is the fluorescence intensity when the excitation and emission polarizers are both vertically oriented. I_{VH} is one when the excitation/emission polarizers are vertically/horizontally oriented. G is the grating factor defined as I_{HV}/I_H

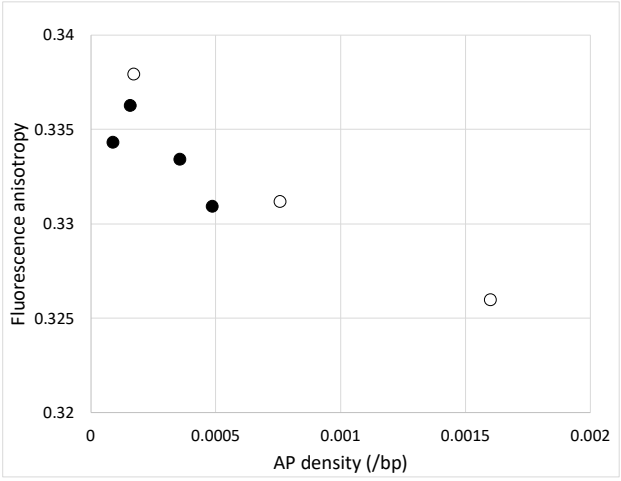

Fig.1. Fluorescence anisotropy of DNA irradiated with $^{40}Ar^{13+}$ (LET:1890 keV/μm) in water (○) and in Tris (●) as a function of averaged AP density.

Results and Discussion

Figure 1 shows relationships between averaged AP density and fluorescence anisotropy, <*r*>, for Ar-irradiated DNA in water (without any radical scavenger) and in Tris (a cell-mimetic condition). The degree of damage localization increases as <*r*> decreases. No significant difference was seen between the two radical scavenging conditions. This result suggests that “indirect” effect (e.g., by OH radical) is not responsible for DNA damage clustering in Ar-irradiated DNA or that most OH radicals densely generated around an argon particle track are eliminated by OH – OH coupling reaction to be H_2O_2 before encountering a radical scavenger.

References

[1] K. Akamatsu *et al.*, Anal. Biochem. **433**, 171 (2013).DOI: 10.1016/j.ab.2012.10.004

[2] K. Akamatsu *et al.*, Radiat. Res. **183**, 105 (2015). DOI: 10.1667/RR13780.1

[3] K. Akamatsu *et al.*, Anal. Biochem. **536**, 78 (2017). DOI: 10.1016/j.ab.2017.08.007

[4] K. Akamatsu *et al.*, Anal. Bioanal. Chem. **413**, 1185 (2021). DOI: 10.1007/s00216-020-03082-w

3 - 24 Development of drug delivery system (DDS), through two repetitions of radiation

S. Harada[a)] and T. Sato[b)]

[a)]Department of Radiology, School of Medicine, Iwate Medical University
[b)]Department of Advanced Quantum Beam Technology, QST

Introduction. We have been developing a drug delivery system (DDS) through two repetitions of radiation and using P-selectin-labeled nanoparticles, which accumulate to the P-selectin antigen (Ag) and release anticancer drugs in response to radiation (radiosensitive nanoparticles). 1) The first radiation to tumors induces the expression of the P-selectin Ag in the endothelium of tumor vessels; 2) the radiosensitive particles are injected intravenously into the host; 3) the injected radiosensitive particles circulate in the body and are trapped in the first irradiated tumor vessels via the Ag-antibody (Ab) reaction of P-selectin; and 4) the trapped radiosensitive particles receive the second radiation dose and localized anticancer drug. Our observations of an increased antitumor effect obtained on using our DDS have been published in the QST Takasaki Annual Report 2021. However, another function of a DDS is to reduce the side effects of the administered anticancer drug. In this study, the ability of our DDS to reduce adverse effects was added to the QST Takasaki Annual Report 2021. We also investigated the compatibility between the enhancement in the antitumor effects and the reduction in the adverse effects of the anticancer drug on using this method.

Preparation of particles. The nanoparticles were prepared by spraying a carboplatin-supplemented mixture of hyaluronic acid and alginate into a CaCl2 solution supplemented with P-selectin Ab and FeCl2 through a 0.8-μm-pore stainless mesh filter. The images of the generated particles captured by the micro-PIXE camera (TIARA, QST) are shown in Fig.. 1. The mean particle diameter was 457 ± 24 nm

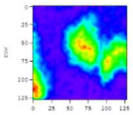

Fig. 1 generated particle

Tumor models, first radiation, induction of P-selectin Ag, and accumulation of P-selectin Ab-labeled particles through P-selectin's Ag-Ab reaction

MM 46 tumors (breast cancer cell lines), which were inoculated into the left hind legs of C3He/N mice, were subjected to a single 10 or 20 Gy of 100 keV X-ray irradiation (first irradiation). The P-selectin Ag was induced proximally, depending on the radiation dose. Peaks were observed 72 h after irradiation. Subsequently, P-selectin Ab-labeled particles were injected into the tail veins of the mice. P-selectin Ab-labeled particles accumulated in the tumors via the P-selectin Ag-Ab reaction, which was completed 9 h after the first irradiation.

Second irradiation and releasing of carboplatin from particles.

The second radiation dose was administered to the accumulated particles. The rupture of the particles by irradiation was determined based on two morphological changes observed in the Pt images obtained by the micro-PIXE camera: 1) Pt release from the particles (Fig. 2A), and 2) particle obfuscation (Fig. 2B, within the red circle). The frequency of rupturing was expressed as the mean percentage of ruptured particles within 10 views of the micro PIXE camera in a 12 × 12 μm scan. It was observed that the frequency of ruptured particles increased; the frequencies were 33.3 ± 2.3% after the 10 Gy dose and 53.4 ± 5.6 % after the 20 Gy dose.

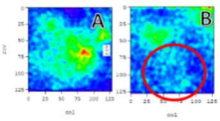

Fig. 2. Particles, releasing their contents upon radiation

Antitumor effect.

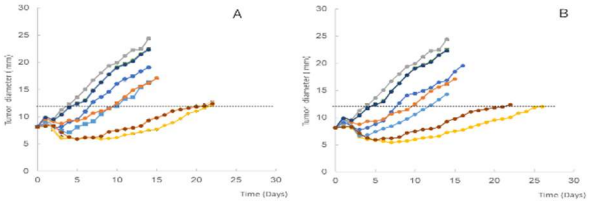

Fig. 3. Antigumor effect. A: 10 Gy, B; 20Gy, ●: No treatment, ●: Unirradiated particle (P-selectin unlabelled) ●: Unirradiated particle (P-selectin labelled), ●: Unencapsulated carboplatin only, ●: Radiation only, ●: Radiation + unencapsulated carboplatin, ●: Radiation + particle (P-selectin unlabelled), ●: Radiation + particle (P-selectin labelled).

The antitumor effect was measured by the alteration in the tumor diameter in the mice in the days after treatment. In the combination of radiation with carboplatin, encapsulated within the P-selectin-labeled particles, the antitumor effect was elongated and enhanced compared with that in any other treatments at the 20 Gy dose (Fig. 3A, B).

Adverse effect.

	MM46 tumor		
	body weight loss	fuzzy hair	dead
10 Gy	0.4 ± 0.2	0.8 ± 0.2	0.0 ± 0.0
20 Gy	1.0 ± 0.0	2.0 ± 0.0	0.0 ± 0.0
P−selectin Unlabelled Particle only	0.0 ± 0.0	0.6 ± 0.2	0.0 ± 0.0
P−selectin Llabelled Particle only	0.0 ± 0.0	0.6 ± 0.2	0.0 ± 0.0
carboplatin+10Gy	4.4 ± 0.4	5.0 ± 0.0	3.2 ± 0.5
carboplatin+20Gy	4.6 ± 0.2	5.0 ± 0.0	3.8 ± 0.5
10 Gy + P−selectin Unlabelled Particle	1.2 ± 0.2	1.8 ± 0.3	0.0 ± 0.0
10 Gy + P−selectin Labelled Particle	0.8 ± 0.2	1.6 ± 0.2	0.0 ± 0.0
20 Gy + P−selectin Unlabelled Particle	1.4 ± 0.2	2.4 ± 0.5	0.0 ± 0.0
20 Gy + P−selectin Labelled Particle	1.2 ± 0.2	2.2 ± 0.3	0.0 ± 0.0

Table. 1. Adverse effect.

The strength of the adverse effects was expressed as the number of mice showing body weight loss, fuzzy hair, and death out of the eight mice. Our carboplatin delivery system significantly reduced the drug's adverse effects (Table 1).

Conclusion. Our drug delivery system increased antitumor effect and reduced adverse effect.

References.

[1] T. Segawa *et. al.* Radiat. Res. **193**, 263 (2020).
DOI: 10.1667/RR15357

Part Ⅱ

4. Quantum Beam Technology

4 - 01 Carbon sputtering yield by C_{60}-ion bombardment

K. Narumi, K. Yamada, Y. Hirano, A. Chiba and Y. Saitoh

Department of Advanced Quantum Beam Technology, QST

C_{60}-ion bombardment have attracted attention of the ion-beam community for a long time from the viewpoint of fundamental science and applications [1, 2]. When a solid target is bombarded with a C_{60} ion, its constituent ions or atoms simultaneously collide with many target atoms in a small space. This induces a lot of phenomena characteristic of C_{60}-ion bombardment: It is well known that huge sputtering is one of such phenomena. It is closely related to C_{60}-ion stopping in solid and secondary-ion emissions, which lead to applications such as secondary-ion mass spectrometry (SIMS). For application use of C_{60}-ion beams, practical data on fundamental processes relating to ion stopping in solid are indispensable; however, there are not enough data on C_{60} ions up to the present. Thus, we have been focusing on sputtering by C_{60} ions and measured sputtering yields systematically [3, 4].

Concerning sputtering by cluster/molecular-ion bombardment, on the other hand, it is well known that nonlinear effect is observed [5], *i.e.*, the sputtering yield is not proportional to the number of the constitutional atoms. We have observed the effect on the Au sputtering yield by C_{60}-and C_{70}-ion bombardment [4].

In the present report, for the sake of systematic measurement of sputtering yields and evaluation of nonlinear effect on sputtering yields, we have measured carbon sputtering yields induced by 0.03-7-MeV C_{60}-ion bombardment.

Carbon sputtering yields were measured with a quartz-crystal microbalance technique. A target carbon film was deposited on a Au electrode of a quartz crystal with resistive heating. The film was conductive and 300-nm thick. C_{60} ions were accelerated to 0.03 to 1.08 MeV and to 1.08 to 6 MeV with the 400-kV ion implanter and the 3-MV tandem accelerator of TIARA, respectively [6]. Sputtering yields by 18-to-100-keV C^+ ions were also measured for comparison.

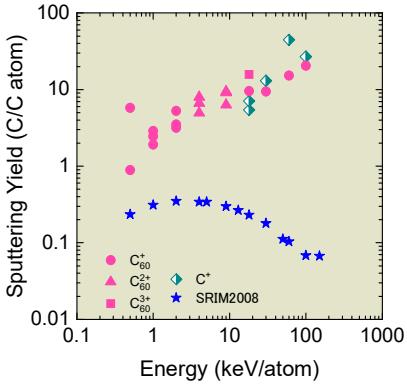

Fig. 1 Dependence of the sputtering yield per atom on energy per atom. Results simulated with the SRIM2008 code are also shown.

Measured carbon sputtering yields are shown in Fig. 1. It should be noted that the abscissa and ordinate represent ion energy per atom and the sputtering yield per atom, respectively. As obvious in the figure, dependence of the sputtering yield per atom on the energy per atom is almost the same for C and C_{60} ions. This indicates that the sputtering yield by C_{60} ions is 60 times as high as that by monatomic C ions, *i.e.*, nonlinear effect on the sputtering yield was not observed.

The measured sputtering yields were compared with those obtained with Monte Carlo simulation using the SRIM2008 code. In the simulation, the target was assumed to be graphite: the lattice binding energy, the surface binding energy and the displacement energy were 3.0 eV, 7.41 eV and 28.0 eV, respectively. The measured sputtering yields are much higher than those obtained with the simulation. In addition, energy dependence of the measured sputtering yield is different from that of the simulation. As known well, the contribution of nuclear collisions is only considered in the SRIM2008 code; thus, the obtained sputtering yields are induced by collisional sputtering. Therefore, the obvious difference between the measured and simulated sputtering yields indicates that the measured sputtering yields are not attributed to collisional sputtering. Further investigation is necessary for discussion on the origin of the carbon sputtering by C_{60}-ion bombardment.

Acknowledgments

The authors are grateful to Dr. Hiroshi Amekura for the preparation of carbon films. This work was supported in part by JSPS KAKENHI Grant Number JP18K05005, and partially supported by the Inter-organizational Atomic Energy Research Program in an academic collaborative agreement among JAEA, QST and the Univ. of Tokyo.

References

[1] H. Dammak *et al.*, Phys. Rev. Lett., **74**, 1135 (1995). DOI: https://doi.org/10.1103/PhysRevLett.74.1135

[2] N. Winograd, Analytical Chemistry, **77**, 142A (2005). DOI: https://doi.org/10.1021/ac053355f

[3] K. Narumi *et al.*, Quantum Beam Science, **6** 12 (2022). DOI: https://doi.org/10.3390/qubs6010012

[4] K. Narumi *et al.*, QST Takasaki Annu. Rep. 2021, **QST-M-39** 106 (2022).

[5] H.H. Andersen and H.L. Bay, Radiat. Effects 19 (1973) 139. DOI: https://doi.org/10.1080/00337577308232233

[6] A. Chiba *et al.*, Quantum Beam Science, **4** 13 (2020). DOI: https://doi.org/10.3390/qubs4010013

4 - 02 Application of dry film resist in proton beam lithography

H. Seki[a)], K. Kawamura[b)], Y. Ishii[c)] and H. Nishikawa[b)]

[a)]SIT Reseach Laboratories, Shibaura Institute of Technology,
[b)]Department of Electrical Engineering, Shibaura Institute of Technology,
[c)]Department of Advanced Radiation Technology, QST

Dry film resist (DFR) is a common material used in printed circuit boards (PCBs) [1]. The benefit of using the DFR is the homogenous film thickness compared to SU-8 film (a typical negative photoresist for MEMS) prepared by a spin coating method. Furthermore, the film thicknesses of the DFR could easily be specified using commercial DFR products. Principally, proton beam lithography, known as PBW, has an advantage over optical and electron beam lithography [2,3] for producing high-aspect-ratio microstructures in thick photoresists such as SU-8 due to MeV protons' straight and deep trajectories. In this work, we report on the examination of applying the PBW to DFRs by studying the sensitivity and developing process.

The DFRs used in this experiment were obtained from Showa Denko Materials Co., Ltd. (RY-5115). The DFR thickness was 15 μm. Before using the DFR, the protective film layer was firstly removed. Then, the lamination process was employed to prepare the DFR on PET film substrates with a thickness of 125 μm. The DFR/PET samples were placed on a hot plate at 110 °C for 10 minutes to enhance the adhesion. Finally, another protective film on the other surface of DFRs was removed before the PBW.

Here, we used the PBW facilities at Shibaura Institute of Technology (Kobe Steel Corp., MB-S1000) with 1 MeV protons and TIARA Takasaki (QST) with 1.7 MeV protons. The beam current was typically 15 – 30 pA with a beam size of about 1 μm. The doses were varied from 0.1 to 50 nC/mm^2 to study the sensitivity of DFR. After the PBW, the irradiated DFRs were developed in a sodium carbonate solution of 1.0 wt% concentration at 30 °C using an ultrasonic cleaner and rinsed in filtered and purified water. The DFRs were evaluated by a laser microscope (OLS4000, Olympus).

Figure 1 shows the relationship between the irradiation proton dose and the maximum height of the DFR after PBW and development. It is seen from the results that the height of the DFRs reached 15 μm, which is the thickness of the DFR film, at a dose above 10 nC/mm^2. Therefore, the sufficient dose for PBW to write the microstructures in DFR was 10 nC/mm^2.

To demonstrate the fabrication of DFR microstructures by PBW, 2x2 pillars were produced. Figure 2 shows the results of the 2x2 pillar pattern of DFRs with diameters of 20, 30, 40, and 50 μm. These micropatterns were made with a dose of 40 nC/mm^2. In this fabrication, the development was achieved under the ultrasonic cleaner for 300 s. However, it should be noted that the DFRs were not developed entirely, and some residual DFRs were observed when the development process was done without using the ultrasonic cleaner.

In summary, the sensitivity of DFRs with proton beam lithography or PBW was studied. It has been shown that the microstructures in thick DFRs can be created using the PBW. This work shows the potential for making high-aspect-ratio microstructures in DFRs.

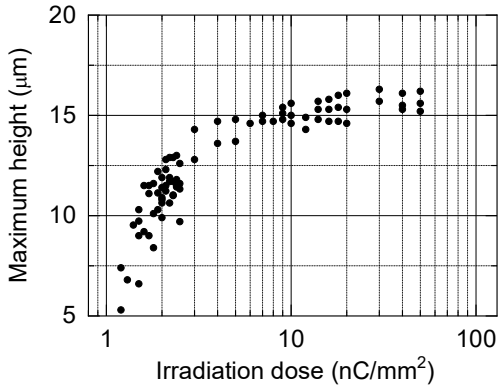

Fig.1 The maximum height in μm of the DFRs after the PBW and development vs. the irradiation doses of 1 MeV protons.

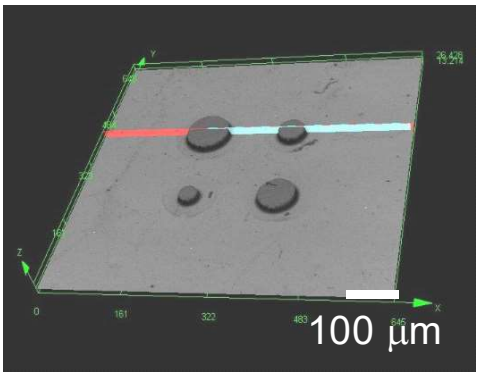

Fig. 2 Laser microscope image of a 2x2 pillar pattern of DFR after fabricating by the PBW and development.

References

[1] F. Khalkhal, K. H. Chaney and S. J. Muller, Microfluid Nanofluid 20, 153 (2016).
[2] N. Uchiya, T. Harada, M. Murai, H. Nishikawa, J. Haga, T. Sato, Y. Ishii and T. Kamiya, Nucl. Instr. and Meth. in Phys. Res. B 260, 405 (2007).
[3] Y. Furuta, H. Nishikawa, T. Satoh, Y Ishii, T. Kamiya, R. Nakao and S. Uchida, Microelectronic Eng. 86, 139 (2009).

4 - 03 Study on high-precision beam energy control for the AVF cyclotron

N. Miyawaki[a)], H. Kashiwagi[a)], S. Watanabe[b)], N. S. Ishioka[b)] and S. Kurashima[a)]

[a)]Department of Advanced Quantum Beam Technology, QST
[b)]Department of Quantum-Applied Biosciences, QST

Introduction

The high-precision control of a beam energy is very important in some experiments in the TIARA AVF cyclotron. For example, in the production of ^{211}At, the production rate increases with the He beam energy, whereas above a certain energy, the isotope ^{210}At, which decays to the highly toxic nuclide ^{210}Po is produced, so the beam energy must be precisely controlled to achieve both a high production rate and no production of ^{210}Po [1]. Previous measurements using our beam energy and position monitor (BEPM) have shown that the cyclotron beam energy does not change in a single operating day, but varies slightly from day to day [2]. The change was considered due to the setting conditions during cyclotron startup and beam tuning. To achieve highly precise control of beam energy, we investigated the parameters responsible for the beam energy change and studied the control of the beam energy using these parameters.

Experiment

The Dee voltage and the correction magnet current were chosen as the parameters causing the beam energy change. This is derived from previous beam tuning histories. To clarify the effect of these parameters on the beam energy, the beam energy was measured with the BEPM at different values of these parameters. The beam trajectory change induced by the beam energy change was also measured by the BEPM. The beam in the experiments was 50MeV $^{4}He^{2+}$, which is used in the ^{211}At production.

Results and Discussion

The measurement results of the beam energy and the horizontal beam position at different Dee voltages are shown in Fig. 1. When the voltage was increased by about 2 kV, the beam energy increased by 0.15 MeV and the horizontal position changed by -15 mm. The horizontal position here was defined as positive to the right and negative to the left with respect to the direction of travel. In the TIARA AVF cyclotron, the beam rotates clockwise and as the beam energy increases, the centrifugal force moves the beam position to the left. This agrees with the measurement results. Then the excitation currents were applied to the harmonic coil, one of the coils used to correct the beam orbit in the cyclotron. Two sets of harmonic coils are installed in the injection and extraction regions of the cyclotron, respectively. The results for only one set in the injection region, where the largest beam energy change was obtained, are shown in Figure 2. When the excitation current of the harmonic coil was varied from -44 A to -6 A, the beam energy increased by about 0.4 MeV and the maximum horizontal position moved to about 10 mm. The excitation current of the harmonic coil was a larger change in the beam energy than the dee voltage and a smaller change in the horizontal position of the beam. Therefore, the excitation current of the harmonic coil is found to be easier to control the beam energy than the dee voltage. Furthermore, by combining these parameters, continuous and precise control of the beam energy over a range of approximately 1% was possible.

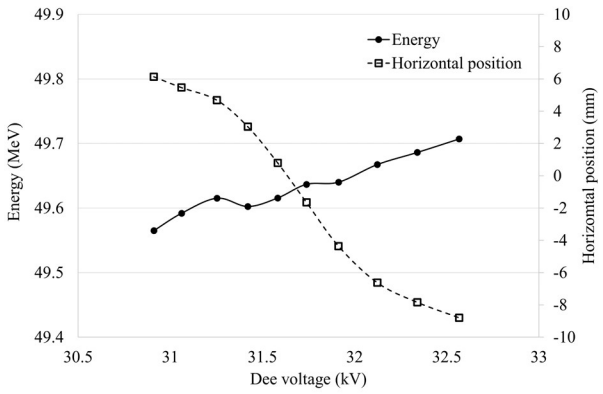

Fig. 1 Measured beam energy and horizontal position at the upstream BEPM with each Dee voltage.

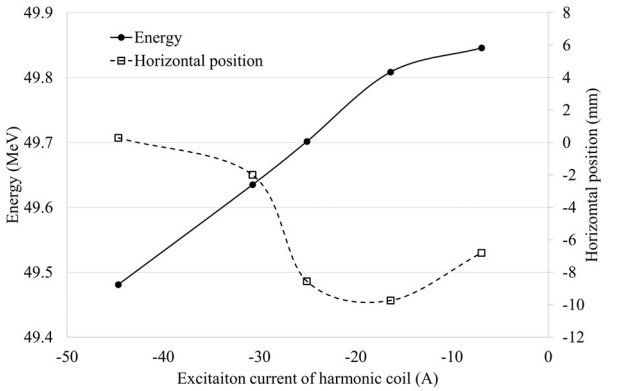

Fig. 2 Measured beam energy and horizontal position at the upstream BEPM with each excitation current of harmonic coil.

Acknowledgments

This work was supported by the JSPS KAKENHI Grant Numbers JP20K08014.

References

[1] Yutian Feng et al., Nuclear Medicine and Biology 100-101, 12 (2021). DOI: 10.1016/j.nucmedbio.2021.05.007
[2] N. Miyawaki et al., QST Takasaki Annu. Rep. 2021, QST-M-39 100 (2022).

4 - 04 Development of new spin-polarized positron source using high-energy proton ion beam

M. Maekawa, A. Miyashita and A. Kawasuso

Takasaki Institute for Advanced Quantum Science, QST

Introduction

The Spin-Polarized Positron Annihilation Spectroscopy method has unique features not found in conventional techniques for evaluating electron spins localized at specific sites, such as atomic vacancies or surface layers. We have developed several spin-polarized positron beam apparatuses equipped with commercial ^{22}Na radioisotopes. Spin polarization and beam intensity are typically ~30 % and ~10^4 e^+/s respectively, however, both performances should be enhanced for further advanced measurements.

As the spin polarization of positrons can be increased by using a nuclide with higher positron emission energy, the above objective can be achieved by generating a large amount of such nuclide with a high nuclear reaction cross section by high-energy ion beam irradiation. There are several nuclides with such properties, for example ^{68}Ge [1]. We are currently focusing on ^{44}Sc. This nuclide can be produced in large quantities though the ^{45}Sc(p,pn)^{44}Sc reaction even with a short irradiation time. The maximum positron emission energy is sufficiently high at 1.5 MeV, which corresponds to a maximum spin polarization of 85 %. In this study, we attempt to generate ^{44}Sc source suitable for producing the spin-polarized positron beam.

Numerical Calculation

The figure 1(a) shows the distribution of ^{44}Sc nuclei calculated using the PHITS code [2] when a scandium (^{45}Sc) metal target is irradiated with a 20 MeV H^+ beam. A production rate of 230 MBq/μA/h of ^{44}Sc is expected within a depth of 0.5 mm from the surface. Although the half-life of ^{44}Sc is 4 hours, positrons can be utilized for approximately a week after the irradiation due to the simultaneous production of ^{44m}Sc with a half-life of 2.4 days. Figure 1(b) slows the simulation of the slow positron generation. Slow positrons of 10^5 e^+/s with a polarization of 58 % are expected just after the H^+ irradiation in 3 hours at 3 μA, which is viable in TIARA cyclotron.

Experimental

A metal Sc target (250 μm x 6 stacked plates) was enclosed in a carbon capsule and irradiated with 20 MeV protons at 2.4 μAh on a water-cooled irradiation stage installed at the LX1 port of TIARA cyclotron. After irradiation, γ-ray spectroscopy was performed using a high-purity Ge detector to quantify the source amount.

Results and Discussion

Figure 2 shows the γ-ray spectrum of the irradiated target. Based on the intensity of prompt γ-rays of ^{44}Sc and positron annihilation 511 keV γ-rays, it was confirmed that ^{44}Sc was produced at a rate of 300 MBq/μA/h, which corresponds to the expected value. Furthermore, we attempted to generate a slow positron beam employing the tungsten moderator, and successfully observed a positron beam as shown in Figure 3. The beam intensity changed in two steps originating from the decay of ^{44}Sc and ^{44m}Sc. Although the exact spin polarization has not yet been measured, it is estimated to be around 50-60 %.

The Sc target can withstand the high current H^+ beam irradiation due to its high melting point (1500 °C) and mechanical robustness. By conducting a 10 μA irradiation for 5 hours, it is expected that ^{44}Sc of 15 GBq and a slow positron beam of 10^6 e^+/s are generated, which may be a world record as the spin-polarized slow positron beam. Ion beam-based ^{44}Sc source is suitable for the spin-polarized positron experiments requiring high positron beam intensity even within a short half-life, such as the positronium Bose-Einstein condensation experiment.

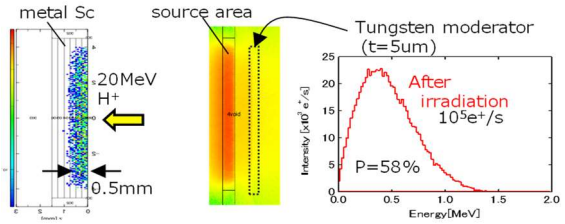

Fig. 1 PHTS simulation of (a) ^{44}Sc production by 20 MeV H^+ irradiation and (b) slow positron generation using tungsten moderator.

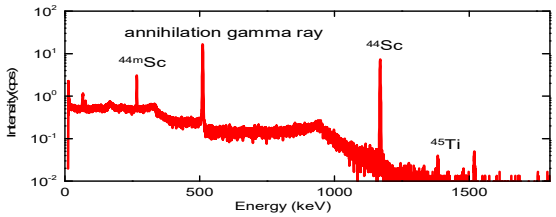

Fig. 2 Gamma ray spectrum from the Sc target after 20 MeV H^+ beam irradiation.

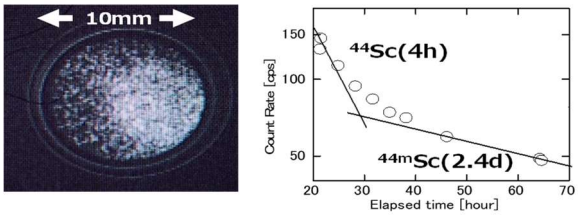

Fig. 3 Profile of slow positron beam and the intensity after irradiation.

References

[1] M. Maekawa et.al., Nucl. Instr. Methods B**308**(2013)9.
[2] T. Sato et.al., J. Nucl. Sci. Technol. **50:9**(2013)913-923.

4 - 05 Radiation effects on Fe-added silica glass studied by positron annihilation spectroscopy

Y. Murakami [a)], M. Yamaguchi [a)], H. Fukazawa [a)],
M. Maekawa[b)] and A. Kawasuso[b)]

a) Nippon Fiber Co.
b) Department of Advanced Radiation Technology, TARRI, QST

Introduction

Nippon Fiber Co. (NFC) is the first company in the world producing continuous long fibers (BASHFIBER®, Fig.1(b)) using fly ash (Fig.1(a)) as the main raw material. For the applications as thermal neutron absorber in the space and nuclear environments, we have also developed the Gd-added material (BASHFIBER US®, Fig.1(c)). Owing to the flexibility and lightweight, fabric can be woven with the BASHFIBER US® (Fig.1(d)). Furthermore, the BASHFIBER® was also found to have robustness under a heavy neutron irradiation as high as 5.85 GGy, while the mechanism is not completely understood.

In this project, we investigate the microscopic origins of the radiation resistance of BASHFIBER® using various methods such as X-ray diffraction (XRD), thermogravimetric and differential thermal analysis (TG-DTA), Raman scattering, and positron annihilation spectroscopy (PAS). PAS is a powerful tool to investigate the void structure included in material. In this report, we summarize the results of PAS measurement on the model glass of BASHFIBER® irradiated with 2 MeV electrons.

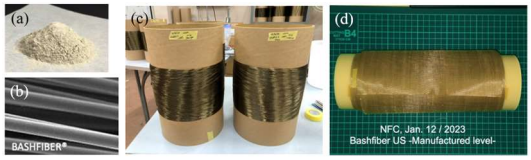

Fig.1. (a) fly ash, (b) SEM image of BASHFIBER®, (c) BASHFIBER US®, (d) BASHFIBER US® fabric

Experimental

A major difference of components between common glass fiber and fly ash fiber would be the presence of Fe. Here, we fabricated the model glass of BASHFIBER® by adding different amounts of Fe_2O_3 (0, 14 and 23wt% of total weight) into silica glass. The samples were prepared in the form of drops through melting at around 1500 °C followed by quenching to room temperature. Subsequently, the samples were irradiated with 2 MeV electrons on a copper plate cooled by running water using the electron accelerator of TARRI, QST.

Positron lifetime measurements were carried out using the anticoincidence method with a ^{22}NaCl source, which can be acquired with one sample (in a conventional set-up, two plate samples are required) [1].

Results and Discussion

Obtained PAS spectra were decomposed into two components by PATFIT code [2]. In Figure2, the intensity ratio of the long-lived (1.3~1.5 ns) component to the short-lived (0.3 ns) component was plotted with Fe_2O_3 content. Long-lived component of the positron lifetime spectrum (positronium, a bound state of an electron and a positron) reflecting the presence of microvoids in material. In the unirradiated states, the intensity decreases with increasing Fe_2O_3 content. This indicates decrease in the amount of microvoid by adding Fe_2O_3.

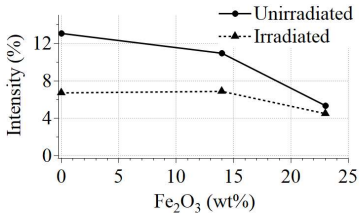

Fig.2. Intensities of long-lived component with different Fe_2O_3 contents in unirradiated state (solid line) and after irradiation (broken line).

After irradiation, the intensity decreases in any Fe_2O_3 contents. This indicates the formation of positron trapping centers (defects) in silica amorphous network competing the positronium formation at microvoids. The difference in intensities before and after irradiation diminishes with the Fe_2O_3 content. Considering the fact that Fe_2O_3 species form amorphous network [3] and the heavier mass of Fe compared to Si, the formation of positron trapping centers is suppressed by adding Fe_2O_3. That is, the radiation resistance would also be improved.

Conclusion

It was found that the Fe_2O_3 addition to silica glass decrease caused the decrease in the long-lived positron annihilation component related to microvoids. This origin is still not clear at present moment, though Fe may exist both in the amorphous network and around microvoids augmenting the structure. Further systematic studies are needed to elucidate the detailed mechanism of radiation resistance of metal-added silica glass and hence to develop new fiber materials in this direction.

References

[1] M. Yamawaki *et al.*, Jpn. J. Appl. Phys. 50, 086301 (2011). DOI:10.1143/JJAP.50.086301
[2] P. Kirkegaard *et al.*, N.J., Computer Physics Communications, 23(3), 307-335 (1981).
[3] B. O. Mysen, Annual Review of Earth and Planetary Sciences, Vol. 11, p.75 (1983).

Part Ⅱ

5. Status of Quantum-Beam Facilities

5-01 Utilization status at the TIARA facility

H. Hanaya[a)], I. Ishibori[a)], S. Watanabe[a)]
N. Kubota[a)], T. Shimizu[b)] and S. Kaneya[c)]

[a)]Department of Advanced Quantum Beam Technology, QST,
[b)]Takasaki Establishment, Radiation Application Development Association
[c)]Beam Operation Co., Ltd.

Research & Industrial Use

Four kinds of accelerators, a cyclotron and three electrostatic accelerators (tandem accelerator, single-ended accelerator and an ion implanter), are used at the TIARA facility to meet various researchers' needs. The activities of research fields that the cyclotron was used for the past 5 fiscal years are shown in Fig. 1. Total utilization time of each fiscal year (FY) was in the range of 480 to 1,280 hours. The utilization time of FY 2018 was lower than the other fiscal years because of repairing of the main coil of the cyclotron. And also, the utilization time of FY 2021 and FY 2022 was lower than FY 2019 and FY 2020 because of changing of the cyclotron daily operating time from 24 hours to 14 hours. The utilization time of "Life Science" and "Material Science" accounted for more than about 60% of the total time.

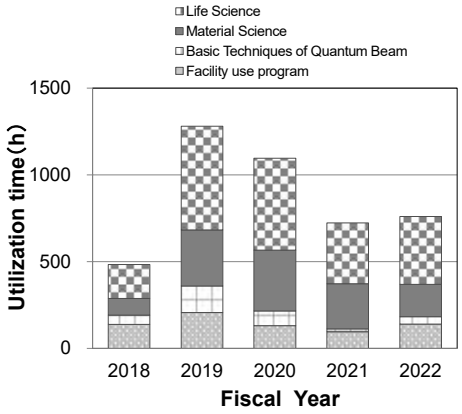

Fig. 1. Research activities for the cyclotron for the past 5 years.

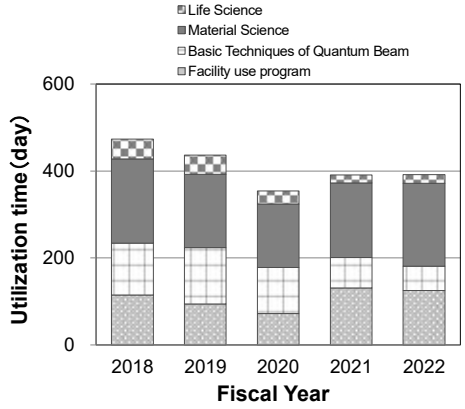

Fig. 2. Research activities for the three electrostatic accelerators for the past 5 years.

On the other hand, for the three electrostatic accelerators, as shown in Fig. 2, the utilization time of "Material Science" and "Basic Technology of Quantum Beam" accounted for more than about 60% of the total time. Total utilization time of each fiscal year was in the range of 390 to 470 days per year except for FY 2020. The utilization time of FY 2020 was reduced to about 350 days per year because of the cancel of experiments under the influence of COVID-19.

The trend of the number of project category (Internal use, Joint research, Cooperation priority research, and Facility use program) for the past 5 years is shown in Fig. 3. The total number of projects was in the range of 59 to 73 per year.

The trend of the number of users in the past 5 years is shown in Fig. 4. The total number of users was in the range of 460 to 665 per year.

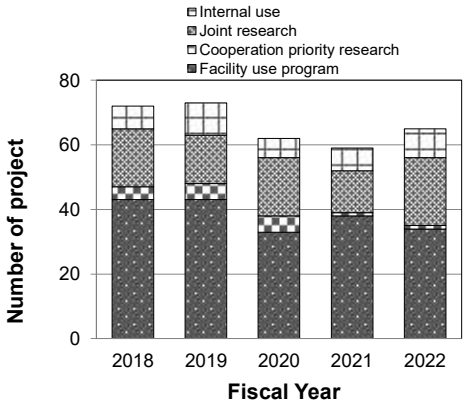

Fig. 3. The number of projects for the past 5 years.

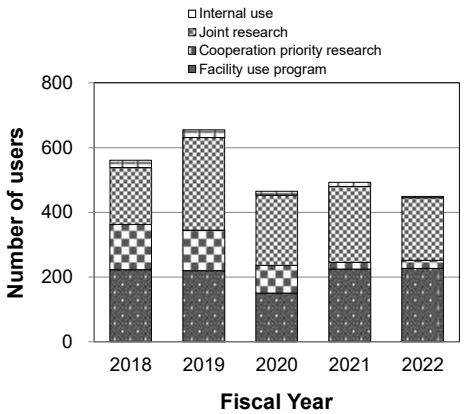

Fig. 4. The number of users for the past 5 years.

5-02 Operation of the AVF cyclotron

K. Yoshida, T. Yuyama, T. Ishizaka, S. Hosoya, I. Ishibori, N. Miyawaki,
H. Kashiwagi, Y. Yuri, T. Nara, S. Ishiro, K. Takano, S. Kurashima

Department of Advanced Quantum Beam Technology, QST

Operation

In fiscal 2022, continuing from last year, the AVF cyclotron was operated daily from 11 am to 22 pm. Although the operation of the cyclotron was smooth without serious trouble, there was concern about suspension of the operation after February due to a sudden rise of electricity prices caused by the war in Ukraine. In December, it became possible to carry out all scheduled operations until March by the additional budgetary measures. The total operation time of the AVF cyclotron eventually amounted to 1269h, and the number of experiments of the year was 168. The accumulative operation time was 90059h and the total number of experiments was 12847 from the first beam extraction in 1991 to March, 2023

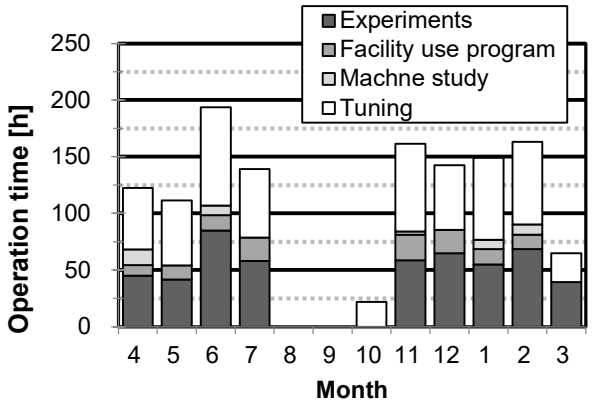

Fig. 1 Monthly operation times in fiscal 2022

Table 1
Statistics for cyclotron operation.

Fiscal year	2022	2021
Beam service time	640 h	708 h
Beam tuning	586 h	627 h
Machine study	42 h	32 h
Total operation time	1269 h	1367 h
Change of particle and/or energy	140 times	143 times
Change of beam course	129 times	141 times
Change of harmonic number	57 times	61 times
The number of experiments	168	189
Cancellation due to machine trouble	0	0

Monthly operation times are shown in Fig. 1. The scheduled maintenances were carried out from the end of July to October and in March. Table 1 shows the statistics of the cyclotron operation of fiscal 2022, with the data of fiscal 2021 for comparison. The percentages of operation time of the year used for regular experiments, facility use program and promotion of shared use program, beam tuning, and beam development are 40.6%, 9.9%, 46.2%, and 3.3%, respectively. Table 2 shows the operation time of each ion source. NANOGAN ion source is used to produce H, D, and He ions. For production of ions heavier than He, HYPERNANOGAN ion source is used. OCTOPUS ion source which has been mainly used for the cocktail beam of M/Q = 5 until fiscal 2021 is a backup ion source for HYPERNANOGAN from fiscal 2022. Therefore, the operation time of OCTOPUS ion source was remarkably reduced. Fractional distribution of major ions used for experiments is shown in Fig. 2. The tendencies of the statistics are similar to those of the past years.

Table 2
Operation times of ion sources.

ECR Ion source	2022	2021
NANOGAN	635 h (47.1%)	504 h (33.3%)
OCTOPUS	13 h (1.0%)	159 h (10.5%)
HYPERNANOGAN	699 h (51.9%)	852 h (56.2%)

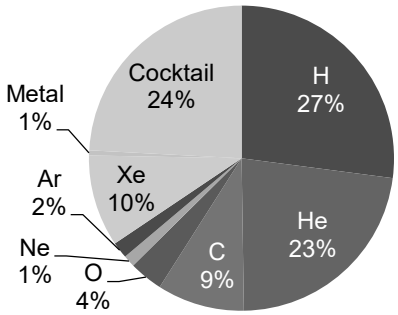

Fig. 2 Ion species used for experiments in fiscal 2022

Machine trouble and maintenance

The number of machine troubles and maintenances of the year were 61 and 68, respectively. Continuing from the last year, the rubber hoses of the cyclotron for cooling water were replaced in summer. In the wake of the fire at the NIRS-930 cyclotron, the smoke detectors in the power supplies for the magnet coils which were installed over 20 years ago were replaced.

The other major items of the maintenance were as follows: 1) Replacement of the controller of the turbo molecular pump of the beam transport line (TTP1). 2) Replacements of the adsorber and the consumable parts of the cryopumps of the cyclotron. 3) Replacement of the fast-closing vacuum valve controller of the HA line. 4) Replacement of the rotary pump of the injection line (HS2). 5) Inspection of the power supplies and the main RF system. 6) Change of lubricating oil for 52 vacuum pumps. 7) Replacements of internal power supply and cooling fan in the control systems.

5-03 Operation of electrostatic accelerators in TIARA

A. Chiba, K. Yamada, Y. Hirano, S. Kanai,
Y. Aoki, M. Hashizume and S. Kurashima

Department of Advanced Quantum Beam Technology, QST

In FY2022, the operation times of three electrostatic accelerators (the 3-MV tandem accelerator, the 3-MV single-ended accelerator and the 400-kV ion implanter) in TIARA were almost the same as in FY2021 when the beam irradiation end time was changed from 22:00 to 17:00. The annual operation times of the tandem accelerator, the single-ended accelerator and the ion implanter were 1134 h, 1297 h and 894 h, respectively. The transitions of the annual operation times since starting operation of each electrostatic accelerator and the accumulated operation times for use patterns are shown in Fig. 1 and Fig. 2, respectively. Although the total operation time of the single-ended accelerator in FY2022 has increased compared to last year, the irradiation time for experiments under internal use and external use (Facility Use Program) has actually decreased due to reduction of users.

Figure 3 shows the utilization rates of ion species in each electrostatic accelerator. The use of H^+ ion beams using the tandem accelerator has expanded, mainly in Facility Use Program. In the ion implanter, the use of ion beams of adenine ($C_5H_5N_5$) developed for multi-qubit formation experiments in the development of quantum sensing technology has been expanding in recent years.

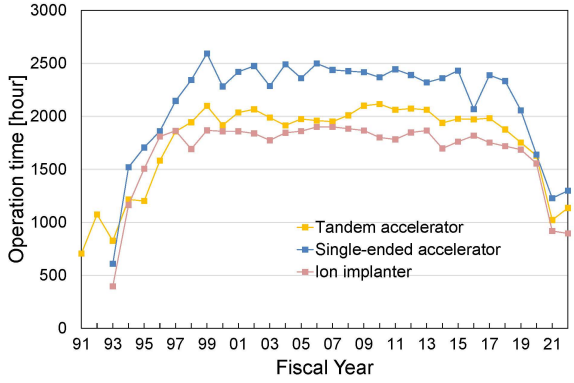

Fig. 1 Transitions of annual operation time.

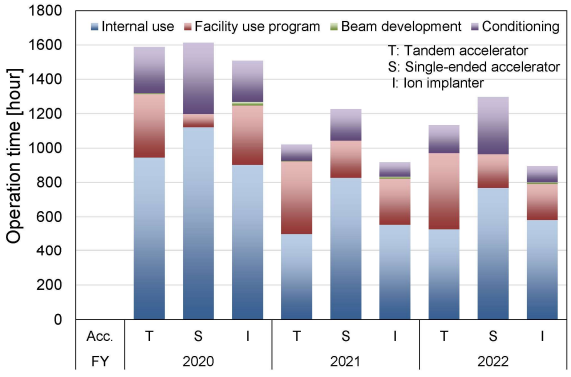

Fig. 2 Operation time for use patterns over the past three years.

Table 1 shows the number of troubles and maintenances in FY2022. As a result of updating the control systems for each accelerator last fiscal year, minor troubles such as hang-up of the device have decreased. Serious troubles that required significant time and costs to recover also rarely occurred in the single-ended accelerator and the ion implanter. On the other hand, there was an increase in serious troubles in the tandem accelerator compared to usual. The main causes of serious troubles were the failure of the high-voltage power supplies which were old and difficult to repair. Maintenance was mainly carried out, such as the renewal of the RF ion source on the single-ended accelerator and various high-voltage power supplies.

Since the daily operation times has been cut in half, the risk that even a minor trouble of the accelerator or related equipment will lead to the cancellation of the experiment has increased. Even a few hours spent repairing equipment or dealing with trouble can derail the experiment. The tandem accelerator had been operating for more than 20 years without cancellation or postponement of experiments, but in FY2022, one experiment for internal use was postponed due to a failure in the cooling system.

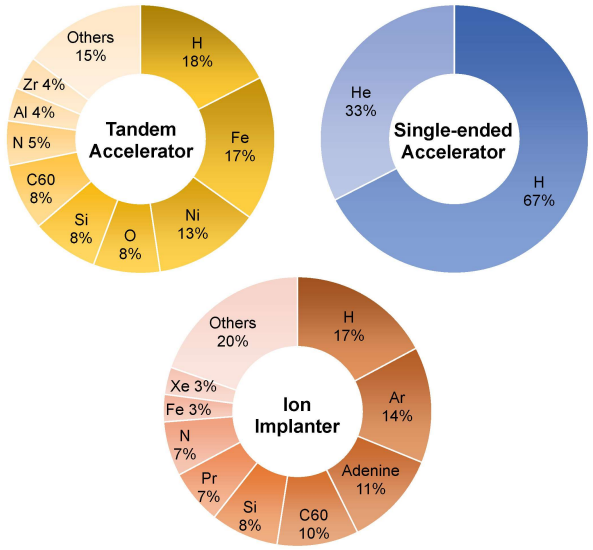

Fig. 3 Utilization rates of ion species.

Table 1
Number of machine troubles and maintenances.

	Tandem Accelerator	Single-ended Accelerator	Ion Implanter
Minor trouble	17	5	13
Serious trouble	9	1	1
Maintenance	30	15	11
Cancellation or Postponement	1	0	0

5-04 Operation, maintenance and utilization status of the gamma-ray irradiation facilities

E. Yokozuka[a)], Y. Nagao[a)], H. Seito[a)], K. Imai[b)], M. Takagi[b)], N. Yagi[b)], K. Akaiwa[b)], S. Kano[b)], T. Agematsu[a)], S. Yamasaki[a)], S. Uno[a), #] and N. Nagasawa[a)]

[a)] Department of Advanced Quantum Beam Technology, QST
[b)] Takasaki Establishment, Radiation Application Development Association
[#] Current affiliation : Beam Operation Co., Ltd

Operation

The ^{60}Co gamma-ray irradiation facilities in Takasaki Advanced Radiation Research Institute (current name: Takasaki Institute for Advanced Quantum Science) were operated almost smoothly in fiscal year (FY) 2022. The food irradiation facility closed at the end of February 2022.

The ^{60}Co gamma-ray irradiation facilities consisting of two buildings with six irradiation rooms cover a wide dose-rate range from 2×10^{-1} Gy/h to 0.9×10^{4} Gy/h as of March 2023. The annual operation times of the first and the second ^{60}Co gamma-ray irradiation facilities were 18,434 h and 27,298 h, respectively, as shown in Fig. 1. Due to seismic retrofitting works on the buildings, the annual operation times of the first and the second ^{60}Co gamma-ray irradiation facilities have been reduced in FY 2021. The annual operation times of the first and second ^{60}Co gamma-ray irradiation facilities in FY 2022 increased from that in FY 2021, when operating times was reduced due to seismic retrofitting works. However, the total annual operation time was lower than that in FY 2020 due to the closure of the food irradiation facility. Additionally, the annual operation time of the first ^{60}Co gamma-ray irradiation facility did not increase significantly due to long-term maintenance.

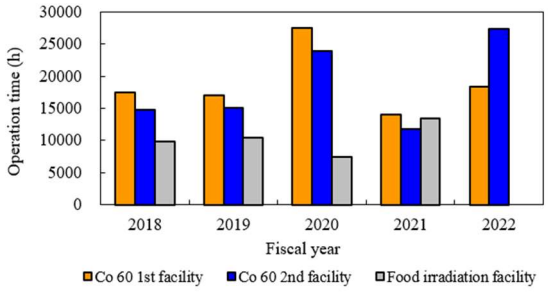

Fig. 1 Annual operation time of the gamma-ray irradiation facilities in the period from FY 2018 to FY 2022.

Maintenance

The ^{60}Co sources at the food irradiation facility were moved to the second ^{60}Co gamma-ray irradiation facility to ensure uniformity of dose distribution in a high-dose-rate field. In addition, the inside of the irradiation rooms of the first ^{60}Co gamma-ray irradiation facilities was repainted for protection of concrete walls. At the first and second ^{60}Co gamma-ray irradiation facilities, we replaced exhaust ducts and replaced indicator lights with LEDs.

The periodical maintenance check mainly on mechanical systems for radiation source transportation is performed every year at one of the gamma-ray irradiation facilities in turn. The maintenance check of the first ^{60}Co gamma-ray irradiation facility was done from October to December 2022 with suspension of operation for 40 days.

Utilization

The two facilities were operated for various research subjects according to the operation plans of the FY 2022. Figure 2 shows the irradiation time and number of experiments in each research field in FY 2022. The facilities were mainly used in the materials science field such as research on metal absorbents, biocompatible protein hydrogels, polymer membrane for fuel cell and radiation-resistant materials and parts of the International Thermonuclear Experimental Reactor (ITER). Furthermore, radiation effects tests on microorganisms and plants in the life science field were conducted.

In the field of materials science, long-term radiation resistance evaluation of fusion reactor equipment and materials are being conducted. On the other hand, in the life science field such as research on the effects of irradiation on animal and plant cells, irradiation time is often short (e.g. the order of a few minutes) and experiments are conducted frequently.

The facility use program is often used to evaluate the radiation resistance of space electronic equipment and nuclear reactor materials.

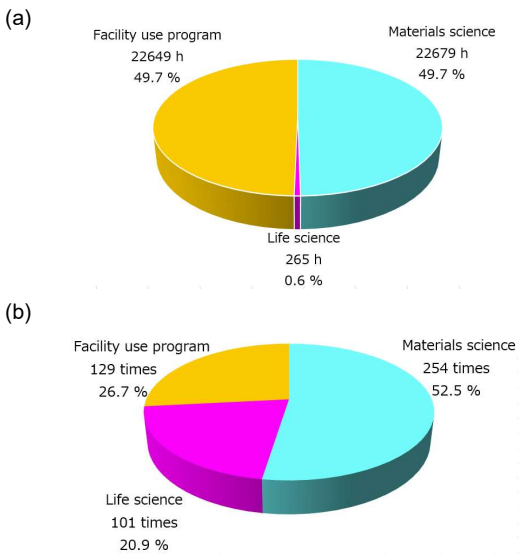

Fig. 2 The irradiation time (a) and number of experiments (b) in each research field in FY 2022.

5-05 Operation, maintenance and utilization status of the electron accelerator

S. Yamasaki [a)], S. Uno [a), #], E. Yokozuka [a)], K. Imai [b)], K. Akaiwa [b)], S. Kano [b)], M. Takagi [b)], N. Yagi [b)], T. Agematsu [a)], Y. Nagao [a)], H. Seito [a)] and N. Nagasawa [a)]

[a)] Department of Advanced Quantum Beam Technology, QST,
[b)] Takasaki Establishment, Radiation Application Development Association
[#] Current affiliation : Beam Operation Co., Ltd

Operation

The electron accelerator in Takasaki Advanced Radiation Research Institute (current name: Takasaki Institute for Advanced Quantum Science) was operated almost smoothly in fiscal year (FY) 2022.The electron accelerator operates from 9:30 to 12:00 and from 13:00 to 17:00 on weekdays, for a maximum of 6.5 hours in a day. The accumulated operation time from the installation to the end of FY2022 reached 29,300 hours.

Maintenance

The main failure cases and maintenance details for the electron accelerator were (1) replacement of the vertical accelerator tube voltage division resistor, (2) electron flow measurement failure and (3) maintenance of the shield door hinges in FY 2022. (1) Bleeder resistance of 1,200 MΩ to 247 MΩ was used for the vertical acceleration tube as a partial pressure resistance, and the resistor more than ten or so stages on the upper side of the acceleration tube had decreased to half the maximum resistance value, so nine resistors were replaced. (2) After the emergency shutdown due to other factors, the beam current fluctuated up to ±3 mA immediately after the start of operation. We determined that a contact failure had occurred and investigated the input and output voltages of the measurement system, repaired the contacts by re-soldering the electronic circuit, and confirmed that they were normal. (3) The shield doors are made of iron with a maximum thickness of 60 cm and a weight of 20 tons. Since the wear of the hinge bearings will impede safe operation and irradiation use, the shield door hinges were replaced in the vertical irradiation room in FY 2021 and in the accelerator room in FY 2022, while that in the horizontal irradiation room has not been replaced yet.

Utilization

The electron accelerator was operated for various research subjects according to the operation plans of the FY 2022. Figure 1 shows annual operation time in the period from FY 2016 to FY 2022 since QST was launched. In FY 2017, the operation time was 750 hours, which is less than the 1,000 hours in previous years, due to repairs on the accelerator power supply, etc. In FY 2020, the operation time was the same as usual due to adjustment operations while responding to the new coronavirus. In FY 2021, there was a long shutdown of about 10 months due to seismic retrofitting works and electronic flow control system update works, etc., therefore, it was reduced to about 300 hours, which is 30% of that in usual years. In FY 2022, there were no major problems, and the instability improvement of the electron flow control system and the maintenance works of the accelerator room shield door were systematically implemented.

Figure 2 shows the irradiation time in each experimental field in FY 2022. The electron accelerator was used by QST users in materials science for the experiments of quantum materials such as diamond for quantum sensors, catalysts for fuel cell and modification of polymers (grafting polymerization, crosslinking and degradation) for biodevices and metal absorbents. It was also used by the facility use program for radiation resistance effect studies on satellites and nuclear reactor materials. More than 60% of the operation time was used for the development of quantum materials, which was having an impact on securing irradiation schedules for other users.

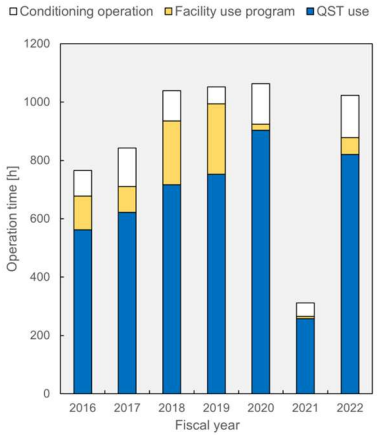

Fig. 1 Annual operation time in the period from FY 2016 to FY 2022.

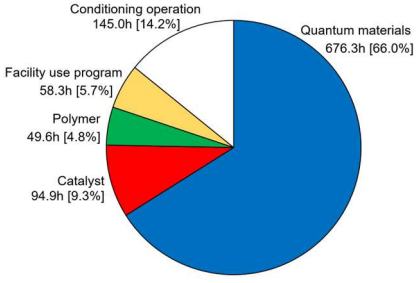

Fig. 2 The irradiation time in each experimental field in FY 2022.

5-06 Radiation monitoring in TIARA

Safety Management Section

Department of Administrative Services, QST

Individual monitoring

(1) Individual monitoring for the radiation workers

Table 1 shows a distribution of effective dose of the radiation workers in FY 2022. The effective dose values of almost all radiation workers were below the detection limit of 0.1 mSv.

The maximum dose of the radiation worker was 0.1 mSv/y, which is due to experiments with unsealed radioisotopes.

Table 1
Distributions of the effective dose of the radiation workers in FY 2022.

Items		Number of persons in each periods				
		1st quarter	2nd quarter	3rd quarter	4th quarter	Annual
Distribution range of effective dose HE:Effective dose *1 (mSv)	HE < 0.1	402	476	518	543	710
	0.1 ≦ HE ≦ 1.0	1	0	0	1	2
	1.0 < HE ≦ 5.0	0	0	0	0	0
	5.0 < HE ≦ 15.0	0	0	0	0	0
	15.0 < HE	0	0	0	0	0
Total number of persons (A)		403	476	518	544	712
Exposure above 1mSv	Number of persons (B)	0	0	0	0	0
	(B)/(A)×100(%)	0	0	0	0	0
Mass effective dose (Person･mSv)		0.1	0.0	0.0	0.1	0.2
Mean dose (mSv)		0.00	0.00	0.00	0.00	0.00
Maximum dose (mSv)		0.1	0.0	0.0	0.1	0.1

*1 The dose by the internal exposure was not detected.

(2) Individual monitoring for the visitors and others

Table 2 shows the number of people who temporarily entered the radiation controlled areas. The effective doses of all people were less than 0.1 mSv.

Table 2
The number of people who temporarily entered the radiation controlled areas in FY 2022.

Periods	1st quarter	2nd quarter	3rd quarter	4th quarter	Total
Number of persons	320	373	740	291	1,724

Monitoring of radioactive gases and dusts

Table 3 shows the maximum radioactive concentrations and total activities for radioactive gases released from the stack of TIARA, during each quarter of FY 2022.

Small amounts of ^{11}C, ^{76}Br and ^{77}Br were detected occasionally during the operation of the cyclotron or experiments, but the particulate substances (^{65}Zn, etc.) were not detected.

Table 3
Monitoring results of released radioactive gases and dust in FY 2022.

Nuclide	Periods / Items	1st quarter	2nd quarter	3rd quarter	4th quarter	Total
^{41}Ar	Maximum concentration	$<1.2\times10^{-4}$	$<1.2\times10^{-4}$	$<1.2\times10^{-4}$	$<1.1\times10^{-4}$	
	Activity	0	0	0	0	0
^{11}C	Maximum concentration	$<1.2\times10^{-4}$	$<1.2\times10^{-4}$	$<1.2\times10^{-4}$	$<1.1\times10^{-4}$	
	Activity	8.5×10^{7}	3.6×10^{7}	2.5×10^{8}	1.7×10^{8}	5.4×10^{8}
^{76}Br	Maximum concentration	—	—	—	3.5×10^{-8}	
	Activity	—	—	—	5.9×10^{5}	5.9×10^{5}
^{77}Br	Maximum concentration	1.8×10^{-8}	—	—	1.0×10^{-8}	
	Activity	3.0×10^{5}	—	—	1.8×10^{5}	4.8×10^{5}
^{65}Zn	Maximum concentration	$<6.3\times10^{-10}$	$<7.1\times10^{-10}$	$<7.2\times10^{-10}$	$<8.2\times10^{-10}$	
	Activity	0	0	0	0	0

Unit : Bq/cm^3 for Maximum concentration, Bq for Activity.

Monitoring for external radiation and surface contamination

The monitoring for external radiation and surface contamination was routinely performed in/around the radiation controlled areas. Neither anomalous value of dose equivalent rate nor surface contamination was detected.

Figure 1 shows a typical example of distribution of the dose equivalent rate in the radiation controlled area of the cyclotron building.

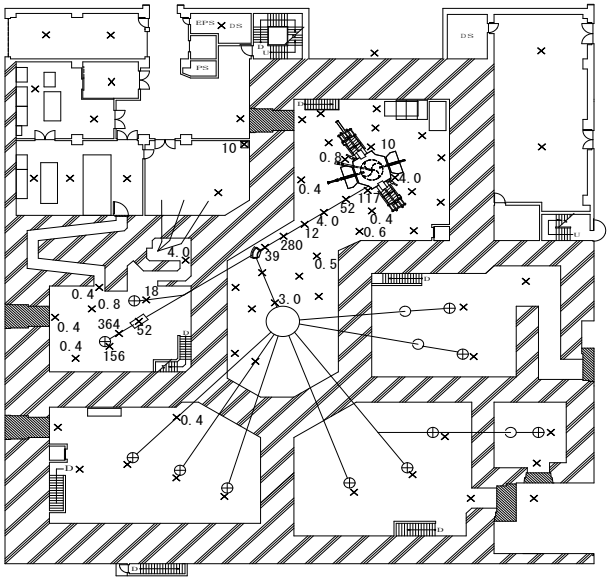

Fig. 1. Dose equivalent rate distribution in the radiation controlled area of the cyclotron building.
Measurement date : 8th and 14th March 2023,
Measuring position : Indicated with × (1 m above floor),
Unit : μSv/h.(The values are not indicated if less than 0.2 μSv/h.)

5-07 Radioactive waste management in TIARA

N. Higuchi [a)], K. Iida [a, b)], H. Hanaya [b)] and S. Watanabe [b)]

[a)]Department of Administrative Services, QST
[b)]Department of Advanced Quantum Beam Technology, QST

Radioactive waste management

The radioactive waste generated in TIARA is managed by Utilization and Coordination Section. The main radioactive waste is the solid waste generated from research experiments and the maintenance of the cyclotron. Other radioactive waste is the liquid waste such as inorganic waste fluids generated from research experiments and the air-conditioning machines in the radiation controlled area. These wastes are managed according to their properties. Radioactive waste is stored in a storage facility and handed over to the Japan Radioisotope Association for disposal.

Solid radioactive waste

Table 1 shows the amounts of various types of solid waste generated in each quarter of FY 2022. Combustible waste consists of papers and clothes, and so on. Flame-retardant waste consists of rubber gloves, plastic articles, and polyethylene articles. Incombustible waste consists of metal pieces and the glasses, and so on. Solid waste emitting α, β, and γ is classified according to the properties.

Liquid radioactive waste

Table 2 shows the amounts of liquid waste generated in each quarter of FY 2022. The main liquid waste is inorganic water, which consists of condensed water generated from the air-conditioner installed in the radiation controlled area and waste water generated from chemical experiments. In Table 2, large amount of inorganic waste water is generated in 1st and 2nd quarters. It is due to the condensed water generated from the air-conditioner. To reduce the inorganic waste water, distillation of the inorganic waste water is carried out. After the distillation, small amount of distillation residual liquid remains, and that is discarded for liquid waste. On the other hand, the purified water prepared by distillation is reused in the radiation controlled area.

Table 1
Radioactive solid waste generated in FY 2022.

Items \ Amounts	Amounts of generation in each period (m^3)					Number of package /drum
	1st quarter	2nd quarter	3rd quarter	4th quarter	Total	
Category β, γ*	0.13	0	0.04	0.30	0.47	17 **
Combustible	0	0	0.02	0.10	0.12	3 **
Flame-retardant	0	0	0.02	0.14	0.16	12 **
Incombustible(Compressible)	0	0	0	0.04	0.04	1 **
〃 (Incompressible)	0	0	0	0	0	0
Laboratory animal	0	0	0	0.02	0.02	1
Filters	0.13	0	0	0	0.13	-
Category α*	0	0	0	0.26	0.26	8
Combustible	0	0	0	0.02	0.02	0
Flame-retardant	0	0	0	0.20	0.20	8
Incombustible(Compressible)	0	0	0	0.02	0.02	0
〃 (Incompressible)	0	0	0	0	0	0
Laboratory animal	0	0	0	0.02	0.02	0
Filters	0	0	0	0	0	-

* defined by amount in Bq (β, γ): < 2 GBq , (α) : < 37 MBq,
** 50-liter drum.

Table 2
Radioactive liquid waste generated in FY 2022.

Items \ Amounts	Amounts of generation in each period (m^3)					Number of package /drum
	1st quarter	2nd quarter	3rd quarter	4th quarter	Total	
Category β, γ*	23.83	17.30	4.39	0.91	46.43	-
1)Inorganic	23.83	17.30	4.39	0.91	46.43	-
Inorganic	23.83	17.30	4.39	0.91	46.43	0
Distillation residual liquid, Sludge	0.00	0.00	0.00	0.00	0.00	2 **
2)Organic	0.00	0.00	0.00	0.00	0.00	0
Organic	0.00	0.00	0.00	0.00	0.00	0
Oil	0.00	0.00	0.00	0.00	0.00	0
Category α*	0.00	0.00	0.00	0.00	0.00	0

* defined by concentrations in Bq/mL (β, γ Inorganic) : < 200 kBq, (Organic) : < 2 kBq, (α) : ≤ 1.85 kBq,
** 50-liter drum.

5-08 The Shared Use Program of QST facilities in Takasaki Institute

S. Nozawa, H. Hanaya and A. Shimada

Department of Research Planning and Promotion, QST

Introduction

Irradiation facilities in Takasaki Institute for Advanced Quantum Science have been opened to many researchers who belongs to universities, public institutes, and R&D divisions of private companies (hereafter 'external users'), under the Shared Use Program of QST Facilities (hereafter 'Shared Use Program).

In this program, external users can conduct irradiation experiments by using gamma-rays, electron beams, and ion beams, these were provided from irradiation facilities of Co-60 gamma-ray, electron accelerator, and TIARA's four ion accelerators. When using these facilities, external users are required to bear the operating costs of each irradiation equipment.

Pricing of Shared Use Program

In pricing system of Shared Use Program, experimental charges have been calculated from the total amount of service charge, irradiation charge, and extra-costs (e.g., additional consumable goods and human support).

Research-and-development's users, who disclose the results of studies by publication, have been partially discounted for the experimental charge. To receive this discount, users were required to submit a research proposal to Research Planning and Promotion Office. The proposals will be considered by expert committee members, in terms of the effectiveness of experimental plans. The approved proposals are implemented with the partially discounted charges. This partial discount not applied at gamma-ray irradiation facilities and electron accelerator.

Number of irradiation experiments under Shared Use Program in FY2022

Number of irradiation experiments under Facility Use Program in FY2022 were shown in Table 1. The number of experiments in Co-60 gamma-ray irradiation facilities was much higher than other irradiation facilities.

In Table 2, number of experiments classified by user's affiliation were shown. AVF cyclotron, 3 MV tandem accelerator, 3 MV single-ended accelerator, 400 kV ion implanter and Electron accelerator were mainly used by researchers who belonging to public sectors such as universities and institutes. On the other hand, many users of Co-60 gamma ray irradiation facilities were belonging to private companies.

Additional information about this program is available at the following QST website:

https://www.qst.go.jp/site/shisetsukyoyo-takasaki/

Table 1
Number of irradiation experiments under the Shared Use Program of QST Facilities in FY2022

Irradiation facility \ Pricing system		Public disclosure	Non-disclosure	Total
TIARA	AVF cyclotron	13	16	29
	3 MV tandem accelerator	27	19	46
	3 MV single-ended accelerator	11	9	20
	400 kV ion implanter	7	15	22
Co-60 gamma-ray irradiation facilities		-*	145	145
Electron accelerator		-*	22	22
Total		58	226	284

*: Discounting was not applied

Table 2
Number of irradiation experiments classified by user's affiliations

Irradiation Facility \ User's affiliation		University	Public institute	Private company	Total
TIARA	AVF cyclotron	17	3	9	29
	3 MV tandem accelerator	28	12	6	46
	3 MV single-ended accelerator	11	9	0	20
	400 kV ion implanter	16	6	0	22
Co-60 gamma-ray irradiation facilities		32	19	94	145
Electron accelerator		15	2	5	22
Total		119	51	114	284

Appendix

Appendix：Publication List

P1-1 Quantum Sensing Project

Papers

1. **Fluorescent HPHT nanodiamonds have disk- and rod-like shapes.**
   Samir Eldemrdash, Giannis Thalassions, Amani Alzahrani, Qiang Sun, Ella Walsh, Erin Grant, Abe Hiroshi, Tamar L. Greaves, Ohshima Takeshi, Petr Gigler, Pavel Matejicek, David A. Simpson, Andrew D. Greentree, Gary Bryant, Brant G. Gibson, Philipp Reineck, Carbon, (206), 268, 2023.
   DOI:https://doi.org/10.1016/j.carbon.2023.02.018
2. **Spin-Dependent Photocarrier Generation Dynamics in Electrically Detected NV-Based Quantum Sensor.**
   Hiroki Morishita, Naoya Morioka, Tetsuri Nishikawa, Hajime Yao, Onoda Shinobu, Abe Hiroshi, Ohshima Takeshi, Norikazu Mizuochi, Physcal Review Applied, 19, 034061, 2023. DOI:10.1103/PhysRevApplied.19.034061
3. **Effects of He ion and electron beam irradiation on a CdTe solar cell dosimeter in a substrate configuration.**
   Tamotsu Okamoto, Fumiya Furumaki, Eiku Sato, Ippei Isogai, Yuji Kurimoto, Yasuki Okuno, Mitsuru Imaizumi, Masafumi Akiyoshi, Ohshima Takeshi, Japanese Journal of Applied Physics, 62, SK1004, 2023.
   DOI:10.35848/1347-4065/acbd92
4. **Electrical detection of nuclear spins via silicon vacancies in silicon carbide at room temperature.**
   Tetsuri Nishikawa, Naoya Morioka, Abe Hiroshi, Hiroki Morishita, Ohshima Takeshi, Norikazu Mizuochi, Applied Physics Letters, (121), 184005, 2023,
   DOI: 10.1063/5.0115928
5. **M-center in low-energy electron irradiated 4H-SiC.**
   Tihomir Knezevic, Amira Hadzipasic, Ohshima Takeshi, Makino Takahiro, Ivana Capan, Applied Physics Letters, 2023. DOI:https://doi.org/10.1063/5.0095827
6. **Distinguishing the EH_1 and S_1 defects in n-type 4H-SiC by Laplace DLTS.**
   Tihomir Knežević, Tomislav Brodar, Vladimir Radulović, Luka Snoj, Makino Takahiro, Ivana Capan, Applied Physics Express, 2023.
   DOI:https://doi.org/10.35848/1882-0786/ac8f83
7. **Linear energy transfer (LET) spectroscopy and relative biological effect estimation by SiC-based dosimeter at clinical carbon-beam cancer therapy field.**
   Kohei Yamaguchi, Yanagisawa Rio, Kohei Osaki, Yuya Ohki, Matsumura Akihiko, Sakai Makoto, Makino Takahiro, Ohshima Takeshi, Kada Wataru, Journal of Physics: Conference Series, 2023. DOI:10.1088/1742-6596/2326/1/012015
8. **Transfer-printing-based integration of silicon nitride grating structure on single-crystal diamond toward sensitive magnetometers.**
   Ryota Katsumi, Takeshi Hizawa, Akihiro Kuwahata, Shun Naruse, Yuji Hatano, Takayuki Iwasaki, Mutsuko Hatano, Fedor Jelezko, Onoda Shinobu, Ohshima Takeshi, Masaki Sekino, Takashi Yatsui, Applied Physics Letters, (121), 16103, 2022. DOI:10.1063/5.0107854
9. **Multiple tin-vacancy centers in diamond with nearly identical photon frequency and linewidth.**
   Yasuyuki Narita, Peng Wang, Keita Ikeda, Kazuki Oba, Yoshiyuki Miyamoto, Takashi Taniguchi, Onoda Shinobu, Hatano Mutsuko, Takayuki Iwasaki, Physical Review Applied (19), 024061, 2023.
   DOI:10.1103/PhysRevApplied.19.024061
10. **Growth of vanadium doped semi-insulating 4H-SiC epilayer with ultrahigh-resistivity.**
    Kazutoshi Kojima, Sato Shinichiro, Ohshima Takeshi, Shin-Ichiro Kuroki, Journal of Applied Physics, 131(24), 245107, 2022.DOI:10.1063/5.0095457
11. **Differences in radiation damage to carrier lifetimes in the neutral and depletion regions of InGaP and GaAs solar cells.**
    Tetsuya Nakamura, Mitsuru Imaizumi, Sato Shinichiro, Ohshima Takeshi, Hidefumi Akiyama, Yoshitaka Okada, Journal of Applied Physics, 132(11), 115701, 2022. DOI:10.1063/5.0099106
12. **Integrated 4H-SiC Photosensors with Active Pixel Sensor-type Circuits for MGy-class Radiation Hardened CMOS UV Image Sensor.**
    Masayuki Tsutsumi, Tatsuya Meguro, Takeyama Akinori, Takeshi Ohshima, Yasunori Tanaka, Shin-Ichiro Kuroki, IEEE Electron Device Letters, 44(1), 100, 2022.
    DOI:10.1109/LED.2022.3226494
13. **Nitrogen related paramagnetic defects: Decoherence source of ensemble of NV- center.**
    Chikara Shinei, Masuyama Yuta, Masashi Miyakawa, Abe Hiroshi, Ishii Shuya, Saiki Seiichi, Onoda Shinobu, Takashi Taniguchi, Ohshima Takeshi, Tokuyuki Teraji, AIP Journal of Applied Physics, 132, 214402, 2022. DOI:10.1063/5.0103332
14. **Quantum nonlinear spectroscopy of single nuclear spins.**
    Jonas Meinel, Vadim Vorobyov, Ping Wang, Boris Yavkin, Mathias Pfender, Hitoshi Sumiya, Onoda Shinobu, Junichi Isoya, Ren-Bao Liu, J. Wrachtrup, Nature Communications, 13, 5318, 2022. DOI:10.1038/s41467-022-32610-8
15. **Quantum-assisted distortion-free audio signal sensing.**
    Chen Zhang, Durga Dasari, Matthias Widmann, Jonas Meinel, Vadim Vorobyov, Polina Kapitanova, Elizaveta Nenasheva, Kazuo Nakamura, Hitoshi Sumiya, Onoda Shinobu, Junichi Isoya, Nature Communications, 13, 4637, 2022. DOI:10.1038/s41467-022-32150-1
16. **Magnetic-field-dependent stimulated emission from nitrogen-vacancy centers in diamond.**
    Felix A. Hahl, Lukas Lindner, Xavier Vidal, Tingpeng Luo, Ohshima Takeshi, Onoda Shinobu, Ishii Shuya,

Alexander M. Zaitsev, Marco Capelli, Brant C. Gibson, Andrew D. Greentree, Jan Jeske, Sience Advances, 8(22), eabn7192, 2022. DOI:10.1126/sciadv.abn7192

17. **Loop-gap microwave resonator for millimeter-scale diamond quantum sensor.**
Daisuke Nishitani, Takayuki Shibata, Kazuhiro Oyama, Fan. Cheng, Yuji Hatano, Tokuyuki Teraji, Onoda Shinobu, Ohshima Takeshi, Takayuki Iwasaki, Mutsuko Hatano, Materials Today Communications, 31, 103488, 2022. DOI:10.1016/j.mtcomm.2022.103488
18. **High-precision robust monitoring of charge/discharge current over a wide dynamic range for electric vehicle batteries using diamond quantum sensors.**
Yuji Hatano, Jaewon Shin, Junya Tanigawa, Yuta Shigenobu, Akimichi Nakazono, TakeharuSekiguchi, Onoda Shinobu, Ohshima Takeshi, Keigo Arai, Takayuki Iwasaki, Mutsuko Hatano, Scientific Reports, 12, 13991, 2022. DOI:10.1038/s41598-022-18106-x
19. **Creation of multiple NV centers by phthalocyanine ion implantation.**
Kimura Kosuke, Onoda Shinobu, Yamada Keisuke, Wataru Kada, Tokuyuki Teraji, Junichi Isoya, Osamu Hanaizumi, Ohshima Takeshi, Applied Physics Express, 15(6), 066501, 2022. DOI:10.35848/1882-0786/ac7030
20. **Millimetre-scale magnetocardiography of living rats with thoracotomy.**
Keigo Arai, Akihiro Kuwahata, Daisuke Nishitani, Ikuya Fujisaki, Ryoma Matsuki, Yuki Nishio, Zonghao Xin, Xinyu Cao, Yuji Hatano, Onoda Shinobu, Chikara Shinei, Masashi Miyakawa, Takashi Taniguchi, Masatoshi Yamazaki, Tokuyuki Teraji, Ohshima Takeshi, Mutsuko Hatano, Masaki Sekino, Takayuki Iwasaki, Communication Physics, 5, 200, 2022. DOI:10.1038/s42005-022-00978-0
21. **Mechanism of improved crystallinity by defect-modification in proton-irradiated GaAsPN photovoltaics: Experimental and first-principle calculations approach.**
Keisuke Yamane, Yuito Maki, Shun One, Akihiro Wakahara, Emil-Mihai Pavelescu, Ohshima Takeshi, Tetsuya Nakamura, Mitsuru Imaizumi, Journal of Applied Physics, 132(6), 065701, 2022. DOI:10.1063/5.0096345
22. **Imaging Current Paths in Silicon Photovoltaic Devices with a Quantum Diamond Microscope.**
S.C. Scholten, G.J. Abrahams, B.C. Johnson, A.J. Healey, I.O. Robertson, D.A. Simpson, A. Stacey, Onoda Shinobu, Ohshima Takeshi, T.C. Kho, J. Ibarra Michel, J. Bullock, L.C.L. Hollenberg, J.-P. Tetienne, Physical Review Applied, 18(1), 014041, 2022. DOI:10.1103/PhysRevApplied.18.014041
23. **Modified divacancies in 4H-SiC.**
N. T. Son, D. Shafizadeh, Ohshima Takeshi, I. G. Ivanov, Journal of Applied Physics, 132(2), 025703, 2022. DOI:10.1063/5.0099017
24. **Hybrid Pixels With Si Photodiode and 4H-SiC MOSFETs Using Direct Heterogeneous Bonding Toward Radiation Hardened CMOS Image Sensors.**
Tatsuya Meguro, Takeyama Akinori, Ohshima Takeshi, Yasunori Tanaka, Shin-Ichiro Kuroki, IEEE Electron Device Letters, 43(10), 1713, 2022. DOI:10.1109/LED.2022.3200124
25. **Characteristic Charge Collection Mechanism Observed in FinFET SRAM Cells.**
Kozo Takeuchi, Keita Sakamoto, Kazuki Yukumatsu, Kyota Watanabe, Yuta Tsuchiya, Takashi Kato, Hideya Matsuyama, Akinori Takeyama, Ohshima Takeshi, Satoshi Kuboyama, Hiroyuki Shindo, IEEE Transactions on Nuclear Science, 69(8), 1833, 2022. DOI:10.1109/TNS.2022.3188993
26. **Threshold voltage instability and hysteresis in gamma-rays irradiated 4H-SiC junction field effect transistors.**
Takeyama Akinori, Makino Takahiro, Yasunori Tanaka, Shin-Ichiro Kuroki, Ohshima Takeshi, Journal of Applied Physics, 131, 244503, 2022. DOI:10.1063/5.0095841
27. **Membrane-supported LSI with integrated heater and temperature monitor for on-site annealing-recovery from 20 kGy gamma ray irradiation damage.**
Tianjiao Gong, Yukio Suzuki, Takeyama Akinori, Ohshima Takeshi, Shuji Tanaka, Sensors and Actuators: A. Physical, 343, 113677, 2022. DOI:10.1016/j.sna.2022.113677
28. **Spin-Optical Dynamics and Quantum Efficiency of a Single V1 Center in Silicon Carbide.**
Naoya Morioka, Di Liu, Oney O. Soykal, Izel Gediz, Charles Babin, Rainer Stohr, Ohshima Takeshi, Nguyen Tien Son, Jawad Ul-Hassan, Florian Kaiser, Jorg Wrachtrup, Physical Review Applied, 17, 054005, 2022. DOI:10.1103/PhysRevApplied.17.054005
29. **Structural analysis of high-energy implanted Ni atoms into Si(100) by X-ray absorption fine structure spectroscopy.**
Entani Shiro, Sato Shinichiro, Honda Mitsunori, Suzuki Chihiro, Taguchi Tomitsugu, Yamamoto Shunya, Ohshima Takeshi, radiation physics and chemistry, 199, 110369, 2022. DOI:10.1016/j.radphyschem.2022.110369
30. **Effects of omecamtiv mecarbil on the contractile properties of skinned porcine left atrial and ventricular muscles.**
Tomohiro Nakanishi, Oyama Kotaro, Hiroyuki Tanaka, Fuyu Kobirumaki-Shimozawa, Ishii Shuya, Takako Terui, Shin'ichi Ishiwata, Norio Fukuda, Frontiers in Physiology, 13, 947206, 2022. DOI:10.3389/fphys.2022.947206
31. **Broadband microwave antenna for uniform manipulation of millimeter-scale volumes of diamond quantum sensors.**
Y. Takemura, K. Hayashi, Y. Yoshii, M. Saito, S. Onoda, H. Abe, T. Ohshima, T. Taniguchi, M.Fujiwara, H. Morishita, I. Ohki, N. Mizuochi, Journal of Applied Physics, 132(22), 224501, 2022. DOI:10.1063/5.0128406

Patents

1. **窒素－空孔複合欠陥を有する材料の製造方法、製造装置、製造プログラム、及び窒素－空孔複合欠陥を有する材料.**
五十嵐 龍治, 神長 輝一, 大島 武, 阿部 浩之, 佐伯 誠一, 特願2023-27810 (2023.2.24).

2. **カラーセンター特性の測定方法および測定装置.**
   増山 雄太, 大島 武, 特願2022-163487 (2022.10.11).
3. **量子素子およびその製造方法.**
   山口 尚秀, 蔭浦 泰資, 笹間 陽介, 谷口 尚, 渡邊 賢司, 小野田 忍, 特願2022-126696 (2022.8.8).
4. **センサ.**
   村田 晃一, 浅田 聡志, 佐藤 真一郎, 増山 雄太, 特願2022-040303 (2022.3.15).
5. **ダイヤモンド単結晶およびその製造方法.**
   小野田 忍, 春山 盛善, 大島 武, 千葉 敦也, 平野 貴美, 五十嵐 龍治, 特許第7070904号 (2022.5.10).

P1-2 Spin-photonics in 2D Materials Project

Papers

1. **Multi-channel dissociative ionization of ethanol in intense ultraviolet laser fields: Energy correlation between photoelectron emission and fragment recoil.**
   Ikuta Tomoya, Hosaka Kouichi, Akagi Hiroshi, Kannari Fumihiko, Itakura Ryuji, Physical Review A, 106(2), 023106, 2022. DOI:10.1103/PhysRevA.106.023106
2. **Half-Metallic Heusler Alloy/MoS_2 Based Magnetic Tunnel Junction.**
   Konstantin V. Larionov, Jose J. Pais Pereda, Li Songtian, Sakai Seiji, Pavel B. Sorokin, ACS Applied Materials & Interfaces, 14(49), 55167, 2022.
   DOI:https://doi.org/10.1021/acsami.2c09655
3. **Study on FeCr thin film for a spintronic material with negative spin polarization.**
   Hirofumi Suto, Tomoya Nakatani, Yohei Kota, Asam Nagarjuna, Hitoshi Iwasaki, Kenta Amemiya, Takaya Mitsui, Seiji Sakai, Songtian Li, Yohei Kota, Yuya Sakuraba, Journal of Magnetism and Magnetic Materials, 557, 169474, 2022. DOI:10.1016/j.jmmm.2022.169474

Patent

1. **鉄含有擬立方晶マンガン基フェリ磁性ホイスラー合金、及び、これを用いた磁気抵抗記憶素子.**
   境 誠司, Bentley Phillip David, 李 松田, 三井 隆也, 藤原 孝将, 増田 啓介, 三浦 良雄, 特願2023-027745 (2023.2.24).

P1-3 Laser-cooled Ion Research Project

Papers

1. **Upconversion time-stretch infrared spectroscopy.**
   Kazuki Hashimoto, Takuma Nakamura, Takahiro Kageyama, Venkata Ramaiah Badarla, Shimada Hiroyuki, Ryoich Horisaki, Takuro Ideguchi, Light : Science＆Applications, 12(1), 48, 2023.
   DOI:https://doi.org/10.1038/s41377-023-01096-4
2. **Multi-channel dissociative ionization of ethanol in intense ultraviolet laser fields: Energy correlation between photoelectron emission and fragment recoil.**
   Ikuta Tomoya, Hosaka Kouichi, Akagi Hiroshi, Kannari Fumihiko, Itakura Ryuji, Physical Review A, 106(2), 023106, 2022. DOI:10.1103/PhysRevA.106.023106

P1-4 Quantum Optical and Spin State Control Project

Paper

1. **Lifetime of spin-orbit induced spin textures in a semiconductor heterostructure probed by quantum corrections to conducitivity.**
   Takahito Saito, Toshimichi Nishimura, Ju-Young Yoon, Jonas Kolzer, Daisuke Iizasa, Micahel Kammermeier, Thomas Schapers, Junsaku Nitta, Kohda Makoto, Physical Review Research, 4(4), 043217, 2022.
   DOI:10.1103/PhysRevResearch.4.043217

Press

1. **材料の種類によらず電子スピン波を観測できる新手法を構築－さまざまな半導体における超並列演算処理へ期待－.**
   東北大学・QST, 2023.1.23 プレス発表; TECH+等に掲載

P1-5 Quantum Materials Theory Project

Papers

1. **Large intrinsic spin Hall conductivity in orthorhombic tungsten.**
   Akashi Ryosuke, Physical Review Materials, 7(2), 026202, 2023.
   DOI:10.1103/PhysRevMaterials.7.026202
2. **Semiconducting electronic structure of the ferromagnetic spinel $HgCr_2Se_4$ revealed by soft-x-ray angle-resolved photoemission spectroscopy.**
   Akashi Ryosuke, Physical Review Letters, 130(18), 186402, 2023.
   DOI:https://doi.org/10.1103/PhysRevLett.130.186402
3. **Lattice dielectric properties of rutile TiO_2: First-principles anharmonic self-consistent phonon study.**
   Akashi Ryosuke, Physical Review B, 107, 094305, 2023.
   DOI:10.1103/PhysRevB.107.094305

P1-6 Rare-earth Quantum Device Project

Paper

1. **Photon extraction enhancement of praseodymium ions in gallium nitride nanopillars.**
   Sato Shinichiro, Shuo Li, Andrew D. Greentree, Manato Deki, Tomoaki Nishimura, Hirotaka Watanabe, Shugo Nitta, Yoshio Honda, Hiroshi Amano, Brant C. Gibson, Ohshima Takeshi, Scientific Reports, 12, 21208, 2022.
   DOI:10.1038/s41598-022-25522-6

P1-7 Quantum Materials Ultrafine Fabrication Project

Papers

1. **Comparison of Photoresist Sensitivity between KrF, EB and EUV Exposure.**
   Oota Yousuke, Sekiguchi Atsushi, Shinji Yamakawa, Tetsuo Harada, Takeo Watanabe, Yamamoto Hiroki, Journal of Photopolymer Science and Technology, 35(1), 49, 2022.
2. **Dependence of Dissolution Kinetics of Main-Chain Scission Type Resists on Molecular.**
   Akihiro konda, Yamamoto Hiroki, Shusuke Yoshitake, Journal of Photopolymer Science and Technology, 35(1), 1, 2022.

Patents

1. **レジスト材料、レジストパターンの製造方法、及び、レジストパターン.**
   吉村 公男, 出崎 亮, 山本 洋揮, タンフン ヂン, 石野 雅彦, 錦野 将元, 前川 康成, 古澤 孝弘, 特願2022-067860 (2022.4.15).
2. **感光性化合物、感光性組成物及びパターン形成方法.**
   山本 洋揮, 特願2022-047100 (2022.3.23).
3. **感光性組成物及びパターン形成方法.**
   山本 洋揮, 特願2022-047099 (2022.3.22).

P2-1 Functional Polymer Project

Papers

1. **Unique Structural Characteristics of Graft-Type Proton-Exchange Membranes using SANS Partial Scattering Function Analysis.**
   Yue Zhao, Yoshimura Kimio, Sawada Shinichi, Motegi Toshinori, Hiroki Akihiro, Aurel Radulescu, Maekawa Yasunari, Macromolecules, 55(16), 7100, 2022.
   DOI:10.1021/acs.macromol.2c00333
2. **Preparation and evaluation of hydrogel film containing tramadol for reduction of peripheral neuropathic pain.**
   Nobuyuki Natori, Yuki Shibano, Akihiro Hiroki, Mitsumasa Taguchi, Atsushi Miyajima, Kazumi Yoshizawa, Yayoi Kawano, Takehisa Hanawa, Journal of Pharmaceutical Sciences, 112(1), 132, 2023.
   DOI:10.1016/j.xphs.2022.05.013
3. **Direct Observation and Semiquantitative Analysis of Hierarchical Structures in Graft-type Polymer Electrolyte Membranes using the AFM Technique.**
   Motegi Toshinori, Yoshimura Kimio, Yue Zhao, Hiroki Akihiro, Maekawa Yasunari, Langmuir, 38(32), 9992, 2022.
   DOI:10.1021/acs.langmuir.2c01398

Patent

1. **レジスト材料、レジストパターンの製造方法、及び、レジストパターン.**
   吉村 公男, 出崎 亮, 山本 洋揮, タンフン ヂン, 石野 雅彦, 錦野 将元, 前川 康成, 古澤 孝弘, 特願2022-067860 (2022.4.15)

Press

1. **低含水性なのに高イオン伝導性な燃料電池膜：グラフト型高分子電解質膜の構造を初めて観察－親水相内のナノ構造を明らかに－.**
   QST, 2022.8.2 プレス発表; 日刊工業新聞等に掲載

P2-2 Advanced Catalyst Project

Papers

1. **Structural analysis of high-energy implanted Ni atoms into Si(100) by X-ray absorption fine structure spectroscopy.**
   Entani Shiro, Sato Shinichiro, Honda Mitsunori, Suzuki Chihiro, Taguchi Tomitsugu, Yamamoto Shunya, Ohshima Takeshi, radiation physics and chemistry, 199, 110369, 2022.
   DOI:10.1016/j.radphyschem.2022.110369
2. **Supreme-black levels enabled by touchproof microcavity surface texture on anti-backscatter matrix.**
   Kuniaki Amemiya, Yuhei Shimizu, Koshikawa Hiroshi, Hiroshi Shitomi, Yamaki Tetsuya, Science Advances, 9(2), eade4853, 2023. DOI:10.1126/sciadv.ade4853
3. **Morphology and chemical state of platinum ions implanted into glassy carbon substrates.**
   Kimata Tetsuya, Kato Sho, Kobayashi Tomohiro, Yamamoto Shunya, Yamaki Tetsuya, Terai Takayuki, J. Appl. Phys., 132, 175303, 2022. DOI:10.1063/5.010352
4. **Effect of γ-ray irradiation on epoxy network polymers with different curing agents.**
   Hajime KISHI, Ken ARIMURA, Idesaki Akira, Takeshi KAKIBE, Satoshi MATSUDA, Polymers for Advanced Technologies, 33(10), 3740, 2022.
   DOI:10.1002/pat.5825
5. **Investigation of Irradiation Effect on REBCO Coated Conductors for Future Radiation-Resistant Magnet Applications.**
   Masami Iio, Makoto Yoshida, Kento Suzuki, Tatsushi Nakamoto, Michinaka Sugano, Toru Ogitsu, Idesaki Akira, IEEE Transactions on Applied Superconductivity, 32(6), 6601905, 2022.
   DOI:10.1109/TASC.2022.3168620
6. **Mechanism of Ion Track Formation in Silicon by Much Lower Energy Deposition than the Formation Threshold.**
   Amekura Hiroshi, Narumi Kazumasa, Chiba Atsuya, Hirano Yoshimi, Yamada Keisuke, Yamamoto Shunya, Ishikawa Norito, Okubo Nariaki, Toulemonde Marcel, Saito Yuuichi, Physica Scripta, 98(4), 045701, 2023. DOI:10.1088/1402-4896/acbbf5
7. **Active Pt-Nanocoated Layer with Pt–O–Ce Bonds on a CeOx Nanowire Cathode Formed by Electron Beam Irradiation.**
   Mori Toshiyuki, Ke Tong, Yamamoto Shunya, Shipra Chauhan, Kobayashi Tomohiro, Isaka Noriko, Graeme Auchterlonie, Roger Wepf, Suzuki Akira, Ito Shigeharu, Fei Ye, ACS Omega, 22(29), 25822 - 25836, 2022. DOI:10.1021/acsomega.2c03348

Patent

1. **燃料電池用酸化触媒及びその製造方法並びに燃料電池.**
   中川 紳好, 石飛 宏和, 阿部 壮真, 山本 春也, 越川 博, 八巻 徹也, 特許第7139567号 (2022.9.12).

Press

1. **光を99.8%以上吸収する 至高の暗黒シート.**
   産総研・QST, 2023.1.18プレス発表; 毎日新聞, 朝日新聞デジタル, 日本経済新聞web版, 茨城新聞web版, 日刊ケミカルニュース等に掲載.

P2-3 Environmental Polymer Project

Papers

1. **Flow filtration/adsorption and simultaneous monitoring technologies of radiocesium ^{137}Cs in river water.**
   Enomoto Kazuyuki, Hoshina Hiroyuki, Kasai Noboru, Keisuke Kurita (JAEA), Ueki Yuuji, Nagao Yuuto, Yonggen Yin, Suzui Nobuo, Kawachi Naoki, Seko Noriaki, Chemical Engineering Journal, 2023. DOI:doi.org/10.1016/j.cej.2023.141696
2. **Pineapple Fiber Hybrids Prepared by the Fusion of radiation-induced Graft Polymerization and Kabachnik-Fields three-component Reaction (RIGP-KF3CR).**
   Bin Jeremiah D. Barba, Celine Grace V. Causapin, Patrick Jay E. Cabalar, John Andrew A. Luna, Seko Noriaki, Omichi Masaaki, Kakuchi Ryohei, Jordan F. Madrid, Journal of Natural Fibers, 19(16), 13550, 2022. DOI:10.1080/15440478.2022.2101040
3. **A-la-carte surface functionalization of organic materials via the combination of radiation-induced graft polymerization and multi-component reactions.**
   Kakuchi Ryouhei, Matsubara Kiho, Madrid Jordan F., Barba Bin Jeremiah D., Omichi Masaaki, Ueki Yuji, Seko Noriaki, MRS Communications, 12(5), 552, 2022. DOI:10.1557/s43579-022-00255-9

Patents

1. **バネ状ろ過システム及びこれを用いる溶解不純物除去方法.**
   保科 宏行, 瀬古 典明, 物部 長順, 物部 長智, 内村 泰造, 特願2023-8484 (2023.1.24)
2. **核酸吸着材及びその製造方法.**
   加地 恵, 本田 拓也, 植木 悠二, 瀬古 典明, 特願2022-143886 (2022.9.9)
3. **セルロースナノファイバーグラフト重合体の製造方法.**
   植木 悠二, 瀬古 典明, 渡邉 朗, 赤井 日出子, 齊藤 貴宏, 澤田 幸子, 特願2022-145428 (2022.9.13).
4. **水質検査装置、水質検査方法、水質検査システム.**
   瀬古 典明, 保科 宏行, 常井 あゆみ, 内村 泰造, 永倉 和泉, 特願2022- 87862 (2022.5.30)
5. **グルカミン誘導体、グルカミン誘導体からなる金属吸着剤、グルカミン誘導体からなる金属吸着剤を備える金属抽出装置、金属抽出キット.**
   保科 宏行, 瀬古 典明, 濱田 崇, 特許第7220904号 (2023.2.3).
6. **ジチオカルバミン酸基を有する金属吸着材とその製造方法及**

び金属抽出方法.
植木 悠二, 瀬古 典明, 特許第7220894号 (2023.2.3).

P2-4 Biocompatible Materials Project

Papers

1. **Synthesis of Small Peptide Nanogels Using Radiation Crosslinking as a Platform for Nano-Imaging Agents for Pancreatic Cancer Diagnosis.**
   Kimura Atsushi, Arai Tadashi, Ueno Miho, Oyama Kotaro, Hao Yu, Shinichi Yamashita, Otome Yudai, Taguchi Mitsumasa, Pharmaceutics, 14(11), 2400, 2022. DOI:10.3390/pharmaceutics14112400
2. **Preparation and evaluation of hydrogel film containing tramadol for reduction of peripheral neuropathic pain.**
   Nobuyuki Natori, Yuki Shibano, Akihiro Hiroki, Mitsumasa Taguchi, Atsushi Miyajima, Kazumi Yoshizawa, Yayoi Kawano, Takehisa Hanawa, Journal of Pharmaceutical Sciences, 112(1), 132, 2023. DOI:10.1016/j.xphs.2022.05.013
3. **Effects of omecamtiv mecarbil on the contractile properties of skinned porcine left atrial and ventricular muscles.**
   Tomohiro Nakanishi, Oyama Kotaro, Hiroyuki Tanaka, Fuyu Kobirumaki-Shimozawa, Ishii Shuya, Takako Terui, Shin'ichi Ishiwata, Norio Fukuda, Frontiers in Physiology, 13, 947206, 2022. DOI:10.3389/fphys.2022.947206
4. **Mice with R2509C-RYR1 mutation exhibit dysfunctional Ca^{2+} dynamics in primary skeletal myocytes.**
   Yoshitaka Tsuboi, Oyama Kotaro, Fuyu Kobirumaki-Shimozawa, Takashi Murayama, Nogomi Kurebayashi, Toshiaki Tachibana, Yoshinobu Manome, Emi Kikuchi, Satoru Noguchi, Takayoshi Inoue, Yukiko U. Inoue, Ichizo Nishino, Shuichi Mori, Ryosuke Ishida, Hiroyuki Kagechika, Madoka Suzuki, Norio Fukuda, Toshiko Yamazawa, Journal of General Physiology, 154(11), e202213136, 2022. DOI:10.1085/jgp.202213136
5. **Heat-hypersensitive mutants of ryanodine receptor type 1 revealed by microscopic heating.**
   Kotaro Oyama, Vadim Zeeb, Toshiko Yamazawa, Takashi Murayama, Hideto Oyamada, Nagomi Kurebayashi, Fuyu Kobirumaki-Shimozawa, Satoru Noguchi, Takayoshi Inoue, Yukiko U. Inoue, Ichizo Nishino, Yoshie Harada, Norio Fukuda, Shin'ichi Ishiwata, Madoka Suzuki, PNAS, 119(32), e2201286119, 2022. DOI:10.1073/pnas.2201286119

Patent

1. **医薬、並びにその製造方法.**
   田口 光正, 廣木 章博, 木村 敦, 大山 智子, 中島 健吾, 青木 伊知男, 村山 周平, 田畑 泰彦, 城 潤一郎, 特許第7156665号 (2022.10.11).

Press

1. **熱中症の発症予測・メカニズム解明にも寄与 タンパク質の過敏な熱応答で体温上昇が止まらない！ —悪性高熱症の熱産生暴走メカニズム—.**
   大阪大学・QST・東京慈恵会医科大学, 2022.8.8プレス発表; 時事メディカル, 日経バイオテク, Asia Research News等に掲載.

P2-5 Element Separation and Analysis Project

Papers

1. **Reaction pathways for palladium(I) reduction in laser-induced particle formation of Pd: An ab initio molecular orbital study.**
   Kurosaki Yuzuru, Nakanishi Ryuzo, Saeki Morihisa, Oba Hironori, Chemical Physics, 569, 111857, 2023.
2. **Structural analysis of high-energy implanted Ni atoms into Si(100) by X-ray absorption fine structure spectroscopy.**
   Entani Shiro, Sato Shinichiro, Honda Mitsunori, Suzuki Chihiro, Taguchi Tomitsugu, Yamamoto Shunya, Ohshima Takeshi, radiation physics and chemistry, 199, 110369, 2022. DOI:10.1016/j.radphyschem.2022.110369
3. **Recovery of the laser-induced breakdown spectroscopy system using a ceramic microchip deteriorated by radiation for the remote elemental analysis.**
   Tamura Koji, Nakanishi Ryuzo, Ohba Hironori, Taira Takunori, Wakaida Ikuo, Journal of Nuclear Science and Technology, 60(2), 175, 2022. DOI:10.1080/00223131.2022.2091056
4. **Dispersive XAFS Study on the Laser-Induced Reduction of a Rh^{3+} Ion Complex: Presence of a Rh^{+} Intermediate in Direct Photoreduction.**
   Saeki Morihisa, Matsumura Daiju, Nakanishi Ryuzo, Yomogida Takumi, Tsuji Takuya, Saito Hiroyuki, Oba Hironori, Journal of Physical Chemistry C, 126, 5607, 2022. DOI:10.1021/acs.jpcc.1c10160

Patent

1. **金属回収装置、金属回収方法、元素分析装置、及び元素分析方法.**
   中西 隆造, 大場 弘則, 佐伯 盛久, 特願2022-188449 (2022.11.25).

P2-6 Advanced Functional Polymer Materials Research Group

Paper

1. **Direct Observation and Semiquantitative Analysis of Hierarchical Structures in Graft-type Polymer Electrolyte Membranes using the AFM Technique.**
   Motegi Toshinori, Yoshimura Kimio, Yue Zhao, Hiroki Akihiro, Maekawa Yasunari, Langmuir, 38(32), 9992, 2022. DOI:10.1021/acs.langmuir.2c01398

Press

1. **低含水性なのに高イオン伝導性な燃料電池膜：グラフト型高分子電解質膜の構造を初めて観察－親水相内のナノ構造を明らかに－.**
   QST, 2022.8.2 プレス発表; 日刊工業新聞等に掲載.

P3-1 Microbeam Radiation Biology Project

Papers

1. **Responses of hematopoietic cells after ionizing-irradiation in anemic adult medaka (*Oryzias latipes*).**
   Kento Nagata, Keita Ohashi, Chika Hashimoto, Alaa El-Din Hamid Sayed, Takako Yasuda, Bibek Dutta, Takayuki Kajihara, Hiroshi Mitani, Michiyo Suzuki, Tomoo Funayama, Shoji Oda, Tomomi Watanabe-Asaka, International Journal of Radiation Biology, 99(4), 663, 2023. DOI:10.1080/09553002.2022.2110328
2. **Effects of γ-irradiation as phytosanitary treatment on the quality of Japanese fruits and the survival of their regulated pests.**
   Kikuchi Masahiro, Seito Hajime, Kobayashi Yasuhiko, Todoriki Setsuko, Yaginuma Katsuhiko, Kishimoto Hidenari, Mochizuki Masatoshi, Mishiro Koji, Radiation Physics and Chemistry, 208, 110918, 2023. DOI:10.1016/j.radphyschem.2023.110918
3. **重イオンマイクロビームを用いた個体の機能解析研究.**
   鈴木 芳代, 舟山 知夫, 放射線生物研究, 57(2), 114, 2022.
4. **Automatic worm detection to solve overlapping problems using a convolutional neural network.**
   Mori Shinichiro, Tachibana Yasuhiko, Suzuki Michiyo, Harada Yoshinobu, Scientific Reports, 12, 8521, 2022. DOI:10.1038/s41598-022-12576-9

Patents

1. **線虫封入カプセル、線虫封入カプセルの製造方法、および、線虫封入カプセルの用途.**
   鈴木 芳代, PCT/JP2022/045039 (2022.12.7).
2. **線虫トラップ用プレート、およびその利用.**
   鈴木 芳代, 服部 佑哉, 齋藤 俊行, 原田 良信, 特許第7229582号 (2023.2.17).
3. **画像認識プログラム、これを用いた画像認識装置、検出対象個体数計数方法、およびこれらに使用する画像認識学習用モデル画像作成装置.**
   森 慎一郎, 鈴木 芳代, 原田 良信, 立花 泰彦, 服部 佑哉, PCT/JP2023/007082 (2023.2.27).

P3-2 Ion Beam Mutagenesis Project

Papers

1. **Comparative analysis of seed and seedling irradiation with gamma rays and carbon ions for mutation induction in Arabidopsis.**
   Hase Yoshihiro, Sato Katsuya, Kitamura Satoshi, Frontiers in Plant Science, 2023. DOI:10.3389/fpls.2023.1149083
2. **Complete Genome Sequence of the Radioresistant Bacterium *Deinococcus aetherius* ST0316, Isolated from Air Dust collected in the Lower Stratosphere above Japan.**
   Sato Katsuya, Kakeru Hagiwara, Kosuke Katsumata, Aya Kubo, Shin-ichi Yokobori, Akihiko Yamagishi, Yutaka Oono, Issay Narumi, Microbiology Resource Announcements, 11(10), e0083622, 2022. DOI:10.1128/mra.00836-22
3. **Development of a simple multiple mutation detection system using seed-coat flavonoid pigments in irradiated Arabidopsis M_1 plants.**
   Kitamura Satoshi, Hirata Shoya, Sato Katsuya, Inamura Rie, Issay Narumi, Ono Yutaka, Scientific Reports, 12, 22467, 2022. DOI:10.1038/s41598-022-26989z
4. **Effects of carbon ion beam-induced mutagenesis for the screening of RED production-deficient mutants of *Streptomyces coelicolor* JCM4020.**
   Masaomi Yanagisawa, Shumpei Asamizu, Sato Katsuya, Ono Yutaka, Hiroyasu Onaka, PLOS ONE, 17(7), e0270379, 2022. DOI:10.1371/journal.pone.0270379

P3-3 Medical Radioisotope Application Project

Papers

1. **Organic cation transporter 3 mediates the non-norepinephrine transporter driven uptake of meta-[^{211}At]astato-benzylguanidine.**
   Oshima Yasuhiro, Sasaki Ichiro, Watanabe Shigeki, Sakashita Tetsuya, Higashi Tatsuya, Ishioka Noriko, Nuclear medicine and biology, 112, 44 - 51, 2022. DOI:10.1016/j.nucmedbio.2022.06.005
2. **Copper-mediated radioiodination and radiobromination via aryl boronic precursor and its application to ^{125}I/^{77}Br–labeled prostate-specific membrane antigen imaging probes.**
   Kondo Yuto, Kimura Hiroyuki, Sasaki Ichiro, Watanabe Shigeki, Oshima Yasuhiro, Yagi Yusuke, Hattori Yasunao, Koda Manami, Kawashima Hidekazu, Yasui Hiroyuki, Ishioka Noriko, Bioorganic & Medicinal Chemistry, 69(8), 336 - 345, 2022. DOI:10.1016/j.bmc.2022.116915
3. **Radioactive isotope separation with 3D-printed flow-based device.**
   Obata Shohei, Sugo Yumi, Manabe Hinako, Arima Yuto, Toda Kei, Ishioka Noriko, Mori Masanobu, Ohira Shinichi, Analytical Sciences, 2023. DOI:10.1007/s44211-022-00254-9
4. **Comparative evaluation of radionuclide therapy using ^{90}Y and ^{177}Lu.**
   Hirofumi Hanaoka, Kazuyuki Hashimoto, Watanabe Satoshi, Matsumoto Shojiro, Sakashita Tetsuya, Watanabe Shigeki, Ishioka Noriko, Keigo Endo, Annals of Nuclear Medicine, 37, 52, 2022. DOI:10.1007/s12149-022-01803-y
5. **Corrosion Behavior of Iron-Chrome Alloys in Liquid Bismuth.**
   Toshihide Takai, Tomohiro Furukawa, Watanabe Shigeki, Ishioka Noriko, Bulletin of the JSME, 9(4), 21-00397, 2022. DOI:10.1299/mej.21-00397
6. **Highly efficient separation of ultratrace radioactive copper using a flow electrolysis cell.**
   Sugo Yumi, Ohira Shin-ichi, Manabe Hinako, Maruyama Yohei, Yamazaki Naoaki, Miyachi Ryoma, Toda Kei, Ishioka Noriko, Mori Masanobu, ACS Omega, 7(18), 15779, 2022. DOI:10.1021/acsomega.2c00828

Patents

1. **放射性同位体の製造装置、製造システム、及び製造方法.**
   坂下 哲哉, 渡辺 茂樹, 宮脇 信正, 石岡 典子, 特許第022-75333 (2022.4.28)
2. **放射性同位体の製造方法、放射性同位体製造装置.**
   石岡 典子, 近藤 浩夫, 渡辺 茂樹, 特許第7185930 (2022.11.30).

P3-4 Radiotracer Imaging Project

Papers

1. **Spatial distributions of cesium and strontium in tea [*Camellia sinensis (L.) Kuntze*] leaves evaluated by micro-PIXE analysis.**
   寺川貴樹, 桃北啓佑, 服部祥尭, 佐藤光義, 石井慶造, 江夏昌志, 山田尚人, 山縣 諒平, 石井 保行, 鈴井 伸郎, 佐藤 隆博, 河地 有木, International Journal of PIXE, 30(1＆2), 41, 2022. DOI:10.1142/S0129083520500059
2. **Flow filtration/adsorption and simultaneous monitoring technologies of radiocesium ^{137}Cs in river water.**
   Enomoto Kazuyuki, Hoshina Hiroyuki, Kasai Noboru, Keisuke Kurita, Ueki Yuuji, Nagao Yuuto, Yonggen Yin, Suzui Nobuo, Kawachi Naoki, Seko Noriaki, Chemical Engineering Journal, 2023. DOI:doi.org/10.1016/j.cej.2023.141696
3. **DynamicMC: An Open-source GUI Program Coupled with MCNP for Modeling Relative Dynamic Movement of Radioactive Source and ORNL Phantom in a 3-dimensional Radiation Field.**
   Yu, Kwan Ngok, Watabe, Hiroshi, Zivkovic, Milena, Krstic, Dragana, Nikezic, Dragoslav, Kim, Kyeong Min, Yamaya Taiga, Kawachi Naoki, Tanaka, Hiroki, Haque, A.K.F, Shahmohammadi Beni, Mehrdad, Health Physics, 2023. DOI:10.1097/HP.0000000000001670
4. **Time-of-flight based neutron background reduction in secondary-electron-bremsstrahlung imaging for in-vivo range verification of proton therapy: a Monte Carlo study.**
   Yabe Takuya, Yamaguchi Mitsutaka, Tsuda Michiko, Nagao Yuuto, Kawachi Naoki, Journal of Instrumentation, 2023.
5. **Simulation study on carbon-ion beam imaging by measuring secondary electron bremsstrahlung using imaging plate.**
   Tsuda Michiko, Yamaguchi Mitsutaka, Kada Wataru, Kamiya Tomihiro, Sakai Makoto, Watabe Hiroshi, Nagao Yuuto, Yabe Takuya, Kawachi Naoki, Journal of Instrumentation, 2022.
6. **Rice immediately adapts the dynamics of photosynthates translocation to roots in response to changes in soil water environment.**
   Miyoshi Yuta, Fumiyuki Soma, Yonggen Yin, Suzui Nobuo, Noda Yusaku, Enomoto Kazuyuki, Nagao Yuuto, Yamaguchi Mitsutaka, Kawachi Naoki, Yoshida Eiji, Tashima Hideaki, Yamaya Taiga, Noriyuki Kuya, Shota Teramoto, Yusaku Uga, Frontiers in Plant Science, 2022. DOI:10.3389/fpls.2022.1024144
7. **Evaluation and optimization of geometry parameters of GAGG scintillator-based Compton Camera for medical imaging by Monte Carlo simulation.**
   Hajar Zarei, Shahla Razaghi, Yuto Nagao, Masatoshi Itoh, Mitsutaka Yamaguchi, Naoki Kawachi, Mohammad Reza Ay, Hiroshi Watabe, Journal of Instrumentation,

18(1), P01035, 2023.
DOI:10.1088/1748-0221/18/01/P01035

8. **The performance study of developed cost-effective Compton Camera based on Ce:GAGG scintillator using experimental measurements and CCMod of GATE simulation module.**
Hajar Zarei, Yuto Nagao, Kohei Yamamoto, Masatoshi Itoh, Mitsutaka Yamaguchi, Naoki Kawachi, Hiroshi Watabe, Journal of Instrumentation, 17(10), P10012, 2022. DOI:10.1088/1748-0221/17/10/P10012
9. **Advantages of using larger-diameter pinhole collimator for prompt X-ray imaging during irradiation with carbon ions.**
Seiichi Yamamoto, Yabe Takuya, Takashi Akagi, Yamaguchi Mitsutaka, Kawachi Naoki, Kei Kamada, Akira Yoshikawa, Jun Kataoka, Journal of Instrumentation (JINST), 17, P09006, 2022. DOI:10.1088/1748-0221/17/09/P09006
10. **Characterization of zinc uptake and translocation visualized with positron-emitting ^{65}Zn tracer and analysis of transport-related gene expression in two *Lotus japonicus* accessions.**
Noda Yusaku, Jun Furukawa, Suzui Nobuo, Yonggen Yin, Keita Matsuoka, Kawachi Naoki, Shinobu Satoh, Annals of Botany, 130(6), 799, 2022.
DOI:10.1093/aob/mcac101
11. **Diversity of Na^+ allocation in salt-tolerant species of the genus *Vigna*.**
Noda Yusaku, Ryohei Sugita, Atsushi Hirose, Kawachi Naoki, Keitaro Tanoi, Jun Furukawa, Ken Naito, Breeding Science, 72, 326, 2022. **2)**
DOI:10.1270/jsbbs.22012
12. **Deep learning-based in vivo dose verification from proton-induced secondary-electron-bremsstrahlung images with various count level.**
Takuya Yabe, Yamaguchi Mitsutaka, Chih-Chieh Liu, Toshiyuki Toshito, Kawachi Naoki, Seiichi Yamamoto, Physica Medica, 99, 130, 2022.
DOI:10.1016/j.ejmp.2022.05.013
13. **イメージングプレートを用いた粒子線の可視化.**
津田 路子, 山口 充孝, 佐鳥 凌太, 加田 渉, 神谷 富裕, 酒井 真理, 長尾 悠人, 河地 有木, Radioisotopes, 2022. DOI:10.3769/radioisotopes.71.109
14. **The ferroelectric phase transition in a 500 nm sized single particle of $BaTiO_3$ tracked by coherent X-ray diffraction.**
Oshime Norihiro, Ohwada Kenji, Machida Akihiko, Fukushima Nagise, Ueno Shintaro, Fujii Ichiro, Wada Satoshi, Sugawara Kento, Shimada Ayumu, Ueno Tetsuro, Watanuki Tetsu, Ishii Kenji, Toyokawa Hidenori, Momma Koichi, Kim Sangwook, Tsukada Shinya, Kuroiwa Yoshihiro, Japanese Journal of Applied Physics (Special Issues: Ferroelectric Materials and Their Applications), 61(SN), 1008, 2022. DOI:10.35848/1347-4065/ac7d94

Patents

1. **師管転流の制御場所決定方法、農作物の生産方法、生きた植物に使用される造影剤.**
尹 永根, 三好 悠太, 鈴井 伸郎, 河地 有木, 特願2022-123629 (2022.8.2).
2. **制動X線スペクトルを用いた人体内散乱の評価手法（発明の名称：粒子線モニタリング装置、粒子線モニタリング方法、粒子線モニタリングプログラム）.**
酒井 真理, 中野 隆史, 荒川 和夫, 菊地 美貴子, 山口 充孝, 長尾 悠人, 河地 有木, 特許第7061741 (2022.4.21).

Press

1. **ナトリウムの可視化で明らかになった多様な耐塩性 －アズキ近縁種の多様な耐塩性が超耐塩性作物創出に道を拓く－.**
農研機構・QST・筑波大学・東京大学, 2023.3.8 プレス発表; 農業協同組合新聞等に掲載.
2. **干ばつを生き抜くイネの戦略 ～RI イメージング技術で初めて捉えた根の水分に対する応答～.**
QST・農研機構, 2023.1.18プレス発表; 読売新聞, 日本経済新聞, 東京新聞, 上毛新聞, 農業協同組合新聞等に掲載.

P3-5 Generation of Radioisotopes with Accelerator Neutrons Project

Paper

1. **Estimated Isotopic Compositions of Yb in Enriched ^{176}Yb for Producing ^{177}Lu with High Radionuclide Purity by ^{176}Yb(*d*,*x*)^{177}Lu.**
Yasuki Nagai, Masako Kawabata, Shintaro Hashimoto, Kazuaki Tsukada, Kazuyuki Hashimoto, Shoji Motoishi, Hideya Saeki, Arata Motomura, Futoshi Minato, and Masatoshi Itoh, Journal of the Physical Society of Japan, 91, 044201, 2022. DOI: 10.7566/JPSJ.91.044201

Patent

1. **α線放出核種の分析方法及び分析装置.**
瀬川 麻里子, 藤 暢輔, 前田 亮, 西中 一朗, 特許第7128479号 (2022.08.23).

P4-1 LCS Gamma-ray Project

Papers

1. **Generation of primary photons through inverse Compton scattering using a Monte Carlo simulation code.**
   Ginfranco Paterno, Paolo Cardarelli, Matteo Bianchini, Angelo Taibi, Illya Drebot, Vittoria Petrillo, Hajima Ryoichi, Physical Review Accelerator and Beams, 25, 084601, 2022.
   DOI:10.1103/PhysRevAccelBeams.25.084601
2. **Scaling Law on Laser-driven Neutron Generation Realizing Single-Shot Resonance Spectroscopy.**
   A. Yogo, Z. Lan, Y. Arikawa, Y. Abe, S.R. Mirfayzi, T. Wei, T. Mori, D. Golovin, T. Hayakawa, N. Iwase, S. Fujioka, M. Nakai, Y. Sentoku, K. Mima, M. Koizumi, F. Ito, J. Lee, T. Takahashi, K. Hironaka, S. Kar, Physical Review X, (13), 011011, 2023. DOI:10.1103/PhysRevX.13.011011
3. **Evidence for enrichment of niobium-92 in the outer protosolar disk.**
   Yuki Hibiya, Tsuyoshi Iizuka, Hatsuki Enomoto, Takehito Hayakawa, The Astrophysical Journal Letters, (942), L15, 2023. DOI:10.3847/2041-8213/acab5d
4. **Neutron Capture Cross-Section of Lead-204 Measured by Mass Spectrometry.**
   Shoji Nakamura, Yuji Shibahara, Atsushi Kimura, Shunsuke Endo, Shizuma Toshiyuki, Journal of Nuclear Science and Technology, 2022.
5. **Low-lying dipole strength distribution in ^{204}Pb.**
   Shizuma Toshiyuki, S. Endo, R. Beyer, A. Kimura, R. Massarczyk, R. Schwengner, T. Hensel, H. Hoffmann, A. Junghans, K. Romer, S. Turkat, A. Wagner, N. Tsoneva, Physical Review C, 106(4), 044326, 2022.
   DOI:10.1103/PhysRevC.106.044326
6. **Comprehensive Analysis of the Neutrino Process in the Core-collapsing Supernovae.**
   Heamin Ko, Dukjae Jang, Myung-Ki Cheoun, Motohiko Kusakabe, Hirokazu Sasaki, Xingqun Yao, Toshitaka Kajino, Takehito Hayakawa, Masaomi Ono, Toshihiko Kawano, Grant J. Mathews, The Astrophysical Journal, 937(2), 116, 2022. DOI:10.3847/1538-4357/ac88cd
7. **Neutron Measurement from Spent Nuclear Fuel via H(n,γ) Method.**
   Yasushi Nauchi, Shunsuke Sato, Takehito Hayakawa, Yasuhiko Kimura, Kenya Suyama, Takao Kashima, Nuclear Instruments and Methods in Physics Research Section A, 1050, 168109, 2023.
   DOI:doi.org/10.1016/j.nima.2023.168109
8. **Absolute quantification of ^{137}Cs activity in spent nuclear fuel with calculated detector response function.**
   Shunsuke Sato, Yasushi Nauchi, Takehito Hayakawa, Yasuhiko Kimura, Takao Kashima, Kazuhiro Futakami, Kenya Suyama, Journal of Nuclear Science and Technology, 2023.
   DOI:https://doi.org/10.1080/00223131.2022.2130462
9. **Calculating off-axis efficiency of coaxial HPGe detectors by Monte Carlo simulation.**
   Mohamed Omer, Shizuma Toshiyuki, Hajima Ryoichi, Mitsuo Koizumi, Radiation Physics and Chemistry, 198, 110241, 2022.
   DOI:10.1016/j.radphyschem.2022.110241
10. **Thermal neutron fluence measurement by Cadmium differential method at laser-driven neutron source.**
    Takato Mori, Akifumi Yogo, Takehito Hayakawa, Seyed R. Mirfayzi, Zechen Lan, Tianyun Wei, Yuki Abe, Yasunobu Arikawa, Mitsuo Nakai, Kunioki Mima, Hiroaki Nishimura, Shinsuke Fujioka, Journal of Physics G: Nuclear and Particle Physics, 49(6), 065103, 2022. DOI:10.1088/1361-6471/ac6272
11. **Non-destructive inspection of water or high-pressure hydrogen gas in metal pipes by the flash of neutrons and X-rays generated by laser.**
    Tianyun Wei, Akifumi Yogo, Takehito Hayakawa, Yasunobu Arikawa, Yuki Abe, Maiko Nakanishi, Seyed Reza Mirfayzi, Zechen Lan, Takato Mori, Kunioki Mima, Shinsuke Fujioka, Masakatsu Murakami, Mitsuo Nakai, Hiroaki Nishimura, Satyabrata Kar, Ryosuke Kodama, AIP advances, 12, 045220, 2022.
    DOI:10.1063/5.0088997
12. **High power light source for future extreme ultraviolet lithography based on energy-recovery linac free-electron laser.**
    Hiroshi Kawata, Norio Nakamura, Hiroshi Sakai, Ryukou Kato, Hajima Ryoichi, Journal of Micro/Nanopatterning, Materials, and Metrology, 21(2), 021210, 2022.
    DOI:10.1117/1.JMM.21.2.021210

Press

1. **発見！レーザーで中性子を発生する新法則― 1 千万分の 1 秒の瞬間で元素を透過識別する装置がコンパクトに―**
   大阪大学・QST・JAEA・福井工業大学・クイーンズ大学,
   2023.1.31プレス発表; 科学新聞,日経クロステック等に掲載.

P4-2 Beam Engineering Section

Papers

1. **Spatial distributions of cesium and strontium in tea [*Camellia sinensis (L.) Kuntze*] leaves evaluated by micro-PIXE analysis.**
   寺川貴樹, 桃北啓佑, 服部祥尭, 佐藤光義, 石井慶造, 江夏昌志, 山田尚人, 山縣 諒平, 石井 保行, 鈴井 伸郎, 佐藤 隆博, 河地 有木, International Journal of PIXE, 30(1＆2), 41, 2022. DOI:10.1142/S0129083520500059
2. **Utilizing a photosensitive dry film resist in proton beam writing.**

Hironori Sek, Keiya Kawamura, Hidetaka Hayashi, Ishii Yasuyuki, Nitipon Puttaraksa, Hiroyuki Nishikawa, Japanese Journal of Applied Physics, 61, SD1006, 2022. DOI:10.35848/1347-4065/ac55e1

3. **Mechanism of Ion Track Formation in Silicon by Much Lower Energy Deposition than the Formation Threshold.**
   Amekura Hiroshi, Narumi Kazumasa, Chiba Atsuya, Hirano Yoshimi, Yamada Keisuke, Yamamoto Shunya, Ishikawa Norito, Okubo Nariaki, Toulemonde Marcel, Saito Yuuichi, Physica Scripta, 98(4), 045701, 2023. DOI:10.1088/1402-4896/acbbf5
4. **Morphological changes of nanostructures on silicon induced by C_{60}-ion irradiation.**
   Oishi Naoto, Murao Yoshiki, Nitta Noriko, Tsuchida Hidetsugu, Tomita Shigeo, Sasa Kimikazu, Hirata Kouichi, Shibata Hiromi, Hirano Yoshimi, Yamada Keisuke, Chiba Atsuya, Saito Yuuichi, Narumi Kazumasa, Hoshino Yasushi, Journal of Vacuum Science and Technology, 40(6), 036103, 2022.
   DOI:10.1116/6.0002073
5. **Structure and Magnetic Properties of Fe Nanoparticles in Amorphous Silica Implanted with Fe Ions and Effect of Subsequent Energetic Heavy Ion Irradiation.**
   A. Iwase, K. Fukuda, Saito Yuuichi, Y. Okamoto, S. Semboshi, H. Amekura, T. Matsui, Journal of Applied Physics, 132(16), 163902, 2022.
   DOI:10.1063/5.0102438
6. **Effects of Energetic Carbon-Cluster Ion Irradiation on Lattice Structures of $EuBa_2Cu_3O_{7-x}$ Oxide Superconductor.**
   Iwase Akihiro, Saitoh Yuichi, Chiba Atsuya, Hori Fuminobu, Ishikawa Norito, quantum beam science, 6(21), 6020021, 2022. DOI:10.3390/ qubs6020021
7. **Flow filtration/adsorption and simultaneous monitoring technologies of radiocesium ^{137}Cs in river water.**
   Enomoto Kazuyuki, Hoshina Hiroyuki, Kasai Noboru, Keisuke Kurita, Ueki Yuuji, Nagao Yuuto, Yonggen Yin, Suzui Nobuo, Kawachi Naoki, Seko Noriaki, Chemical Engineering Journal, 2023.
   DOI:doi.org/10.1016/j.cej.2023.141696
8. **Evaluation and optimization of geometry parameters of GAGG scintillator-based Compton Camera for medical imaging by Monte Carlo simulation.**
   Hajar Zarei, Shahla Razaghi, Yuto Nagao, Masatoshi Itoh, Mitsutaka Yamaguchi, Naoki Kawachi, Mohammad Reza Ay, Hiroshi Watabe, Journal of Instrumentation, 18(1), P01035, 2023.
   DOI:10.1088/1748-0221/18/01/P01035
9. **The performance study of developed cost-effective Compton Camera based on Ce:GAGG scintillator using experimental measurements and CCMod of GATE simulation module.**
   Hajar Zarei, Yuto Nagao, Kohei Yamamoto, Masatoshi Itoh, Mitsutaka Yamaguchi, Naoki Kawachi, Hiroshi Watabe, Journal of Instrumentation, 17(10), P10012, 2022. DOI:10.1088/1748-0221/17/10/P10012

Patents

1. **低分子量ポリテトラフルオロエチレンの製造方法.**
   田中 孝之, 佐藤 数行, 塚本 充郎, 大島 明博, 長澤 尚胤, 清藤 一, 山崎 翔太, 特願2022-08358 (2022.5.16).
2. **荷電粒子ビーム強度分布可変装置、荷電粒子ビーム強度分布可変方法、二次粒子生成装置、及び放射性同位体生成装置.**
   福田 光宏, 百合 庸介, 特許第7181524号 (2022.11.22).
3. **放射性同位体の製造装置、製造システム、及び製造方法.**
   坂下 哲哉, 渡辺 茂樹, 宮脇 信正, 石岡 典子, 特許第022-75333 (2022.4.28).

QST Takasaki Annual Report 2022
(Ed) YAMAMOTO Hiroyuki

Date of Publishing : March 2024
Editorial committee : YAMAMOTO Hiroyuki, OHSHIMA Takeshi, ISHIOKA Noriko S.,
SAITOH Yuichi and TAGUCHI Mitsumasa

Publication : Takasaki Institute for Advanced Quantum Science
National Institutes for Quantum Science and Technology
1233 Watanuki, Takasaki, Gunma 370-1292, Japan

Tel : +81-27-346-9232
E-mail : taka-annualrep@qst.go.jp
Homepage : https://www.qst.go.jp/site/taka/

QST-M-47

https://www.qst.go.jp